



Size-independent separation of vertically focused particles using the principal component of acoustic radiation force in a continuous flow

Husnain Ahmed, Ghulam Destgeer, Jinsoo Park, Jin Ho Jung, Raheel Ahmad, Kwangseok Park, and Hyung Jin Sung*

Flow control Laboratory, Department of Mechanical Engineering, KAIST, Daejeon, 34141, South Korea.
Email: husnain@kaist.ac.kr, hjsung@kaist.ac.kr, URL: <http://flow.kaist.ac.kr/>

Introduction

We demonstrate a microfluidic method for the continuous separation of similar sized polystyrene (PS 5 μm) and polymethylmethacrylate (PMMA 5 μm) particles using the vertical component of acoustic radiation force. Previously our study group[1] and Ma *et. al*[2] utilized the forces in the horizontal plane for the manipulation of particles based on its mechanical properties. A particle suspended in fluid experiences a direct acoustic radiation force (ARF) when a traveling SAW originating from interdigitated transducer (IDT) patterned on piezoelectric substrate coupled with the fluid inside a microfluidic channel at Rayleigh angle ($\sim 22^\circ$). The ARF can be resolved into vertical F_v and horizontal F_h components where the former being 2.5 times greater than the latter. To date, majority of the SAW-based microfluidic devices rely on horizontal component of the ARF that migrates the pre-aligned particles laterally across the microchannel width.[1]–[3] Although vertical component of the ARF is more than twice the horizontal component, it has been ignored in the past. In the present work, we utilized the vertical component of acoustic radiation force for the continuous separation of similar sized particles (different materials) by steeply focusing them in the vertical plane. This method enables high-throughput and efficient separation of particles over a wide range of flow rates.

Working Mechanism

The acoustofluidic particle separation device is composed of a piezoelectric substrate (LN) with interdigitated transducer (IDT) deposited on top of it. A straight PDMS microchannel having two inlets and two outlets port is mounted above the IDT in such a way that the IDT is placed between the second inlet and first outlet. A mixture of PS and PMMA particles solution is injected through the first of the two outlets with the flow rate of Q_1 (500 $\mu\text{L/hr}$) and a sheath flow in the form of deionized water is introduced through the second outlet with the flow rate of Q_2 (4500 $\mu\text{L/hr}$) to focus the particles mixture in the downward streamlines before the separation zone. Similarly, one of the two outlets was used to suck the fluid at a flow rate of Q_3 (500 $\mu\text{L/hr}$) or Q_4 (4500 $\mu\text{L/hr}$) while the remaining fluid was collected at the other outlet (Q_3 or Q_4).

Results

During power off, all the particles were kept on flowing through the lower streamlines and collected through the second outlet, results in no separation (see Figure 1(A)). Previous studies have shown that the deflection of PS particles is greater than that of the PMMA particles for a particular frequency range (125-140MHz).[1] So, once the AC signal of 140MHz was given to the device, the horizontal component F_h of ARF slowed down the motion of the particles against the direction of flow due to resultant drag force F_d on the particles and the major component F_v of ARF pushed both PS and PMMA particles in the upper streamlines based on their acoustic impedance. By manipulating the flow rate at both the outlets PS particles were collected through the first outlet and PMMA particles were collected through the second outlet as shown in Figure 1(B).

Sample analysis

The collected sample at each outlet was analyzed by using hemocytometer chip (see Figure 2(A)). Five samples (10 μL each) from each outlet were examined for particles counting. PS and PMMA (5 μm) particles were collected through 1st and 2nd outlet with 86.70% and 98.1% efficiency respectively (see Figure 2(B)). The comparatively low efficiency at the 1st outlet was attributed to the large size distribution of manufactured PMMA particles. In future, we are keen to use NIST standard particles to minimize the problem of the large size distribution of particles. In addition to the separation of PS and PMMA particles, we are looking to further explore the properties of different material particles like fused silica, melamine, glass and silicon dioxide microspheres etc.

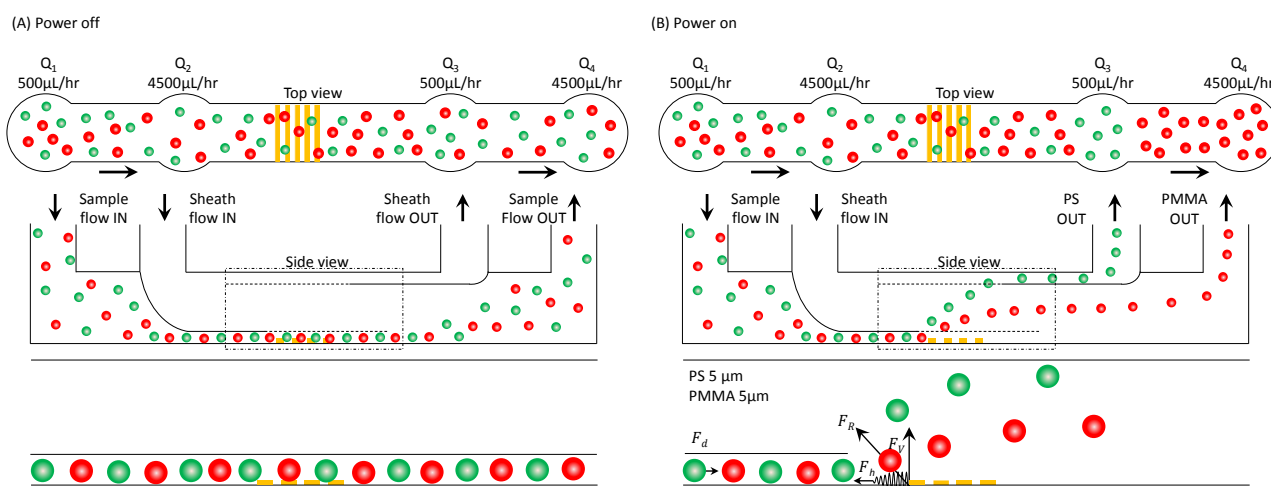


Figure 1: A schematic diagram showing the vertical component of acoustic radiation force-based particle size independent separation device composed of a straight interdigitated transducer patterned on the lithium niobate substrate and PDMS microchannel positioned on top of it. (A), (B) Showing the top side views and particles separation zone when the SAW was turned off and on respectively. Particles are slowed down by the horizontal component of ARF F_h and pushed in the upward direction depending on acoustic impedance of particles due to the vertical component of ARF F_v .

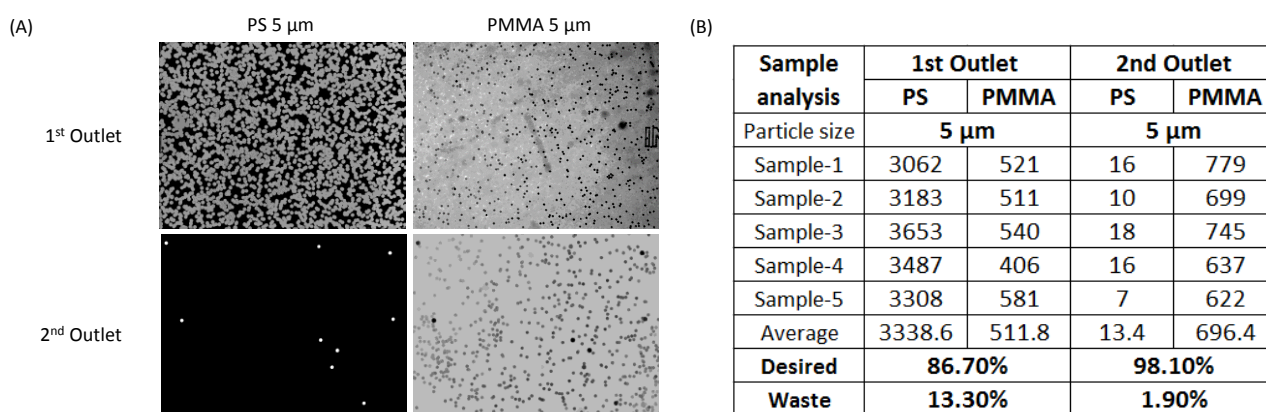


Figure 2: Experimental images (A) and sample analysis (B) of particles collected from 1st and 2nd outlet.

Conclusion

We currently separated two different material PS and PMMA particles having a similar diameter (5 μm) but different acoustic impedance in a continuous flow by utilizing the larger component of ARF. Our future target is to manipulate fused silica, melamine, glass and silicon dioxide microspheres using a similar technique.

Acknowledgement

This work was supported by the Creative Research Initiatives (no. 2017-013369) program of the National Research Foundation of Korea (MSIP), the KUSTAR-KAIST Institute, and KAIST-funded K-Valley RED&B Project (2016).

References

- [1] G. Destgeer, J. H. J. H. Jung, J. S. J. S. Park, H. Ahmed, K. Park, R. Ahmad, H. J. H. J. Sung, B. H. B. H. Ha, J. S. J. S. Park, J. H. J. H. Jung, A. Alazzam, and H. J. H. J. Sung, "Acoustic impedance-based manipulation of elastic microspheres using travelling surface acoustic waves," *RSC Adv.*, vol. 7, no. 36, pp. 22524–22530, 2017.
- [2] Z. Ma, D. J. Collins, J. Guo, and Y. Ai, "Mechanical Properties Based Particle Separation via Traveling Surface Acoustic Wave," *Anal. Chem.*, vol. 88, no. 23, pp. 11844–11851, Dec. 2016.
- [3] G. Destgeer, B. H. Ha, J. Park, J. H. Jung, A. Alazzam, and H. J. Sung, "Microchannel anechoic corner for microparticle manipulation via travelling surface acoustic waves," in *Physics Procedia*, 2015, vol. 70.



Hydrodynamic interactions in acoustofluidic multibody simulations in the Rayleigh limit and beyond

Thierry Baasch¹, Ivo Leibacher¹ and Jürg Dual¹

¹Department of Mechanical Engineering, Institute for Mechanical Systems, ETH Zurich, Zurich, Switzerland
E-mail: baasch@imes.mavt.ethz.ch

Introduction

In acoustophoresis, sound is used for the contactless handling of particles and cells.

The acoustic radiation force, a non-zero time averaged effect, is the main driving factor of the particle motion in the acoustic field, besides hydrodynamic and contact forces.

Theoretical values for this acoustic radiation force can be obtained for single spherical particles at simplified conditions [1,2]. A recent study presented a simplified model for the acoustic interactions of multiple particles in the Rayleigh limit [3]. However, to achieve satisfying results for the dynamics of multiple particles, the hydrodynamic interactions and contact laws should be taken into account, this has only been done very recently [4].

We combined the analytical model of the acoustic particle-particle interactions with a Stokesian dynamics formulation [5] for the hydrodynamic interactions and a Moreau type time-stepper [6], able to handle non-smooth set-valued contact laws. Good qualitative agreement could be found between numerically obtained trajectories and experiments [4].

Using the semi-analytical model [3] limits the application range of the algorithm to the Rayleigh limit, i.e. wavelengths much larger than the particle diameter.

In surface acoustic wave applications, however, the wavelength is close to the particle diameter [7] and the acoustic forces cannot be calculated using Rayleigh limit approximations.

This issue is resolved by using the FEM COMSOL Multiphysics Software to calculate the acoustic radiation force.

Exemplarily, we numerically investigate the One Cell Per Well (OCPW) technology by Collins et al. [7]. Interestingly, we observe a frequency based stability exchange of the equilibrium points, not explainable by the linear Gor'Kov theory and find that the acoustic particle-particle interactions only play a minor role in the trapping efficiency of the OCPW technology.

Methods

The equations of motion of multiple acoustically and hydrodynamically interacting particles are given by,

$$\mathbf{M}\ddot{\mathbf{q}} - \mathbf{R}\dot{\mathbf{q}} = \mathbf{F}_a + \mathbf{F}_c,$$

where \mathbf{M} is the inertial matrix, \mathbf{R} the hydrodynamic resistance matrix, \mathbf{F}_a the vector of the acoustic forces and \mathbf{F}_c the vector of the contact forces.

In the Stokes limit approximation the particles reach their terminal velocity instantly and the accelerations are neglected.

The dynamical problem then reduces to finding the \mathbf{R} matrix and the force vectors \mathbf{F}_a and \mathbf{F}_c at every time-step.

Multiple methods on modelling and approximating \mathbf{R} in the Stokes limit have been published, we adapt the method presented by Durlofsky et al. [5]. They approximate \mathbf{R} by pairwise adding the nearfield lubrication terms to the far field hydrodynamic interactions.

The acoustic force vector depends on the positions of the particles and can be found by either using a semi-analytical formulation [3] or using the FEM COMSOL Multiphysics software.

At each time-step, the resistance matrix and acoustic radiation force are determined. We use a proximal point algorithm to find the contact forces such that the impenetrability condition is fulfilled, as described in [4].

Results

The algorithm was used to calculate the trajectories of Kisker glass particles in a one-dimensional acoustic standing wave. These results were compared with experiments as shown in Fig. 1. Additionally we simulated the one cell per acoustic well trapping used in surface acoustic wave technology as shown in Fig. 2. Here the acoustic forces are simulated using COMSOL as the wavelength is too small to apply Rayleigh limit techniques.

100 μm

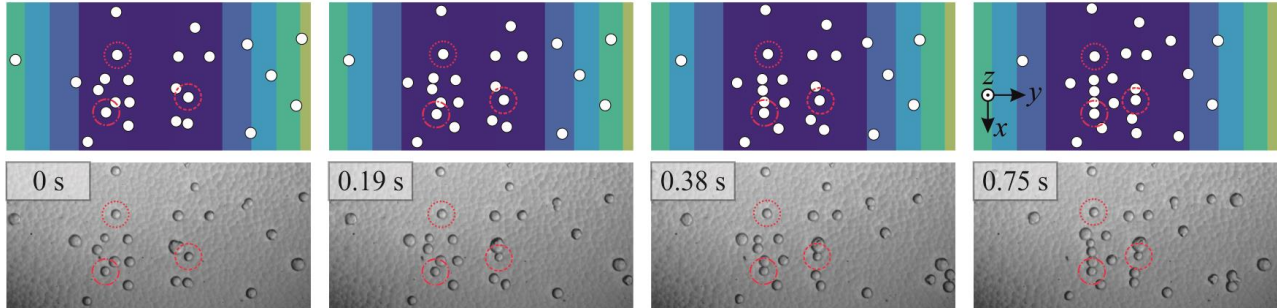


Figure 1 shows multiple Kisker glass particles of 10 μm diameter immersed in water. An acoustic standing wave is established in the y direction at a frequency of 1481 kHz. The four bottom panels show the experimental results. In the course of 0.75 seconds the particles gather at the pressure nodal line. The particles can be seen to form chains, this is due to the acoustic particle-particle interactions. Ultimately, the particles collect in several repelling chains in the pressure nodal line forming a striped pattern often observed in experiments [4]. The top panels show the corresponding multibody simulation. The colored background illustrates the Gor’Kov potential. Areas of high potential are marked in green whereas areas of low potential are colored blue. The hydrodynamics, incorporating near field lubrication and far field interactions, are introduced using the resistance matrix. The only free parameter was the pressure amplitude of the wave, where 0.8 MPa yielded good results. The three particles marked by red circles are chosen exemplarily to show the good agreement between simulation and experiment.

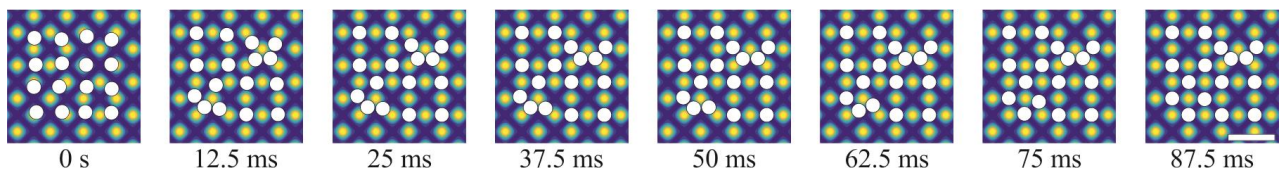


Figure 2 shows the trajectories of multiple 6.1 μm polystyrene particles immersed in water. The background pressure field consists of two orthogonal standing waves of 14 μm wavelength, which is typical for surface acoustic wave (SAW) applications. The colored background of the panels shows the squared pressure amplitude, yellow areas indicate high pressures and blue areas are pressure nodes. In the course of the simulation the particles migrate from their initial positions to the pressure nodal points. The simulation is carried out using COMSOL Multiphysics to calculate the acoustic radiation force at each time-step. Although the particles start touching, our algorithm prevents overlapping of the bodies and hence is very stable during the time-stepping. The scale bar in the last panel is 20 μm long.

Conclusion

We expanded existing acoustofluidic multibody dynamics models by hydrodynamic effects and augmented the range of applicability to wavelengths close to the particle diameter. We were able to simulate the trajectories of multiple acoustically and hydrodynamically interacting particles. Our numerical results allow us to gain deeper insights in the particle chain formation and the one cell per acoustic well technology.

References

- [1] L. P. Gor’Kov. Soviet Physics Doklady. Vol. **6**. (1962).
- [2] M. Settnes, and H. Bruus. Physical Review E **85.1** (2012).
- [3] G. T. Silva and H. Bruus. Phys. Rev. E **90.6**, 063007 (2014).
- [4] T. Baasch, I. Leibacher, and J. Dual. The Journal of the Acoustical Society of America **141.3** (2017).
- [5] L. Durlofsky, J. F. Brady, and G. Bossis. Journal of fluid mechanics **180** (1987).
- [6] J. Moreau. *Unilateral Contact and dry friction in finite freedom dynamics*. Springer Vienna (1988).
- [7] D. J. Collins, B. Morahan, J. Garcia-Bustos, C. Doerig, M. Plebanski and A. Neild. Nature communications **6** (2015).



Effective modeling of acoustic boundary layers in acoustofluidic systems with curved oscillating walls

Jacob S. Bach and Henrik Bruus

Department of Physics, Technical University of Denmark, Kongens Lyngby, Denmark
 E-mail: jasoba@fysik.dtu.dk, URL: <http://www.fysik.dtu.dk/microfluidics>

Introduction

One essential concept in microscale acoustofluidics in water at MHz frequencies, is the acoustic boundary layers that occupy a narrow region of short width $\delta \sim 0.5 \mu\text{m}$ near the walls. Remarkably, these thin boundary layers are responsible for the damping of the acoustic wave and the generation of acoustic streaming, both being bulk phenomena occurring on the large length scale $d \gg \delta$. To study this, we extend the current effective boundary-layer models for first-order acoustics and second-order streaming to systems with oscillating curved walls. We calculate analytically the variations on the short length scale δ perpendicular to the walls, and use this in the boundary conditions on effective fields varying only on the long length scale d .

Effective model for first-order boundary layers

In our first-order analysis, we make a Helmholtz decomposition [1] of the first-order acoustic velocity field $\mathbf{v}_1 = \mathbf{v}_1^\delta + \mathbf{v}_1^d$, with $\nabla \cdot \mathbf{v}_1^\delta = 0$ and $\nabla \times \mathbf{v}_1^d = \mathbf{0}$. Here, the superscripts denotes whether a field varies on the short length scale δ or the long one d , respectively. The governing equations for \mathbf{v}_1^δ , \mathbf{v}_1^d and the pressure p_1 all take the form of damped Helmholtz equations,

$$\nabla^2 \mathbf{v}_1^d + k_c^2 \mathbf{v}_1^d = \mathbf{0} \quad \text{and} \quad \nabla^2 p_1 + k_c^2 p_1 = 0, \quad \text{with} \quad k_c^2 = (1 - i\Gamma)k_0^2, \quad (1a)$$

$$\nabla^2 \mathbf{v}_1^\delta + k_s^2 \mathbf{v}_1^\delta = \mathbf{0}, \quad \text{with} \quad k_s^2 = \frac{2i}{\delta^2}, \quad (1b)$$

$$\mathbf{v}_1^{\delta 0} + \mathbf{v}_1^{d 0} = \mathbf{V}_1, \quad \text{at all surfaces.} \quad (1c)$$

Here, $k_0 = \omega/c_0$ is the wavenumber at angular frequency ω and speed of sound c_0 , $\Gamma \sim 10^{-5}$ is the bulk damping coefficient for water at MHz frequencies, \mathbf{V}_1 is the velocity of the wall, and superscript "0" denotes values at the surface. Using the approximation $\nabla^2 \mathbf{v}_1^\delta \approx \partial_\perp^2 \mathbf{v}_1^\delta$, we obtain $\mathbf{v}_1^\delta \approx \mathbf{v}_1^{\delta 0} e^{ik_s \zeta}$, where $\mathbf{v}_1^{\delta 0} \equiv \mathbf{V}_1 - \mathbf{v}_1^{d 0}$, and ζ is the perpendicular (\perp) distance to the

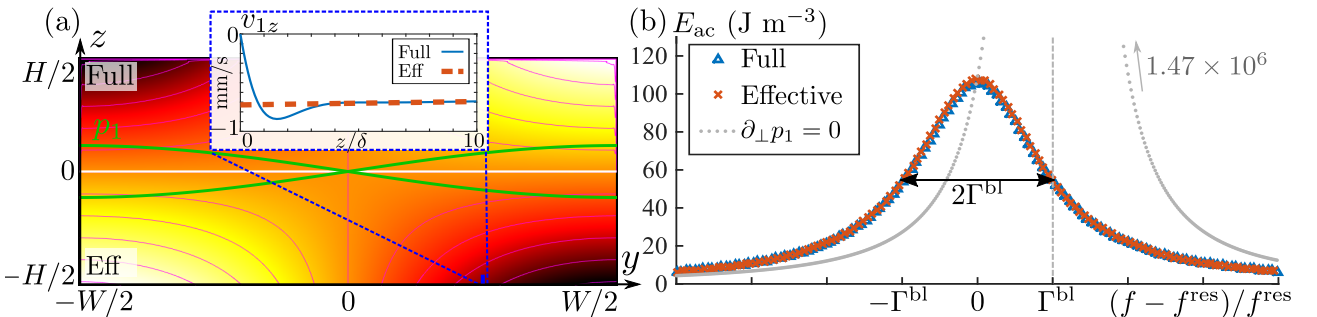


Figure 1: First-order results for a rectangular channel of height $H = 160 \mu\text{m}$ and width $W = 380 \mu\text{m}$ for the standing half-wave resonance p_1 (green) at frequency $f^{\text{res}} = 1.967 \text{ MHz}$. (a) Velocity comparison: full v_{1z} (upper) and effective v_{1z}^d (lower) from -1 mm/s (black) to 1 mm/s (white). Inset: velocity profiles close to the lower surface at $y = W/4$ (short blue line). (b) The acoustic energy density E_{ac} as a function of frequency f close to f^{res} for three models: full, effective, and the simple $\partial_\perp p_1 = 0$ neglecting the novel k_s^{-1} -term in Eq. (2).

surface. Incompressibility $\nabla \cdot \mathbf{v}_1^\delta = 0$ then leads to the boundary condition on p_1 ,

$$\partial_\perp p_1 = i\omega\rho_0 V_{1\perp} - \frac{i}{k_s} \left[\partial_\perp^2 p_1 + k_0^2 p_1 + i\omega\rho_0 \nabla_\parallel \cdot \mathbf{V}_{1\parallel} \right], \quad \text{at all surfaces}, \quad (2)$$

where ρ_0 is the fluid mass density. For a rectangular channel, we compare in Fig. 1 analytical and numerical results from the effective model, with a full numeric model, where the boundary layers are resolved [4]. There is excellent agreement between the full and effective models: Same p_1 and E_{ac} , same boundary-layer damping $\Gamma^{\text{bl}} = \frac{\delta}{2H} \gg \Gamma$, same frequency shift $f^{\text{res}} = (1 - \Gamma^{\text{bl}}) \frac{c_0}{2W}$, and same \mathbf{v}_1 , even the tiny $v_{1z} \sim (k_0\delta)v_{1y}$ component neglected in standard pressure acoustics.

Effective model for acoustic streaming

In our second-order analysis, we consider the length-scale decomposition $\mathbf{v}_2 = \mathbf{v}_2^\delta + \mathbf{v}_2^d$ and $p_2 = p_2^\delta + p_2^d$ into the short δ part and long d part, respectively. Solving the short-scale part of the Navier–Stokes equation together with the boundary condition $\mathbf{v}_2 + \langle \frac{i}{\omega} \mathbf{V}_1 \cdot \nabla \mathbf{v}_1 \rangle = \mathbf{0}$ [3], we derive a boundary condition for $\mathbf{v}_{2\parallel}^d$ in the direction of the surface tangent vector \mathbf{e}_\parallel ,

$$\mathbf{v}_{2\parallel}^{d0} = -\frac{\mathbf{e}_\parallel}{2\omega} \cdot \left\{ \langle \mathbf{v}_1^{\delta 0} \cdot \nabla \mathbf{v}_1^{\delta 0} \rangle + \langle i\mathbf{v}_1^{\delta 0} [2\nabla \cdot \mathbf{v}_1^d - 4\partial_\perp v_\perp^d + (2-i)k_s v_{1\perp}^{\delta 0}] \rangle + 2\langle i\mathbf{V}_1 \cdot \nabla \mathbf{v}_1^d \rangle + 2\langle i\mathbf{v}_1^{\delta 0} \cdot \nabla \mathbf{V}_1 \rangle \right\}. \quad (3)$$

A similar but lengthier expression is derived for the perpendicular part $\mathbf{v}_{2\perp}^{d0}$. For the rectangular channel in Fig. 1, we find at $z = \pm H/2$, where $\mathbf{v}_{2\parallel}^{d0} = v_{2y}^{d0} \mathbf{e}_y$ and $v_{2\perp}^{d0} = \mp v_{2z}^{d0}$, that

$$v_{2y}^{d0} = -\frac{1}{2\omega} \left\{ \langle (3-i)v_{1y}^{d0} \partial_y v_{1y}^{d0} \rangle \right\} = +\frac{3U^2}{8c_0} \sin(2k_0 y), \quad (4a)$$

$$v_{2z}^{d0} = \mp \frac{\delta}{4\omega} \left\{ k_0^2 \langle (11-i)v_{1y}^d v_{1y}^d \rangle - \langle (9-3i) \partial_y v_{1y}^d \partial_y v_{1y}^d \rangle \right\} = \mp \frac{k_0 \delta U^2}{8c_0} [1 + 10 \cos(2y)], \quad (4b)$$

where we in the last expressions have inserted $v_{2y}^{d0} = U \cos(k_0 y)$. Eq. (4a) is the well-known result by Rayleigh, while v_{2z}^{d0} is a new result with $|v_{2z}^{d0}| \sim \frac{11}{3} k_0 \delta |v_{2y}^{d0}|$. In Fig. 2, we compare the effective model to a full model with resolved boundary layers [4]: Outside the boundary layers we find good agreement, while, as expected, deviations are seen inside the boundary layers.

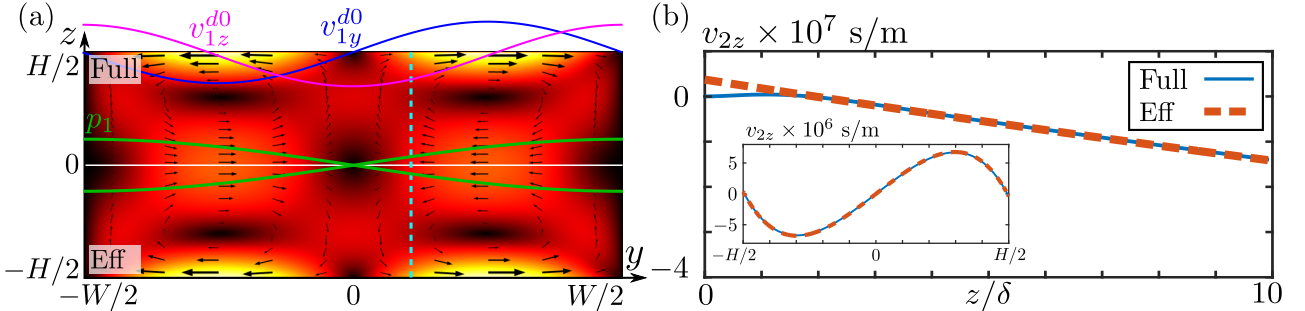


Figure 2: Second-order results for the same setup as in Fig. 1(a). (a) Comparison between full \mathbf{v}_2 (upper) and effective \mathbf{v}_2^d (lower) from 0 $\mu\text{m/s}$ (black) to 1 $\mu\text{m/s}$ (white). The blue and magenta line show the profiles of the boundary conditions in Eqs. (4a) and (4b), respectively. (b) Comparison between full and effective velocity profiles close to the lower wall at $y = W/8$ (dashed cyan line in (a)), and all the way across (inset).

Conclusion

We have developed effective models for acoustic boundary layers over curved oscillating walls. From the first-order analysis, we reproduce both damping, resonance frequency shift, and the perpendicular velocity. In the second-order analysis, we provide a boundary condition for all components of the long-range streaming which is valid over curved oscillating walls. Our results form the basis for future efficient modeling of larger microfluidic systems in 3D.

References

- [1] W. L. Nyborg. J. Acoust. Soc. Am. **30**(4), 329-339 (1958).
- [2] C. Lee and T. Wang. J. Acoust. Soc. Am. **85**(3), 1081-1088 (1989).
- [3] J. Vanneste and O. Bühler. Proc. R. Soc. A. **467**, 1779-1800 (2010).
- [4] P. B. Muller, R. Barnkob, M. J. H. Jensen, and H. Bruus, Lab Chip **12**, 4617-4627 (2012).



Vortex beam acoustical tweezers as “quiet” bubble traps

Diego Baresch¹, Axel Huerre¹, Marco De Corato¹ and Valeria Garbin¹

¹ Department of Chemical Engineering, Imperial College London, London SW7 2AZ, E-mail: d.baresch@imperial.ac.uk

Micron-sized gas bubbles or droplets are widely used as contrast agents in ultrasound medical imaging and carriers for targeted drug delivery. In this application, surfactants are very efficient to prolong bubble lifetime against dissolution. Bubbles stabilised by a monolayer of colloidal particles are becoming central in catalysis, encapsulation, and drug delivery. Despite their importance in applications, our fundamental understanding of their dynamic deformation is still limited. The ultrafast compression of a particle-laden interface has recently been explored by exposing particle-stabilised bubbles to ultrasound. Their rich response including buckling, shape oscillations and directional particle desorption [1-2] (see example in Fig. 1) calls for a better understanding of these complex interfaces under rapid and sometimes extreme deformation. In particular, these investigations could benefit from an improved control over the bubble's external environment so as to exclude the influence of surrounding walls or neighboring bubbles. An isolated, spherical bubble is importantly the ideal study case to compare experimental observations with theoretical models.

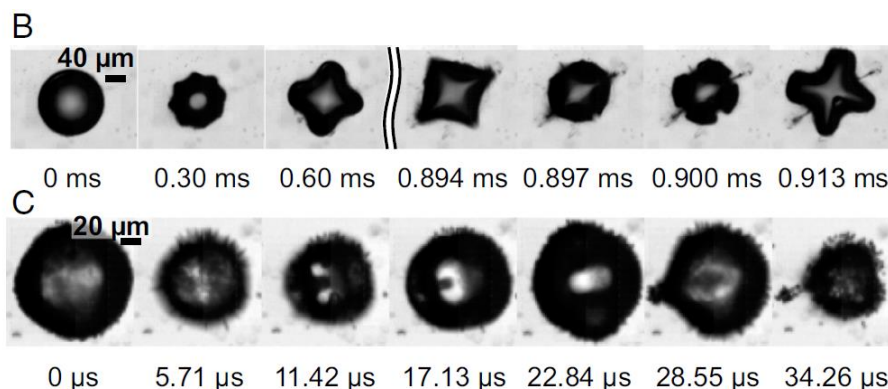


Figure 1: Resolved optical imaging of a particle-coated (1-5 μm) bubble (20-100 μm) under 40kHz ultrasound exposure. Shape oscillations and directional particle expulsion are triggered depending on the initial bubble size. Figure reproduced from [2].

Acoustic levitation and optical tweezing are efficient techniques to counter the upward buoyancy of bubbles [3,4]. The first uses the radiation pressure of a spatially fixed standing acoustic wave and relies on the sub-resonant trapping of the bubble near a pressure anti-node. Therefore, the bubble is forced to oscillate on its monopole breathing mode that can rapidly become non-linear even under moderate pressure fields. The latter uses the optical radiation pressure of a Laguerre-Gauss laser mode and has the great advantage to operate as a “quiet trap” in that it does not excite perceptible acoustic oscillations of the bubble under continuous excitation [5]. Nevertheless the high optical power required and the use of high numerical aperture objectives generally limit their use to small bubbles (of radius $< 50 \mu\text{m}$) and in confined trapping volumes.

Here we investigate the possibility of using single-beam acoustical tweezers [6] to trap and manipulate bubbles in the 10-100 μm range, and ultimately particle-coated bubbles. These tweezers are based on the propagation of a focused acoustic vortex (AV) having its wavefront spiralling around the propagation axis. The radiation pressure exerted by the AV on a bubble was predicted by using a full three-dimensional analytical framework [7]. The scattering coefficients of a free bubble can be calculated from the ECAH theory including thermo-viscous effects. Computing the scattered field for an incident AV then leads to the derivation of the total acoustic force. Figure 2 shows an AV is predicted to stably trap a bubble inside the zero acoustic pressure core in the lateral direction (Fig. 2c), while the pushing force counteracts its upward buoyancy (Fig. 2d). To our knowledge, this is the first prediction of a stable 3D trap for bubbles using single-beam acoustical tweezers.

We will particularly investigate the ability of this bubble trap to combine the strength of large acoustic stresses with the “quiet” operation feature of optical levitation traps. As the bubble is predicted to be trapped in a

pressure null, we expect the bubble to solely be driven in its dipolar oscillation mode at the trapping beam frequency.

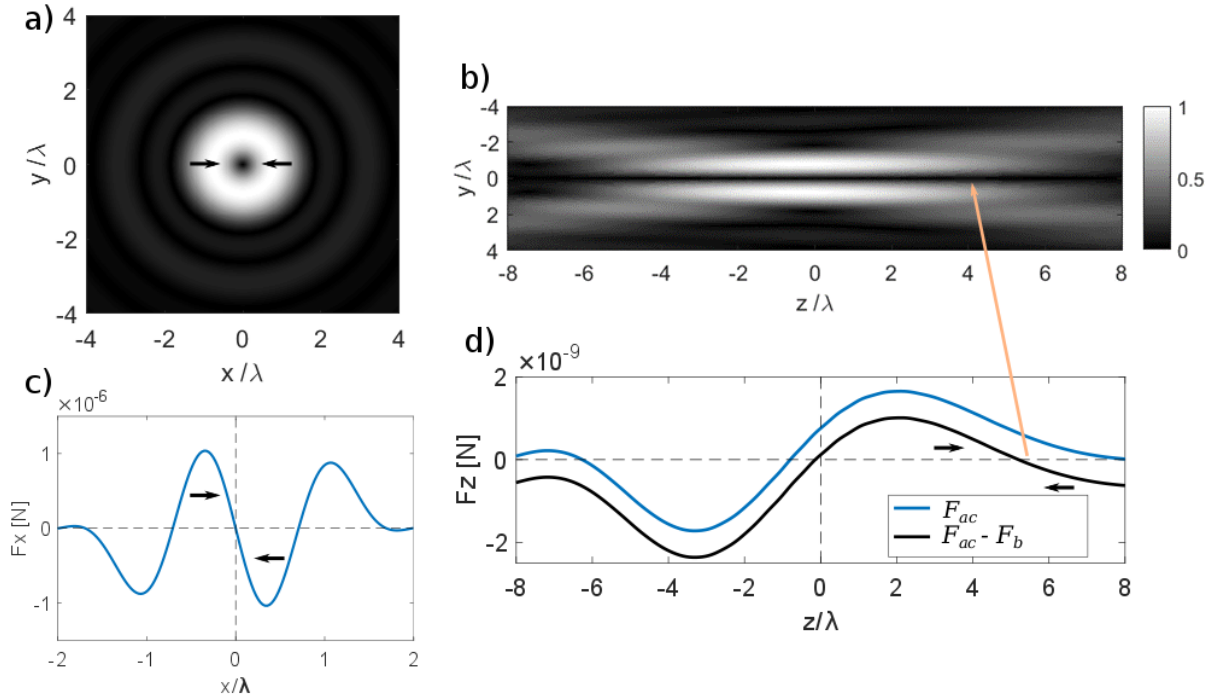


Figure 2: Acoustic pressure field of a focused AV (2.25 MHz) in the lateral a) and the axial directions b). The gray scale from 0 to 1 indicates zero and maximal pressure regions respectively. The lateral pressure gradient traps the particle in the zero pressure core c) while the axial pushing force F_{ac} can balance the bubble's buoyancy F_b d).

We will describe the experimental apparatus based on an 8-element focused piezoelectric transducer operating at 2.25 MHz. Bubbles are generated by a simple electrolysis setup and are released near the propagation axis of the AV. We will investigate the extension of the trapping to particle-coated bubbles whose response to acoustic radiation forces have remained unexplored.

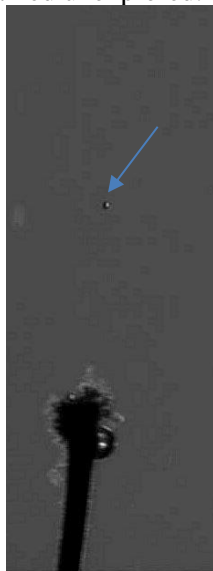


Figure 3: Photograph of a free bubbles ($\approx 20 \mu\text{m}$) pushed by an acoustical vortex beam. The bubble is released from the bottom by the cathode of an electrolysis wire ($100 \mu\text{m}$).

This work opens the way to the use of acoustical tweezers as a novel toolkit for soft matter and single-bubble experiments.

References

- [1] V. Poulichet and V. Garbin, 2015, *PNAS*, **112** (19), 5932
- [2] V. Poulichet, A. Huerre and V. Garbin, 2017, *Soft Matter*, **13**, 125-133
- [3] A. Eller, 1968, *Journ. Acoust. Soc. Am.*, **43**, 170
- [4] V. Garbin *et al.*, 2007, *Appl. Phys. Lett.*, **90**, 114103
- [5] B.T. Unger and P.L. Marston, 1987, *Journ. Acoust. Soc. Am.*, **83**, 970
- [6] D. Baresch, J-L Thomas and R. Marchiano, 2016, *Phys. Rev. Lett.*, **116**, 024301
- [7] D. Baresch, J-L Thomas and R. Marchiano, 2013, *Journ. Acoust. Soc. Am.*, **133**, 25-36



Miniaturized ultra-selective tweezers for 3D isotropic particles trapping

M. Baudoin^{1,*}, A. Riaud^{1,2}, J.C. Gerbedoen¹, O. Bou Matar¹, and J.L. Thomas¹

¹Univ. Lille, CNRS, Centrale Lille, ISEN, Univ. Valenciennes, UMR 8520, IEMN - International Laboratory LEMAC/LICS, F-59000 Lille, France. *E-mail: michael.baudoin@univ-lille1.fr, URL:

<http://www.acoustofluidics.org>

²Sorbonne Universités, UPMC Univ Paris 06, CNRS UMR 7588, Institut des NanoSciences de Paris, 4 place Jussieu, 75006 Paris, France

Introduction

With the emergence of regenerative medicine, cell printers, labs on chips, and complex microsystems, the contactless *selective* manipulation of microscopic objects such as particles, cells or drops has become a key issue. A large span of methods using magnetic [1-2], optical [3-4] and acoustical forces [5-7] have been considered to achieve this task. Nevertheless, magnetic tweezers are limited to the manipulation of magnetic particles or require the attachment of magnetic microbeads to the manipulated object. Optical tweezers require intense light flux, which can cause detrimental local overheating. Indeed, optical radiation pressure (like acoustical radiation pressure), is proportional to the intensity of the wave divided by the wave speed. Thus, photons yield a very small impulsion at each impact, and require high power to achieve pico-Newton trapping forces. Due to their low speed (relatively to light), acoustical waves appear as a tremendous alternative for particles trapping. Indeed, the acoustic wave momentum exceeds the one of light by several orders of magnitude at equivalent input power, limiting spurious heating. Another advantage of acoustical tweezers is that wave synthesis systems based on piezoelectric materials are available for frequency ranging from a few MHz to several GHz. This large span of actuation frequencies enables the trapping of millimetric to nanometric particles.

Selective acoustical tweezers

In both acoustics and optics, the *collective* manipulation of particles can be achieved with plane standing waves. However, the *selective* manipulation of particles requires to focalize the wave in the vicinity of the particle in order to localize the trap. In optics, particle trapping is simply obtained with focalized waves. Indeed, particles are naturally attracted to the center of the beam. However, selective trapping of particles denser and/or stiffer than the surrounding medium with acoustic waves is trickier. Indeed, it is well known that this type of particles is trapped at nodes (i.e. at the minima of the wave intensity) of standing waves, and expelled from the antinodes. Thus, particles would be ejected from the center of a focused beam (corresponding to a maximum of the intensity). This problem can be overcome by using a class of acoustic waves called acoustical vortices (also called Bessel beams) as first suggested in the mid 2000'th by Pr. Marston [8]. Acoustical vortices are the solutions of Helmholtz equation in cylindrical coordinates. Their wavefront twists around a zero-intensity axis, where the wave self-interfere destructively. This axis is surrounded by a high intensity ring that maintains the trapped particle at the center of the beam. The selective trapping of particles with acoustical vortices has been shown experimentally in 2D [5,6] and then in 3D [7] by using complex wave synthesis systems based on transducers arrays. The major drawback of these systems is that they require a high-end programmable electronics, not available for high frequency applications (> 100 MHz) and whose price skyrockets when approaching this critical frequency.

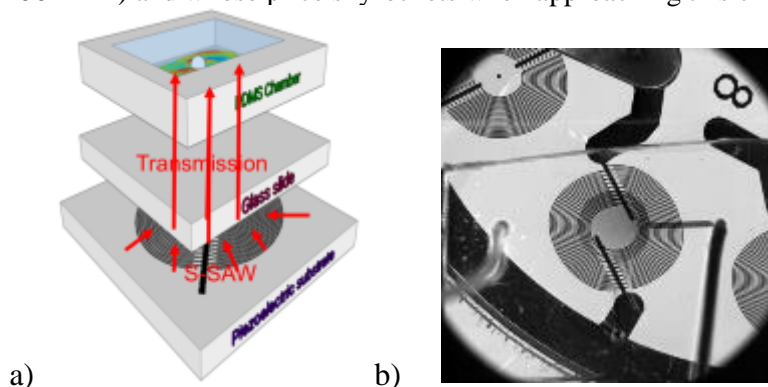


Figure 1: a) Principle of acoustic tweezers based on spiraling IDTs: Spiraling electrodes are deposited at the surface of a piezoelectric substrate. They generate a swirling surface acoustic wave (S-SAW) at the surface of the piezoelectric substrate, which creates an acoustic vortex in a microfluidic chamber after crossing a glass slide. Particles are trapped at the center of the acoustical vortex. b) Top view of an actual tweezer with a

Tweezers based on spiraling IDTs and surface waves

To overcome this difficulty, we developed alternative acoustic tweezers based on spiraling interdigitated transducers (IDTs) [9]. IDTs are electrodes sputtered at the surface of piezoelectric substrates and patterned by photolithography technics. They enable the synthesis of high frequency surface waves, that is to say waves propagating at the surface of the piezoelectric substrate. They were originally developed to conceive signal processing devices such as band-pass filters or delay line and are commonly used in mobile phones. Until recently, IDTs had only been considered to synthesize plane waves and in very few cases focused waves. To synthesize acoustical vortices, we developed some specific IDTs [9] whose spiraling shape encodes the phase of the field like a hologram. The shape can be precisely computed to generate an acoustical vortex after crossing one or several layers of solid material, opening perspective for remote manipulation of particles without cross contamination. With these devices, we have shown that we were able to trap particles and displace them individually with forces up to several hundred pico-Newtons.

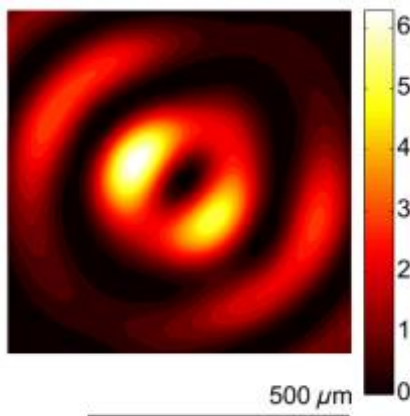


Figure 2: Potential well corresponding to an acoustical vortex synthesized with a spiraling IDT. The particle is trapped at the center. The force exerted on the particle is proportional to the gradient of this potential. This figure shows the anisotropy of the trap resulting from the anisotropy of the piezoelectric coupling coefficients.

A new generation of IDT-based selective acoustical tweezers

For applications, tweezers based on spiraling IDTs have many attractive features: they are selective, flat, easily integrable and compatible with disposable substrates. Nevertheless, some drawbacks remain with the current systems: (i) In addition to the central ring, the cylindrical Bessel beam comprises several secondary rings of decreasing intensity that also exert forces on particles (Fig. 2). (ii) Due to the anisotropy of the piezoelectric substrate, the amplitude of the swirling wave differs in the different directions, leading to an anisotropic trapping force (Fig. 2). (iii) Finally, with these SAWs-based tweezers the trapping remains essentially 2D, even if the degeneracy of *anisotropic* vortex in the *isotropic* liquid incidentally leads to a force of lower intensity in the z-direction (orthogonal to the substrate) [10]. In this presentation, we will show how we can design a new generation of IDT-based acoustic tweezers that addresses simultaneously all these issues.

Conclusion

In this presentation, we will introduce a new class of acoustical tweezers based on spiraling electrodes, which combines the advantages of previous tweezers based on swirling SAWs [9], along with enhanced selectivity, isotropy of the trap and 3D trapping capabilities.

References

- [1] I. De Vlaminck and C. Dekker, *Annu. Rev. Biophys.* **41**, 453 (2012).
- [2] F. Martinez-Pedrero and Pietro Tierno, *Magnetic, Phys. Rev. Applied* **3**, 051003 (2015).
- [3] A. Ashkin, J. M. Dziedzic, J. E. Bjorkholm, and Steven Chu, *Opt. Lett.* **11**, 288 (1986).
- [4] J.R. Moffitt, Y.R. Chemla, S.B. Smith, and C. Bustamante, *Biochemistry* **77**, 205 (2008).
- [5] C.R.Courtney, C.E.Demore, H.Wu, A.Grinenko, P.D.Wilcox, S.Cochran, and B.W.Drinkwater, *App. Phys. Lett.*, **104**(15):154103 (2014)
- [6] A. Riaud, J.-L. Thomas, E. Charron, A. Bussonnière, O. Bou Matar, and M. Baudoin, *Phys. Rev. Applied* **4**, 034004 (2015)
- [7] D. Baresch, J.-L. Thomas, and R. Marchiano, *Acoustical Tweezers, Phys. Rev. Lett.* **116**, 024301 (2016)
- [8] P. L. Marston, *J. Acoust. Soc. Am.*, **120**(6):3518–3524 (2006).
- [9] A. Riaud, M. Baudoin, O. Bou Matar, L. Becerra and J.-L. Thomas, *Phys. Rev. Appl.*, **7**, 024007 (2017)
- [10] A. Riaud, J.-L. Thomas, M. Baudoin, and O. Bou Matar, *Phys. Rev. E* **92**, 063201 (2015).

Acoustic streaming in inhomogeneous fluids – a numerical study

Jonas T. Karlsen¹, Wei Qiu¹, Per Augustsson², and Henrik Bruus¹

¹Department of Physics, Technical University of Denmark, Kongens Lyngby, Denmark

²Department of Biomedical Engineering, Lund University, Lund, Sweden

E-mail: bruus@fysik.dtu.dk, URL: <http://www.fysik.dtu.dk/microfluidics>

Introduction

Acoustic streaming in inhomogeneous fluids cannot be understood from the classical theory of Lord Rayleigh [1]. In particular, recent experimental observations [2,3], suggest that boundary-driven acoustic streaming is suppressed in the bulk of density-stratified fluids, which enables the controlled manipulation of submicrometer particles [3]. Recently, we derived the theory of the acoustic force density acting on inhomogeneous fluids [4]. We further hypothesized that the ability of the acoustic force density to stabilize certain inhomogeneity configurations [4,5] is responsible for the observed suppression of streaming. In this work, we investigate this hypothesis by unifying the theories of acoustic streaming and the acoustic force density. We use the unified theory in a numerical study of acoustic streaming in inhomogeneous fluids. Several interesting new phenomena emerge, some of which we also observe experimentally in a parallel study.

Description

In brief, our unifying theory exploits the fact that all time-averaged acoustic flows are driven by a non-zero divergence in the oscillation-time-averaged acoustic momentum-flux-density tensor $\langle \mathbf{\Pi}_{ac} \rangle$, which suggests the general definition of the acoustic force density $\mathbf{f}_{ac} = -\nabla \cdot \langle \mathbf{\Pi}_{ac} \rangle$ [4]. We demonstrate that acoustic streaming in homogeneous viscous fluids [1], and the acoustic force density in inhomogeneous inviscid fluids [4], are special cases of this general principle.

We simulate acoustic streaming in the microchannel sketched in Fig. 1(a). The simulation is based on the separation of time scales [4]. At each time on the slow hydrodynamic time scale, the fast-time-

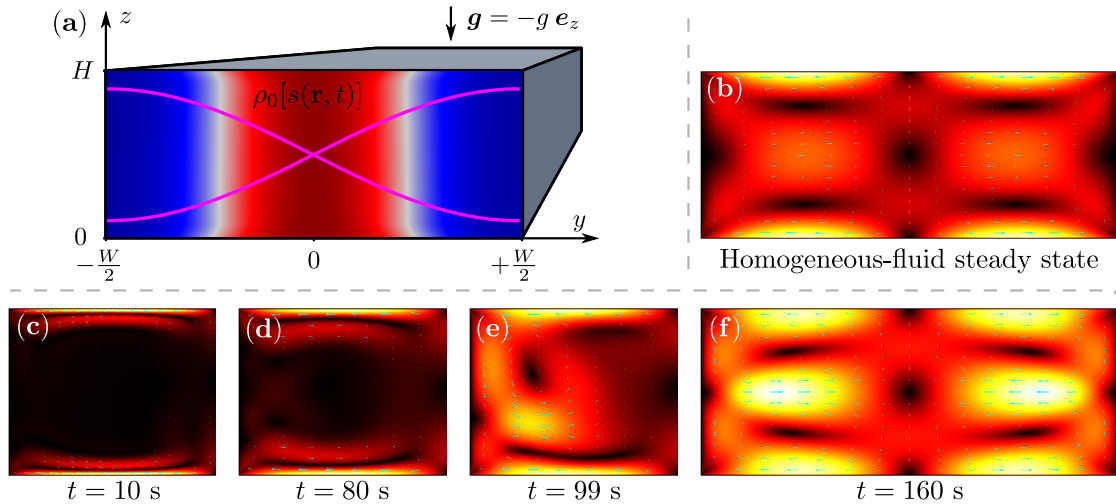


Figure 1: (a) Contour plot of the iodixanol concentration field $s(\mathbf{r}, t)$ at $t = 10$ s, from low at the sides (dark blue, fluid density $\rho_0 = 1000$ kg/m³) to high in the center (dark red, $\rho_0 = 1100$ kg/m³) inside a microchannel of width $W = 375$ μm and height $H = 150$ μm . Initially, at $t = 0$ s, the denser center fluid column is vertical, and although it is acoustically stabilized at the center, it flattens by diffusion on a time scale of 100 s, and streaming deforms it near the walls. (b) Steady streaming velocity (from 0 $\mu\text{m/s}$ black, to 40 $\mu\text{m/s}$ white) in a homogeneous fluid, shown for reference. (c)-(f) Unsteady streaming velocity in the inhomogeneous fluid evolving in time from $t = 10$ s to $t = 160$ s as the density-inhomogeneity flattens. In the first phase (c)-(d), streaming is suppressed in the bulk, while recirculation is confined close to the walls. (e) A rapid transition changes the suppressed streaming pattern at a point of critically weak inhomogeneity. (f) Steady streaming in a sustained weakly inhomogeneous fluid emerges. The flow rolls are wider and the speeds larger than in (b).

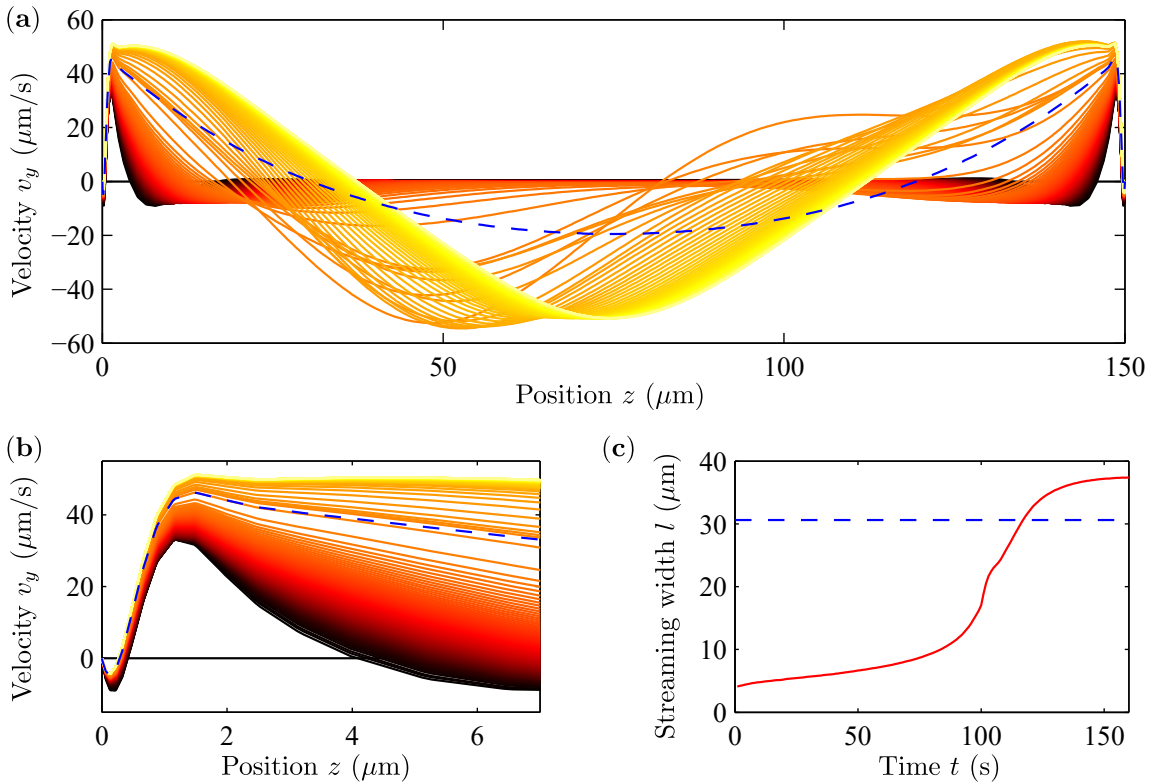


Figure 2: (a) The horizontal component of the streaming velocity v_y plotted along the vertical position z in $y = W/4$ for all times from $t = 0$ s to $t = 160$ s in steps of 1 s (black curve, $t = 0$ s; through red; to yellow, $t = 160$ s). The dashed blue curve shows the homogeneous-fluid steady state solution. (b) Same as in (a) but for a narrow range close to the wall. (c) The width l of the streaming region (red curve) plotted as a function of time t . Initially, the streaming roll is confined close to the wall with $l \approx 4$ μm . The width of the streaming region grows and finally exceeds the homogeneous-fluid value (dashed blue line) as the weakly inhomogeneous steady state is approached.

scale acoustics (viscous, inhomogeneous) is solved. This allows calculation of the instantaneous force density \mathbf{f}_{ac} (including streaming and inhomogeneity-induced forces), which enters the slow-time-scale hydrodynamic equations. The system of equations can then be integrated in time. Due to diffusion of the density-modifying solute, acoustic streaming in an inhomogeneous fluid is time-dependent.

Figure 1(c)-(f) shows the time-dependent acoustic streaming velocity field, which may be compared to the homogeneous-fluid steady streaming in Fig. 1(b). In the first 80 s [Fig. 1(c)-(d)], the streaming rolls are squeezed flat close to the walls, and the streaming is suppressed in the bulk, which is at rest. At $t = 99$ s [Fig. 1(e)], a critical transition takes place, and finally, at $t = 160$ s [Fig. 1(f)], a steady state streaming pattern sustaining a weakly inhomogeneous fluid is approached. Figure 2(a)-(b) shows the profile of the horizontal streaming velocity v_y along the height of the channel and how it evolves in time. The velocity profile demonstrates significant differences from homogeneous-fluid streaming, especially at short times, where the streaming is confined near the walls. We characterize the width of the streaming region as the orthogonal distance l from the wall to the center of the streaming roll. A plot of l as a function of time is shown in Fig. 2(c).

Conclusion

We have unified the theories of acoustic streaming and the acoustic force density acting on inhomogeneous fluids, and developed a numerical model of acoustic streaming in inhomogeneous fluids. The model confirms our hypothesis that a density-stratified media leads to suppression of acoustic streaming away from walls for time scales up to ~ 80 s in typical experiments. We have presented several time-dependent signatures of the model, and in a parallel study we have observed them experimentally.

References

- [1] Lord Rayleigh. *Philos. Trans. R. Soc. Lond. A* **175**, 1 (1884).
- [2] P. Augustsson, J. T. Karlsen, H.-W. Su, H. Bruus, and J. Voldman. *Nat. Commun.* **7**, 11556 (2016)
- [3] P. Augustsson, J. T. Karlsen, and H. Bruus. *Procs. pp. 158-159, 20th International Conference on Miniaturized Systems for Chemistry and Life Sciences, MicroTAS 2016*, Dublin, 9 - 13 October 2016.
- [4] J. T. Karlsen, P. Augustsson, and H. Bruus. *Phys. Rev. Lett.* **117**, 114504 (2016).
- [5] J. T. Karlsen and H. Bruus. *Phys. Rev. Applied* **7**, 034017 (2017).



Time-averaged acoustic forces from travelling substrate waves: the effect of channel boundaries

David Collins^{1,2}, Citsabehsan Devendran³, Richard O'Rourke¹, Adrian Neild³ and Ye Ai¹

¹Engineering Product Design-Development Pillar, Singapore University of Technology and Design, Singapore ²Department of Electrical Engineering and Computer Science, Massachusetts Institute of Technology, Cambridge, MA, USA

³Laboratory for Micro Systems, Department of Mechanical and Aerospace Engineering, Monash University, Clayton, Victoria, Australia

Email: david_collins@sutd.edu.sg, ye_ai@sutd.edu.sg. Web: http://people.sutd.edu.sg/~ye_ai/

Introduction

Acoustic patterning is the result of particle migration in a time-averaged acoustic force potential landscape. Typically, this is derived from either whole-channel resonance conditions or the intersection of classical, travelling waves with counter-propagating components. The latter is typically the case in devices using surface acoustic waves (SAW), a common method of generating acoustic fields in acoustofluidic systems where displacements are coupled from the substrate to a bounding material. In such a system, two interdigital transducers (IDTs) are positioned on either side of a microfluidic channel, with the resulting 1D periodic acoustic field used to manipulate suspended micro-objects. Four IDTs oriented 90 degrees to each other can be similarly be used to create a 2D periodic field. In this work, however, we report the generation of a 1D periodic time-averaged periodic acoustic force with a single travelling wave (one IDT), and the generation of a 2D field with only the imposition of a 1D substrate wave (two IDTs). We produce this effect through the imposition of arbitrary wall boundaries in the path of the acoustic beam; these walls act to create acoustic beams in the fluid with a sharply finite extent. This discontinuity that is imposed in the beam source generates regions of constructive and destructive interference according to the Huygens-Fresnel Principle, which states that every point along a wavefront acts as an independent source of spherical wavefronts. This ultimately results in time-averaged acoustic potentials whose locations are a function of wall position and orientation. Importantly, this principle permits the generation of acoustic patterns that can be arbitrarily located and oriented within acoustofluidic systems, and increases manipulation fidelity in acoustofluidic systems.

System principles

Suspended micro-objects will migrate towards minimum energy potential locations in the presence of an acoustic field. For most particles that are denser than the surrounding media, these locations exist at the acoustic time-averaged pressure minima. Whereas these minima are usually found at periodic locations along the axis of counter-propagating waves in most other SAW systems, we impose additional such locations using supplementary channel features that are in the path of the SAW. If the channel boundary is parallel to the advancing substrate wavefronts, as illustrated in Figure 1a below, the sharp boundary at the lower three-

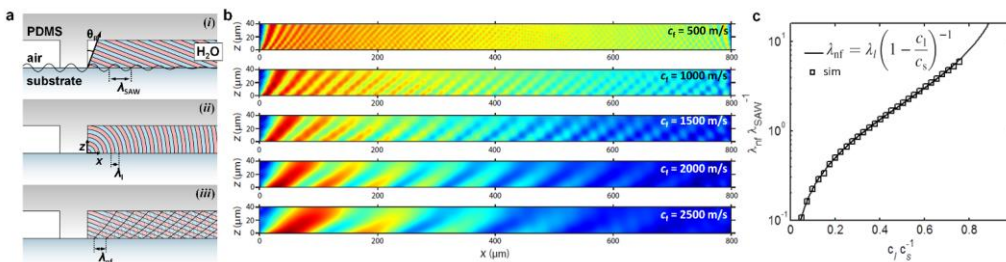


Figure 1: (a) Principle of periodic pattern generation from wall/substrate-wave interaction. (i) The classical wavefronts combine with (ii) cylindrical ones arising from the channel corner, resulting in (iii) time-averaged interference patterns. (b) This system is simulated for a range of fluid sound speeds (red = high time-average pressure, blue = low time-average pressure), with (c) good agreement between the periodicity here (with spacing λ_{nf}) and an analytical model that is based on the interference of wavefronts as per (a). Figure adapted from Devendran et al. [1].

material corner of the channel acts effectively as a source of cylindrical waves (here considered in the x-z plane) according to the Huygens-Fresnel principle. These then interfere with the fluid wavefronts emanating from the substrate, where the alternate constructive and destructive interference results in distinct acoustic force potential gradients along the propagation direction. The acoustic waves are coupled into the fluid from a travelling SAW, generated by a series of interdigitated electrodes on a piezoelectric 128° X-Y Lithium Niobate. Applying an AC signal across these electrodes with a frequency corresponding to IDT resonance, with $f = c_s/\lambda_{SAW}$, results in a SAW that drives acoustic patterning in the microfluidic channel.

Results and discussion

Figure 1b shows the fully coupled simulated time-averaged pressure distribution in a bounding fluid that results from a rightward-propagating SAW for a range of sound speeds. As shown in Figure 1c, the spatial periodicity from these simulation results matches those from the analytical model proposed for this system [1][†], which predicts this based on the interference of the classical wavefronts emanating from the substrate with cylindrical ones emanating from the channel corner. This system is analogous to those examined elsewhere [2][‡], with the exception of the use of a higher aspect ratio channel to minimize the impact of wall reflections and particles smaller than those that can be readily influenced by forces arising from the travelling wave itself- [3][‡]. Figure 2a further shows that this effect can be used for particle patterning (here 2 μm diameter polystyrene spheres), with the measured $\lambda_{inf} = 0.63 \pm 0.03 \lambda_{SAW}$ corresponding closely to the $0.61 \lambda_{SAW}$ spacing predicted by the model in Figure 1c. Importantly, the extent of this patterning region can be scaled with applied power, meaning patterning can be limited to particular channel regions without the imposition of pulsed AC fields- [4][†].

This effect is not limited to this particular orientation of substrate wave and channel features; the corner waves (combined with the wavefronts arising directly from the substrate) will result in a time-averaged periodic field perpendicular to any wall in the path of the beam. This is noted in Figure 2b, which shows 2D 1 μm fluorescent green particle patterning in a combined standing SAW and wall-interaction acoustic field. A 1D standing SAW generates particle patterning along the SAW propagation axis, as per previous work [5][‡], while the channel features result in a periodic acoustic field that is orthogonal to the SAW one. Finally, Figure 2c demonstrates that SAW/wall interactions can result in time-averaged fields for a variety of wall angles; these features can take on a variety of shapes and still generate appreciable acoustofluidic effects.

Conclusion

In this work we demonstrate and characterize a novel methodology for acoustofluidic patterning. In contrast to previous work, acoustic patterning is generated using arbitrary wall features rather than through the imposition of channel resonance conditions or counter-propagating waves. This technique expands the ability to orient and localize acoustic fields on-chip for refined particle and cell manipulation without complicated acoustic actuation strategies.

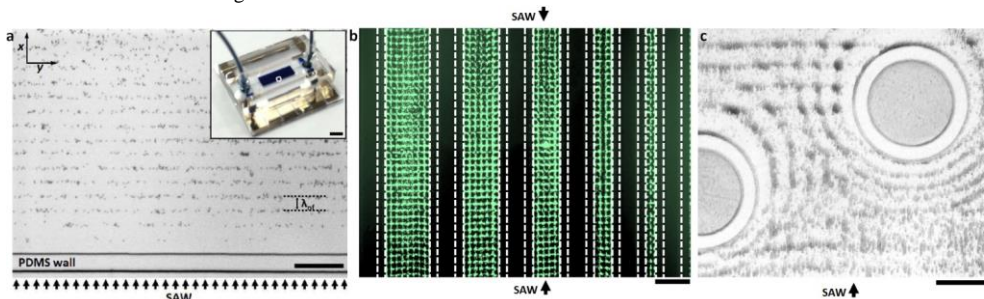


Figure 2: Periodic microfluidic patterning from Huygens-Fresnel wave interference. (a) Matching the spacing (λ_{inf}) in Fig. 1(c) with a substrate/fluid sound speeds corresponding to Lithium Niobate and water, particles are patterned by a single 48 μm wavelength travelling wave and its interaction with a polydimethylsiloxane (PDMS) wall (scale bar is 100 μm). Inset shows region on device pictured (scale bar is 2 mm). Figure here adapted from Devendran et al. [1][†]. (b) 2D patterning arising from a 1D field with the addition of channel walls (outlined in dotted white) in the path of the SAW (scale bar is 160 μm, $\lambda_{SAW}=60$ μm). (c) Arbitrary wall features result in a range of complex acoustic patterns (scale bar is 100 μm, $\lambda_{SAW}=80$ μm).

References

- [1][†]- C. Devendran, D. J. Collins, Y. Ai and A. Neild, *Phys. Rev. Lett.*, 2017, **118**, 154501.
- [2][‡]- G. Destgeer, B. H. Ha, J. Park, J. H. Jung, A. Alazzam and H. J. Sung, *Anal. Chem.*, 2015, **87**, 4627-4632.
- [3][‡]- V. Skowronek, R. W. Rambach, L. Schmid, K. Haase and T. Franke, *Anal. Chem.*, 2013, **85**, 9955-9959.
- [4][†]- D. J. Collins, C. Devendran, Z. Ma, J. W. Ng, A. Neild and Y. Ai, *Science Advances*, 2016, **2**, e1600089.

[5] C. Wood, S. Evans, J. Cunningham, R. O'Rorke, C. Wälti and A. Davies, *Appl. Phys. Lett.*, 2008, **92**, 044104.



Optimising SSAW devices for cancer cell separation using finite element modelling

Jerome A. Cuenca¹, Liam Johnston¹, Fangda Wu¹, Hanlin Wang¹, Jin Li², David Barrow², Xin Yang¹

¹Sensors, Signals and Imaging Group, School of Engineering, Cardiff, Wales, United Kingdom
E-mail: cuencaj@cardiff.ac.uk

²Centre for High Frequency Engineering, School of Engineering, Cardiff, Wales, United Kingdom

Introduction

The aim of this research is to develop a lab-on-chip system which separates and detects circulating tumour cells (CTCs) amongst blood cells using acoustofluidics. In particular, this presentation will focus on a numerical method to optimise of the acoustofluidic device by understanding the effect that the geometry of a polydimethylsiloxane (PDMS) microfluidic channel has on the standing surface acoustic wave (SSAW). The novelty in this work is the development of a 2D finite element model using COMSOL Multiphysics[®], allowing us to fundamentally understand ideal structures before any costly fabrication. This model shows that the dimensions of the PDMS must be carefully considered to avoid dampening of the SSAW. Where possible, excess PDMS in contact with the substrate must be minimised as the peak anti-node pressure decreases by as much as 45%.

Clinical importance of CTC detection

The detection of CTCs in whole blood has recently become important for biological studies on cancer progression, however, separating them from red blood cells (RBCs) is challenging due to a low volume ratio; ca. 1 CTC to 10⁸ RBCs. Although there are current FDA approved methods to separate and identify these unhealthy cells, these approaches require labels which alters their properties and biases the search towards known antigens. Acoustofluidic methods are an alternative which separates cells based on differences in their mechanical properties. The advantage of this technique is that the cells require no modification, leaving the CTCs intact for further analysis and ultimately providing more information for the prognosis of the patient.

Separating CTCs using acoustic radiation forces

Implementation is achieved by flowing the cells down a microfluidic channel whilst in the presence of a SSAW, which induces an acoustic radiation force and influences their end trajectory at the end of the channel. The well-known equation for the acoustic radiation force on a spherical particle in an

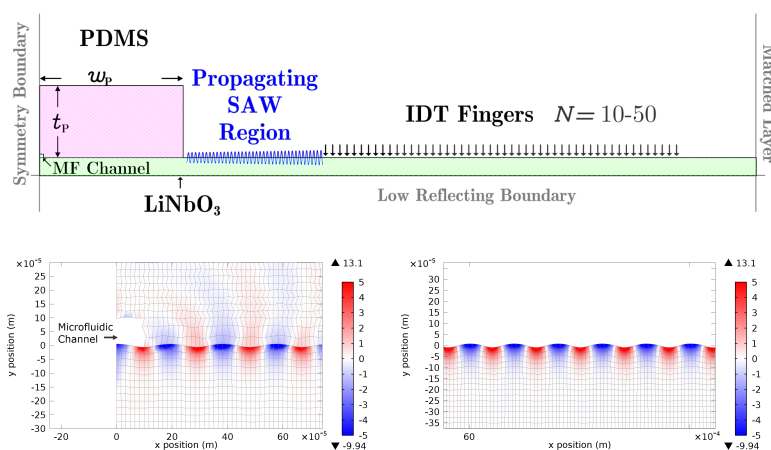


Figure 1: Schematic of the 2D model (top) and an example result of the Rayleigh wave in the labelled 'Propagating SAW Region' (bottom-right) and the leaky Rayleigh wave in the PDMS region (bottom-left). Colour bars show pressure in Pascals.

Model Parameters

LiNbO₃ $v_{\text{shear}} = 3828$ m/s
 LiNbO₃ $v_{\text{pressure}} = 6609$ m/s
 LiNbO₃ $\rho = 4640$ kg/m³
 IDT pitch = 50 μm (17.8 MHz)
 IDT shear force = 1 Pa
 PDMS Young's Modulus = 1.07 GPa
 PDMS $\rho = 920$ kg/m³
 PDMS Poisson Ratio = 0.49

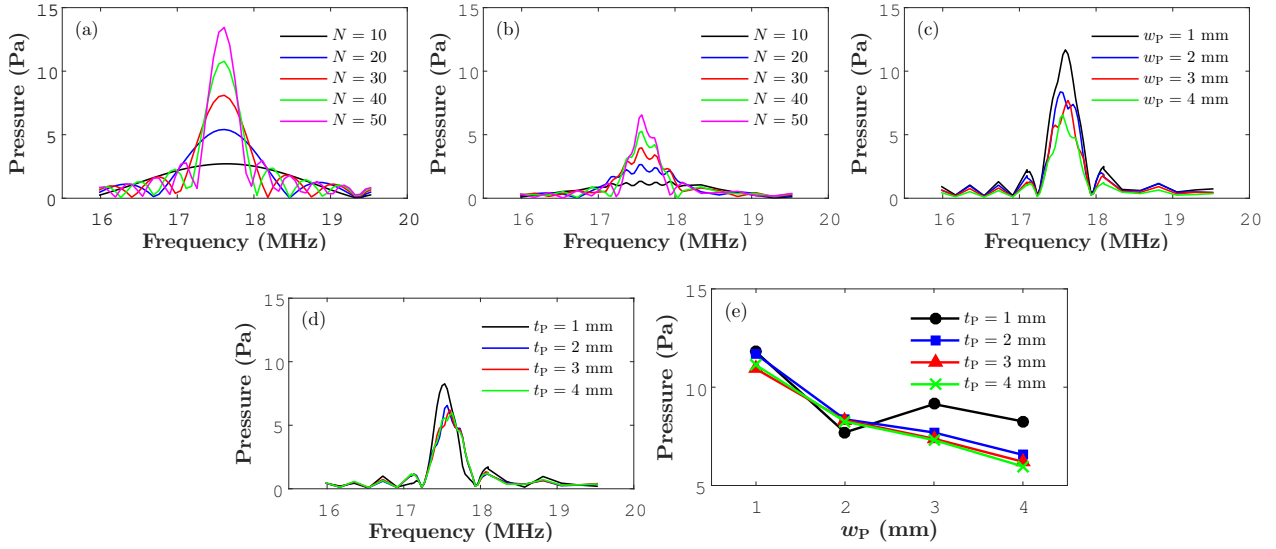


Figure 2: Anti-node pressure as a function of frequency. Simulations of (a) LiNbO₃ substrate with varying N without a PDMS channel (b) with a PDMS channel where $w_P = 4$ mm and $t_P = 2$ mm (c) fixed $N = 50$ and $t_P = 2$ mm with varying PDMS width, (d) fixed $N = 50$ and $w_P = 4$ mm with varying PDMS height, (e) maximum pressure across the frequency band as a function of both width and height.

inviscid fluid has been derived by Bruus[1]:

$$F_{\text{rad}} = -V_{\text{part}} \nabla \cdot \left(f_{\kappa} \frac{1}{2} \langle p_{\text{in}}^2 \rangle - f_{\rho} \frac{3}{4} \langle v_{\text{in}}^2 \rangle \right) \quad (1)$$

where V_{part} is the particle volume, $f_{\kappa} = \kappa_{\text{fluid}} - \kappa_{\text{part}}$ is the compressibility coefficient, $f_{\rho} = 2\rho_{\text{fluid}}(\rho_{\text{part}} - \rho_{\text{fluid}}) / (2\rho_{\text{part}} + \rho_{\text{fluid}})$ is the density coefficient and $\langle p_{\text{in}} \rangle$ and $\langle v_{\text{in}} \rangle$ are the instantaneous pressure and velocity at the particle location, respectively. The force is directly proportional to the squared pressure gradient ($-\nabla \langle p_{\text{in}}^2 \rangle$). The pressure gradient across the width of the channel is a sinusoidal standing wave, where the node is the end lateral trajectory of the cells. The larger the anti-node, the larger pressure gradient and therefore the radiation force, so it is important to maximise the anti-node pressure. In this work, we developed a base 2D model with a SSAW induced by an IDT on a LiNbO₃ substrate and have progressively modified it by adding PDMS of varying geometries to understand its influence on the anti-node pressure.

COMSOL simulation of PDMS damping

Firstly, the number of IDT fingers (N) on the LiNbO₃ substrate was varied to obtain a SSAW. The simulation was then carried out in the presence of the PDMS microfluidic channel that is shown in Fig. 1. The results in Fig. 2a and 2b show that by increasing N , the amplitude of the standing wave in the channel increases linearly which is expected since increasing the number of electrodes further reinforces the SSAW. Fig. 2b shows the frequency response in the presence of a typically sized 4 mm wide PDMS block (channel height = 100 μm , channel width = 200 μm , the example model in Fig. 1). In this case, the standing wave amplitude dramatically decreases by at least 45% of its original value, demonstrating that the PDMS material has a large affect on the overall performance of the device. This is mainly due to a transmitted leaky wave into the PDMS. In Fig. 2c, fixing the number of fingers ($N = 50$) and height ($t_P = 2$ mm) and decreasing the PDMS width further demonstrates that the reduction in the peak is caused by the leaky wave when the width is large as there is more PDMS absorbing some the pressure wave. Also, the height has little influence on the anti-node pressure at values greater than 2 mm, as shown in Fig. 2d. At a height of 1 mm, the leaky pressure waves reflect from the top air boundary, and in some cases reinforces the anti-node pressure as shown in Fig. 2e.

Conclusion

In general, for the application of CTC cell sorting, understanding the device performance involves minimising the PDMS used to make the channel. Fabricating PDMS with precise surface patterns is a challenging task, and we are currently pursuing our fabrication limits. The simulations presented here are a portion of the work that is ongoing within our group, where we hope to present more of our findings on the optimisation of our device.

References

- [1] H. Bruus, Lab on a Chip, **12**, 6, 1014-101 (2012).

Characterization of microchannel anechoic corner formed by travelling surface acoustic waves

Ghulam Destgeer, Husnain Ahmed, Jin Ho Jung, Jinsoo Park, Raheel Ahmad, Kwangseok Park, and Hyung Jin Sung*

Flow Control Laboratory, Department of Mechanical Engineering, KAIST, Daejeon, 34141, South Korea.
 Email: destgeer@kaist.ac.kr, hjsung@kaist.ac.kr, URL: <http://flow.kaist.ac.kr/>

Introduction

Acoustofluidic manipulation of micro-objects inside microfluidic channels by using surface acoustic waves (SAWs) have shown great potential over the past decade.[1] As the SAW-based systems are broadly categorized into travelling and standing waves devices, depending upon the dominant mode of wave propagation within the microfluidic channels, a deep understanding of the complex acoustic field formation within the fluidic domain and the consequent manipulation of suspended micro-objects is still developing.[2] It has been observed previously that the coupling of SAWs with the fluid inside a microchannel radiates a longitudinal waves within the fluid at Rayleigh angle (θ_t) that generates a region void of strong acoustic field and termed as microchannel anechoic corner (MAC).[3] In the present study, we delve deeper into characterizing the MAC formation by exploring effects of various parameters such as microchannel height (h_m), width (w_m), SAW frequency (f_{SAW}), etc. on the manipulation of suspended polystyrene particles inside the microchannel. **Figure 1** shows a schematic diagram presenting the device design and highlights basic concepts used during experimentation. A single interdigitated transducer (IDT) is combined with a winding polydimethylsiloxane (PDMS) microchannel to deflect suspended particles across their streamlines at two separate locations upstream and downstream of the microchannel. The particles diameter and SAW frequency are chosen in such a way that the acoustic radiation force by the travelling waves dominate particle motion.

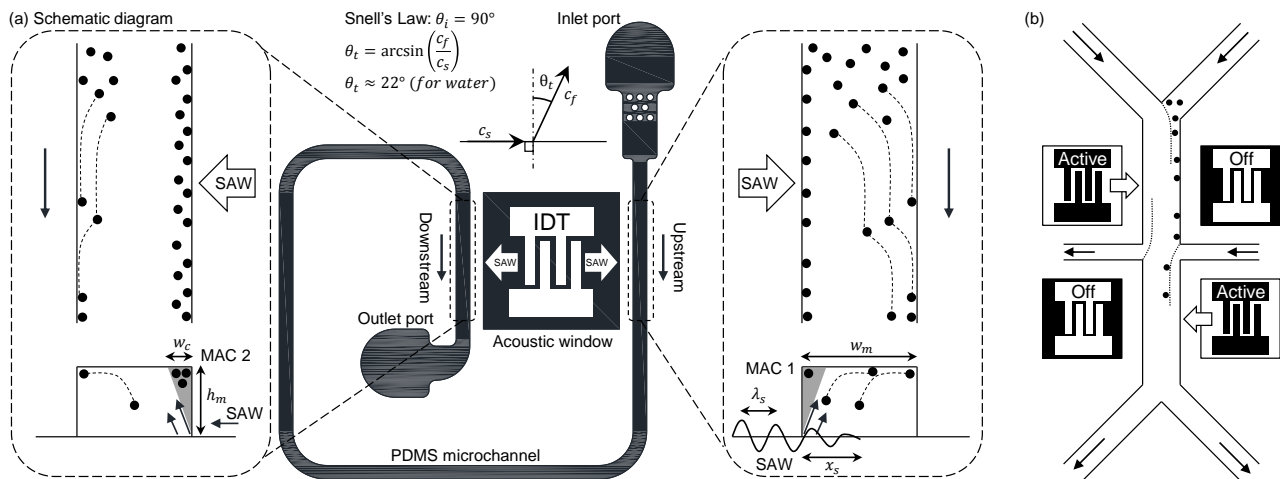


Figure 1: (a) Schematic diagram of the acoustofluidic characterization device composed of an interdigitated transducer (IDT) and a polydimethylsiloxane (PDMS) microfluidic channel with a single inlet port and single outlet port. The IDT radiates surface acoustic waves (SAWs) in both directions perpendicular to the electrodes such that the rightward and leftward leaky SAWs couple with the fluid inside the microfluidic channel at two locations thus forming two microchannel anechoic corners (MAC 1 and 2), respectively. The winding microchannel is designed to initially push the particles, using rightward SAWs, in the top right corner of the microchannel during the upstream flow so that the same particles could occupy the MAC 2 region during the downstream flow where leftward SAWs may or may not be able to deflect them from their streamlines. The deflection of the particles depends upon their locations with reference to the MAC width (w_c), height of the microchannel (h_m), width of the microchannel (w_m), incident wave frequency (f_{SAW}) and wavelength (λ_s), SAW attenuation length within the microchannel (x_s), Rayleigh angle (θ_t), etc. Any particle randomly occupying the MAC 1 region will not be deflected by the rightward SAW in the first place. The propagation angle of the leaky SAWs inside the microchannel depends upon the speeds of sound inside the substrate and the fluid. The Rayleigh angle (θ_t) is calculated to be $\cong 22^\circ$ by using the Snell's law such that the incident angle of wave is $\theta_i = 90^\circ$, the substrate is Lithium niobate ($c_s \cong 3950 \text{ ms}^{-1}$) and the fluid is water ($c_f \cong 1480 \text{ ms}^{-1}$). (b) A schematic diagram showing a straight microchannel with multiple inlet and outlet ports, and IDTs positioned on opposite sides of the microchannel. Side channels are used to hydrodynamically change the focusing position of the particles being pushed by the rightward SAWs into the top right corner of microchannel.

Results and discussions

The deflection of $5\ \mu\text{m}$ polystyrene particles flowing at different flow rates ($50, 100, 1000\ \mu\text{lh}^{-1}$) by SAWs ($110, 120, 140\ \text{MHz}$) has been performed inside microchannels with heights of $110\ \mu\text{m}$ and $30\ \mu\text{m}$ as shown in **Figure 2**. The formation of MAC regions within the $110\ \mu\text{m}$ high microchannel is quite prominent. However, for a microchannel with a much lower height of $30\ \mu\text{m}$, these regions shrink to a very unobservable point.

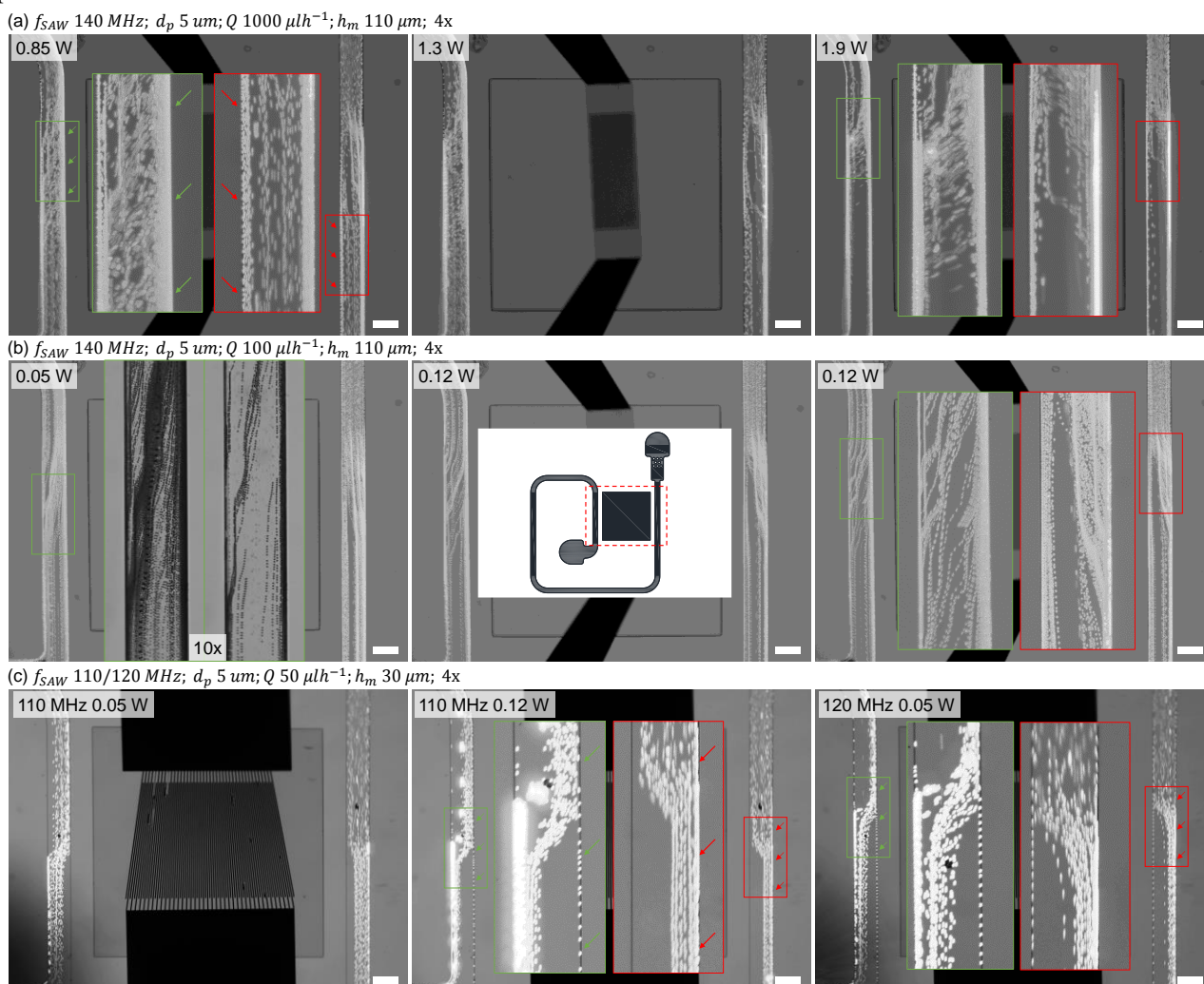


Figure 2: (a) Polystyrene $5\ \mu\text{m}$ diameter particles pumped ($1000\ \mu\text{lh}^{-1}$) through the microchannel ($w_m \times h_m$: $200\ \mu\text{m} \times 110\ \mu\text{m}$) are deflected by $140\ \text{MHz}$ SAWs originating from a straight IDT. At input power of $0.85\ \text{W}$, some of the particles being pushed against the microchannel ceiling and opposite side wall during the upstream flow indicated with a red color rectangle, maintained their position within MAC 2. However, the closed-up view of the downstream microchannel, marked with a green color rectangle, indicates that there are particles within a region of $\sim 30\ \mu\text{m}$ of the right side wall which are unaffected by the leftward SAWs thus ensuring the existence of an anechoic corner region. As the input power is increased to 1.3 and $1.9\ \text{W}$, more particles are pushed into the top-right corner during upstream region of the microchannel; however, there is a significant number of non-deflected particles present in the MAC 1 region or being sucked into it by a strong acoustic streaming flow. The closed-up view downstream region for $1.9\ \text{W}$ shows that the MAC 2 width has decreased to less than $20\ \mu\text{m}$ where the particles are not pushed along SAW propagation direction. (b) For a flow rate of $100\ \mu\text{lh}^{-1}$ and a similar microchannel height of $110\ \mu\text{m}$, we observed the formation of MAC 1 and 2 at both sides of the IDT. However, it can be noted that a much lower power is used to deflect that particles here. (c) The phenomenon has significantly altered for a microchannel with a height of $30\ \mu\text{m}$ as the SAWs originating from a slanted IDT at 110 or $120\ \text{MHz}$ frequency almost totally deflected the particles flow at $50\ \mu\text{lh}^{-1}$ without showing a significant presence of MAC 1 or 2. The closed-up views of the microchannels show that at $110\ \text{MHz}$ ($0.12\ \text{W}$) or $120\ \text{MHz}$ ($0.05\ \text{W}$) nearly all of the particles were deflected by the SAWs, only indicating a MAC width of less than $\sim 5\ \mu\text{m}$. The scale bars are $200\ \mu\text{m}$ long.

Acknowledgements

This work was supported by the Creative Research Initiatives (no. 2017-013369) program of the National Research Foundation of Korea (MSIP) and the KUSTAR-KAIST Institute.

References

- [1] L. Y. Yeo and J. R. Friend, *Annu. Rev. Fluid Mech.*, **46**, 379–406, 2014.
- [2] C. Devendran, T. Albrecht, J. Brenker, T. Alan, and A. Neild, *Lab Chip*, **16**, 3756–3766, 2016.
- [3] G. Destgeer, B. H. Ha, J. Park, J. H. Jung, A. Alazzam, and H. J. Sung, *Anal. Chem.*, **87**, 4627–4632, 2015.



In-line micro/nanoparticles trapping, queuing, and sorting via 3D micro-vortex array induced by ultrahigh frequency acoustic waves

Weiwei Cui^{1,2}, Hongxiang Zhang¹, Meihang He¹, Yang Yang¹, Mark Reed^{2,3}, Xuexin Duan¹

¹State Key Laboratory of Precision Measuring Technology & Instruments, Tianjin University, Tianjin 300072, China. E-mail: xduan@tju.edu.cn. ²Department of Electrical Engineering and ³Department of Applied Physics, Yale University, New Haven, Connecticut 06520, United States

Introduction

Streaming forces in combination with acoustic radiation forces have provided a variety of interesting strategies for micro/nanoparticles manipulations in microfluidics. Recently, acoustic streaming induced by locally focused and high frequency surface acoustic waves (SAWs)^{1,2} has emerged as a promising tool for manipulations at micro/nano scale due to its excellent bio-compatibility, easy to control, and versatile capabilities. In this work, we demonstrate a novel micro/nano scale manipulation tool using three-dimensional (3-D) micro-vortex array which is generated by a ultrahigh frequency thickness-extensional (TE) mode piezoelectric solidly mounted resonator (SMR). Theoretical and experimental analysis demonstrate the efficient manipulations of micro/nanoparticles including in-line trapping, enriching, queuing, and size-selective sorting with the tunable 3-D vortex array. Particles with diameter from 200 nm to 10 μm can be well trapped by combining different parameters of applied power and flow rate. Besides, the trapped particles can be selectively released from a set position, forming the basis of in-line queuing and sorting.

System principles

Figure 1a presents the schematic of the integrated SMR microfluidic chip with locating the SMR in the center of a PDMS channel. The SMR comprises a piezoelectric (PZ) thin film sandwiched by two metal electrodes to form the resonating region (i.e. the pentagon region in figure 1b). A Bragg reflector containing six aluminum nitride (AlN) and SiO₂ layers is fabricated below sandwich structure to attenuate acoustic waves leaking to the Si substrate. Different from SAWs, the SMR works at TE mode, and its resonant frequency is dependent on the thickness of the PZ layer³. The TE acoustic beam is mainly localized in the center of the resonating region and sharply decreases towards the boundaries (figure 1c), resulting in highly focused acoustic fields. Using AlN film with a thickness of 1 μm as the PZ layer, the resonant frequency of SMR is measured as 1970 MHz. When the ultrahigh frequency (UHF) acoustic wave couples into microfluids, large body force (on the order of 10¹³ N/m⁵) is generated in the SMR-liquid interface within a short decay length⁴. Figure 1 d-e reveal the generation of 3-D vortex array around the SMR edges via both finite element simulation and microparticle tracing experiments (micro PIV). Polystyrene (PS) particles with diameter of 9 μm, 1 μm, and 200 nm were respectively introduced into the 3-D vortex acoustofluidic chip to test its particle capture and queue capability. For sorting experiment, mixtures of 20 μm, 9 μm, 1 μm PS particles were introduced into the chip

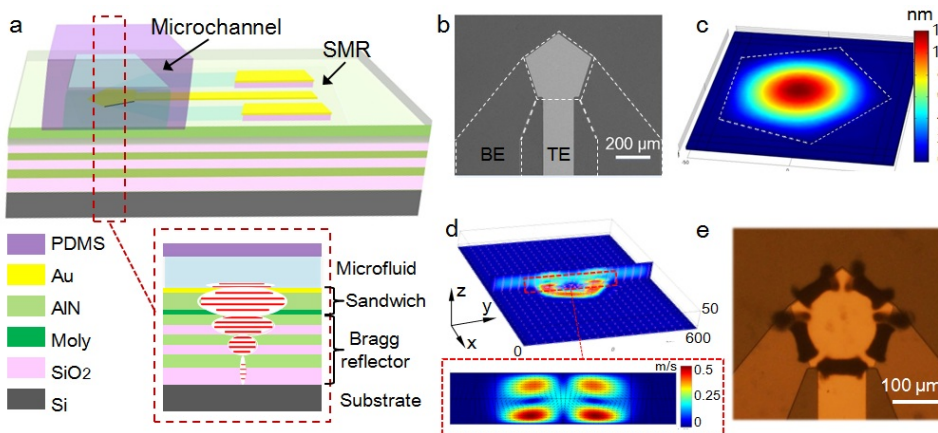


Figure 1: (a) Schematic of integrated acoustofluidic chip. (b) Scan electric microscopy (SEM) image of the fabricated SMR. (c) 3-D simulation results of SMR-triggered acoustic fields. (d) 3-D simulation of the acoustic fields induced vortex streaming within microchannel. (e) Optical microscopy image of SMR triggered vortices traced by 1 μm PS particles.

with a flow rate of 2 μL/min. Optical microscopy (15 fps) was used to record the experiments in real time. Streaming forces, viscous force (F_s) and inertial force (F_I) dominate the manipulations of micro/nanoparticles

inside the vortices. Figure 2 a-b present the theoretical analysis of 10 μm particle trapping and local motion in a size-dependent equilibrium position.

Results and discussion

Figure 2 c presents the trapped PS particles by the 3-D vortex array, showing its good capacity of particle trapping and enriching from 200 nm to 9 μm (the trapped 1 μm ones is not shown here). The trapping effect can be tuned by altering the applied power and flow rate. For a given flow rate, higher power contributes to improved trapping efficiency. For a given applied power, the trapped particles in the vortices would travel along the vortices under an appropriate flow and escape from the vortices when the flow rate is higher than a critical value. Figure 2 d presents the queuing effect of different sized PS particles with 20 mW applied power and 2 $\mu\text{L}/\text{min}$ flow rate. The queue is actually a result of particle releasing from a stable point from the vortices in downstream as presented in figure 2 d. Especially, by further optimizing the flow rate and applied power, different sized particles can be selectively released. Figure 2 e presents the selective capture of 20 μm PS particle from the mixture suspension. As the density of PS particles ($1.05 \text{ g}/\text{cm}^3$) is very close to blood cells, the vortex sorter can be potential used for whole blood cell sorting applications.

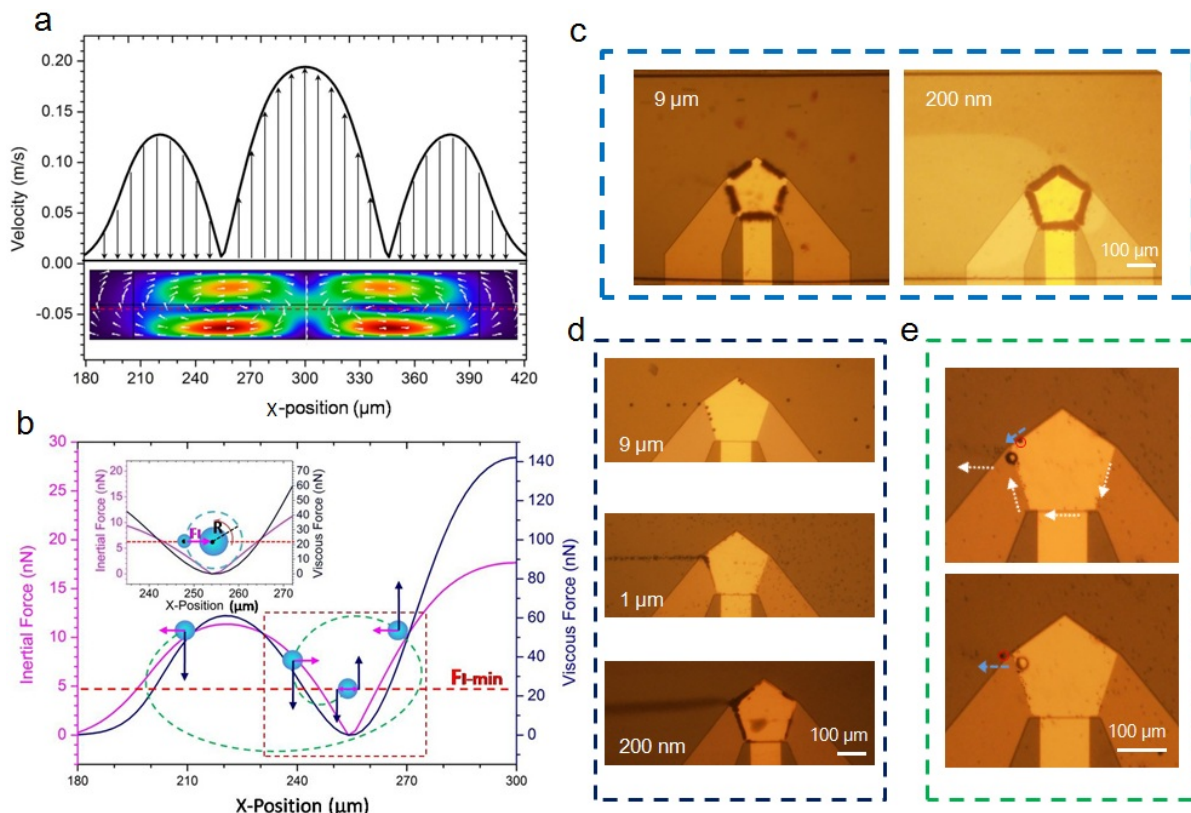


Figure 2: (a) Velocity distribution on the simulated vortex field, wherein arrows direct the velocity direction in the z-axis. (b) Forces analysis of the particles within vortex field. (c) In-line trapping of micro/nanoparticles from the flow (2 $\mu\text{L}/\text{min}$). (d) Queuing of particles of different diameters with applied power of 20 mW and flow rate of 2 $\mu\text{L}/\text{min}$. (e) Size selective trapping based microparticles sorting: the 20 μm PS particles are trapped while the other PS particles with diameter of 9 μm (blue arrow) and 1 μm (white arrow) are released.

Conclusion

Directly generating and tuning vortices in micro/nanofluidics has remained as a challenge in the field of acoustofluidics, as well as manipulations of sub-micron particles. The acoustic device applied in this work offers a simple but effective acoustofluidic strategy to generate 3-D microfluidic vortices, and its potential in micro/nanoscale particle manipulations including trapping, queuing, and sorting have been successfully demonstrated. Due to its ultrahigh frequency, acoustic waves are decayed within several micrometers, and the particles are dominated by the vortex streaming forces, which is different from previous reported acoustofluidic technologies. Additionally, considering the IC-compatible fabrication process of the device, this platform is very convenient to be integrated with different analysis tools in downstream as well.

References

- [1] D.J. Collins, Z. Ma, and Y. Ai, *Anal. Chem.* **88**, 5513-5522 (2016).
- [2] R.J. Shilton, M. Travaglini, F. Beltram, and M. Cecchini, *Adv. Mater.* **26**, 4941-4946(2014).
- [3] W.Pang, H. Zhao, E.S. Kim, H. Zhang, H. Yu, X. Hu, *Lab Chip* **12**, 29-44(2012).
- [4] W. Cui, H. Zhang, H. Zhang, Y. Yang, M. He, W. Pang, D. Zhang, X. Duan, *Appl. Phys. Lett.* **109**, 253503(2016).



High Throughput Acoustophoresis in Parallel Plastic Microchannels

Ryan Dubay¹, Ryan Silva¹, and Jason Fiering¹

¹Draper, Cambridge, MA, USA
E-mail: jfiering@draper.com

Introduction

Numerous studies have shown that ultrasonic stimulation in microchannels is effective for manipulating and separating particles within a fluid. [1] However, a drawback to these microfluidic devices is limited throughput, typically on the order of 0.1 ml/min. Such rates preclude the expansion of acoustofluidics into applications such as bioprocessing, where throughput requirements may exceed 10ml/min. In principle, the performance of microfluidic acoustic devices can be preserved if channels are configured in parallel, but two hindrances to implementation are the cost of large micromachined chips in silicon or glass and the establishment of uniform excitation of each resonating microchannel in accordance with its wall thickness.[2]

Here we present an approach to fabricating parallel acoustofluidic devices and address both of these hindrances. The devices are constructed from a thermoplastic, enabling a large footprint while keeping the production cost low. Additionally, we take advantage of the ease of plastic fabrication and isolate each microchannel from its neighbor by an air gap. Thus, its mechanical behavior is close to that of a single independent microchannel, while multiple inlets and outlets converge in a bifurcated network. Using a parallel 4-channel test device, we show improved performance with the air gaps (slots) as the channels are used to focus red blood cells (RBCs) across a range of frequencies spanning both odd and even modes.

Methods

Two devices were fabricated from polystyrene sheets using a desktop micromill, and the layers were thermocompression bonded. Each contained a parallelized array of 4 channels with bifurcations connecting a single inlet and outlet. Bifurcations and overall path lengths were designed to maintain similar mean wall shear stress as well as equal flow distribution through each channel. One device had continuous walls (no slots) between the neighboring channels (Figure 1A), whereas the second included slots between them (Figure 1B). All other dimensions were constant, and channel and wall width were based on a previous polystyrene single-channel design demonstrated to focus RBCs.[2] Chips were mounted to identical piezoelectric transducers. Diluted whole blood (7.5% hematocrit) flowed through each chip at a total rate of 100 μ L/min.

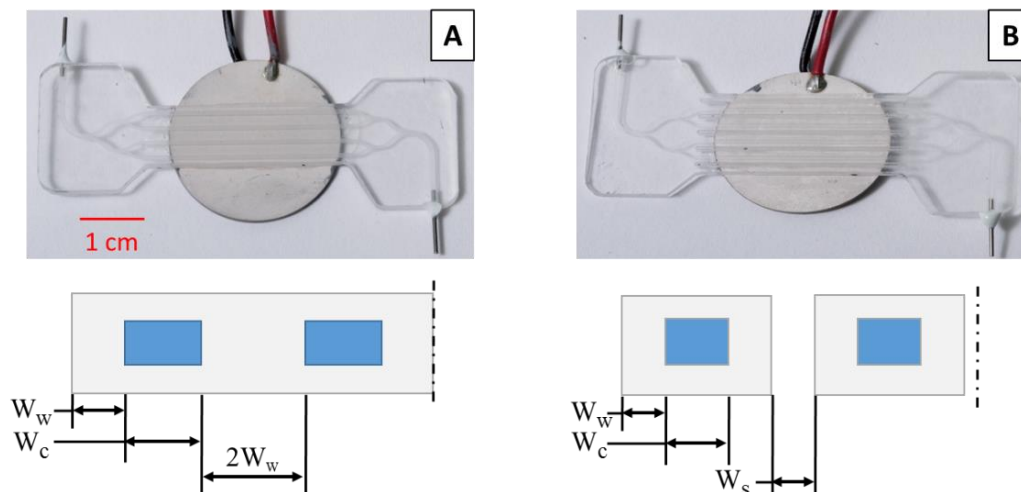


Figure 1. Photographs of parallel channel device mounted to transducer and cross section diagrams below to show relative dimensions (not to scale). A) No slot design with W_w width of the wall, W_c width of the fluid cavity, and dashed line indicating symmetry plane. B) Slotted design where dimensions are the same as (A), and W_s is the width of the slot.

Results

A microscope image was taken at the downstream end of each channel as it was driven at frequencies from 0.300—1.75 MHz in 10 kHz intervals, while holding temperature and average dissipated power constant (26°C, 2.0 W). The images were used to quantify the degree and position of RBC focusing at each frequency. Raw image files were inverted such that pixel intensity correlates to RBC concentration and pixel intensity was measured across the width of the channel as plotted in Figure 2. A peak in pixel intensity corresponds to a stream of focused RBCs. To further compare uniformity of blood cell focusing among channels, the prominence of the peaks in pixel intensity were calculated at each frequency. Prominence is defined as the difference between the highest peak and the max of the flanking minor peaks.[3] The optimum frequency, i.e., that with the highest prominence overall, was tabulated for the odd and even modes (Table 1).

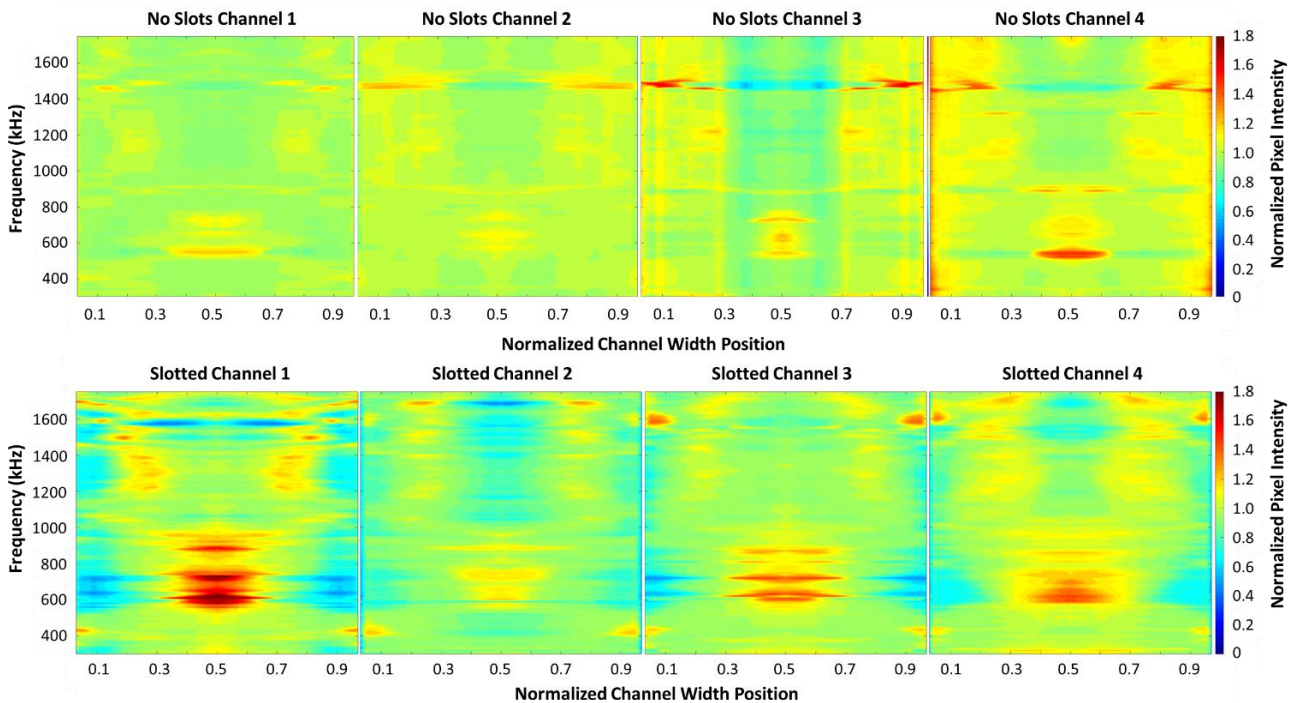


Figure 2. Pixel intensity (showing maximum focusing of RBCs as red) at each frequency and across width of channel. No-slot device (top), and slotted device (bottom). To eliminate illumination artifacts, pixel intensity was normalized to mean for each image, and the right half of the channel is a mirrored image of the left to enforce symmetry.

Table 1. Analysis of optimum frequency for each channel for no-slot and slotted device, showing mean and standard deviation among the four channels. Optimum frequency is that which produced highest peak prominence in pixel intensity. In odd mode RBCs focus to the center axis of channel; in even mode bilateral focusing streams were observed.

Device Design	Odd Mode Mean Frequency (kHz)	Odd Mode Std. Dev. Frequency (kHz)	Even Mode Mean Frequency (kHz)	Even Mode Std. Dev. Frequency (kHz)
No Slots	577.5	45.00	1475.0	23.80
Slotted	615.0	17.32	1555.0	10.00

Conclusion

The results suggest that the slotted device has improved performance over the no-slot device. Figure 2 shows that the slotted device has higher dynamic range in pixel intensity, which corresponds to stronger acoustic focusing of RBCs. Table 1 shows that in the slotted device, the optimum excitation frequency for both odd and even modes is more repeatable from channel to channel than in the no-slot device. This study indicates that a large scale array of microchannels could be fabricated from plastic for high throughput applications.

References

- [1] H. Bruus, et al. *Lab Chip* **11**, 3579 (2011).
- [2] R. Barnkob, H. Bruus. *Acoustical Society of America*, Portland, OR, 18 – 22 May 2009.
- [3] A. Mueller, et al. *J. Micromech. Microeng.* **23**(12): p. 125006 (2013).
- [4] L. Arg, et al. *pp. 254 – 263, ACM Sigspatial GIS 2013*, Orlando, FL, 5 – 8 November 2013.



Intra-droplet acoustic separation of two particle species in a droplet microfluidic system

Anna Fornell¹, Kevin Cushing¹, Johan Nilsson¹, and Maria Tenje^{1,2}

¹Department of Biomedical Engineering, Lund University, Lund, Sweden

E-mail: anna.fornell@bme.lth.se

²Department of Engineering Sciences, Science for Life Laboratory, Uppsala University, Sweden

Introduction

In this paper we demonstrate a continuous method for binary separation of microparticles encapsulated in water-in-oil droplets based on the acoustic properties of the particles. Droplet-based microfluidic platforms are becoming an increasingly popular alternative for on-chip miniaturization of cell- and bead-based assays [1,2]. The idea is to use micrometer-sized water droplets as individual reaction chambers for biological and chemical experiments at a high throughput. However, standard assays often contain one or several particle manipulation and separation steps, and one limitation for the full implementation of droplet-based systems is the lack of methods to separate one encapsulated particle species from another into different daughter droplets. Previously, we have reported on an acoustic method for focusing and concentrating one particle species (polystyrene microbeads) inside droplets by using bulk acoustic waves [3]. The aim of this work is to investigate the possibility to separate two different particle species into either the center or side daughter droplets in a trident-shaped droplet splitter depending on the acoustic properties of the encapsulated particles.

Experimental

The microfluidic system is shown schematically in Figure 1. The system consists of dry-etched silicon channels that are anodic bonded to a glass lid. The microfluidic channels were hydrophobic surface-treated with silane. The width of the main channel is 370 μm and the depth is 100 μm . The droplet splitter consists of a trifurcation where the side outlet channels are angled 20° with respect to the main channel. Compared with our previous droplet splitter [3] the key feature in this new droplet splitter design is that it allows to set up and maintain a standing wave all the way to the droplet splitting position. A piezoelectric transducer (1 mm thick yielding 2 MHz fundamental resonance frequency, APC-840, APC International) was glued on the silicon side of the chip using cyanoacrylate glue, and the transducer was actuated by an AC-signal from a function generator after amplification of the signal. Actuation of the transducer generates bulk acoustic waves in the device, and when the applied frequency is matched to the channel width a half-wavelength standing wave is set between the main channel walls. In the experiment the actuation frequency was 1.80 MHz and the voltage was kept at 22 V_{pp} to avoid excessive heating of the device.

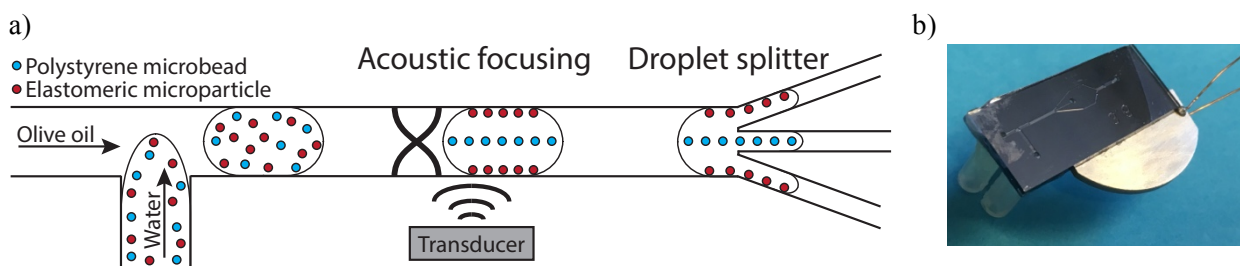


Figure 1: a) Illustration of acoustic particle-positioning in combination with a trident-shaped droplet splitter. At resonance polystyrene beads (positive acoustic contrast factor particles) are moved towards the pressure nodal line and enriched in the center daughter droplets while the elastomeric microparticles (negative acoustic contrast factor particles) are moved towards the pressure anti-nodal lines and enriched in the side daughter droplets. b) A photograph of the silicon-glass device. The dimensions of the chip are 1 x 2 cm^2 .

The fluid flows were controlled by syringe pumps connected to the microfluidic chip. The flow rate of the water phase was 4 $\mu\text{l}/\text{min}$ and the flow rate of the continuous phase was 8 $\mu\text{l}/\text{min}$. Olive oil was chosen as the continuous phase as it has similar acoustic properties as water ($v_{\text{olive oil}} = 1,450 \text{ m/s}$, $\rho_{\text{olive oil}} = 0.91 \text{ kg}/\text{dm}^3$, $v_{\text{water}} = 1,497 \text{ m/s}$, $\rho_{\text{water}} = 1.00 \text{ kg}/\text{dm}^3$). In the water phase a mixture of polystyrene microbeads (10 μm diameter) and elastomeric microparticles ($7.1 \pm 2.9 \mu\text{m}$ diameter) were suspended. Polystyrene microbeads were used as positive acoustic contrast particles since polystyrene microbeads are commonly used in bead-

based assays and as they also mimic the acoustic behavior of most cells. As negative acoustic contrast particles elastomeric microparticles were fabricated in-house from polydimethylsiloxane (PDMS) [4]. PDMS has the advantages that it is a biocompatible and cheap material, and it also has the possibility to be surface-functionalized to bind specific cells or biomolecules.

Results and discussion

In the experiment water-in-oil droplets containing a mixture of polystyrene microbeads and elastomeric microparticles were generated in a T-junction. The droplets were transported downstream the main channel by the flow and reached the trident-shaped droplet splitter. In the droplet splitter each original droplet was split into three approximately equal-sized daughter droplets (8 nl). Initially, the transducer was not actuated and the two particle species were randomly distributed in the entire original droplet, and after the droplet splitter all three daughter droplets contained both particle species (see Figure 2A). However, at acoustic actuation of the system at the fundamental resonance frequency of the system, the polystyrene microbeads were moved towards the pressure nodal line located along the center line of the droplet while the elastomeric microparticles were moved towards the pressure anti-nodal lines at the channel walls instead (see Figure 2B). This resulted in that the two particles species were enriched in the center respective the side daughter droplets. The volume ratio between the center and side daughter droplets can be varied by changing the flow ratios between the center and side outlets, and consequently the enrichment can be varied. It was observed that in addition to the acoustic force the encapsulated particles were also affected by the internal fluid advection that is present in moving droplets [5].

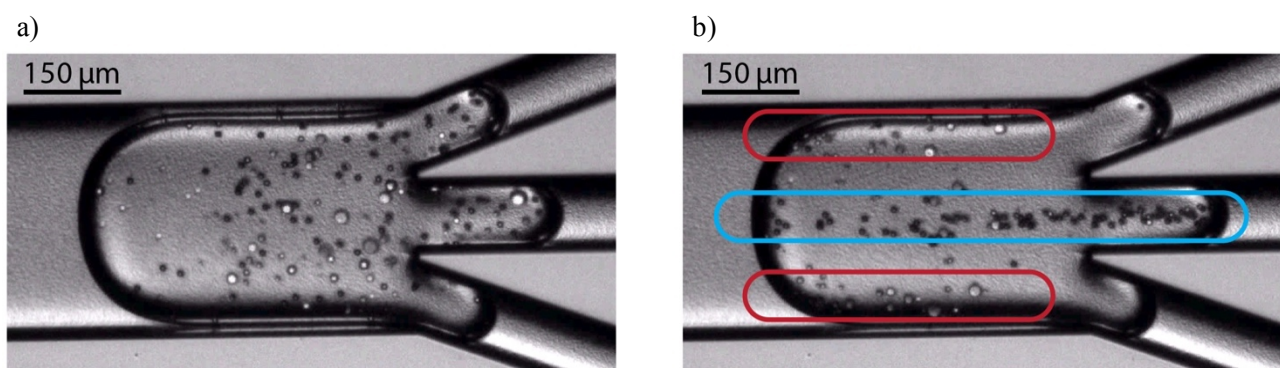


Figure 2: a) Without ultrasound the polystyrene microbeads (black dots) and the elastomeric microparticles (grey polydisperse dots) are distributed in the entire droplet. b) At acoustic actuation of the system the polystyrene microbeads are moved towards the pressure nodal line located along the center of the droplet while the elastomeric microparticles are moved towards the anti-nodal lines at the channels walls. As a result, in the trident-shaped droplet splitter the polystyrene microbeads are enriched in the center daughter droplets while the elastomeric microparticles are enriched in the side daughter droplets. In the area marked with the blue box the majority of the particles are polystyrene microbeads while the red boxes mark areas where the majority of the particles are elastomeric microparticles.

Conclusion

By combining acoustophoresis with a trident-shaped droplet splitter we have shown continuous binary separation of encapsulated microparticles into different daughter droplets. The separation is based on the acoustic properties of the encapsulated particles. We show that polystyrene microbeads (positive acoustic contrast factor particles) are enriched in the center daughter droplets while elastomeric microparticles (negative acoustic contrast particles) are enriched in the side daughter droplets. The presented technology holds promises for the development of new droplet-based cell- and bead-assays where the differentiation of one particle species from another is required.

References

- [1] R. Seemann, M. Brinkmann, T. Pfohl, and S. Herminghaus. *Rep Prog Phys.* **75**, 16601 (2012).
- [2] T. Schneider, J. Kreutz, and D.T. Chiu. *Anal Chem.* **85**, 3476–3482 (2013).
- [3] A. Fornell, J. Nilsson, L. Jonsson, P.K. Periyannan Rajeswari, H.N. Joensuu, and M. Tenje. *Anal. Chem.* **87**, 10521–10526 (2015).
- [4] K.W. Cushing, M.E. Piyasena, N.J. Carroll, G.C. Maestas, B.A. López, B.S. Edwards, S.W. Graves, and G.P. López. *Anal. Chem.* **85**, 2208–2215 (2013).
- [5] C.N. Baroud, F. Gallaire, and R. Dangla. *Lab Chip.* **10**, 2032–2045 (2010).



Surface acoustic wave guiding and steering on lithium niobate

Jiyang Mei¹, and James Friend¹

¹Department of Mechanical and Aerospace Engineering, University of California San Diego, San Diego, USA

E-mail: jfriend@eng.ucsd.edu, URL: <http://friend.ucsd.edu/>

Introduction

Lateral diffraction of waves is a major constraint in current surface acoustic wave (SAW) devices inevitably resulting in energy dissipation along certain direction. Though one may seek to minimize its effects by the choice of a low diffraction propagation direction, there are situations in which fluid or particle manipulation at disparate locations in a micro device is expected. The difficulties in controlling the direction of wave propagation make these applications inefficient as well [1]. However, these limitations may both be overcome by the use of waveguides for such surface waves, where the term waveguide implies a geometrical structure, such as, a thin conducting film.

The concept of thin film waveguide was first introduced by White and Seidel. They suggested that thin films of finite width deposited on an isotropic substrate can be used to guide elastic surface waves in the substrate. The pioneering theoretical investigation of structures which depend upon a velocity differential for guidance is that of Tiersten [2]. Another type of waveguide is the shorting-strip (or $\Delta v/v$) waveguide, which was first proposed by Engan [3], consisting of a very thin strip of metal on a piezoelectric substrate. The metal strip short circuits the electric field associated with the piezoelectric surface wave and, as a result, produces a slight reduction Δv in the velocity of that wave under the strip. The situation of aluminum strip on LiNbO_3 have been considered by Schmidt and Coldren [4], where an accurate theory was discussed. Although the guiding mechanism has so far been widely understood, the applications are generally associated with long delay lines [5] and structural health monitoring [6][7], while that in the context of acoustofluidics is still lacking. This paper shows that the introduction of waveguide overcomes diffraction and expands the ability to transmit waves from one dimensional to two, which reveals the potential of manipulation waves for acoustofluidic applications.

Materials and Methods

The SAW-based acoustofluidic device is composed of a piezoelectric substrate (LiNbO_3) and a focused interdigital transducer (FIDT), as well as a guiding layer, deposited on top. The FIDT was designed as a concentric circular shape, with a degree of arc at 60° , first finger curvature 1.70mm , 16 pairs of $24.87\mu\text{m}$ wide fingers, corresponding to a resonant frequency at 40MHz , and was fabricated through photolithography. Various shapes of aluminum strip were deposited using the same method. The substrates used in the experiment were $128^\circ YX$ cut and another Z cut Lithium Niobate. Absorbers were placed both at the front and behind the pairs of IDT's. A laser doppler vibrometer (LDV, UHF120, Polytec) was used to measure the amplitude over distance in order to determine the actual focal point of the FIDT. Moreover the amplitudes of the wave is measured both before it enters and after it exits the guiding layer, so that a relative energy flow was quantified.

Results and Discussion

In the 1980s, Green and Kino had predicted that the effective focal length f was shifted by an amount [8]

$$z = \frac{2Rb}{1 - 2b} \quad (1)$$

where R is curvature of transducer finger and constant b represents the anisotropy of the substrate material. Positive values of b tend to defocus the transducer, while negative values of b bring the focal plane closer toward the transducer. However, Other researchers [9] [10] have showed experimentally that concentric circular IDT focused around 1.5 – 2 times of geometric focal length. According to our data, Figure 1 the real focal length of SAW on $128^\circ YX \text{LiNbO}_3$ is about 2 times of the geometrical

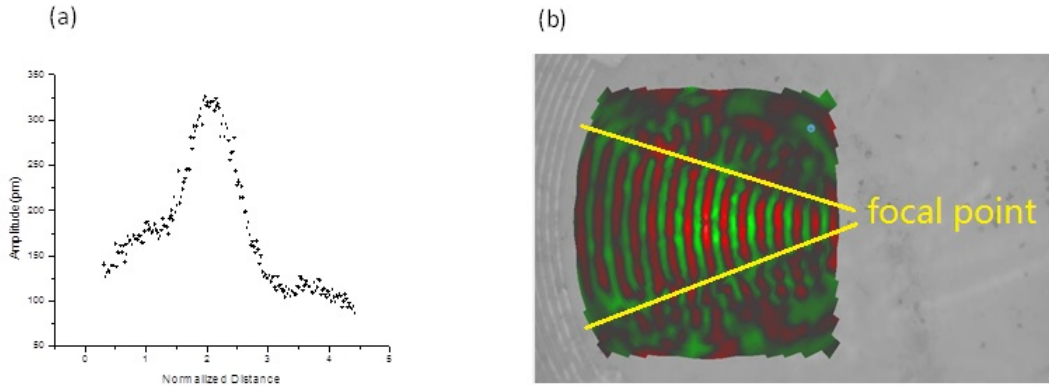


Figure 1: (a)amplitude vs normalized distance plot, (b)the scan image from LDV.

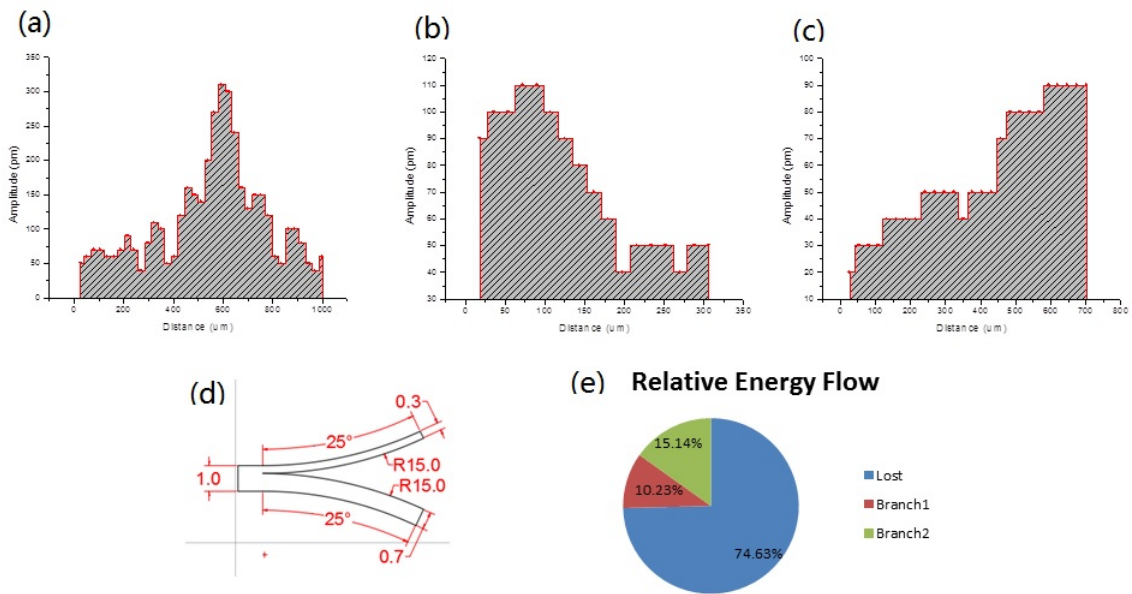


Figure 2: As wave propagates from left to right, when it enters (d)the Y shape guiding structure, amplitude vs verticle distance on the guiding layer of (a)entrance, (b)upper exit, (c)lower exit were plotted. (e)shows the energy flow percentage after going through the waveguide

focal length, while normalized distance was defined as the ratio of the actual distance divided by the geometrical length. With the entrance of waveguide structure deposited at the real focal point, since energy of wave has a proportionality of square of amplitude, the energy flow was calculated as the integral of squared amplitude over the waveguide width. Therefore, the result is shown in Figure 2. More than 25 percent of the energy deviated away from the original direction, indicating its ability of turning wave along the guiding layer at some extent.

Conclusion

Our data has disclosed the fact that Waveguide holds the ability of confining the lateral extent of the surface wave on the substrate, and thus overcomes the limitation of diffraction, so as to realize guiding of waves in desired directions and low energy dissipation. More results concerning the Z cut LiNbO₃ will be presented as well at the conference. Further study should focus on accurate manipulation of energy to distinct locations using powerful guided SAW, actuating fluids and particles within, for potential bio applications.

References

- [1] Oliner, A. A. Waveguides for acoustic surface waves: A review. *Proceedings of the IEEE* **64**, 615–627 (1976).
- [2] Tiersten, H. Elastic surface waves guided by thin films. *Journal of Applied Physics* **40**, 770–789 (1969).
- [3] Engan, H. *Experiments with Elastic Surface Waves in Piezoelectric Ceramics* (Norwegian Institute of Technology, Electronics Research Laboratory, 1969).
- [4] Schmidt, R. V. & Coldren, L. Thin film acoustic surface waveguides on anisotropic media. *IEEE Transactions on Sonics and Ultrasonics* **22**, 115–122 (1975).
- [5] Adams, P. & Shaw, H. Surface acoustic waveguide for long time delay. In *1972 IEEE Ultrasonics Symp.*
- [6] Raghavan, A. & Cesnik, C. E. Review of guided-wave structural health monitoring. *Shock and Vibration Digest* **39**, 91–116 (2007).
- [7] Siqueira, M., Gatts, C., Da Silva, R. & Rebello, J. The use of ultrasonic guided waves and wavelets analysis in pipe inspection. *Ultrasonics* **41**, 785–797 (2004).
- [8] Green, J., Kino, G. & Khuri-Yakub, B. Focused surface wave transducers on anisotropic substrates: a theory developed for the waveguided storage correlator. In *1980 Ultrasonics Symposium*, 69–73 (IEEE, 1980).
- [9] Shilton, R., Tan, M. K., Yeo, L. Y. & Friend, J. R. Particle concentration and mixing in microdrops driven by focused surface acoustic waves. *Journal of Applied Physics* **104**, 014910 (2008).
- [10] Wu, T.-T., Tang, H.-T., Chen, Y.-Y. & Liu, P.-L. Analysis and design of focused interdigital transducers. *IEEE transactions on ultrasonics, ferroelectrics, and frequency control* **52**, 1384–1392 (2005).



High efficiency centrifuge using isotropic piezoelectric substrate

Tilvawala Gopesh¹, Naiqing Zhang¹, and James Friend¹

¹Department of Mechanical and Aerospace Engineering, University of California San Diego, San Diego, USA

E-mail: jfriend@eng.ucsd.edu, URL: <http://friend.ucsd.edu/>

Introduction

Research conducted with ultrasonics and acoustics to manipulate fluids at the microscale: microscale acoustofluidics has seen exponential growth in the last 2 decades, with extensive reviews by Friend *et al* [1], Ding *et al* [2], Yeo *et al* [3] and more recently Destgeer *et al* [4]. The majority of research conducted with SAW for microfluidics has utilized the 128° YX cut of Lithium Niobate. Recently, there have been some studies which demonstrate the use of X-cut Lithium Niobate [5]. A common characteristic, though not a hindrance is the anisotropic nature of the crystals used for acousto-fluidics. The 128° YX and X-cut Lithium Niobate can generate SAW's of the same frequency and amplitude only in one direction. Any veering from the propagation direction is affected by beam steering, change in vibrational amplitude and electromechanical coupling coefficients as a result of the anisotropic nature of the substrate. Kurosawa *et al* demonstrated this for the 128° YX Lithium Niobate wafer, showing both the vibration displacements and velocities being 250% higher in the X-propagation direction compared to the Y-propagation [6].

The design of IDT's to generate SAW on these substrates is based on their anisotropic properties. A variety of different IDT designs have previously been described by Campbell [7]. A circular IDT pattern to manipulate particles with precursor swirling Rayleigh waves was recently described by Riaud *et al* [8]. In this paper we present a spiral IDT pattern on for the first time on an isotropic piezoelectric substrate used to create a high efficiency microfluidic centrifuge. Starting with two straight IDT's: one printed along the X-direction and the second perpendicular to it, in the Y-direction, the isotropic nature of the substrate was verified by observing Rayleigh wave generation in both directions. Subsequently, detailed analysis was used to develop a custom spiral pattern that was patterned on the isotropic substrate to create a high efficiency centrifugation device.

Materials and Methods

Starting with an isotropic piezoelectric substrate, IDT's with a design frequency of 40MHz were fabricated to generate waves in both the x and y directions of the substrate. Absorbers were placed both at the front and behind the pairs of IDT's. A laser doppler vibrometer (LDV, UHF120, Polytec) was used to measure the response just in front of the IDT's in both directions to demonstrate the isotropic nature of the substrate.

Subsequently, a detailed analysis was used to develop a spiral pattern ensuring wave generation into a central circular region at the same angle through 360°. A radially spatial electrode pattern designed to generate a SAW with 60MHz resonant frequency was formulated using custom MATLAB code to create a mask and fabricated using standard photolithography procedure. The IDT curvature was designed to generate a SAW at a constant angle, α as shown in figure 1, with spiral symmetry from the center to drive effective rotation of objects placed at the center, particularly fluid objects.

The equation used to design the spiral in polar coordinates (ρ, θ) is as follows:

$$\theta = \sqrt{A\rho^2 - 1} - \tan^{-1}(\sqrt{A\rho^2 - 1}) - \sqrt{AR_1^2 - 1} + \tan^{-1}(\sqrt{AR_1^2 - 1}) \quad (1)$$

where $A = \frac{1}{R_2^2 \sin^2 \alpha}$; R_1, R_2 are outer and inner radius of the spiral IDT respectively; α is the offset angle for SAW propagation.

We then determined the number of spiral lines by considering the finger width for specific frequency f (= 60 MHz in this case).

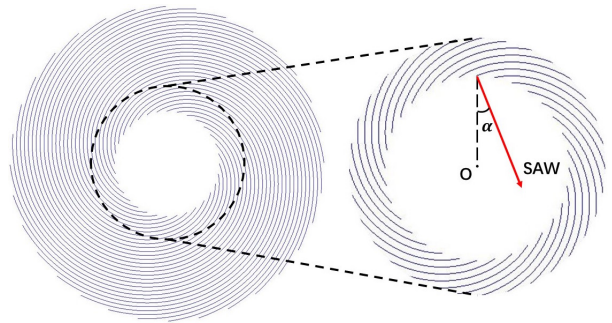


Figure 1: Image of the spiral pattern generated in MATLAB, with perpendiculars to the tangent of the spiral all pointing at an angle α relative to the central circle.

$$R_2 \frac{2\pi}{n} \sin \alpha = \frac{\lambda}{4} = \frac{v}{4f} \Rightarrow n = \frac{8\pi f R_2 \sin \alpha}{v} \quad (2)$$

where R_2 is the inner radius of the spiral IDT; $n/2$ is the number of spiral IDT fingers; α is the offset angle for SAW propagation; λ , f , v are wavelength, frequency, and phase velocity of surface acoustic wave propagating on LN respectively.

Absorbers were placed at radii on the outside of the spiral and in the central region to create an efficient acoustic absorber for minimizing interactions between the multiple Rayleigh waves which would otherwise give rise to standing waves. Scans of the spiral pattern using the LDV indicate a unique Rayleigh wave moving in a circular formation at the same frequency.

Results and Discussion

Figure 2, shows the plot of the displacement in the X and Y directions as a function of the driving voltage. In comparison to the plots obtained by Kurosawa, the amplitudes of the displacement in both directions are equivalent. The scans from the LDV were used to verify Rayleigh wave propagation in both the directions.

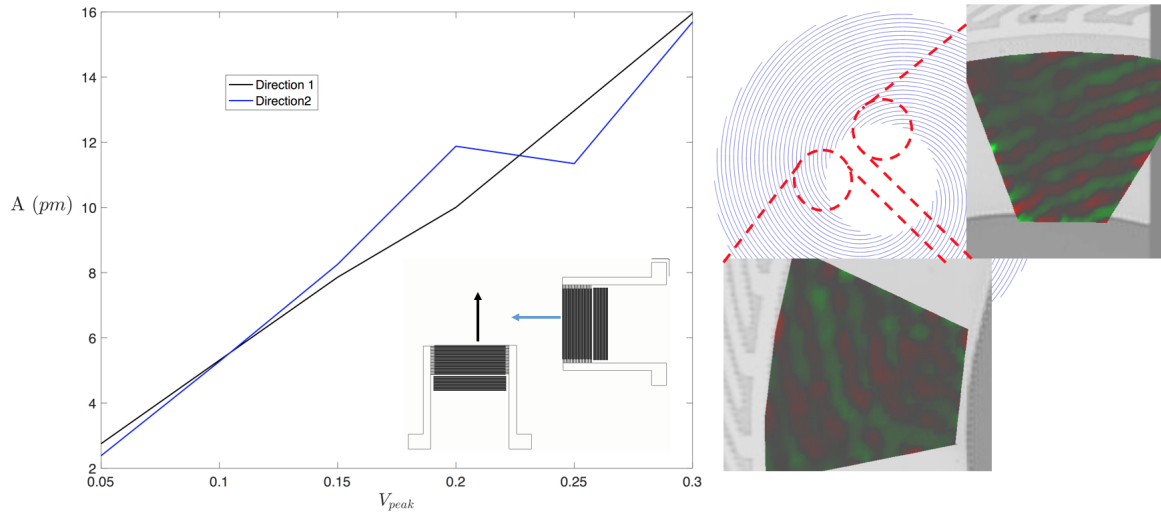


Figure 2: Plot of the amplitude as a function of the input voltage. Image of LDV scans from different regions of the spiral IDT pattern, both indicating Rayleigh waves at 60MHz.

Conclusions

Two straight IDTs were fabricated and tested to provide the first demonstration of Rayleigh waves generated on an isotropic substrate. The amplitudes in both directions were similar at the same driving voltage and frequency. Using mathematical analysis, a complex spiral IDT pattern was fabricated and tested on the substrate. Finally, LDV scans for the spiral pattern are presented which look promising to develop a high efficiency microfluidic centrifuge.

References

- [1] Friend, J. & Yeo, L. Y. Microscale acoustofluidics: Microfluidics driven via acoustics and ultrasonics. *Reviews of Modern Physics* **83**, 647 (2011).
- [2] Ding, X. *et al.* Surface acoustic wave microfluidics. *Lab on a Chip* **13**, 3626–3649 (2013).
- [3] Yeo, L. Y. & Friend, J. R. Surface acoustic wave microfluidics. *Annual Review of Fluid Mechanics* **46**, 379–406 (2014).
- [4] Destgeer, G. & Sung, H. J. Recent advances in microfluidic actuation and micro-object manipulation via surface acoustic waves. *Lab on a Chip* **15**, 2722–2738 (2015).
- [5] Riaud, A. *et al.* Anisotropic swirling surface acoustic waves from inverse filtering for on-chip generation of acoustic vortices. *Physical Review Applied* **4**, 034004 (2015).
- [6] Kurosawa, M., Takahashi, M. & Higuchi, T. Ultrasonic linear motor using surface acoustic waves. *IEEE Transactions on Ultrasonics, Ferroelectrics, and Frequency Control* **43**, 901–906 (1996).

- [7] Campbell, C. K. Applications of surface acoustic and shallow bulk acoustic wave devices. *Proceedings of the IEEE* **77**, 1453–1484 (1989).
- [8] Riaud, A., Baudoin, M., Matar, O. B., Becerra, L. & Thomas, J.-L. Selective manipulation of microscopic particles with precursor swirling rayleigh waves. *Physical Review Applied* **7**, 024007 (2017).



Isolation and Enrichment of Rare Circulating Tumor Cells from Whole Blood Using Acoustic Microstreaming

Neha Garg^a, Trisha Westerhof^b, Dylan Boyle^a, Edward Nelson^b, Abraham Lee^a

^a Department of Biomedical Engineering, University of California, Irvine, CA, USA

Email: gargn1@uci.edu, URL: <http://biomint.eng.uci.edu/>

^b Department of Medicine, University of California, Irvine, CA, USA

Introduction

Interest in separation, enrichment and analysis of rare circulating tumor cells (CTCs) has increased dramatically as an alternative to invasive biopsies due to its capability in non-invasively providing accurate information about cancer progression and intensity in real-time.¹ Although CTCs are effective in gauging the body's response to the chosen treatment method, they present inherent challenges in their isolation from blood. CTCs are very rare in the presence of billions of hematopoietic cells (1-10 CTCs/mL) and undergo epithelial to mesenchymal transition (EMT), leading to both genotypic and phenotypic heterogeneity which limits the effectiveness of immune-selection based isolation mechanisms.² Several label-free methods utilizing hydrodynamic forces, dielectric forces and surface acoustic forces have been developed but they do not utilize whole, unprocessed blood and instead demonstrate device functionality with pre-processed samples.³ In this work, we present a microfluidic technology based on acoustic microstreaming to trap complete populations of cells/particles spiked in whole blood for concentrations as low as 10 cells per milliliter. The trapped cells can then be released in a small volume (20 μ L) leading to an enrichment ratio of 213 for spiked breast cancer cells (MCF-7) with respect to white blood cells (WBCs).

Device Description

Due to inherent heterogeneity, we are utilizing cell size as a marker for isolating the rare cells from whole unprocessed blood sample. Acoustic Microstreaming is a phenomenon in which localized streaming patterns occur near an oscillating surface.

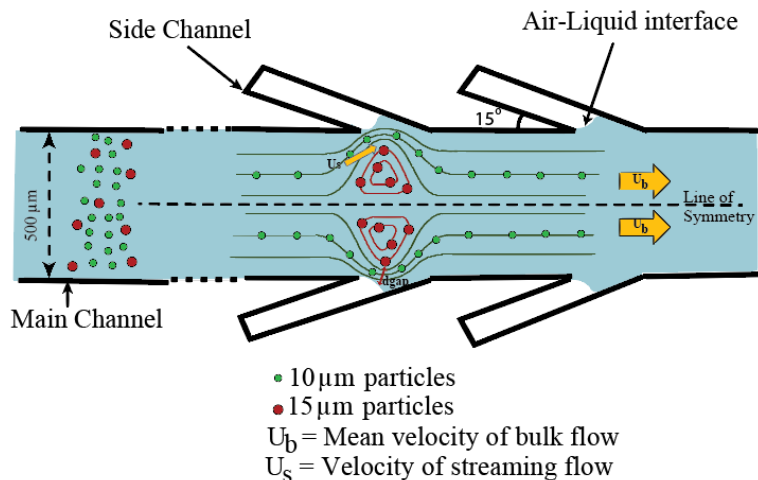


Figure 1: Schematic of the LCAT device demonstrating the main channel and the dead-end side channels. The air is trapped in the side channels forming the air-liquid interface along the edge of main channel. It shows the trapping of large particles (diameter $> 2d_{gap}$, red) in closed loop streamlines and release of smaller particles (diameter $< 2d_{gap}$, green) via open streamlines in bulk flow after the actuation of air-liquid interfaces using a PZT. [d_{gap} is the width between the critical streamline and the bubble surface]

Here, we are utilizing acoustic microstreaming in a microfluidic device called as Lateral Cavity Acoustic Transducer (LCAT). The LCAT device uses an array of dead end side channels to trap air bubbles along the edge of main channel. When these bubbles are actuated by an acoustic source, microstreaming velocity at the interfaces causes size-based trapping of cells/particles (Fig. 1). Larger sized particles will be pushed away from the bubble and enter in closed loop streamlines while small particles remain in open streamline allowing them to release in bulk flow. We use this phenomenon to continuously trap target rare cells/particles in microvortices, and then deactivate the vortices to release them into a smaller volume.

Results

We fabricated the LCAT devices with standard soft lithographic techniques using PDMS followed by plasma bonding on cover slips to aid in efficient energy transfer from the piezoelectric transducer (PZT) to the device. Two syringe pumps (for sample and wash buffer flow) were coupled with the device via tygon tubing. The device was actuated using a function generator coupled to the PZT. Trapped particles/cells were released after turning off the function generator for enumeration and downstream processing. We first optimized the device using 15 μm diameter particles in concentrations ranging from 10,000/mL to 10/ mL spiked in 10 μm particles (million/mL) to yield 97.88% trapping efficiency (Fig. 2a). To increase the purity and subsequently the enrichment ratio, we removed 80% of the non-target particles using PBS washing and voltage switching from 2.75V_{pp} to 2.0V_{pp} for 30sec.

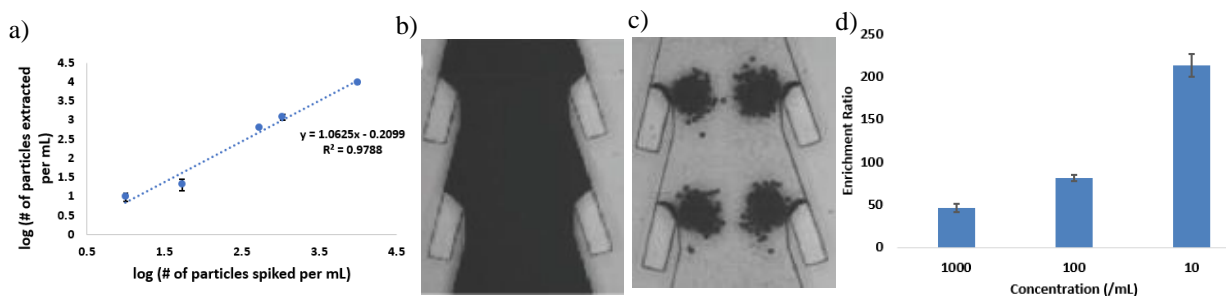


Figure 2: a) Plot showing an average trapping efficiency of 97.88% for 15 μm particles spiked among 10 μm (million/mL) particles. b) Bright Field image of the spiked whole blood flow in the device operating at 25 $\mu\text{L}/\text{min}$ and 2.75V_{pp}. c) Bright Field image of the pure microvortices showing the trapped 25 μm particles spiked initially at 10,000/mL concentration. d) Plot showing the MCF-7 cell enrichment ratio vs spiking concentration in whole blood

There are about a billion red blood cells, one billion platelets and one million white blood cells in 1mL of whole blood. To demonstrate the device capability with high cellular load (Fig. 2b), we flowed 25 and 15 μm diameter particles spiked in whole blood. We utilized washing & voltage switching to remove non-target RBCs/WBCs and obtain pure microstreaming vortices (Fig. 2c) which resulted in an enrichment ratio of 479 (25 μm) and 531 (15 μm) at 10/mL spiking concentration. Finally, we validated the device with MCF-7 breast cancer cells and obtained an enrichment ratio of 213 at 10/mL spiking concentration (Fig. 2d).

Conclusion

Here, we demonstrate an easy to fabricate and a portable device that utilizes acoustic microstreaming to trap and enrich cells/particles at targeted rare-cell concentrations from whole unprocessed blood.

References

- [1] C. Jin, S. M. McFaul, S. P. Duffy, X. Deng, P. Tavassoli, P. C. Black, H. Ma, Lab Chip, 14, pp.32-44 (2014).
- [2] A. Tedimety, A. Syeed, Y. Nie, C. Long, K. Kready, J. Zhang, Integrative Biology, 9, 22-49 (2017).
- [3] Yu, Z. T. F., Aw Yong, K. M. & Fu, J. Small 10, 1687–1703 (2014).



Modeling Particle Populations in Acoustophoretic Manipulation: Separation Performance and Cell-Parameter Estimation

Fabio Garofalo¹

¹Department of Biomedical Engineering, Lund University, Lund, Sweden
E-mail: fabio.garofalo@bme.lth.se,

Introduction

One of the most important field of application of acoustophoresis is the separation of different cell types [1]. As cells are characterized by distributed physical properties, the results of acoustophoresis exhibit smooth transitions in cell separation regimes, as well as the superposition of different cell populations at the outlet streams [2]. At today, tools aiming to quantify the separation performance are based upon simulations of single-particle trajectories and, as not incorporating distributions, they do not describe properly the experimental observations. Here, the foundation of modeling for particle populations during acoustophoresis is addressed [3].

Theory

Theoretical analysis considers the differential equations for the particle population $\mathbf{Q}(t) = [\mathbf{X}(t), \mathbf{P}]$ in the space+parameter coordinates $\mathbf{q} = [\mathbf{x}, \mathbf{p}]$, i.e. $\mathbf{x} = [x, y, z]$ is the position and $\mathbf{p} = [\kappa_p, \rho_p, r_p]$ are the acoustic parameters,

$$\dot{\mathbf{X}}(t) = \mathbf{f}^x[\mathbf{X}(t), \mathbf{P}, t], \quad (1a)$$

$$\mathbf{X}(0) = \mathbf{X}_0, \quad (1b)$$

where $\mathbf{f}^x(\mathbf{x}, \mathbf{p}, t)$ is the spatial drift determined by the acoustic radiation force, the hydrodynamics, the buoyancy, and the associated parameters. The parameter coordinates \mathbf{P} are constant during the motion and distributed with mean $E[\mathbf{P}] = \mathbf{m}^p$ and covariance $\text{cov}[\mathbf{P}, \mathbf{P}] = \mathbf{s}^{pp}$. The number of particles N must be large to compute meaningful statistics, i.e. $N \approx 10^5 - 10^6$. In order to (i) perform a notable reduction in the computational requirements and (ii) gain further insight on the separation process, equation (1) is rewritten as a transport equation for the particle density $\rho(\mathbf{x}, \mathbf{p}, t)$,

$$\partial_t \rho(\mathbf{x}, \mathbf{p}, t) = -\nabla_{\mathbf{x}} \cdot [\mathbf{f}^x(\mathbf{x}, \mathbf{p}, t) \rho(\mathbf{x}, \mathbf{p}, t)], \quad (2a)$$

$$\rho(\mathbf{x}, \mathbf{p}, 0) = \rho_0(\mathbf{x}, \mathbf{p}). \quad (2b)$$

Moment analysis of equation (2) in the space+parameter coordinates leads to the mean-covariance dynamics ($\mathbf{m} = [\mathbf{m}^x, \mathbf{m}^p]$, $\mathbf{s} = \text{sym}[\mathbf{s}^{xx}, \mathbf{s}^{xp}, \mathbf{s}^{pp}]$, $\mathbf{f} = [\mathbf{f}^x, \mathbf{0}]$, and $\mathbf{J}(\mathbf{q}, t) = \nabla_{\mathbf{q}} \mathbf{f}$),

$$\dot{\mathbf{m}}(t | \rho_0) = \mathbf{f}[\mathbf{m}(t | \rho_0), t], \quad (3a)$$

$$\dot{\mathbf{s}}(t | \rho_0) = \mathbf{J}[\mathbf{m}(t | \rho_0), t] \mathbf{s}(t | \rho_0) + \mathbf{J}^T[\mathbf{m}(t | \rho_0), t] \mathbf{s}(t | \rho_0), \quad (3b)$$

subjected to the initial distribution Eq. (2b) that in terms of the means and (cross-)covariances read as

$$\mathbf{m}^x(0 | \rho_0) = E[\mathbf{X}_0], \quad \mathbf{s}^{xx}(0 | \rho_0) = \text{cov}[\mathbf{X}_0, \mathbf{X}_0], \quad \mathbf{s}^{xp}(0 | \rho_0) = \text{cov}[\mathbf{X}_0, \mathbf{P}], \quad (4)$$

Solving for the mean \mathbf{m}^x and the covariances \mathbf{s}^{xx} and \mathbf{s}^{xp} , it is possible to approximate the time-dependent particle density $\rho(\mathbf{x}, \mathbf{p}, t)$, and, most interestingly, the spatial marginal ρ^x that corresponds to the likelihood,

$$\rho^x(\mathbf{x}, t | \rho_0^x; \theta) = \frac{1}{(2\pi)^{3/2} |\mathbf{s}^{xx}(t | \rho_0^x; \theta)|^{1/2}} \mathcal{G}\{[\mathbf{s}^{xx}(\mathbf{x}, t | \rho_0^x; \theta)]^T [\mathbf{x} - \mathbf{m}^x(\mathbf{x}, t | \rho_0^x; \theta)]\}, \quad (5)$$

where $\mathcal{G} = e^{-\xi^T \xi / 2}$, and $\theta = [\mathbf{m}^p, \mathbf{s}^{pp}]$ is the statistics for the parameters, that by definition, are constants during the ensemble motion, resulting $\dot{\mathbf{m}}^p = \mathbf{0}$ and $\dot{\mathbf{s}}^{pp} = \mathbf{0}$.

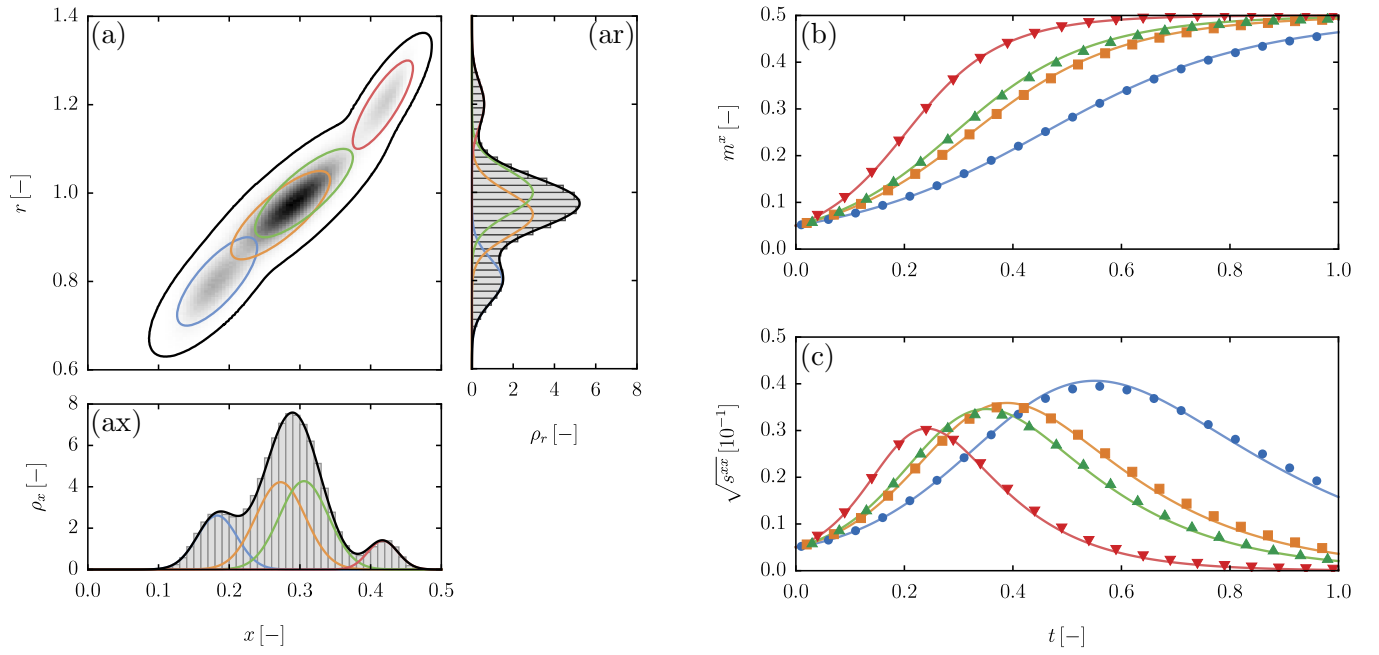


Figure 1: Simulations results for the prototypical model Eq. (6). Probability density function $\rho(x, r, t)$ at $t = 0.35$ (a) from direct simulations (black shaded density) and approximated by mean-covariance dynamics (black line $\rho = 0.1$) with four kernels (colored ellipsis). Corresponding spatial marginal $\rho^x(x, t)$ (ax) and radius marginal $\rho^r(r, t)$ (ar) from direct simulations (gray bins) and approximated by mean-covariance dynamics (black lines) of four kernels (colored Gaussians). Dynamics of the first-order moments m_i^x (b) and the spatial dispersions $\sqrt{s_i^{xx}}$ (c) for the four kernels (same colors as in panel (a), (ax) and (ar)) computed from direct simulations (symbols) and by mean-covariance dynamics (lines).

Results

As an example, the proposed method is applied to a prototypical model of acoustophoretic separation for populations described by the supersposition of four gaussian kernels, and governed by the equation of motion

$$\dot{X}_i(t) = R_i^2 \sin[2\pi X_i(t)], \quad (6)$$

in which the subscript “ i ” denotes the i -th kernel. In these equations, X_i are the particle positions for the i -th kernel, R_i are the particle radii normally distributed with average m_i^r and variance s_i^{rr} . Direct simulations of Eq. (1) adapted to Eq. (6) were performed with $N = 10^6$ total particles subdivided in four kernels with un-normalized weights $w = \{0.5, 1.0, 1.0, 0.2\}$, all starting at position $m^x(0) = 5 \cdot 10^{-2}$ with initial spatial dispersion $\sqrt{s^{xx}(0)} = 0.05 \cdot 10^{-1}$. Four average radius were considered $m^r = \{0.8, 0.95, 1.0, 1.2\}$ with standard deviation $\sqrt{s^{rr}} = 5 \cdot 10^{-2}$, and initial cross-covariance $s^{xr}(0) = 0$. Figure 1 compares the results of the direct simulations (symbols) and the reconstruction based on the solution of equations (3) (lines) (see caption for details). Here it is shown that the proposed method is a very good approximation for the direct dynamics, while requiring significantly lower computational efforts, i.e. only 12 equations were solved (4 kernels \times 3 variables in Eq. (4)).

Other examples include (i) a full 3D model for separation of red blood cells and white blood cells in SIP buffer at different concentrations [2], and (ii) the estimation of cell acoustic parameters from synthetic dataset at the input-output sections [3].

Conclusion

The foundations of modeling particle populations during acoustophoretic manipulations is presented. The proposed framework allows to quantify the separation performance and enables for the calculation of cell physical parameters from the analysis of experimentally-derived cell spatial distributions at the inlet/outlet sections of the device.

References

- [1] Augustsson Per et al., *Microfluidic, label-free enrichment of prostate cancer cells in blood based on acoustophoresis*, Anal Chem **84**, 7954-7962 (2012). Petersson et al., *Free-flow acoustophoresis: microfluidic-based mode of particle and cell separation*, Anal Chem **79**, 5117-5123 (2007).
- [3] Urbanski A et al., *Rapid and effective enrichment of mononuclear cells from blood using acoustophoresis*, Nat Biomed Eng (submitted).
- [3] Garofalo F et al., *Quantifying Free-Flow Acoustophoretic Separation of Cell Populations by Using Mean-Covariance Dynamics*, (in preparation).

Bulk Material Reduction in Silicon-Glass Acoustofluidic Devices: Improved Channel-Resonance Modes and Reduced Geometry Dependence

Fabio Garofalo^{1,*}, Thomas Laurell¹ and Henrik Bruus²

¹Department of Biomedical Engineering, Lund University, Lund, Sweden

²Department of Physics, Technical University of Denmark, Kongens Lyngby, Denmark

*E-mail: fabio.garofalo@bme.lth.se,

Introduction

Channel resonance detection and fabrication reproducibility of acoustophoretic devices are important research topics. It is well known that even nominally identical devices perform differently during experiments. This is due to a variety of causes that range from the intrinsic tolerances in the chip manufacturing (etching process, glass-lid thickness tolerance) to the uncontrolled uncertainties in the device fabrication (dicing of the piezoelectric transducer and chip coupling, manifold design).

By considering the model and the indicators introduced in Ref. [1], we focus on the study of the impact that bulk material reduction, i.e. removing unnecessary bulk silicon, has in terms of suppressing undesired resonance modes. Bulk material reduction is anticipated to prevent situations where the energy is localized in the channel, called channel resonances in the following, are over-shadowed by the response of the entire system. These situations disable the detection of channel resonances by means of impedance measurements [1]. Selective removal of bulk material increases the relative contribution of the channel to the overall system resonance and enables the detection of channel resonance features in the impedance spectra. The impact on the coupling of acoustic energy into the glass lid by removing bulk material is also discussed.

Model Setting

We consider a two-dimensional cross-section of a prototypical acoustofluidic device similar to that used in our previous study [1]. The only difference being the introduction of air-filled pockets that reduces the thickness of the surrounding silicon walls to 100 μm , see Fig. 1. The air pockets reduce the bulk material in the system and thereby the total acoustic energy stored in the silicon as well as the glass lid.

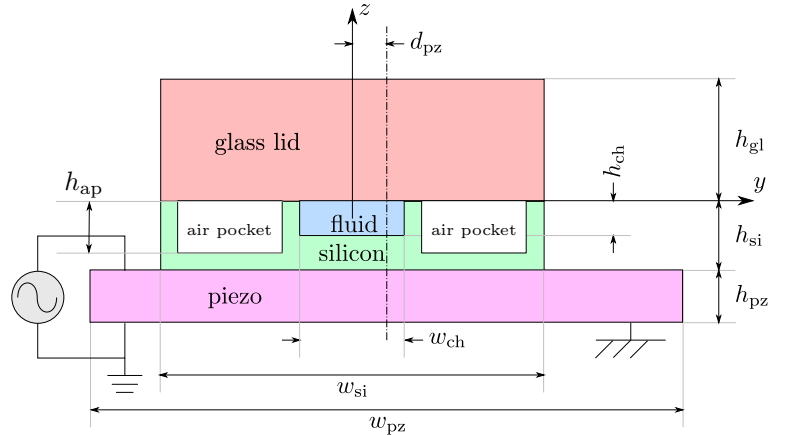


Figure 1: 2D cross section of the acoustophoretic device used in the numerical simulations.

The macroscopic indicators used in this study are

$$\text{total energy } \hat{H}(\omega), \quad \text{channel energy } \hat{H}_{\text{ch}}(\omega), \quad \text{impedance } \hat{Z}(\omega) = \mathbf{i} \frac{\phi_{\text{app}}^2}{\omega \hat{L}(\omega)},$$

where $\omega = 2\pi f$ is the angular frequency at driving frequency f , ϕ_{app} is the potential applied to the piezoelectric actuator, and \hat{L} is the complex-valued Lagrangian. Further details are given in Ref. [1], where also the link between the acoustophoretic performance and the electrical impedance response is discussed.

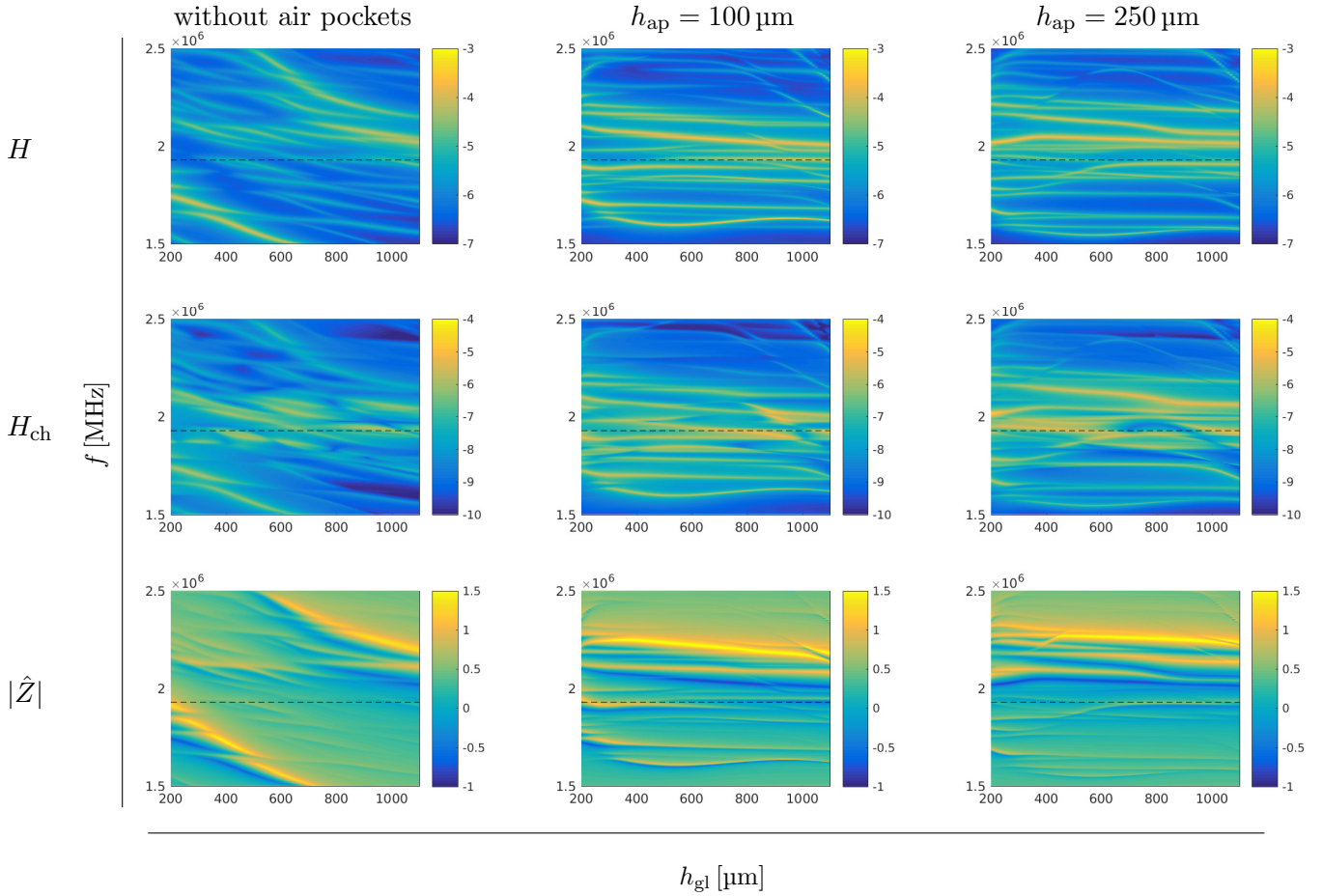


Figure 2: \log_{10} of system energy H , channel energy H_{ch} , and impedance $|\hat{Z}|$ for an acoustophoretic chip as function of the driving frequency f and the glass height h_{gl} , in the case without air-pockets, with air pockets $h_{\text{ap}} = 100 \mu\text{m}$ and $h_{\text{ap}} = 250 \mu\text{m}$. The dashed lines is the channel resonance frequency $f = 1.929 \text{ MHz}$ for $h_{\text{gl}} = 1100 \mu\text{m}$.

Results

Figure 2 shows results of the numerical simulations for three acoustophoretic devices with $d_{\text{pz}} = 250 \mu\text{m}$ and $h_{\text{gl}} = 1100 \mu\text{m}$, without and with the air pockets for $h_{\text{ap}} = 100 \mu\text{m}$ and $250 \mu\text{m}$. The device without air pockets is that considered in Ref. [1], for which the maximum in the channel energy occurs at $f = 1.929 \text{ MHz}$, but which is hidden by the global feature of the spectra (see the mechanical behavior in Fig. 6 and electric impedance in Fig. 9(b1) in Ref. [1]). Firstly, it must be noted that for the pocket-less device the resonance peaks drift to lower frequencies as the glass gets thicker whereas the cases with air pockets display significantly lower or no drift, i.e. the devices equipped with air pockets tolerate variations in the glass height better. This is due to the reduction in the contact area between the silicon and the glass that prevents the energy-coupling with the cover glass. Furthermore, the air-pocketed devices show the emergence of resonance peaks close to 1.929 MHz for broad intervals of the height of the glass lid. This is also appreciable in the channel energy spectra for $h_{\text{ap}} = 100 \mu\text{m}$, while it is partially true for $h_{\text{ap}} = 250 \mu\text{m}$. Finally, the impedance spectra for the air-pocketed devices show trench-like features (minima) that are related to channel resonances and that are detectable by impedance measurements through the piezoelectric ceramic.

Conclusion

The present work outlines the importance of engineering the chip design for optimal acoustophoresis performance. Specifically, by reducing bulk material in the chip, the influence of resonance modes that overlay the channel resonances can be significantly suppressed and the relative importance of channel resonances for the system increases, possibly enabling channel-resonance monitoring by direct impedance measurements. Furthermore, the decoupling of energy modes from the glass lid decreases the sensitivity of resonances frequencies when the thickness of the glass lid is varied.

References

- [1] Garofalo F, Laurell T, and Bruus H, *Performance study of acoustophoretic microfluidic silicon-glass devices by characterization of material- and geometry-dependent frequency spectra*, <https://arxiv.org/abs/1610.02794> Phys Rev Appl (in press, 2017).



Ultrasound Characterization of Cell Suspensions by Speed-of-Sound Measurements of Neutrally Buoyant Samples

Kevin Cushing^{1,*}, Fabio Garofalo^{1,§}, Cecilia Magnusson², Lars Ekblad³, Henrik Bruus⁴ and Thomas Laurell¹

¹Department of Biomedical Engineering, Lund University, Lund, Sweden

²Department of Translational Medicine, Lund University, Lund, Sweden

³Division of Oncology, Clinical Sciences, Lund University and Skåne University Hospital, Lund University, Lund, Sweden

⁴Department of Physics, Technical University of Denmark, Kongens Lyngby, Denmark

*E-mail: kevin.cushing@bme.lth.se

§E-mail: fabio.garofalo@bme.lth.se

Introduction

We present an experimental method including error analysis for the measurement of the ensemble-averaged density and compressibility of cells and microbeads using speed-of-sound measurements of neutrally buoyant microparticle or cell suspensions [1]. Measurement of density and compressibility of microparticles is a problem of paramount importance in acoustofluidics, as no standardized method is available and these parameters are an essential prerequisite to predict and characterize any acoustophoretic processing. Our method holds potential for becoming an easy-to-use reference in measuring microparticle acoustic properties.

Material and Methods

The density of the cells was determined using a neutrally buoyant selection process where various non-fixed and fixed cell types (DU145 prostate cancer cells, MCF-7 breast cancer cells, LU-HNSCC head and neck squamous carcinoma cells, WBCs, and RBCs) were suspended in various isotonic density solutions (300-340 mOsm/kg_{H2O}) with Percoll and centrifuged (200 x gravity for 5 minutes). The measured density (using the DSA 5000M density/sound velocity meter: Anton-Paar) of the solution that allowed the cells to be neutrally buoyant upon centrifugation was taken to be the density of the suspended cells. To obtain compressibility measurements on cell types, neutrally buoyant suspensions were prepared in different volume fractions followed by suspension speed of sound measurements with the density/sound velocity meter. The speed of sound values obtained with various volume fractions were then fitted to the linear Wood's equation [2]

$$\tilde{c} = \alpha(\tilde{\kappa}, \tilde{\rho})x + 1,$$

Where $\tilde{c} = c_s/c_f$ is the suspension/fluid speed of sound ratio, $\tilde{\kappa} = \kappa_p/\kappa_f$ is the particle/fluid compressibility ratio, $\tilde{\rho} = \rho_p/\rho_f$ is the particle/fluid density ratio and x is the volume fraction of the particles. The slope α in neutrally buoyant conditions

$$\alpha(\tilde{\kappa}, 1) = \frac{1}{2}(1 - \tilde{\kappa}),$$

was then used to determine the compressibility of the suspended particles.

Results

Method validation was performed by computing the density and the compressibility of different polymer microbeads. Sensitivity analysis for the proposed method has four regimes that depend on the slope of the linear fitting: for $\alpha < 1/4$ and $\alpha > 1$ the method is mainly sensitive to speed of sound measurements, for $\alpha > 1/4$ and $\alpha < 1/2$ it is mainly sensitive to density measurement, and for $\alpha > 1/2$ and $\alpha < 1$ it is mainly sensitive on the slope calculation. In Fig.1 we plot the sensitivity factors (s) on particle compressibility (κ_p) for the fluid ($s_{\kappa_p}^{\rho_f}$) and particle densities ($s_{\kappa_p}^{\rho_p}$), the slope ($s_{\kappa_p}^{\alpha}$), and the fluid speed of sound ($s_{\kappa_p}^{c_f}$) as a function of the average slope $\bar{\alpha}$. The slopes for the PS and PMMA beads are reported as examples for which compressibility measurements were sensitive to speed of sound error (PS) and density measurement errors (PMMA).

These speed of sound measurements on cell suspensions showed an increase in speed of sound as the cell volume fraction was increased (Figure 2). Furthermore, because the slopes of the fitted curves were small the speed of sound measurements were in a sensitivity regime where the error in the suspension speed of sound gave the most important contribution to the compressibility calculation.

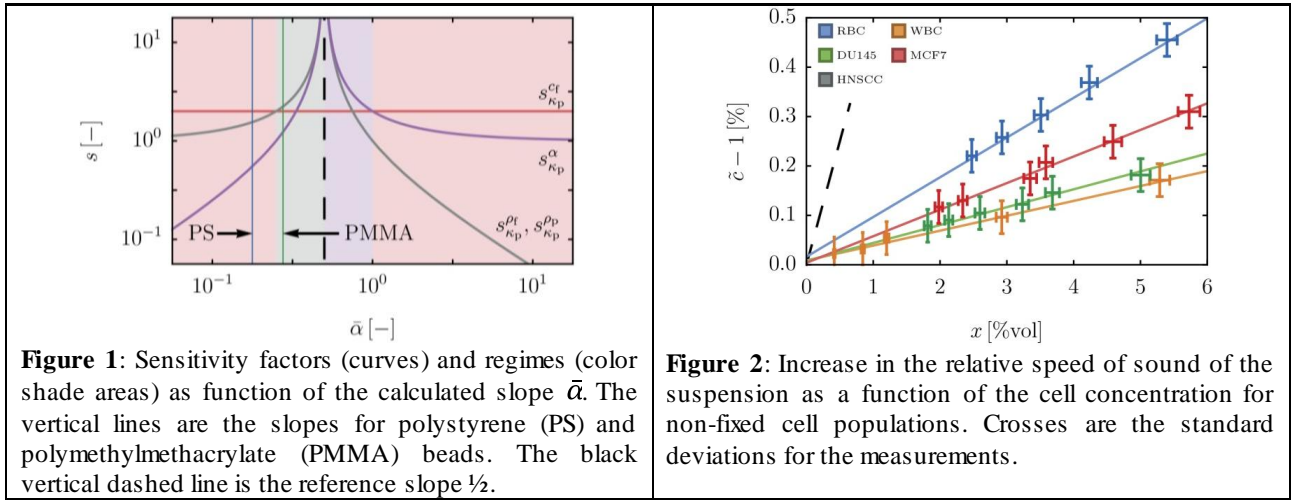


Table 1: Acoustic physical properties and standard deviations (numbers in parentheses) for the neutrally buoyant density solutions (subscript f) and the different non-fixed and fixed (fx) cell types (subscript p). Reference values are extracted from [3].

Sample	Slope		Physical Parameters				Reference Values	
	$\bar{\alpha}$ [-]	$\bar{\rho}_f$ [kg/m ³]	\bar{c}_f [m/s]	$\bar{\kappa}_f$ [TPa ⁻¹]	$\bar{\rho}_p$ [kg/m ³]	$\bar{\kappa}_p$ [TPa ⁻¹]	$\bar{\rho}_p$ [kg/m ³]	$\bar{\kappa}_p$ [TPa ⁻¹]
RBC	0.080(2)	1102.95(1)	1510.2(5)	397.5(3)	1100.(5)	334.(2)	1100	330
RBCfx	0.058(1)	1109.9(4)	1510.1(5)	398.3(3)	1091.(5)	356.(2)	N.A.	N.A.
WBC	0.0301(7)	1055.74(1)	1506.4(5)	417.4(3)	1054.(1)	393.(1)	N.A.	N.A.
WBCfx	0.0257(8)	1046.09(1)	1505.9(5)	421.5(3)	1045.(1)	400.(1)	1019	399
DU-145	0.036(1)	1064.7(2)	1507.2(5)	413.4(3)	1062.7(2)	384.(1)	N.A.	N.A.
DU-145fx	0.026(1)	1037.32(1)	1505.9(5)	425.1(3)	1035.8(2)	404.(1)	1018	425
MCF-7	0.0548(8)	1056.60(1)	1507.0(5)	416.8(3)	1054.6(3)	373.(1)	1068	380-422
MCF-7fx	0.0369(3)	1037.32(1)	1506.4(5)	424.8(3)	1035.1(3)	394.7(5)	N.A.	N.A.
LU-HNSCC-25	0.045(3)	1062.82(2)	1507.0(5)	414.3(3)	1061.4(3)	377.(3)	N.A.	N.A.
LU-HNSCC-25fx	0.0236(3)	1041.66(1)	1506.3(5)	423.1(3)	1039.9(3)	403.8(4)	N.A.	N.A.

The physical properties (density and compressibility) of the cell types that were derived using this method are listed in Table 1. The values show that fixing cell populations leads to reduce the density and increased the compressibility of all cell populations. Finally, from the determined density and compressibility values the acoustic scattering coefficients and the acoustic contrast factors could be computed (data not shown for the sake of brevity).

Conclusions

We propose a method that combining a neutrally buoyant selection process and speed of sound measurements can be used to measure the average ensemble density and compressibility of a particle population. The method has been presented together with the corresponding sensitivity analysis. Finally, density and compressibility of cells, commonly encountered in acoustophoretic separation, have been obtained by our method and compared with reference values.

References

- [1] Cushing et al, Ultrasound Characterization of Microbead and Cell Suspensions by Speed of Sound Measurements of Neutrally Buoyant Samples, Anal Chem (submitted, 2017).
- [2] Wood AB, *A textbook of Sound*, AIP Publishing (1956).
- [3] Hartono et al, Lab on Chip 11, 4072 (2011). Dukhin et al, Colloids and Surface B: Biointerfaces 52, 121-126 (2006). Yang et al, Scientific Report 6, 23946 (2016).

Acoustophoretic particle manipulation in microscale droplets for high throughput analysis of cell secretome

Michael Gerlt¹, Amanda Aho¹, Dominik Hümmer², Petra S. Dittrich², Jürg Dual¹

¹Department of Mechanical and Process Engineering, Institute for Mechanical Systems, ETH Zurich, Zurich

²Department of Biosystems Science and Engineering, Bioanalytics Group, ETH Zurich, Bern

E-mail: gerlt@imes.mavt.ethz.ch, URL: www.zfm.ethz.ch/e/exp-dyn

Introduction

For various applications in droplet microfluidics (e.g. single cell analysis, liquid solid separation, affinity measurements ...) it is necessary to be able to analyse cell secretome. Before label-free analysis of the cell secretome of single cells using mass spectrometry, the cell has to be separated in a small volume. A possible procedure to achieve this goal could be as follows: Enclosing cells inside microscale droplets (diameter < 300 μm) and introduction of the droplets into a microfluidic system (e.g. etched Si wafer). In this system the cells are dragged to the desired trajectory by acoustic radiation forces followed by splitting of the droplets at a bifurcation to separate cell from its secretome and finally ejecting the droplets to analyze their content, see Fig. 1.

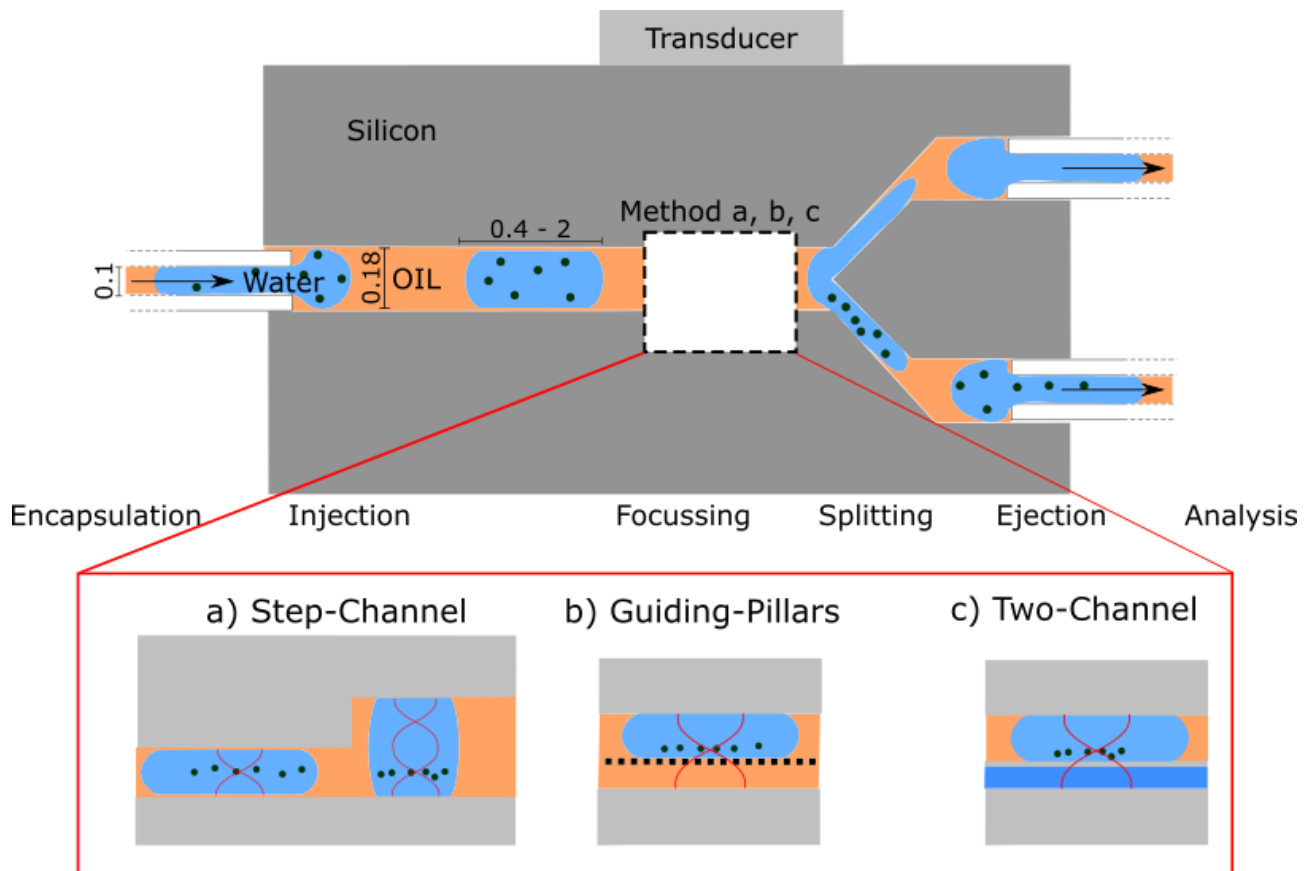


Figure 1: Sketch of the microfluidic setup used for cell manipulation inside microscale droplets. All units in [mm]. On the bottom the different methods to manipulate the position of the acoustic pressure node which are used in this work are shown. a) The Step-Channel design makes use of a pre-focus step. b) In the Guiding-Pillars Design small structures are utilized to guide the droplets while not influencing the acoustic pressure field. c) The Two-Channel is based on an previously published work [6] where it has been shown that a small (< 60 μm) thick channel wall does not influence the acoustic pressure field

The focusing of the cells inside the droplets needs to be contactless and should not affect the viability of the cells. Acoustophoresis utilizes ultrasonic standing waves to generate forces that can be used to position particles inside microscale droplets [1,2]. In order to separate cell and secretome at the bifurcation, the cells need to be dragged towards one of the channel walls. Manipulation of the position of the acoustic pressure node is challenging but has already been shown in literature [3,4,5,6].

Position adjustment of the acoustic pressure node

The standard $\lambda/2$ -mode (focusing of particles in the middle of the channel) and λ -mode (focusing in the top or bottom of the channel, depending on the initial particle position) of the ultrasonic standing wave don't lead to a reliable separation. In literature many approaches exist to influence the position of the acoustic pressure node. These are based on the manipulation of the acoustic signal (e.g. pulse width modulation [3]), device stack adjustments (planar resonant devices [4]) and variations in channel design (e.g. impedance matched channel walls [5]). This work focuses on variations in the channel design. Three different design approaches are examined as shown in Fig. 1. The Step-Channel design consists of two different channel widths. In the first part of the channel the particles are prefocused using the $\lambda/2$ -mode. In the second part with double width the λ -mode is excited using the same frequency. If the step does not influence the acoustic pressure field too much, the particles should stay in the lower pressure node of the wide channel due to the prefocusing. The Guiding-Pillars design uses small (30 μm) structures to guide the droplets and simultaneously avoid an influence on the acoustic pressure field. The Two-Channel design is based on the phenomena, that a thin silicon wall (< 60 μm) between two fluid filled channels is 'acoustically transparent'. The position of the acoustic pressure node can thus be controlled by the bypass channel thickness.

Device fabrication

Standard silicon wafers (thickness: 500 μm) are dry etched using deep reactive-ion etching (DRIE). After the etching step, glass (thickness: 700 μm) is anodically bonded to the silicon to be able to visually inspect acoustic forces on the particles under a microscope. Piezos (PZT, dimensions: 10 mm x 2 mm x 1 mm) are glued on the backside of the Silicon chip using conductive polymer H20E. The capillaries are inserted to the sides of the chips and then glued to achieve a stable position and impede leaking of the devices. This system is used to minimize forces on droplets during in- and ejection.

Experiments

Different particles (polystyrene and yeast cells) are focused inside water droplets using different media as the continuous phase with different surfactant concentrations. We plan to show successful injection and ejection of micron size droplets. Multiple designs are utilized to manipulate the position of the acoustic pressure node of the $\lambda/2$ -mode which should lead to a stable trajectory of the cells near one of the channel walls. The acoustic force on the particles is calculated for different modes. Successful separation of cell and secretome is examined.

Conclusion

In this work one possible methodology to achieve high throughput analysis of single cell secretome using acoustic radiation force is examined.

References

- [1] S. Oberti, "Micromanipulation of Small Particles within Micromachined Fluidic Systems," PhD Thesis, ETH Zürich 2009.
- [2] A. Fornell, J. Nilsson, L. Jonsson, P. K. Periyannan Rajeswari, H. N. Joensson, and M. Tenje, *Anal. Chem.*, vol. 87, no. 20, pp. 10521–10526, 2015.
- [3] P. Glynne-Jones, R. J. Boltryk, N. R. Harris, A. W. J. Cranny, and M. Hill, *Ultrasonics*, vol. 50, no. 1, pp. 68–75, 2010.
- [4] P. Glynne-Jones, R. J. Boltryk, and M. Hill, *Lab Chip*, vol. 12, no. 17, pp. 1417–1426, 2012.
- [5] I. Leibacher, S. Schatzer, and J. Dual, *Lab Chip*, vol. 14, no. 3, pp. 463–70, 2014.
- [6] E. J. Fong *et al.*, *Analyst*, vol. 139, no. 5, pp. 1192–200, 2014.



Acoustic streaming in sharp-edge-based devices: Spatial effects

Po-Hsun Huang¹, Marten Darmawan², Nitesh Nama², and Tony Jun Huang^{1*}

¹Department of Mechanical Engineering and Material Sciences, Duke University, NC, USA

*E-mail: tony.huang@duke.edu, URL: <http://acoustofluidics.pratt.duke.edu/>

²Department of Engineering Science and mechanics, The Pennsylvania State University, PA, USA

Introduction

Acoustic streaming effect induced by oscillating sharp-edges has been exploited for various microfluidic applications, such as mixing, pumping, and micro-object manipulation [1-3]; the dependence of acoustic streaming pattern on the location of sharp-edge structure, however, has yet to be answered. Herein we explore the effect of the location of sharp-edge on the generation of acoustic streaming pattern. Through this investigation, we can provide a fundamental understanding on how to implement the sharp-edge-based devices.

Experimental setup

To investigate the distribution of acoustic streaming strength inside the channel, we prepare a simple device consisting of a piezoelectric transducer, a single-layer PDMS straight channel, and a glass coverslip [Fig. 1]. The transducer is bonded onto the coverslip together with the PDMS channel. The channel is fabricated with sharp-edges constructed at five specific locations. Once vibrated by the transducer at different frequencies, the coverslip's vibration mode alters and accordingly, alters the distribution and strength of the acoustic streaming.

Results and discussion

We first perform numerical simulation to verify if the coverslip vibrates at and near the resonance frequency of the transducer, its vibration modes also changes and therefore, changes the displacement distribution. The simulation indicates that under vibration at/near the resonance frequency (4~6 kHz), symmetric distribution of displacement of the coverslip is observed [Fig. 2a-b]. Following simulation, we use 1.36- μm polystyrene beads to visualize the streaming patterns inside the channel. Experimental images and PIV analysis show that upon vibration, the streaming velocity significantly decreases as the sharp-edge is located closer to the centerline of the coverslip and transducer [Fig. 2c], which is in good agreement with the simulation. When activated under different frequencies and voltages, the sharp-edges at different locations also induce varying streaming velocity; yet it is worthwhile noting that regardless of the frequency, the distribution of acoustic streaming remains symmetric [Fig. 2d-e].

At five specific location, we further fabricate three sharp-edges (which are 600 μm apart), making the channel containing 15 sharp-edges. The plots presented in Fig. 3a confirm once again that the acoustic streaming strength is inversely proportional to the distance between the sharp-edge structure and the centerline. Besides the distribution along x-direction, we also fabricate devices with three parallel channels to investigate the acoustic streaming patterns along y-direction. Interestingly, the acoustic streaming is stronger in the channel 1 and 3, which are the closest and farthest channels to the transducer, respectively, than in the channel 2 [Fig. 3b]. Moreover, regardless of the channel position and driving frequency, the acoustic streaming strength along x-direction is still symmetric. Collectively, the acoustic streaming pattern of each sharp-edge structure inside the channel is significantly altered by the location of sharp-edge structure

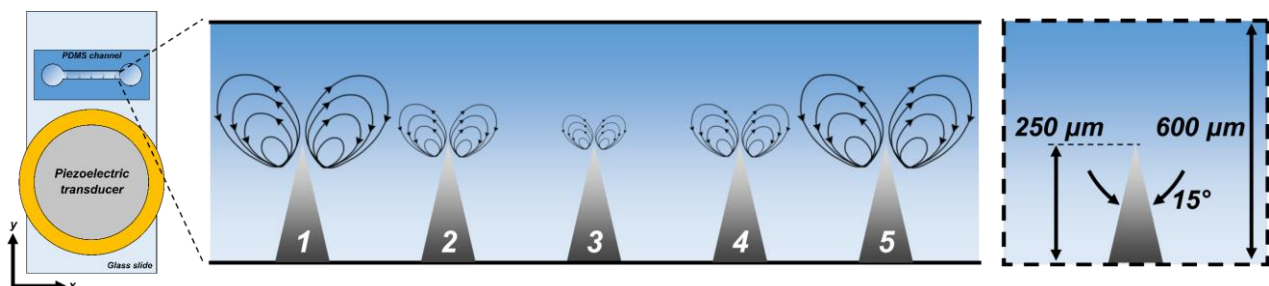


Figure 1: Schematics showing the design of our device and sharp-edge structure to investigate the acoustic streaming patterns developed at different location within the microfluidic channel. Triangular sharp-edge structures are constructed at five specific locations (denoted as location 1 ~ 5) inside the microfluidic channel and each of them is 2.5 cm apart from each other; Position-3 is aligned along the centerline of the piezoelectric transducer and glass slide.

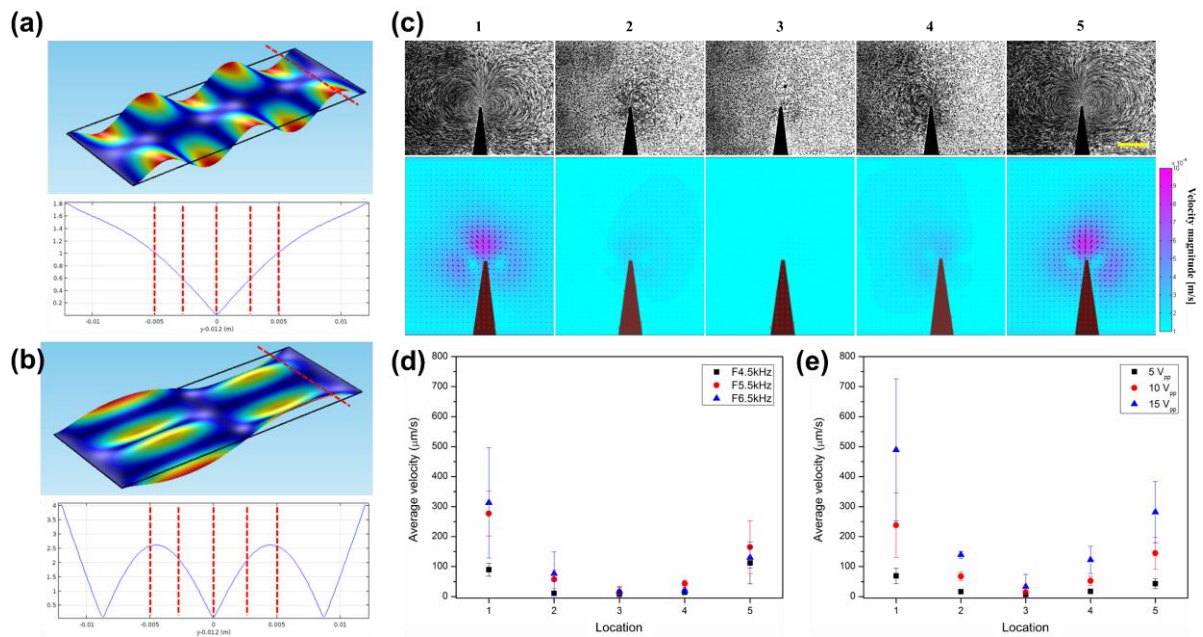


Figure 2: (a) & (b) Numerical simulation indicating the symmetric distribution of displacement under two different vibration modes. (c) Stacked images and PIV analysis showing the symmetric distribution of streaming velocity when the piezoelectric transducer is activated at 5.5 kHz. Plots showing the average streaming velocity under (d) different driving frequencies and (e) different driving voltages of the transducer. Data represents $n = 3$ devices \pm standard deviation.

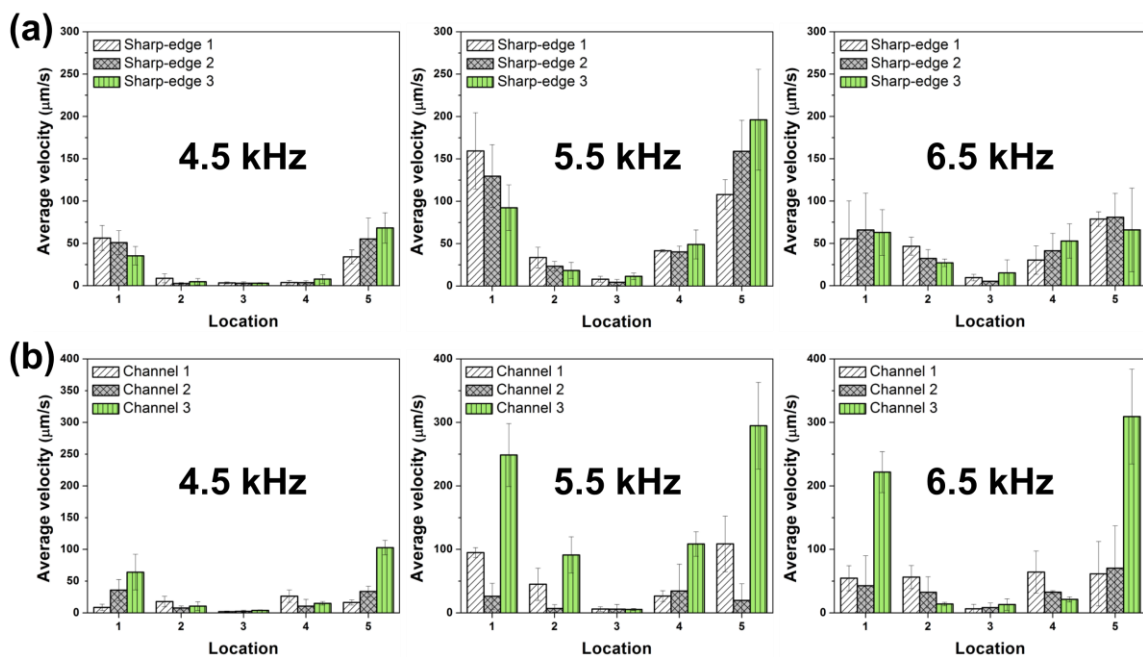


Figure 3: Plots showing the average streaming velocity of each sharp-edge structure under varying frequencies: (a) when 15 sharp-edge structures are constructed in a single channel, (b) three parallel channels along y-direction are constructed, and each channel contains 5 sharp-edge structures. Data represents $n = 3$ devices \pm standard deviation.

Conclusion

In summary, we investigate the dependence of acoustic streaming pattern on the location of sharp-edges. We discover that the acoustic streaming pattern alters along both x- and y-direction, and with this fundamental understanding, we can provide the community a design rule on how to efficiently utilize the acoustic streaming generated by acoustically oscillated sharp-edges for various microfluidic applications.

References

- [1] P.-H. Huang *et al.*, *Lab on a Chip*, **13**, 3847-3852 (2013).
- [2] P.-H. Huang *et al.*, *Lab on a Chip*, **14**, 4319-4323 (2014).
- [3] N. Nama *et al.*, *Lab on a Chip*, **14**, 2824-2836 (2014).



Acoustofluidic fluid propulsion enabled by microscale vibration

Po-Hsun Huang¹, Nitesh Nama², and Tony Jun Huang^{1*}

¹Department of Mechanical Engineering and Material Sciences, Duke University, NC, USA
E-mail: tony.huang@duke.edu, URL: <http://acoustofluidics.pratt.duke.edu/>

²Department of Engineering Science and Mechanics, Pennsylvania State University, PA, USA

Introduction

Efficient and reliable fluid propulsion in microscale is essential but challenging. Though syringe pumps and various micropumps have long been employed for fluid propulsion, they still remain bulky and complex in configuration [1,2]. Herein we report a newly discovered fluid propulsion phenomenon induced simply by the microscale vibration of acoustic transducer. Our acoustic-based fluid propulsion mechanism is simple and straightforward yet reliable and controllable and is moving-parts-free and micro/nanostructures-free.

Concept and experimental setup

Our device is simply comprised of a single-layer PDMS channel (unless otherwise specified, the channel is 600 μm wide and 100 μm high) without any micro/nanostructures inside, a piezoelectric transducer and a glass coverslip; the transducer is bonded adjacent to the PDMS channel along the channel-length direction onto the coverslip [Fig. 1a]. Upon actuation, the transducer vibrates out-of-plane and accordingly, oscillates the coverslip, which, in turn, generates a travelling wave propagating along the channel [Fig. 1b]. The generated travelling wave thus propels fluids through the microchannel [Fig. 1b]. Besides, the travelling wave is reflected from the edges of the coverslip, which forms a standing wave that can be observed through Chladni patterns on the coverslip when the transducer vibrates [Fig. 1c].

Results and discussion

To validate the fluid propulsion performance, we track the movement of 6 μm polystyrene beads. We investigate how various design parameters affect the fluid-propulsion performance. With a channel depth of 50 μm , our acoustic-based device propels beads at a velocity as high as ~ 50 mm/sec, corresponding to a pumping flow rate of 90 $\mu\text{L}/\text{min}$ and a pumping pressure of ~ 2500 Pa; however, as the channel depth increases, the average velocity drastically decreases [Fig. 2a]. If the channel width downstream is remained constant while increasing the one upstream, the average velocity increases because more fluid is propelled into the channel [Fig. 2b]. Using epoxy to bond the transducer outperforms the other bonding methods, since the epoxy provides firm, high-strength bonding and acts as an efficient acoustic-coupling layer [Fig. 2c]. Additionally, the thickness of the coverslip and PDMS also significantly affect the performance. As the thickness of the coverslip and PDMS decreases, the average velocity increases [Fig. 2d-e], because thinner coverslips and PDMS tend to vibrate more vio-

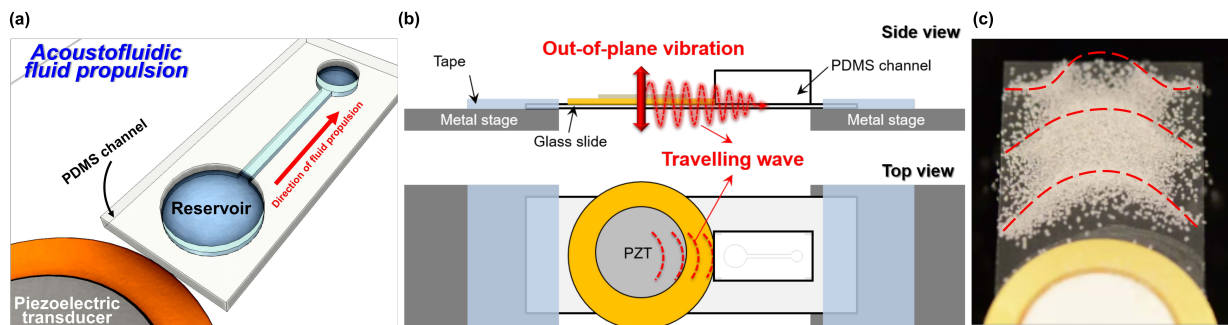


Figure 1: Schematics showing the concept and experimental setup for acoustic-based fluid propulsion. (a) The acoustic-based fluid propulsion device is simply made by bonding a piezoelectric transducer adjacent to a PDMS channel (along the direction of channel length) onto a glass coverslip. (b) Once activated, the transducer vibrates out-of-plane and thus generates a travelling wave, which, in turn, propels fluid through the channel. (c) Chladni pattern on a coverslip indicating the formation of travelling wave due to the vibration of the coverslip.

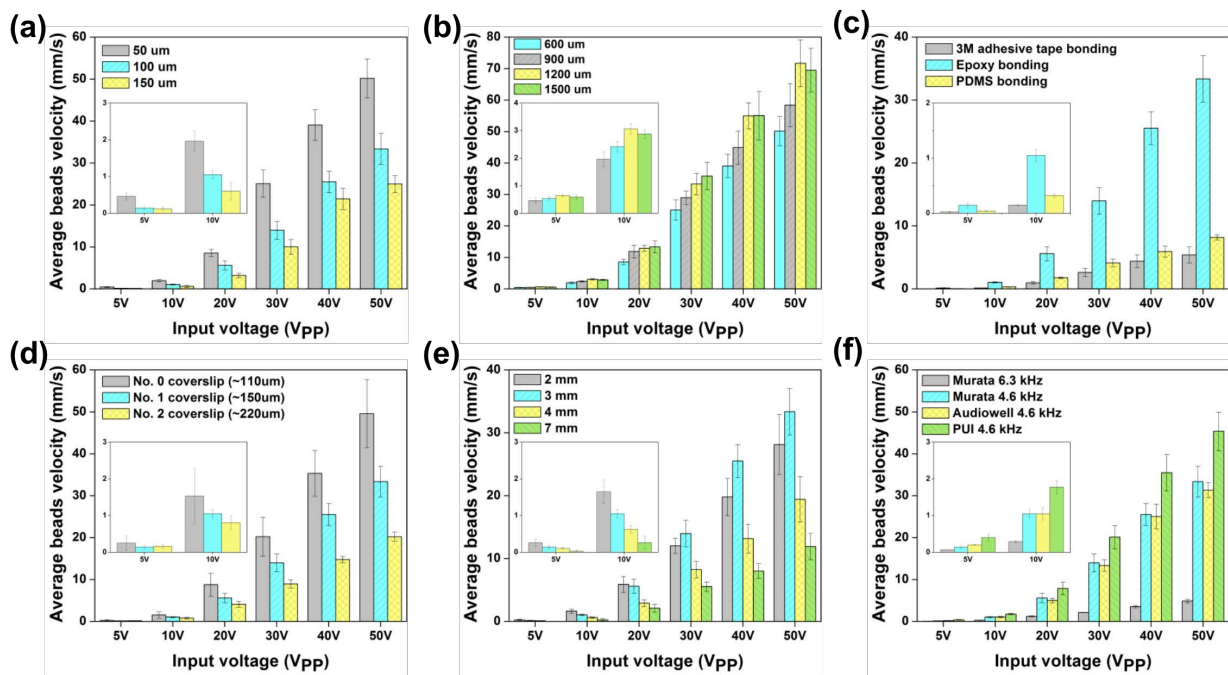


Figure 2: Graphs showing the average velocity of beads propelled through the channel at the driving frequency of 5.5 kHz and under different driving voltages of transducer, when (a) channel depth varies, (b) channel width varies, (c) bonding method changes, (d) the thickness of coverslip changes, (d) the thickness of PDMS changes, and (d) using different transducers. Data represent average of $n = 3 \sim 6$ devices \pm standard deviation.

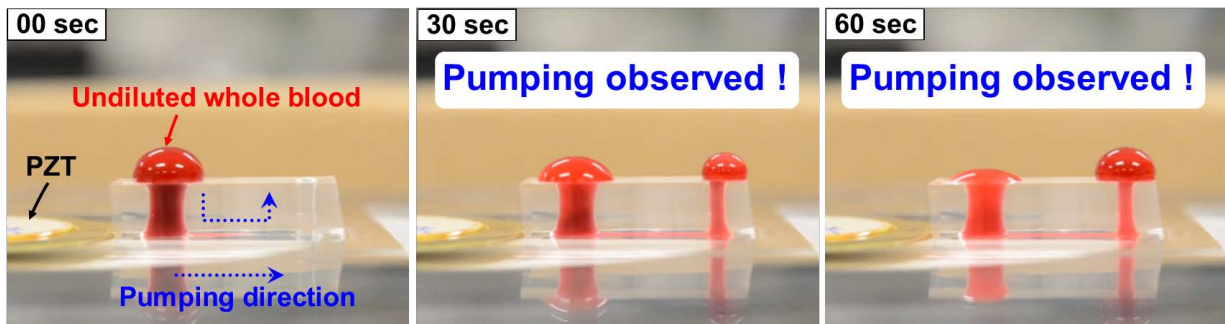


Figure 3: Photographs showing the delivery of undiluted human whole blood from the left reservoir to the right reservoir using our acoustic-based fluid propulsion technique. The results prove our technique a promising microfluidic pump for the pumping of versatile fluids, from normal fluids, such as DI water, ethanol and isopropanol, to biological fluids, such as PBS, cell culture medium, to undiluted whole blood.

lently. To demonstrate the simplicity, compatibility and ease of operation, our fluid-propulsion devices are bonded with several commercially available piezoelectric transducers. Regardless of the sizes and resonance frequencies of the transducers tested, fluid propulsion occurs in all the cases [Fig. 2f]. The results presented in Fig. 2 have proved our device powerful, reliable, and controllable for fluid propulsion. Using our fluid propulsion device, we can transport various fluids, such as undiluted whole blood, from one reservoir to another through the microchannel [Fig. 3], demonstrating our device capable of handling biological fluids.

Conclusion

In summary, we demonstrate a new class of acoustic-based fluid propulsion technique. Our technique can propel fluids at a wide range of velocity by adjusting various design parameters. Unlike existing fluid propulsion techniques, our technique necessitates no mechanical/electrical moving parts and particularly, no micro/nanostructures is needed inside microfluidic channels, making our technique not only simple and compact, but also reliable and controllable for manipulating various fluids in versatile microfluidic applications.

References

- [1] S.N. Khaderi et al., Lab on a Chip **11**, 2002-2010 (2011).
- [2] P.-H. Huang et al., Lab on a Chip **14**, 4319-4323 (2014).



The impact of fluid flow on acoustic streaming patterns

Carl Johannesson¹, Per Augustsson¹, Thomas Laurell¹ and Mikael Evander^{1,2}

¹Department of Biomedical Engineering, Lund University, Lund, Sweden
E-mail: carl.johannesson@bme.lth.se, URL: www.bme.lth.se

²Acousort AB, Lund, Sweden

Introduction

We have examined acoustic streaming in an acoustofluidic trapping system based on a glass capillary and a piezo transducer. It has previously been shown that in a similar system four stream vortices are centered over the transducer, perpendicular to the wave propagation. [1,2] In this experimental study we visualize acoustic streaming in a trapping capillary with and without flow along the channel to better understand how this combined flow field may affect the capture efficiency in seed trapping. Our main finding is that the combined flow pattern is highly dependent on the flow velocity profile in the channel and that this will have strong effect on the capture rate in seed trapping of e.g. bacteria and exosomes.

Method

The system consisted of a glass capillary with rectangular cross-section (ID $2 \times 0.2 \text{ mm}^2$) that was mounted on top of an ultrasonic transducer (Pz26, Meggitt, Denmark) with a thin layer of glycerol as coupling layer and placed in a holder, Fig 1.

The flow profile in the capillary was calculated and plotted, Fig 2 (blue arrows), in MATLAB using the Poiseuille equation for a channel with rectangular cross-section (width 2 mm, height 200 μm).

To image the streaming pattern, 500 nm fluorescent polystyrene particles (Fluoro-Max G500, ThermoFisher Scientific, USA) were used at 10^{-4} \%w/v which allowed the particles to follow the stream vortices without being trapped by the acoustic radiation force. Ultrasound was applied at the $\lambda/2$ -resonance frequency of the system, which was monitored with a LabVIEW software [3], at $\sim 4.1 \text{ MHz}$ and 10 V. Images were taken with a CCD camera at half of the height of the channel as the particles followed the streaming vortices. Vortice imaging was performed at flow rates of 0, 10 and 20 $\mu\text{l/min}$.

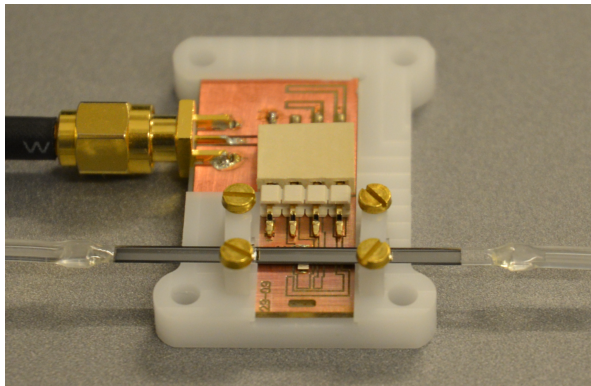


Figure 1: Picture of the setup with a glass capillary, with silicone tubing glued to the ends, mounted over a transducer (the small white piece under the capillary) in a plastic holder. The ultrasonic transducer ($\sim 1 \times 3 \text{ mm}^2$) was soldered to a PCB and connected to an arbitrary function generator.

Results and discussion

The flow profile calculations show that for the central part of the width of the channel the flow profile is flat and decreases parabolically at the walls. This indicates that the vortices should be equally affected in the center of the channel and less affected closest to the walls.

The image of the streaming without any flow, Fig. 2a, shows the four fairly symmetrical stream vortices centered over the transducer rotating towards the center along the capillary length. At a flow of 10 $\mu\text{l/min}$ from the left in the image, Fig. 2b, the stream vortices are distorted as the flow profile is superimposed on the streaming pattern. The effect is most visible where the flow works against the direction of the stream vortices and reduces the flow velocity or even breaks the vortices partially and flushes away some tracer particles. Finally, when the flow is increased to 20 $\mu\text{l/min}$, Fig 2c, the two vortices to the right are counteracted by the flow in the capillary and the particles can not be retrieved to the center and are lost. However, the force components in the vortices acting perpendicular to the flow at the center still manage to move particles towards the capillary walls but not back to the center again. The particle recirculation effect seen at lower

flow rates is eliminated at 20 $\mu\text{l}/\text{min}$ and this gives an approximation of the magnitude of the velocity in the stream vortices. 20 $\mu\text{l}/\text{min}$ in average flow rate corresponds to a maximum flow velocity of ~ 1.3 mm/s in this geometry according to the velocity calculations. This is in good agreement with estimation of the particle velocity in the streaming vortice images based on the particle traces and the exposure time.

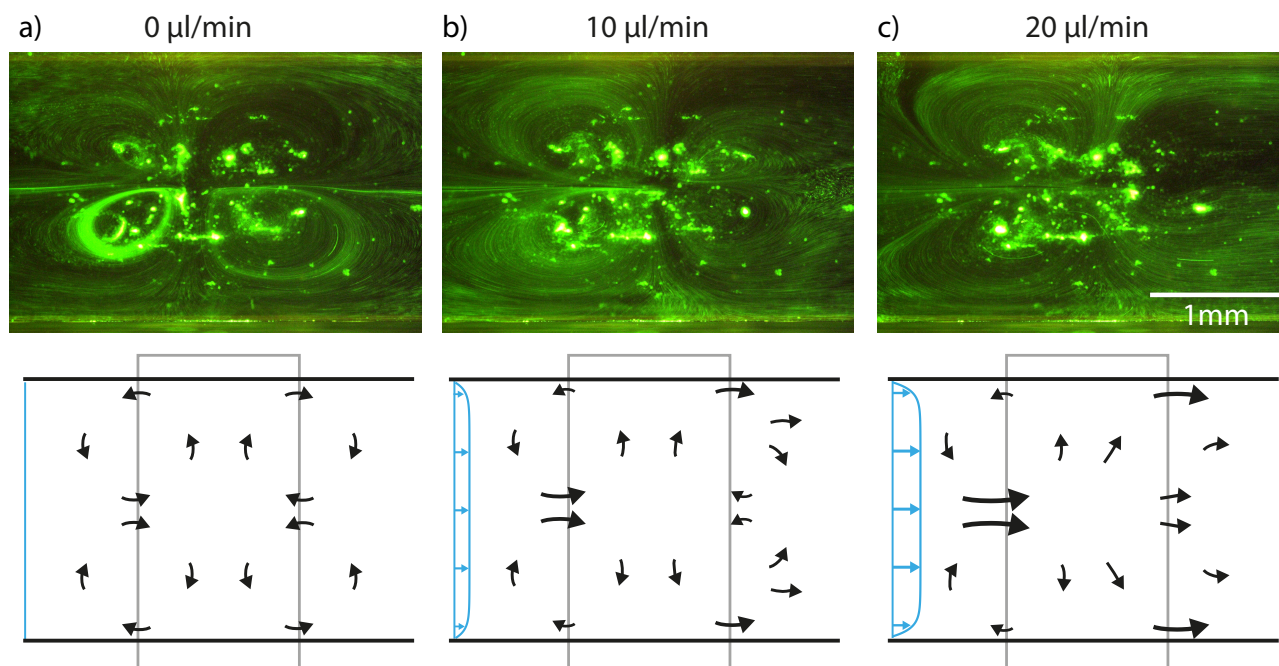


Figure 2: Images and corresponding simplified schematics of the flow and streaming pattern in the capillary above the transducer for different flow rates. In the schematics, the channel walls are marked with black lines, the transducer outline is marked with a gray rectangle, the flow profile is shown with blue arrows to the left in each image and the resulting fluid motion is marked with black arrows. The flow rates are 0, 10 and 20 $\mu\text{l}/\text{min}$ in a), b) and c), respectively. The bright clusters in the background are particles sticking to the surface of the capillary.

In seed-trapping, i.e. trapping of small particles by first trapping larger particles, the secondary radiation force between the seed-particles and the smaller particles is highly dependent on the inter-particle distance. The streaming pattern is assumed to have large impact on the trapping performance since it determines the degree of exposure of the small particles to the seed-cluster. Focusing and recirculation are likely two very important factors. Focusing of the incoming particles helps to translate the small particles in proximity of the seed-cluster and the recirculation gives any unbound particles repeated chances to come into the capture range of the secondary radiation force. The recirculation is most sensitive to the flow rate and it can therefore be important to set the flow rate below the streaming velocity in order to get high nanoparticle recoveries. The two downstream vortices are also helping to retain larger particles in the trapping zone against the flow in the channel and that component in the force field is of course there even at higher flow rates. At higher flow rates than tested in this study it's also likely that the focusing effect of the two upstream vortices will be counteracted entering a new threshold flow rate regime when the trapping performance is drastically changed.

Conclusion

In microfluidic systems, the general flow pattern can be superimposed with different streaming patterns. In this case, we have shown that the resulting pattern of the flow and the acoustic streaming in a trapping system depends on the flow rate, and that the effect of the streaming also changes. The streaming can help to recirculate particles to the trapping zone under certain flow rates/velocities, in this case approximately 20 $\mu\text{l}/\text{min}$ or 1.3 mm/s, respectively. This gives a rough approximation that the velocity in the streaming vortices also is around 1.3 mm/s at the given frequency and voltage. Even at higher flow rates the streaming helps to focus and retain particles to the trapping zone in the center of the channel. The effect of the changed flow pattern on different particle sizes and seed-trapping remains to be investigated as well as a more extensive velocity field characterization.

References

- [1] B. Hammarström, T. Laurell and J. Nilsson. *Lab Chip* **12**, 4296-4304 (2012).
- [2] J. Lei, P. Glynn-Jones and M. Hill. *Lab Chip* **13**, 2133-2143 (2013)
- [3] B. Hammarström *et al.* *Lab Chip* **14**, 1005-1013 (2014).



On-demand droplet capture and release by using acoustic radiation forces

Jin Ho Jung, Ghulam Destgeer, Jinsoo Park, Husnain Ahmed, Kwangseok Park and Hyung Jin Sung*

Department of Mechanical Engineering, KAIST, Daejeon 34141, Korea
E-mail: hjsung@kaist.ac.kr, URL: <http://flow.kaist.ac.kr>

Introduction

Recently, droplet microfluidics has attracted much attention for integrating conventional experimental platforms into a small size chip. The droplets are useful as chemical reactors because of their merits such as the reagent evaporation, the accurate experiment conditions, and the prevention of cross contamination.[1] In a microfluidic platform, the droplets could be generated uniformly, separated, coalesced, monitored, split, and captured. Among the operations, the droplet capture and release is highly required for the short-term monitoring of a single cell in the droplets. The cell-laden droplets could be captured at specific locations by using geometrical traps inside the microchannel.[2] However, the passive droplet capture methods lacked the control required to capture specific droplets. Anchoring the droplet at specific microwells in the microchannel by applying a DC electric field was demonstrated.[3] This active droplet capture technique could provide the on-demand droplet manipulation, but it required high voltage over 1 kV. Moreover, the droplets in the multiple microwells was not demonstrated. In this study, we demonstrated a droplet manipulation platform based on surface acoustic waves (SAWs) for on-demand droplet capture and release. A slanted finger interdigitated transducer (SF-IDT) was adapted to control the SAW beam width and position. The effective aperture of the SAW beam was decreased to 100 μm . The position of the SAW beam center can be controlled by tuning the corresponding frequency. The droplets can be captured or released from the microwells by shifting the position of the SAW beam.

Experimental

A schematic diagram of the microfluidic device for the droplet capture and release is shown in Figure 1. The device is composed of polydimethyl siloxane (PDMS) microchannel and a piezoelectric substrate patterned with SF-IDTs. The PDMS channel was fabricated with a soft lithography technique. The height and width of the microchannel are 40 μm and 100 μm , respectively. The microwell area is 100 μm \times 100 μm while that of the microwell neck is 50 μm \times 70 μm . The microwell has a bottleneck shape, therefore captured droplets can be locked in the microwell unless there is no external disturbance. The water-in-oil droplets were produced from T-junction geometry. The experimental images were recorded using a high speed camera (pco. 1200hs PCO camera) attached to a microscope (Olympus IX71). AC electrical signals were produced from an RF signal generator (N5171B, Keysight Technologies) after amplification (UP-3015, Unicorn Tech.) and the SAW voltage was measured with an oscilloscope (DSO-X 2022A, Keysight Technologies). The pitch of the fingers (λ) ranges from 28 to 36 μm , which corresponds to a range of SAW frequencies ($f_{\text{SAW}} = c_s/\lambda$, c_s is the speed of sound in LiNbO_3) from 109 to 141 MHz. The effective aperture of the SAW beam can be estimated

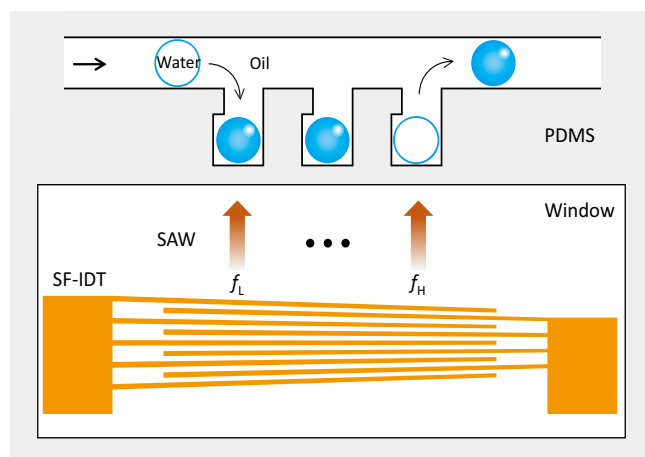


Figure 1: Schematic diagram of the microfluidic droplet capture and release platform composed of a polydimethyl siloxane (PDMS) microchannel and a piezoelectric substrate patterned with slanted finger interdigitated transducers (SF-IDT). The position of the SAW beam can be controlled by tuning the corresponding frequency. The droplets can be captured or released by acoustic radiation force (ARF) at specific microwells.

as,

$$A_i \cong \frac{f_i}{N(f_H - f_L)} A_0 \quad (1)$$

where f_i is the working frequency, N is the number of finger pairs, f_H and f_L are the highest and lowest frequencies generated from the SF-IDT, and A_0 is the total aperture.

Results and discussion

Experimental demonstration of the droplet capture and release by the SF-IDTs is shown in figure 2. The acoustic radiation force pushed the droplet away from the SAW beam center when the acoustic impedance of the droplet was higher than that of the continuous phase fluid. When the SAW beam was carefully aligned at the end of the microwell (figure 2 (a)), the droplet stopped at the entrance of the microwell. After $t = 60$ ms, the droplet entered the microwell within the next 300 ms. When the SAW beam center was aligned at the middle of the microwell (figure 2 (b)), the droplet was pushed from the microwell into the main fluid path.

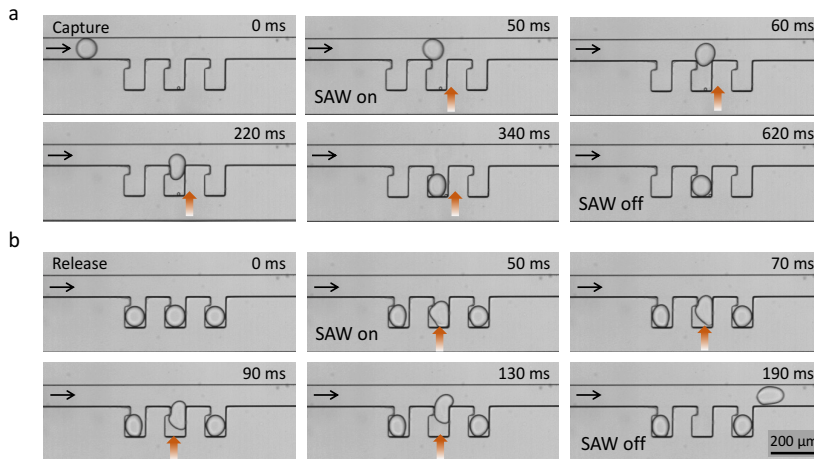


Figure 2: Experimental images of the droplet (a) capture and (b) release demonstration in the microfluidic channel. The droplet diameter was $100 \mu\text{m}$, which was same size as the channel width. (a) When the SAW beam was aligned at the end of the microwell, the droplet was stopped by the SAW ($t = 50$ ms). After 60 ms and onwards, the droplet entered the microwell within 300 ms. (b) When the SAW beam was align at the middle of the microwell, the droplet was pushed by the ARF from the microwell into the main fluid path.

In order to observe the droplet capture sequence, the droplet displacement and velocity were measured at 1 ms intervals. The flow rate of the continuous and dispersed phase fluids were $197 \mu\text{l/hr}$ and $3 \mu\text{l/hr}$, respectively. At high input voltage, the droplets were completely overpowered by the ARF and captured in the microwells as their velocities decrease to zero.

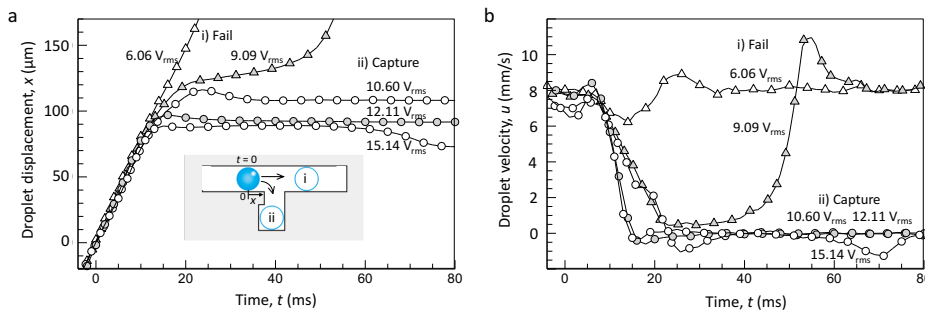


Figure 3: The droplet (a) displacement and (b) velocity in the x-direction. The SAW frequency was 117 MHz to locate the SAW beam at the end of the entrance of the microwell. The flow rates of the continuous and dispersed phase fluids were $197 \mu\text{l/hr}$ and $3 \mu\text{l/hr}$, respectively.

Conclusion

In summary, we have demonstrated the droplet capture and release platform based on the SAWs. The SAW beam position can be controlled by tuning the corresponding frequency. With careful alignment of the SAW position, the droplet can be capture or released at the specific microwells.

Acknowledgment

This work was supported by the Creative Research Initiatives (no. 2017-013369) program of the National Research Foundation of Korea (MSIP) and the KUSTAR-KAIST Institute.

References

- [1] H. Song, D. Chen, and R. Ismagilov. *Angew. Chem. Int. Ed. Engl.* **45**, 7336-7356 (2006).
- [2] W. Shi, J. Qin, N. ye, B. Lin. *Lab Chip* **8**, 1432-1435 (2008).
- [3] W. Wang, C. Yang, Y. Liu, C. Li. *Lab Chip* **5**, 559-562 (2010).



Methods to linearize acoustic radiation force for acoustophoresis applications

M.H. Kandemir^{1,2}, R.M. Wagterveld¹, D. Yntema¹, K.J.Keesman^{1,2}

¹Wetsus, European Center of Excellence in Sustainable Water Technology, Oostergoweg 9, 8911 MA, Leeuwarden, The Netherlands. E-mail: hakan.kandemir@wetsus.eu, URL: <http://wetsus.eu>

²Wageningen University & Research, Bornse Weiland 9, 6708WG Wageningen, The Netherlands

Introduction

In this study we propose methods to linearize the acoustic radiation force. The expression for the acoustic radiation force on a spherical particle is derived by Gor'kov [1]. It contains a sinusoidal term, therefore the expression and the equation of motion (EOM) are non-linear [2]. With linearization, we express the particle as a single degree of freedom (SDOF) vibrating system. Here we consider an acoustophoresis application in a half-wavelength resonator and present linearization methods based on the initial and target position of the particle.

The non-linear equation of motion

The acoustic radiation expression for a spherical particle in a standing acoustic wave field is

$$F_{ac} = 4\pi kr^3 \left(\frac{P_0^2}{\rho_0 c_0^2} \right) \Phi(\rho, c) \sin(2kz) \quad (1)$$

where r is the particle radius, $\Phi(\rho, c)$ is the acoustic contrast factor, ρ_0 is the density of the medium and c_0 is the speed of sound in the medium. Assuming Stokes drag and stationary fluid in the direction of the wave, the EOM is

$$\left(\frac{4}{3} \pi r^3 \rho \right) \ddot{z} + (6\mu\pi r) \dot{z} + 4\pi kr^3 \left(\frac{P_0^2}{\rho_0 c_0^2} \right) \Phi(\rho, c) \sin(2kz) = 0 \quad (2)$$

where ρ is the particle density, c is the speed of sound in the particle and μ is the viscosity of host medium. This EOM is a second-order non-linear ordinary differential equation. By reducing the order of equation to one, an analytical solution is possible [3].

The SDOF vibrating system

A SDOF vibrating system is composed of a mass connected to ground by a spring and a damper element. The EOM for free vibrations of such a system is

$$m\ddot{z} + b\dot{z} + Kz = 0 \quad (3)$$

where m is the mass, b is the damping coefficient, K is the spring coefficient. The SDOF system parameters can be expressed in terms of mass, damping and spring coefficients. The undamped natural frequency of the system is $\omega_n = \sqrt{K/m}$ and the damping ratio is $\zeta = b/(2\sqrt{K/m})$. The value of the damping ratio determines if the system is underdamped ($\zeta < 1$), overdamped ($\zeta > 1$) or critically damped ($\zeta = 1$). The damped natural frequency of the system is $\omega_d = \omega_n \sqrt{\zeta^2 - 1}$. Analytical solutions are possible for such systems and they can differ depending on the value of ζ .

Equivalent SDOF parameters for the particle in a standing acoustical wave field are $m = 4/3\pi r^3 \rho$ for the mass and $b = 6\mu\pi r$ for the damping coefficient. The spring parameter K cannot be directly extracted. It is, however, possible to derive it if the acoustic radiation force is linearized.

The SDOF vibrating system

The direct extraction of the spring coefficient results in

$$K = 4\pi kr^3 \left(\frac{P_0^2}{\rho_0 c_0^2} \right) \Phi(\rho, c) \frac{\sin(2kz)}{z} \quad (4)$$

The nonlinearity is arising from $\sin(2kz)/z$ term, and if it is linearized, a linear SDOF representation is possible. The linearization can be carried out to represent any range, i.e. the full period of sine or given two positions. Here we consider a particle in a half wavelength resonator, starting from a known position and expected to go to a final position. The motion of the particle after it reaches and/or passes the final position is ignored. Consider the particle starts at a position such that $2kz_0 = \theta_1$ and z_f is the position that the particle

is expected to arrive after an unknown τ amount of time with $2kz_f = \theta_2$. In what follows, it is assumed that the target position is closer to the node $z = 0$, thus $\theta_2 < \theta_1$. If an average value is found such that

$$\sin(2kz) \cong \left(\frac{\sin(2kz)}{2kz} \right)_{av} 2kz \quad (5)$$

the nonlinear spring force can be expressed linearly between θ_1 and θ_2 , which would be the first linearization method. Then, the corresponding spring coefficient would be $K = (K_l K_{ni} 2kz)/z$, where

$$K_l = 4\pi k r^3 \left(\frac{P_0^2}{\rho_0 c_0^2} \right) \Phi(\rho, c) \quad (6)$$

is the linear part and K_{ni} is the linearized non-linear part. For the first linearization method, the average value of $\sin(x)/x$ between two given positions is considered as

$$K_{n1} = \frac{1}{2kz_0 - 2kz_f} \int_{2kz_f}^{2kz_0} \frac{1}{x} \sin(x) dx \quad (7)$$

A similar problem is encountered while solving the period of pendulum [4]. Second method is $K_{n2} = K_{n1}^{3/8}$. Third method considers the work done between two positions and calculates the equivalent spring coefficient as

$$\int_{2kz_f}^{2kz_0} \sin(2kx) dx = \int_{2kz_f}^{2kz_0} K_{n3} x dx \quad (8)$$

Fourth and final method is calculating the RMS value of $\sin(x)/x$ between two positions, which is

$$K_{n4} = \sqrt{\frac{1}{2kz_0 - 2kz_f} \int_{2kz_f}^{2kz_0} \left(\frac{1}{x} \sin(x) \right)^2 dx} \quad (9)$$

To illustrate the linear model, we consider a case where $r = 5 \mu\text{m}$, $\rho = 1050 \text{ kg/m}^3$, $c = 1700 \text{ m/s}$, the water temperature is 25°C , the amplitude of acoustical waves is $P = 1 \text{ MPa}$, the excitation frequency is $f = 2 \text{ MHz}$ and the particle starts $z_0 = 171 \mu\text{m}$ and final position is $z_f = 19 \mu\text{m}$. Thus, $2kz_0 = 0.9\pi$ and $2kz_f = 0.1\pi$ and the region of interest is $0.1\pi < \theta < 0.9\pi$. For such a case, the linearized force profiles and sample path calculations are plotted in Figure 1.

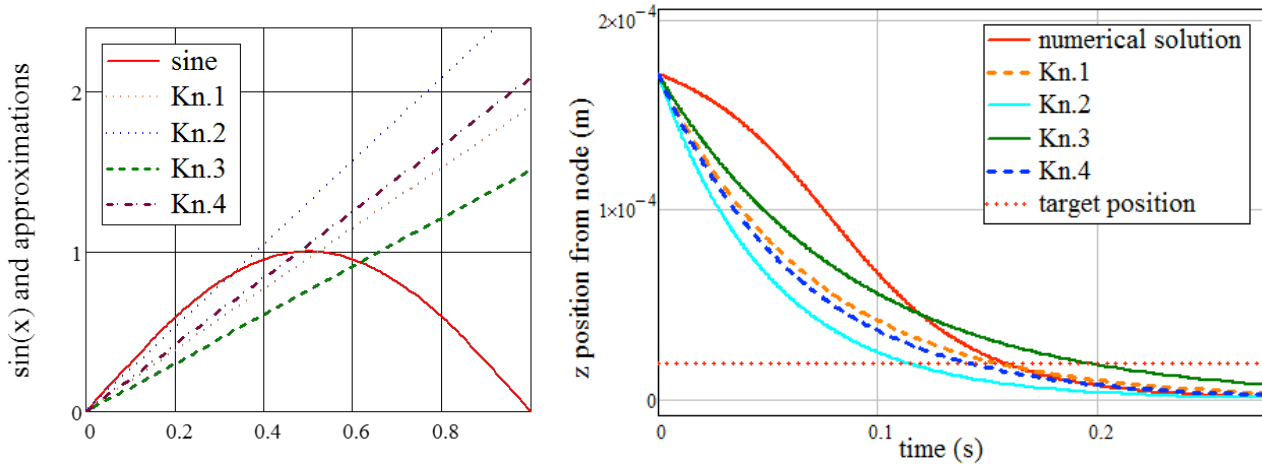


Figure 2: Linearized force profiles (left) and path calculations (right).

Conclusion

We presented a new approach to solve the EOM of a particle by linearizing the acoustic radiation force. The particle and excitation parameters determined the SDOF system parameters and a sample path calculation are presented. It is observed that the first and fourth linear solutions predict the time between two positions close to the numerical solution, within 6%.

References

- [1] Gor'Kov, L. P. Soviet Physics Doklady (Vol. 6, p. 773). (1962)
- [2] Groschl, M. Acustica, 84 (October 1997), 432–447. (1998)
- [3] Bruus, H. Lab on a Chip, 12(6), 1014–21. (2012)
- [4] Molina, M. I. Phys. Teach., 35. (1997).

Spatial Distribution of Radiation and Streaming Forces in a Channel in Combination with Standing Surface Acoustic Wave

Byungjun Kang¹, Junki Baek¹, Chanryeol Rhyou¹, and Hyungsuk Lee¹

¹School of Mechanical Engineering, Yonsei University, Seoul, Republic of Korea
 E-mail: crbox@yonsei.ac.kr, URL: <http://leelab.yonsei.ac.kr>

Introduction

This work includes the numerical study regarding the spatial ratio of the radiation force and drag force in the channel for acoustophoresis based on the standing surface acoustic wave (SSAW). Although several numerical studies found that both pressure and streaming fields are not homogeneous in a channel [1-4], the spatial distribution of the radiation force and the streaming one, which can determine the displacement of particles in the channel, have not been examined. **In this study, we calculated the ratio of the radiation force to the drag force in a channel in combination with SSAW and investigated how it determined motions of particles as a function of particle size.**

Model

A 2D numerical model was developed using COMSOL Multiphysics. It consists of the channel (DI water), the channel wall (10:1 PDMS) and SAW substrate (128° XY LiNbO₃) [Fig. 1 (a)]. In our model, the generation and propagation of SAW, and the pressure propagation in the channel and channel wall were simulated. SAW was modeled using the constitutive equations for piezoelectric materials. SAW was produced by exerting sinusoidal electrical signals to the interdigital transducers (IDTs) on the piezoelectric substrate. Perturbation theory was used to calculate the pressure fields in the channel and its wall, and streaming fields in the channel [2]. Thermoacoustics module and the Pressure Acoustics module were also used to ... utilized for the channel and the channel wall, respectively. Motions of the piezoelectric substrate, channel and channel wall were coupled by Thermoacoustic-Acoustic-Structure Boundary, the Acoustic-Structure Boundary, and the Acoustic-Thermoviscous Acoustic Boundary modules. The radiation force and the drag force from the acoustic streaming for a polystyrene particle were calculated at every position inside the channel to obtain the spatial distribution. The mesh size was set to be smaller than 50δ for the channel and δ for the channel boundary, where δ was the thickness of viscous boundary. For the SAW substrate, the maximum mesh size was set to be $10\lambda_{SAW}$, where λ_{SAW} was the wavelength of SAW. For the channel wall, the maximum size was $10\lambda_{PDMS}$. The pressure field of the channel and the channel wall, stress field and the electrical field of the SAW substrate were calculated in the frequency domain at a frequency $f_{SAW} = C_{SAW}/\lambda_{SAW}$, where C_{SAW} is the speed of SAW in the substrate. The streaming field was calculated by using the stationary study solver.

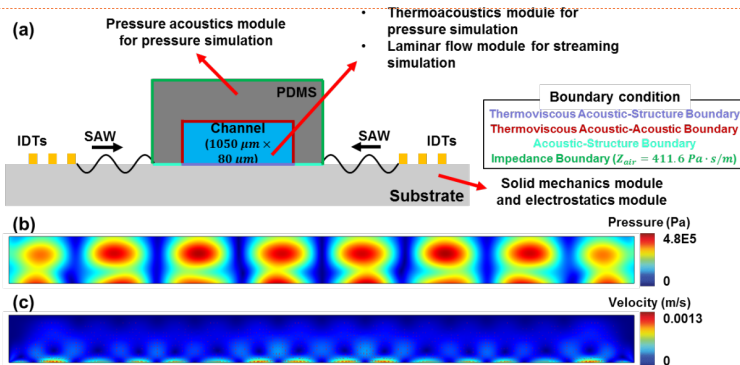


Figure 1: (a) Cross-sectional sketch of our 2D model, domain conditions and boundary conditions. (b) First-order pressure field, P_1 in the channel (c) Streaming velocity field $\langle v_2 \rangle$ in the channel

Comment [L1]: 무슨 말인지 모르겠다. rephrase 필요.

Comment [L2]: 어떤 constitutive equation 을 얘기하는 것인가? 구체적이지 않다면 의미없는 문장으로 보인다.

Comment [L3]: Thermoacoustics and pressure module 이 왜 사용된 것인지 명확치 않다. channel 과 channel wall 에 무엇을 하는데 사용된 것인가?

Comment [L4]: maximum mesh size 아닌가? 아니고, 채널 사이즈라면 보다 명확하게 표현되어야 하겠다. 앞 문장에서는 mesh 를 이야기해서 헷갈린다.

Comment [L5]: 어떤 표현인지 명확하지 않다. 하나의 주파수에서만 계산되었다는 것인가?

Comment [L6]: 시계 통일하도록. 위 부분에 있는 문장들과도 통일하도록. where 부분 역시 과거로 통일하면 좋겠다.

Comment [L7]: Boundary condition box 의 내용을 색으로만 표현하는 것은 잘 와닿지 않는다. 다시 수정하도록. 예를 들어서, plot 의 legend 를 다는 것과 같이 색으로 줄을 긋고 그것이 나타내는 것이 무엇인지는 black font 를 이용해서 쓰면 어떤가?

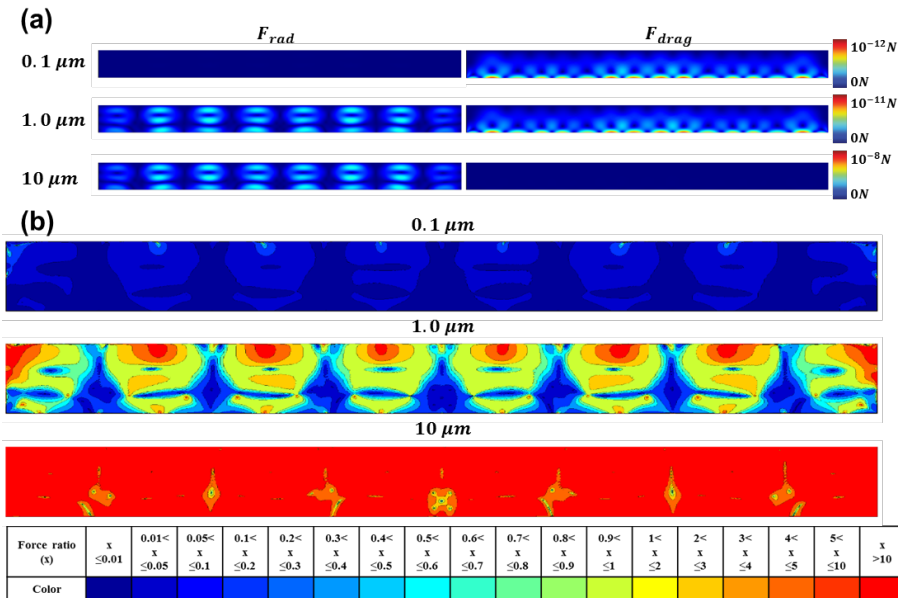


Figure 2: (a) Radiation force and drag force for a polystyrene particle with a diameter of 0.1, 1.0, and 10 μm, respectively and (b) the ratio of two forces (x) at each position in the channel.

Result

Using our 2D model, the first-order pressure field and the streaming velocity field in the channel under SSAW was calculated as in figure 1 (b) and (c). The radiation force and the drag force on a polystyrene particle with various diameter ($d_{PS} = 0.1, 1.0, \text{ and } 10 \mu\text{m}$) were calculated in the channel [Fig. 2 (a)]. When the particle was small ($d_{PS} = 0.1$), the drag force was much higher than the radiation force. When the particle size increased, the radiation force became more dominant. This result is quite reasonable because the radiation force and the drag force is proportional to the cube of the diameter (d_{PS}^3) and the diameter (d_{PS}), respectively. The ratio of the radiation force and the drag force at each position was calculated as figure 2 (b). As expected, the force ratio (x) was close to 0 for a small particle and much higher than 1 for a large particle in the channel. The force ratio for a particle with intermediate diameter ($d_{PS} = 1.0 \mu\text{m}$) sharply changed in the channel. In other words, both of the radiation-dominant and the streaming-dominant acoustophoretic motion of particles can simultaneously exist in a single microchannel. This result indicates that the critical size of a particle would depend on the local region in a channel. Thus, the critical size of a particle should be defined as a diameter of the particle when the particle begins to exhibit a radiation-dominant acoustophoretic motion throughout the channel. In addition, the effect of particle and solution property on the critical size for the channel should be evaluated.

Conclusion

In this study, we evaluated the distribution of the radiation force and drag force inside the channel subject to acoustophoresis. The effect of particle size on the force distribution was also investigated. Our study can be applied to see how the property of solution and particle, and the channel dimensions determine the force distribution. Furthermore, by comparing our results with the particle tracing simulation, the critical particle size for manipulation using SAW can be determined.

References

- [1] P. B. Muller, R. Barnkob, M. J. H. Hensen and H. Bruus. *Lab on a Chip* **12**, 4617-4624 (2012).
- [2] N. Nama, R. Barnkob, Z. Mao, ... and T. J. Huang. *Lab on a Chip* **15**, 2700-2709 (2015).
- [3] C. Devendran, T. Albrecht, J. Brenker, ... and A. Neild. *Lab on a Chip* **16**, 3756-3766 (2016).
- [4] N. R. Skov and H. Bruus. *Micromachines* **7**, 182 (2016).

Comment [LB]: Ref. 포맷 다시 확인하도록... 이 있는 표현인가?



Critical design aspects on high throughput multiplex acoustophoresis

Andreas Lenshof¹, Anke Urbansky¹, Stefan Scheduling² and Thomas Laurell^{1,3}

¹Department Biomedical Engineering, Lund University, Lund, Sweden

E-mail: Andreas.Lenshof@bme.lth.se, URL: <http://www.bme.lth.se>

²Department of Laboratory Medicine, Lund Stem Cell Center, Lund University, Lund, Sweden

³Department of Biomedical Engineering, Dongguk University, Seoul, Korea

Introduction

We present an acoustofluidic device for multiplex particle separation with increased separation performance and throughput. Previously reported acoustic devices for multiplex cell and particle separation have shown limited throughput [1]. In order to substantially increase throughput, we have redesigned and developed a new separation system that enables unmatched particle separation performance of heterogeneous samples at a volume throughput of 200 μ l/min, which corresponds to approximately 91.000 particles/s.

Critical design aspects for an efficient resonator

To realize an efficient resonator for multiplex acoustophoresis, a few important design aspects need to be considered. Firstly, in order to effectively separate different particle types in free flow acoustophoresis, it is important to congregate all particles into the same flow vector, preferably performed in a two dimensional acoustic pre-alignment step [2]. At higher flow rates, the particle retention time in the pre-alignment sound field is shortened and the particles do not have time to pre-align, resulting in reduced separation resolution. Hence, to enable un-impaired separation performance at elevated flow rates, we elongated the pre-alignment channel 200% as compared to earlier work [1]. At higher flow rates, a larger acoustic radiation force in the separation zone is also needed to counter act the shorter transition time in the separation channel. This, however, results in higher driving voltages of the separation transducer, which in turn results in higher electro-mechanical power dissipation and thus thermal rise in the transducer. The temperature increase in turn may affect the speed of sound in the fluid, resulting in a shift in the acoustic resonance peak and thereby loss of performance. As earlier presented, it is of paramount importance to maintain a constant temperature, within a degree, during acoustophoresis separations. Previous acoustophoresis designs relied on temperature control via a Peltier-element in contact with the acoustic chip. The direct contact to the Peltier-element, however, dissipated a significant amount of acoustic energy from the piezo-actuator which limited the maximum system throughput. To alleviate these short comings the new acoustophoresis system incorporates a non-contact air-cooling solution, free from acoustic power losses, that also fulfills the thermal requirements, Figure 1.

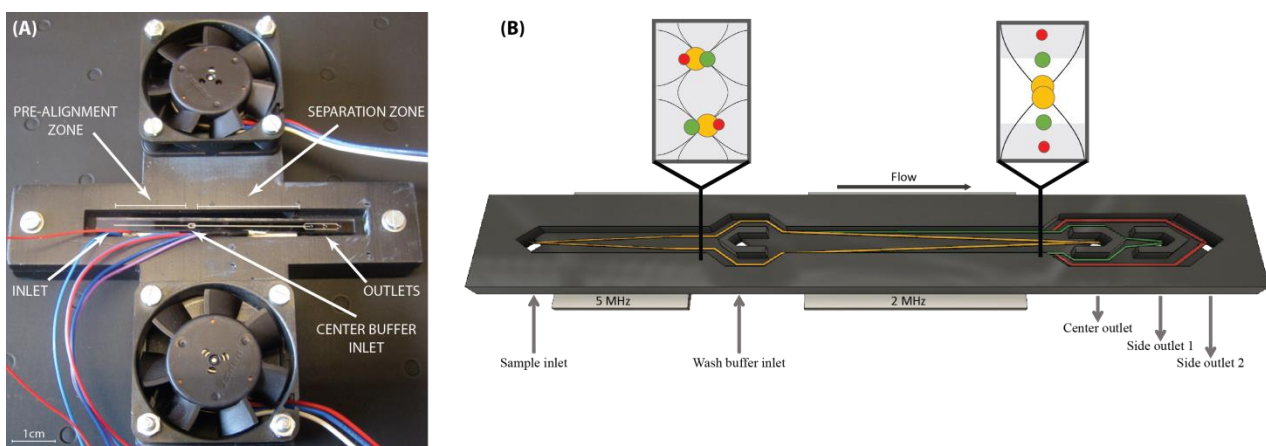


Figure 1: (A) 3-D printed chip holder designed for air cooled acoustophoresis separation enabling high piezo ceramic actuation voltages without thermal drift of the system. The fans blow air through the rectangular opening where the separation chip is visible. The design also includes a free-hanging mounting of the chip via the connecting tubing to minimize dissipation of acoustic energy from the acoustic channel resonator. (B) Schematic of the separation chip. Beads are pre-aligned by the 5MHz transducer and are acoustically separated according to size in the separation zone. Laminar flow is utilized to fractionate the three different particle sizes to each outlet.

Evaluation of the air cooling design

To evaluate the air cooling, temperature was monitored over time from start of the system to the four minute mark. The effect of air cooling as well as the influence of flow cooling as the device was perfused at two different flow rates, 400 μ l/min and 800 μ l/min (this corresponds to sample flow rates of 100 μ l/min and 200 μ l/min respectively). As seen in figure 2, the air cooling effect is clearly visible, green and purple lines. Although not efficient to cool the device down to room temperature, it is good enough to keep the temperature stable, even at the higher driving voltages needed at higher flow rates, which is a prerequisite to be able to achieve an efficient and reliable separation. It is also seen that fluid flow has a stabilizing effect on the temperature as well, but it is slower and less efficient in heat transport.

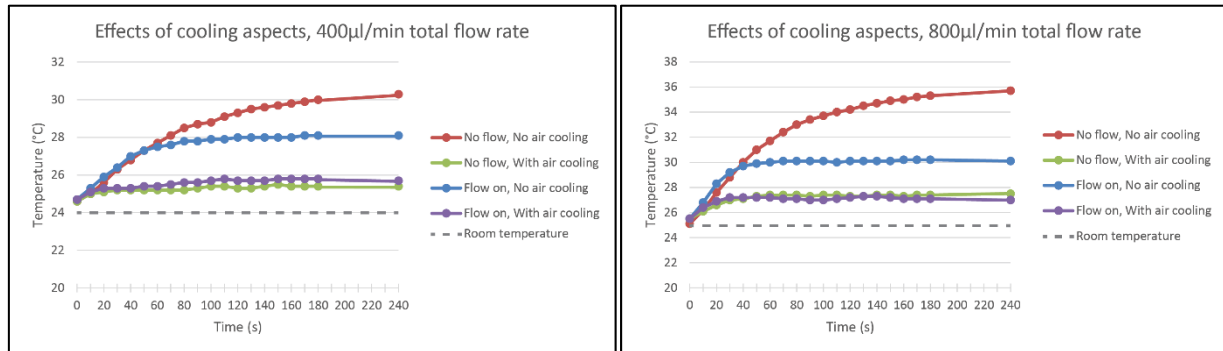


Figure 2: Graphs showing the temperature measured on the chip over time at two different flow rates. The air cooling effect is clearly seen, green and purple lines. Although not efficient to cool the device down to room temperature, it is sufficient to keep the temperature stable, even at the higher driving voltages needed at the higher flow rate, which is a prerequisite to be able to achieve an efficient and reliable separation. It is also seen that fluid flow has a cooling and stabilizing effect on the temperature as well (blue line), but it is slower in reaching a steady state value and less efficient in heat transport.

High throughput bead data

Using the previously mentioned improvements, we successfully demonstrate high throughput fractionation of 7 μ m, 5 μ m, and 3 μ m polystyrene beads as seen in figure 3, with average recoveries of 99.8%, 96.8% and 97.2% respectively in their designated outlets, at a sample flow rate of 200 μ l/min. The purity at 200 μ l/min for the three bead fractions were 97.6%, 93.7% and 100% respectively. This exceed previously reported throughput [1] 20 fold, and at improved separation performance.

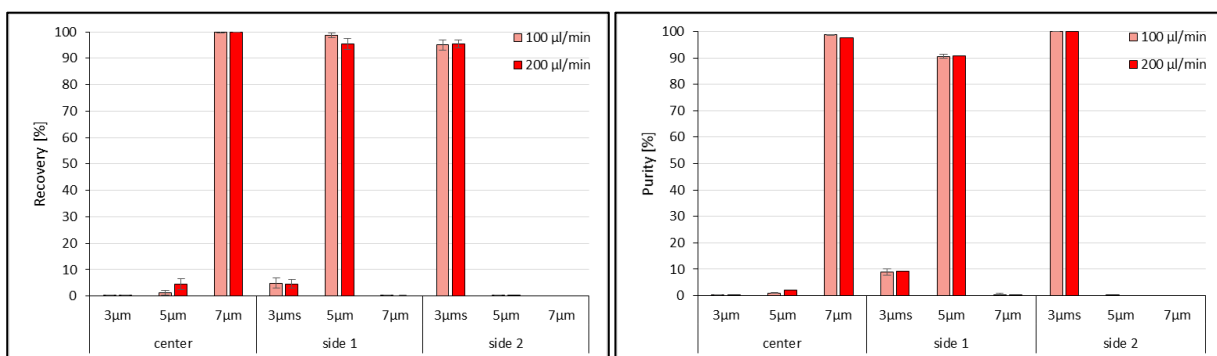


Figure 3: Recovery and purity of 3 μ m, 5 μ m and 7 μ m polystyrene bead separation at 100 μ l/min and 200 μ l/min sample flow rates.

Conclusion

We have successfully demonstrated an improved separation device for multiplex acoustophoresis which outperforms previously reported multiplex separations systems, both in efficiency and throughput.

References

- [1] C. Grenvall, C. Magnusson, H. Lilja and T. Laurell. *Anal. Chem.***87**, 5596-56047 (2015).
- [2] P. Augustsson, C. Magnusson, M. Nordin, H. Lilja and T. Laurell. *Anal. Chem.***84**, 7954-7962 (2012).



Investigation of interparticle radiation force between two spheres in acoustophoresis

Abhishek Ray Mohapatra¹, and Kian-Meng Lim¹

¹Department of Mechanical Engineering, National University of Singapore, Singapore
E-mail: limkm@nus.edu.sg

Introduction

Acoustophoresis is the manipulation of particles using acoustic field in a fluid medium. The nature and magnitude of the force depends on the relative mechanical properties of the particle and the surrounding medium and the amplitude of the acoustic wave. In applications where there are multiple particles, the radiation force deviates from the case where there is only one isolated particle. The resultant radiation force depends on the primary incident field and also the scattered field from the surrounding particles. Hence, for the precise manipulation, we need to understand the interaction between the particles due to the scattered acoustic field. This interaction between the particles is also referred to as the secondary radiation force or the interparticle radiation force. In this study, we conducted a series of experiments to study the interparticle radiation force between two isolated polystyrene beads in water (only two particles in the observation region of $400\mu\text{m} \times 400\mu\text{m}$). The interparticle force was estimated based on a simple mathematical model.

Experimental set-up and method

Fig. 1 shows the laboratory set-up and the microfluidic device used in the study. The microfluidic device is a resonance chamber mounted on a piezoelectric transducer. The resonance chamber is $400\mu\text{m} \times 40\mu\text{m}$ cross-section glass capillary with wall thickness of $40\mu\text{m}$ and length of 50mm . The transducer was excited by a signal generator and a bipolar amplifier. The excitation frequency of 1.875

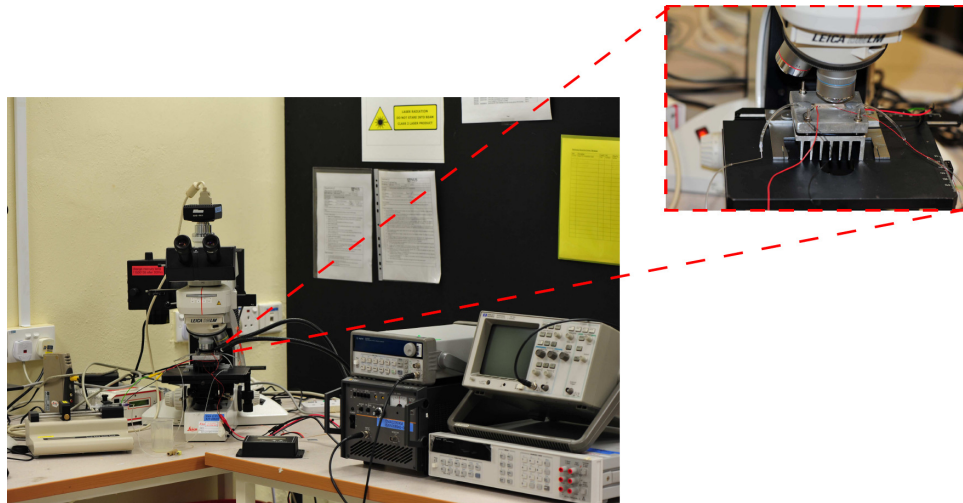


Figure 1: The experimental set-up and the microfluidic device for conducting acoustophoresis experiment.

MHz was chosen so that the width of the channel corresponds to half of the wavelength. To monitor voltage and power input to the transducer, the amplifier was connected to an oscilloscope and a high frequency multimeter. The experimental observations were captured from top by a CCD mounted to the microscope. An external light source was used to illuminate the channel; however, the fluorescent micro-spheres ($9.9\mu\text{m}$ polystyrene beads) were observed by the blue light obtained from the excitation filter of the microscope. During the experiment, the temperature was monitored using a thermistor.

The media files of the experimental observations were post processed to find the trajectories of the beads for each observation. During the experiment, repeated observations were taken for each

pair of beads. Total five different pairs of the beads were trapped in the observation region for the study. For calculation of the interparticle force, observations that satisfy the following two criteria were used: (1) the beads are close to the pressure node (within a distance of less than $30\mu\text{m}$ from the pressure node), and (2) the line joining the centers of the beads is nearly perpendicular to the incident wave (if θ is the angle between line joining the centers of the beads and the incident wave, $80^\circ < \theta \leq 90^\circ$). The trajectories of the observations were fitted by second order polynomial to calculate the velocity of the beads. The velocity of the beads were used to compute the fluid drag force acting on the beads. A simple mathematical model based on Stokes flow past the beads and hydrodynamic interaction between the beads is used for the fluid drag calculation.

Results

Fig. 2 shows the variation of radial component of interparticle or secondary radiation force F_r^s for five different pairs of $9.9\mu\text{m}$ diameter polystyrene beads with respect to normalized center to center distance r/a , where a is the radius of the beads. This force is calculated based on the balance of the fluid drag, and the primary and secondary radiation forces acting on the spheres in a quasi-static equilibrium state.

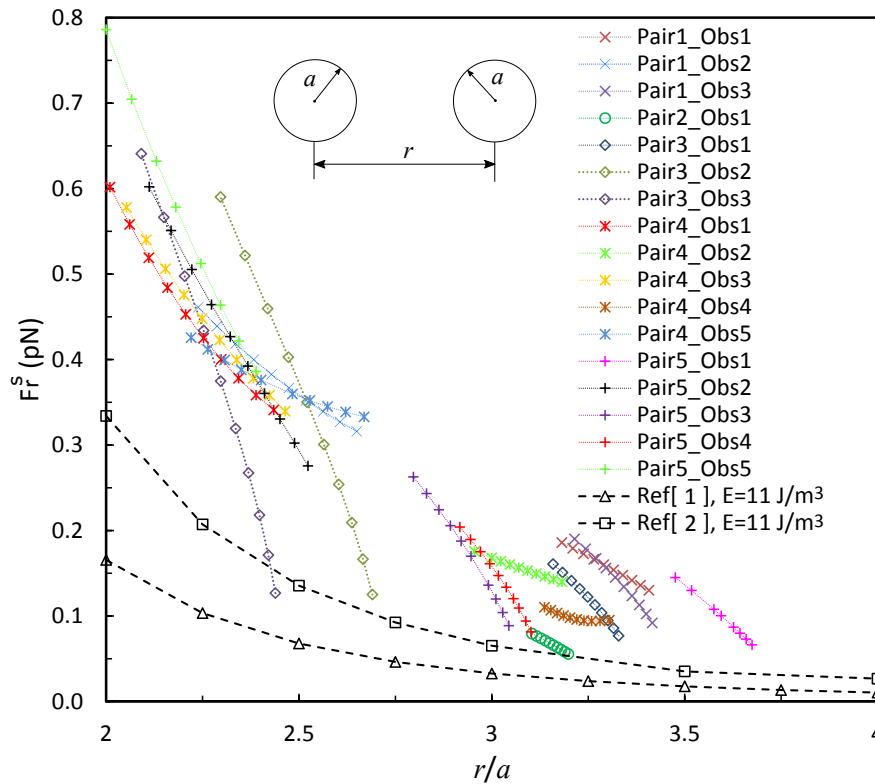


Figure 2: Interparticle radiation force along radial direction between two $9.9\mu\text{m}$ diameter polystyrene beads.

The results are compared with theoretical interparticle radiation force reported by Silva et al. [1] and Sepehriahnama et al. [2]. The theoretical interparticle radiation force was calculated for acoustic energy density $E_{ac} = 11\text{J}/\text{m}^3$ at pressure node in transverse plane ($\theta = \pi/2$). The interparticle radiation force found in this study is two or three times larger than those predicted theoretically, but the values are in the same order of magnitude.

Conclusion

Experimental observations show that the interparticle radiation force between two spherical particles decreases with interparticle distance, as expected from theory. The results obtained in this study are larger than those reported by theoretical calculations. One possible reason for this discrepancy could be due to the viscosity of the fluid which is not considered in the previous theoretical studies [1, 2].

References

- [1] G. T. Silva, and H. Bruus. Physical Review E, **90(6)**, 063007, 2014.
- [2] S. Sepehriahnama, K.-M. Lim, and F. S. Chau. The Journal of the Acoustical Society of America, **137(5)**, 2614-2622, 2015.



Mechanical Properties Based Particle Separation via Traveling Surface Acoustic Wave

Zhichao Ma, David J. Collins and Ye Ai*

Pillar of Engineering Product Development, Singapore University of Technology and Design, Singapore 487372, Singapore
E-mail: aiye@sutd.edu.sg

Introduction

Most microfluidics-based sorting methodologies utilize size differences between suspended micro-objects as the defining characteristic by which they are sorted. Sorting based on mechanical properties, however, would provide a new avenue for sample preparation, detection and diagnosis for a number of emerging biological and medical analyses [1, 2]. In this study, we demonstrate separation of polystyrene (PS) and poly(methyl methacrylate) (PMMA) microspheres based entirely on their difference in mechanical properties using traveling surface acoustic waves (TSAWs). We theoretically examine the correlation of the applied TSAW frequency, particle density and sound speed with respect to the resultant acoustic radiation force (ARF) that acts to translate particles, and experimentally corroborate these predictions by translating PS and PMMA particles simultaneously in a stationary flow. Even when PS and PMMA particles have the same diameters, they exhibit distinct acoustophoretic responses as a function of their mechanical properties and the applied TSAW frequency. By specifically matching the appropriate acoustic frequency to the desired particle size, each particle population can be selectively translated and sorted. We demonstrate that this mechanical properties based sorting can continuously separate these particle populations with at least 95% efficiency in the mixed 10/15 μm diameter PS and PMMA particle solutions tested.

Comparison of ARF Factors for PS and PMMA Particles

A particle suspended in a fluid and exposed to a traveling wave acoustic field is subject to a time-averaged acoustic radiation force (ARF, F_T), which can be expressed as $\langle F_T \rangle = Y_T \pi a^2 \langle E \rangle$, where Y_T is the ARF factor, $\langle E \rangle$ is the mean energy density of the incident wave, and a is the radius of the spherical particle [3]. Thus, for the same-sized particles subject to an acoustic field with the same energy intensity, the ARF is proportional to the dimensionless factor Y_T . As depicted in Fig. 1a, to experimentally evaluate the different acoustophoretic responses of the same-sized PS and PMMA particles, an aqueous suspension containing a mixture of 15 μm PS and 15 μm PMMA particles was introduced into the disposable PDMS channel then laterally translated across the channel in the direction of acoustic propagation with the application of an AC signal to the chirped interdigital transducers (CIDTs). The acoustic radiation force is balanced by Stokes drag force $F_D = 6\pi\mu a v$, where μ is the dynamic viscosity, a is the particle radius, and v is the particle velocity relative to the flow. Thus, the ratio of the acoustic radiation force on the PS and PMMA particles, R_T , can be derived by the relative average velocities of their translations. To quantify the acoustophoretic responses at varying $\kappa = 2\pi a f / c_f$, (a , f , and c_f are respectively the particle radius, the acoustic field frequency, and the sound speed in the fluid) four frequencies 43.04/45.52/50.77/56.57 MHz were selected that correspond to κ values of 1.35/1.43/1.60/1.78, respectively. Fig. 1b,c shows the trajectories of a PS particle and a PMMA particle exposed to a 56.57 MHz TSAW field ($\kappa = 1.78$). Fig. 1d shows the comparison between the theoretical curve and the experimental measurement of the R_T value, in which $R_T > 1$ at $\kappa = 1.35$ and 1.43, while $R_T < 1$ at $\kappa = 1.60$ and 1.78. These experimental measurements follow the theoretical prediction with regard to relative imparted acoustic radiation force.

Particle Separation Based on Mechanical Properties

To demonstrate the effective separation according to the particle's mechanical properties, we utilize our acoustophoretic microfluidic system to separate 15 μm PS and 15 μm PMMA particles in a 45.52 MHz TSAW field, corresponding to $\kappa = 1.43$, at which the ARF imparted on PS particles is maximized relative to that on PMMA ones. The PS particles were selectively translated to outlet A in the direction of wave propagation (farther from the IDTs), while the PMMA particles still exited the sorting region via outlet B, as shown in Fig. 2d. Similarly, the PMMA particles can be selectively translated at κ value conditions that maximize the force imparted on them relative to those of PS. Accordingly, we performed the selective PMMA particle separation in a 56.57 MHz TSAW field, corresponding to $\kappa = 1.78$, as shown in Fig. 2e. We also demonstrate the separation of 10 μm PS and 10 μm PMMA particles, while maintaining optimized $\kappa =$

1.43 by altering the applied frequency as 68.28 MHz, as shown in Fig. 2f. We further demonstrate the separation of 10 μm PS particles from 15 μm PMMA particles, despite the fact that the smaller PS particle frontal area as 44% of that for the larger PMMA particles. We maintain the application of a 68.28 MHz TSAW field, which corresponds to $\kappa = 1.43$ for PS particles and $\kappa = 2.14$ for PMMA particles. Despite this smaller size of the PS particles, we demonstrate the selective displacement and separation of 10 μm PS particles from 15 μm PMMA particles due to the larger radiation force acting on the 10 μm PS particles, as shown in Fig. 2g.

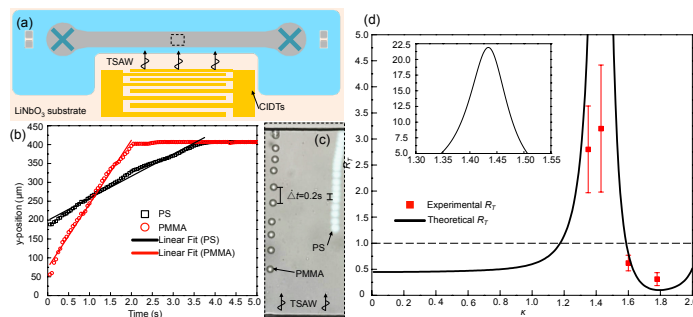


Figure 1: Experimental measurement of ARF factors of PS and PMMA particles. (a) Disposable PDMS channel containing suspended 15 μm PS and PMMA particles was placed on the SAW transducers, where prepatterned chirped IDTs generate acoustic waves at 43.04/45.52/50.77/56.57 MHz. (b) Tracked y-position for the two particles and their linear fit during the lateral translation. (c) One each of PS (fluorescent) and PMMA (plain) particles are translated in a 56.57 MHz TSAW field. (d) Comparison of $R_T = Y_T(\text{PS})/Y_T(\text{PMMA})$ between the theoretical model and our experimental measurements.

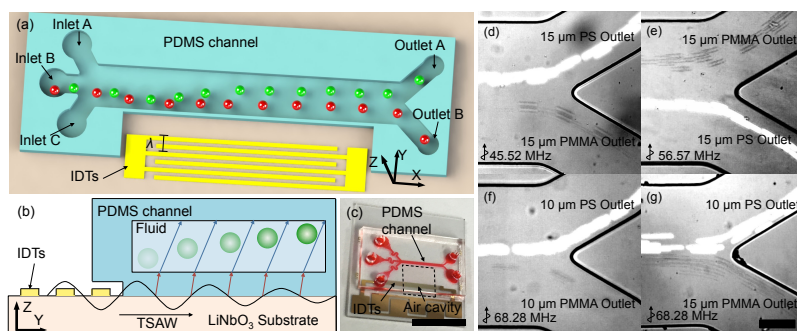


Figure 2: (a) Three-dimensional perspective illustration of the separation chip. (b) Cross-section of the device. A disposable PDMS channel is placed on a reusable TSAW transducer where the pre-patterned IDTs generate the TSAW that couples into the microchannel. Particles flowing through the channel are translated by dissimilar distances according to the difference in their mechanical properties and thus are collected in different outlets. (c) Photograph of the assembled device. The scale bar is 5 mm. (d) In the 45.52 MHz TSAW field, the 15 μm PS particles were translated into the lower outlet while the 15 μm PMMA particles flowing into the upper outlet due to the $Y_T(\text{PS}) > Y_T(\text{PMMA})$ relationship at $\kappa = 1.43$. (e) In contrast to the condition in (d), in the 56.57 MHz TSAW field the 15 μm PMMA particles are translated to the upper outlet when $Y_T(\text{PS}) < Y_T(\text{PMMA})$ at $\kappa = 1.78$. (f) Similar to the situation at (d), the 10 μm PS and PMMA particles are separated in the 68.28 MHz TSAW field while maintaining $\kappa = 1.43$. (g) The 10 μm PS particles can be separated from 15 μm PMMA particles with a larger radiation force acting on the 10 μm PS particles. These images are obtained by overlapping 40 frames recorded every 0.05 s. The scale bar is 100 μm .

Conclusion

In the present work, our experimental studies confirm the divergent ARF factor peaks for PS and PMMA particles, and the experimentally derived force factor ratios of $Y_T(\text{PS})$ to $Y_T(\text{PMMA})$ at $\kappa = 1.35/1.43/1.60/1.78$ were comparable with the predictions made from a theoretical model that accounts for acoustic scattering. Based on the distinct acoustophoretic responses arising from the difference in their mechanical properties, same-sized PS and PMMA particles (10 and 15 μm) were efficiently separated in a continuous flow using TSAW fields at varying resonant frequencies (45.52/56.57/62.28 MHz). Though the radiation force scales with a^2 , we also demonstrated that it is feasible to exert a larger radiation force on 10 μm PS particles than 15 μm PMMA particles at an optimized κ value and, also, to implement separation at efficiencies greater than 95%.

References

- [1] P. Augustsson, J. T. Karlsen, H. -W. Su, H. Bruus and J. Voldman. *Nat. Commun.* **7**, 11556 (2016).
- [2] P. Li, Z. Mao, Z. Peng, L. Zhou, Y. Chen, P. -H. Huang, C. I. Truica, J. J. Drabick, W. S. El-Deiry, M. Dao, S. Suresh and T. J. Huang. *Proc. Natl. Acad. Sci. U. S. A.* **112**, 4970-4975 (2015).
- [3] T. Hasegawa and K. Yosioka, *J. Acoust. Soc. Am.* **46**, 1139-1143 (1969).



From modulated acoustic radiation forces and liquid column stabilization to radiation torques and special force conditions

Philip L. Marston¹, Likun Zhang², David B. Thiessen³, and Timothy D. Daniel¹

¹Physics & Astronomy Dept., Washington State Univ., Pullman, WA, 99164-2814, USA
E-mail: marston@wsu.edu, URL: <https://physics.wsu.edu/>

²Physics Dept., University of Mississippi, University, MS, 38677, USA

³Voiland Sch. Chem. Engineering & Bioeng., Washington State University, Pullman, WA, USA

Introduction

Various manifestations of acoustic radiation forces are examined together with some theoretical considerations and recent results. Partial-wave phase shifts are useful when analyzing radiation forces.

Modulated radiation forces and surface modes of acoustically levitated drops and bubbles

Modulated acoustic radiation forces (MARF) were introduced as a method for ultrasonically exciting low-frequency modes of acoustically levitated hydrocarbon drops in water for the purpose of measuring the mode frequencies [1]. Double-sideband-suppressed-carrier modulation facilitated excitation at particular frequencies. Analysis of the response involved projections of the stress distribution [1,2]. The method was extended to drops levitated in air [3] and to large air bubbles in water [4], which included related theory [5].

Liquid columns: Stabilization and forced low-frequency oscillation

Long liquid columns become unstable and break up into drops because of a surface tension instability (STI) appreciated in the 19th century by Plateau, Clerk Maxwell, and Rayleigh [6]. MARF was deployed as a method for exciting the low-frequency modes of such columns [2,6,7,8] and some acoustic radiation-force (ARF) based methods were demonstrated for suppressing the STI. This includes active ARF control (using feedback) for a density matched column and passive stabilization of columns in air (in reduced gravity) using appropriately designed sound fields [2,6,9,10]. The relevant translational radiation force for columns in standing waves was derived and the columns were positioned suitable for equilibrium [6,11].

Special acoustic radiation force conditions on spheres

For some situations involving spheres centered in axisymmetric cylindrical wave-fields, it is helpful to consider idealized wave-fields of acoustic Bessel beams or Bessel standing waves. This is facilitated by scattering formulations [12-16] that included the case of higher-order Bessel wave-fields. One outcome in the progressive wave case is that special conditions were found giving negative forces (forces opposite the beam direction) [12]. Such situations were not considered paradoxical because the negative force conditions (since 2006 often described as negative ARF "islands" in the relevant parameter space [12]) were always found to be associated with situations involving suppressed scattering in the backward hemisphere relative to the forward hemisphere. The relevance of the scattering pattern was analytically established first for spheres in Bessel beams and then for arbitrary passive objects in general progressive wave invariant beams [16-18]. Figure 1 (re-plotted from [12]) shows calculated negative ARF islands in (ka, β) domain where a is the sphere radius, $k = \omega/c$ is the acoustic wave number, and β is the Bessel beam's conic angle. Power absorption (which is non-negative for passive objects [18]) by the sphere or other target objects gives rise to a positive force contribution [16-18]. For plane waves in an inviscid fluid, the radiation force on passive objects is non-negative [18], though it may be negative for active objects [18].

Phase shift and wave-field parameters for special radiation force conditions

When analyzing the scattering by spheres in plane waves, it can be helpful to express the partial-wave amplitudes using phase shifts. Those phase shifts become complex if there is absorption, but in the non-absorption case they become real and will be denoted by δ_n [19]. Radiation force expressions involving the δ_n are available for plane-wave and Bessel-related axisymmetric traveling and standing wave-fields [19,20]. This approach gives insight into special radiation force conditions. For progressive waves special conditions concern negative and vanishing forces, while for standing waves they involve non-trivial vanishing force conditions [20]. For ordinary plane standing waves this approach facilitates the discovery of conditions for vanishing force at small but finite ka that depend on the fluid properties [20]. Plane-standing-wave ARFs are closely related to the evolution of particle suspensions and the associated resonator frequency shifts [21].

Radiation torque and power absorption for axisymmetric objects and vortex wave-fields

When optically isotropic spheres are illuminated by circularly polarized light, a detailed analysis from Maxwell's equations shows the radiation torque is proportional to the optically absorbed power P_{abs} [22]. This analysis was generalized to axisymmetric objects in acoustic vortex beams, first for paraxial vortex beams [23], and then to more general non-paraxial vortex beams and standing waves [24]. The steady rotation rate may be estimated by balancing the radiation torque with viscous drag [22]. The oscillating viscous boundary layer (Stokes layer) contributes to the acoustic P_{abs} [25].

Fundamental scattering research using acoustically controlled deformation of liquid drops

Radiation pressure induced deformation of levitated drops [2,5] provides a fruitful approach for investigating relationships between wave-front shapes and complicated optical caustic wave-fields [26-28].

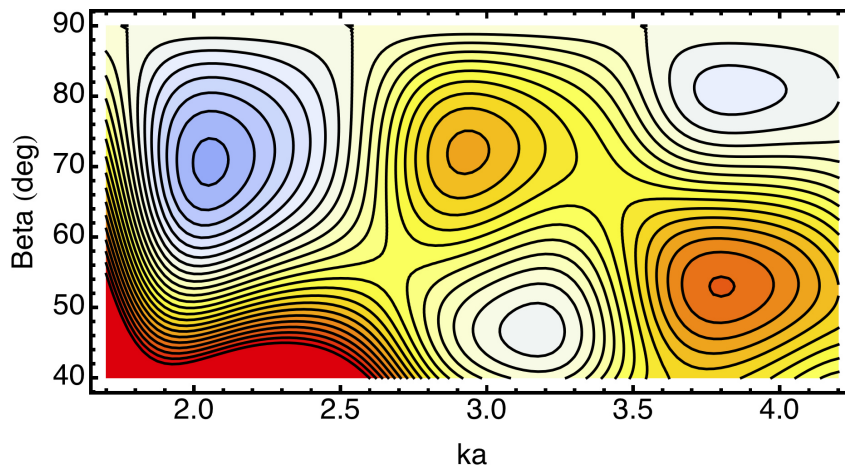


Figure 1: The dimensionless progressive wave radiation force function Y_p for a hexane drop in water from [12] shown using the contour method of [20]. The illumination is a zero-order Bessel beam. The contour interval is 0.02. In the blue and white regions $Y_p < 0$ while Y_p is positive in the pink, yellow, tan, and red regions. The solid-red region (lower left) is from a saturation of the display at $Y_p = 0.3$. Three negative ARF islands are visible separated by positive saddle-shaped regions. The liquid properties are as in [12].

Conclusion

It is intended that this summary illustrate connections between selected research topics over the past 40 years associated with acoustic radiation force manipulation of objects. It is often helpful to make use of quantum scattering notation [16,19,20]. The sponsors included ONR and NASA. In the broader context there can be fruitful analogies between acoustical, optical, and quantum-mechanical (matter-wave) forces [29].

References

- [1] P. L. Marston and R. E. Apfel. *J. Acoust. Soc. Am.* **67**, 27-37 (1980).
- [2] P. L. Marston and D. B. Thiessen. *Annals of the New York Academy of Sciences* **1027**, 414-434 (2004).
- [3] E. H. Trinh, P. L. Marston, and J. L. Robey. *Journal of Colloid and Interface Science* **124**, 95-103 (1988).
- [4] T. J. Asaki, D. B. Thiessen, and P. L. Marston. *Phys. Rev. Lett.* **75**, 2686-2689 (1995); (e) 4336 (1995).
- [5] T. J. Asaki and P. L. Marston, *J. Acoust. Soc. Am.* **97**, 2138-2143 (1995).
- [6] P. L. Marston. *Phys. Fluids* **29**, 029101 (2017).
- [7] S. F. Morse, D. B. Thiessen, and P. L. Marston. *Phys. Fluids* **8**, 3-5 (1996).
- [8] J. B. Lonzaga, C. F. Osterhoudt, D. B. Thiessen, and P. L. Marston. *J. Acoust. Soc. Am.* **121**, 3323-3330 (2007).
- [9] M. J. Marr-Lyon, D. B. Thiessen, and P. L. Marston. *J. Fluid Mech.* **351**, 345-357 (1997).
- [10] M. J. Marr-Lyon, D. B. Thiessen, and P. L. Marston. *Phys. Rev. Lett.* **86**, 2293-6 (2001); (e) **87**, 209901 (2001).
- [11] W. Wei, D. B. Thiessen, and P. L. Marston. *J. Acoust. Soc. Am.* **116**, 201-208 (2004); (e) **118**, 551 (2005).
- [12] P. L. Marston. *J. Acoust. Soc. Am.* **120**, 3518-3524 (2006).
- [13] P. L. Marston. *J. Acoust. Soc. Am.* **121**, 753-758 (2007).
- [14] P. L. Marston. *J. Acoust. Soc. Am.* **124**, 2905-2910 (2008).
- [15] P. L. Marston. *J. Acoust. Soc. Am.* **125**, 3539-3547 (2009).
- [16] L. Zhang and P. L. Marston. *Phys. Rev. E* **84**, 035601(R) (2011).
- [17] L. Zhang and P. L. Marston. *J. Acoust. Soc. Am.* **131**, EL329-EL335 (2012).
- [18] P. L. Marston and L. Zhang. *J. Acoust. Soc. Am.* **139**, 3139-3144 (2016).
- [19] L. Zhang and P. L. Marston. *J. Acoust. Soc. Am.* **140**, EL178-EL183 (2016).
- [20] P. L. Marston and L. Zhang. *J. Acoust. Soc. Am.* **141**, 3042-3049 (2017).
- [21] C. S. Kwiatkowski and P. L. Marston. *J. Acoust. Soc. Am.* **103**, 3290-3300 (1998).
- [22] P. L. Marston and J. H. Crichton. *Phys. Rev. A* **30**, 2508-2516 (1984).
- [23] B. T. Hefner and P. L. Marston. *J. Acoust. Soc. Am.* **106**, 3313-3316 (1999).
- [24] L. Zhang and P. L. Marston. *Phys. Rev. E* **84**, 065601(R) (2011).
- [25] L. Zhang and P. L. Marston. *J. Acoust. Soc. Am.* **136**, 2917-2921 (2014).
- [26] P. L. Marston and E. H. Trinh. *Nature* **312**, 529-531 (1984).
- [27] G. Kaduchak and P. L. Marston. *Applied Optics* **33**, 4687-4701 (1994).
- [28] P. L. Marston, *J. Quantitative Spectroscopy and Radiative Transfer* **63**, 341-351 (1999).
- [29] A. A. Gorlach, M. A. Gorlach, A. V. Lavrinenko, and A. Novitsky. *Phys. Rev. Lett.* **118**, 180401 (2017).



Contactless manipulation device controlled by two-phase flow for lab-on-a-chip applications.

Walid Messaoudi, Martyn Hill, Peter Glynne-Jones

Mechatronics, Faculty of Engineering and the Environment, University of Southampton, Southampton, United Kingdom
 Email: wmm1e12@soton.ac.uk

Introduction

There is demand in microfluidic environments to be able to manipulate and control the trapping locations of acoustophoretic systems. This has importance, for example, in tissue engineering, cell-cell interaction studies, and systems that might benefit from repetitive manipulation tasks [1].

Concept

A challenge in creating dynamic position control in resonators is that the resonances are typically strongly determined by the geometry of the device. The concept presented here is to change the material properties of key parts of the acoustic path through flowing non-miscible liquids of different acoustic properties through control channels which underlie the active manipulation area. By changing the spatial configuration of the two-phase flow in the control channel, the force field in the manipulation cavity is modulated and controlled.

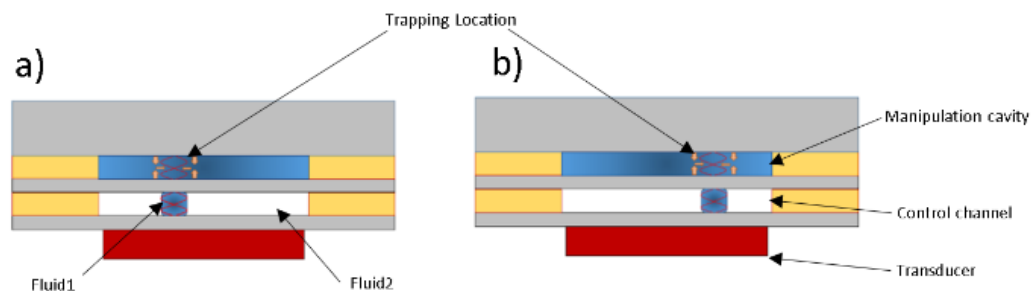


Figure 1: Schematic of the concept. Cross section along length of control channel, showing a droplet of control fluid 1 in two positions at different times. In each case trapping is only seen above the droplet of control fluid 1, as a result of layer designs that cause resonance to only be supported when this fluid is in the acoustic path.

Modelling and design choices

While using air as the second control fluid was considered, the compressibility of a gas makes it difficult to manipulate position control droplets accurately in the control channel. A range of liquids were assessed on the criterion of non-miscibility and significant speed of sound difference. Modelling suggests that differences in the density of the control liquids is less important. The work presented here is based upon a combination of water and silicon oil (*Poly(dimethylsiloxane)*) control fluids. The glass and silicone/acrylic tape layers used in the design also affect the resonances that are found. It was important to prevent the walls of the control channel (which at this stage are fabricated by laser cutting, and are thus relatively thick) from causing levitation in the manipulation cavity. Thus, the properties of the tape (3M 9731) were measured using time of flight measurements in a stack of tape. The tape was also found to provide a strong, solvent-resistant seal to the fluidic channels.

	Silicon oil (PDMS)	Water	Glass	Acrylic tape
Speed of sound (m.s ⁻¹)	1030	1480	4540	1340
Density (kg.m ⁻³)	0.95	1	2.6	1.1
Acoustic impedance	979	1480	11804	1474

Table 1: control fluid and device structure properties

Modelling revealed a number of design rules which are described below:

- a) In order for there to be sufficient contrast in the acoustic trapping above the two control fluids (i.e. for the trapping to be localized above the control droplet), a thicker control layer tended to be favorable.
- b) While it is possible to consider designs in which the transducer is placed on the same side as the manipulation cavity, it was found that this tended to result in devices with lower spatial trapping resolution. This can be seen in figure 2 (b)

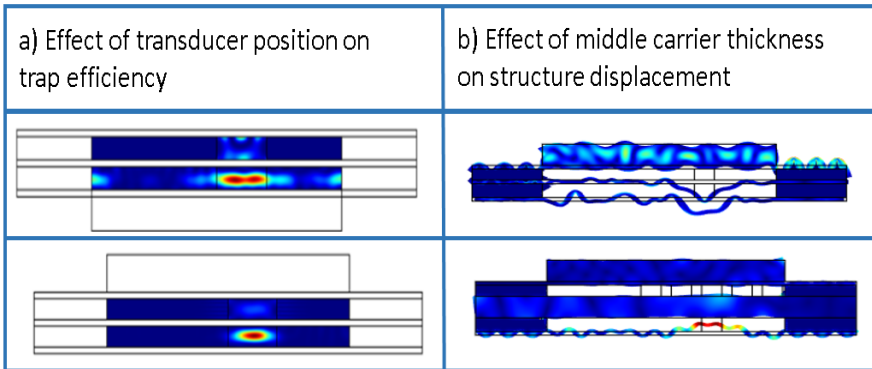


Figure 2- Example of COMSOL 2D Slices used to find optimal configuration

c) In designs in which the control droplet has dimensions of order less than the acoustic wavelength trapping efficiency was significantly decreased.

d) If the layer separating the two fluid channels (the “middle carrier layer”) was too thin (e.g. coverslip thickness, 170µm), then significant flexural waves are found to be formed in that layer, which reduces the level of spatial localization of the trapping. An example of this is seen in figure 2(a).

These rules were followed to design an efficient device that is modelled in fig3 and built in fig4:

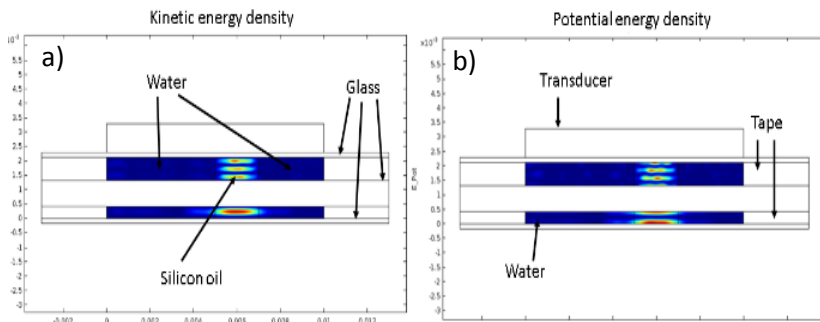


Figure 3: Model of device design. Trapping locations in the manipulation cavity are indicated by the maxima in the kinetic energy density (a) that is plotted; these coincide with the position of the control droplet. Graph (b) represent the potential energy density. The kinetic energy maxima being an attraction point and the potential energy maxima being a repelling point coming from Gorkov equation $F^{Rad} = -\nabla U$ with $U = V(f \cdot E_{pot} - 1.5 \cdot f \cdot E_{kin})$ [2].

Final design and fabrication

The device consists of a 1mm thick PZT transducer (PZT26, Ferroperm) glued on a 170 µm glass carrier layer. The control channel is formed by laser cutting a stack of 5 layers of tape, giving a thickness of 700 µm. A thick glass carrier is placed on top of it to give the device stiffness as described above, its thickness is 950 µm. The manipulation cavity is made by laser cutting 3 layers of tape (420 µm). The final reflector is a coverslip of thickness 170 µm. Fluid ports are formed by drilling 2 holes at each end of both of the thinner glass layers, and coupling them to acrylic layers to support tubing and provide extra stiffness. Manipulation results will be illustrated on the accompanying poster.

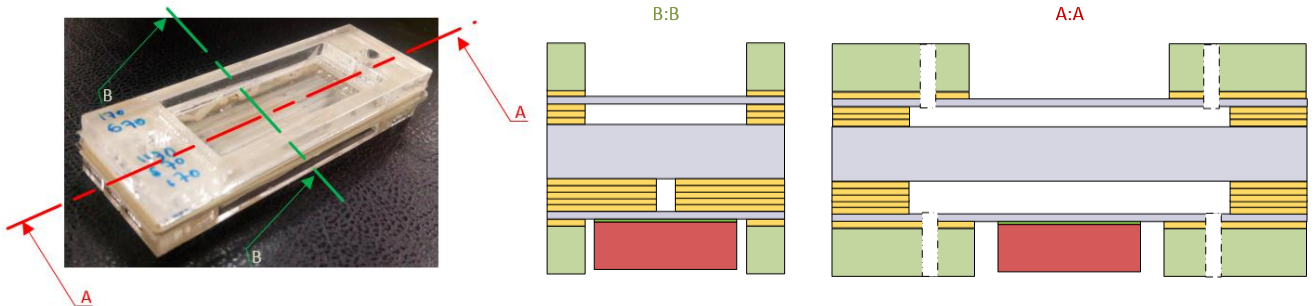


Figure 4: Schematics and picture of the final device using manufacturing techniques described above.

References

- [1] B.W Drinkwater. “Dynamic-field devices for the ultrasonic manipulation of micro particles.” 2016, 16, 2360
- [2] H. Bruus “Acoustofluidics 7: The acoustic radiation force on small particles.” Lab on a Chip, 2012, 12 1014-1021



Detection of Microsphere Surface Reaction Using Acoustic-Gravity Field

Akihisa Miyagawa¹, Makoto Harada¹, Tetsuo Okada¹

¹Department of Chemistry, Tokyo Institute of technology, Meguro-ku, Tokyo 152-8551, Japan
E-mail : miyagawa.a.aa@m.titech.ac.jp, URL : <http://www.chemistry.titech.ac.jp/~okada/index.html>

Introduction

We developed a combined acoustic-gravitational field for the separation and characterization of microspheres [1,2]. The levitation position of a particle in this field is determined by its acoustic properties such as density and compressibility but is independent of its size. If these acoustic properties are modified by a reaction that occurs on the particle surface, the levitation position of the particle changes accordingly. This principle allows us to quantify the molecules involved in the reaction. Thus, the quantity of the reactant can be determined from the position change.

Experimental

The avidin-biotin binding was examined as the model reaction. An avidin-bound polystyrene microsphere (PS) reacted with biotin-bound gold nanoparticle (AuNP). The behavior of the AuNP-coated PS (AuPS) was studied in the acoustic-gravitational field. A fused silica cell (30 mm in length, 8 mm in width, and 12.62 mm in height) with a rectangular through-channel (3.0 mm in width and 1.5 mm in height) was used. The cell wall thickness (5.56 mm) and the channel height (1.50 mm) were equal to the half-wavelengths of 500-kHz ultrasound in silica glass and water, respectively. The cell was pasted on a transducer using nail enamel as an adhesive. Because the resonance frequency depends on the instrumental setup and the experimental conditions, the ultrasound frequency was daily optimized to confirm the stable levitation of particles. The node of the standing wave was formed at the center of the channel filled with water. The AuPSs were introduced to the cell and entrapped by the standing wave. The behavior of a single AuPS was observed by a CCD camera.

Principle

According to Yoshioka and Kawasaki [3], the ultrasound radiation force imposed on a particle (F_{ac}) given by

$$F_{ac} = -\frac{8\pi}{3\lambda} r^3 E_{ac} A \sin\left(\frac{4\pi z}{\lambda}\right) \quad A = \frac{5\rho' - 2\rho}{2\rho' + \rho} - \frac{\gamma'}{\gamma} \quad (1)$$

where r is the radius of the particle; λ is the ultrasound wavelength; E_{ac} is the average ultrasound energy density; z is the distance from the node of the ultrasound standing wave (defined as the levitation position, $z = 0$ at the node); ρ and γ are the density and compressibility of medium, respectively; and the single quotation mark represents the corresponding properties of the particle

The particles in the acoustic-gravitational field simultaneously undergo the sedimentation and ultrasound radiation forces. They are levitated at the equilibrium levitation position, z , given by

$$z = \frac{\lambda}{4\pi} \sin^{-1} \left\{ \frac{(\rho - \rho')g\lambda}{AE_{ac} 2\pi} \right\} \quad (2)$$

where g is the gravitational acceleration. Eq. (2) suggests that z is a function of the particle density and compressibility but is independent of the particle size. Thus, we can recognize changes in these acoustic properties of a particle from the difference in the levitation coordinate in the acoustic-gravitational field.

Eq. (2) predicts that the levitation position of a microsphere was lowered when its density increases. In the present study, the density increase was caused by the binding of AuNPs to PSSs, as schematically shown in Fig. 1. Because the change in z is approximately proportional to the quantity of AuNPs bound on a PS, the number of AuNPs bound to it can be determined from z .

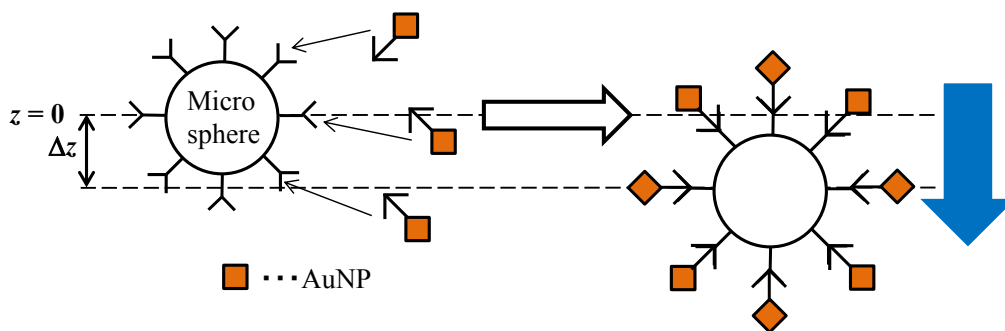


Figure 1: Schematic illustration of levitation position change by reactions between a microsphere and AuNPs.

Result and discussion

With increasing amount of AuNPs bound to the PS, z decreases mainly due to the increase in the density; a change in the compressibility plays a minor role in the determination of z . At a constant voltage (V) supplied to drive the transducer, there is a linear relationship between the number of AuNPs bound to a single PS (n) and the difference in z between AuNP-bound and unreacted PS (Δz). This levitation behavior is similar to that found for epoxide particles in our previous work [4]. Fig. 2(a) shows the images of entrapped single AuPSs with different n values. Obviously, z decreases with increasing n as predicted by Eq. (2). Fig 2(b) shows the relationship between Δz and n . At $V = 4.5$ and 5.4 V, there are linear relationships represented by $\Delta z = 1.30 \times 10^{-2} n$ and $\Delta z = 7.16 \times 10^{-3} n$. Obviously, a lower voltage gives higher sensitivity. Thus, the number of AuNPs bound on a microsphere can be quantified using the Δz values. The standard deviation for Δz was about $4 \mu\text{m}$. When 3σ is defined as the detection limit, 1000 AuNPs per PS can be detected, indicated that 1000 avidin molecules involved in the surface reaction can be detected by the present method. Although an avidin molecule binds four biotin molecules, an avidin on the PS react with one biotin-bound AuNP because AuNP is much larger than avidin and covers other binding sites of the same avidin molecule.

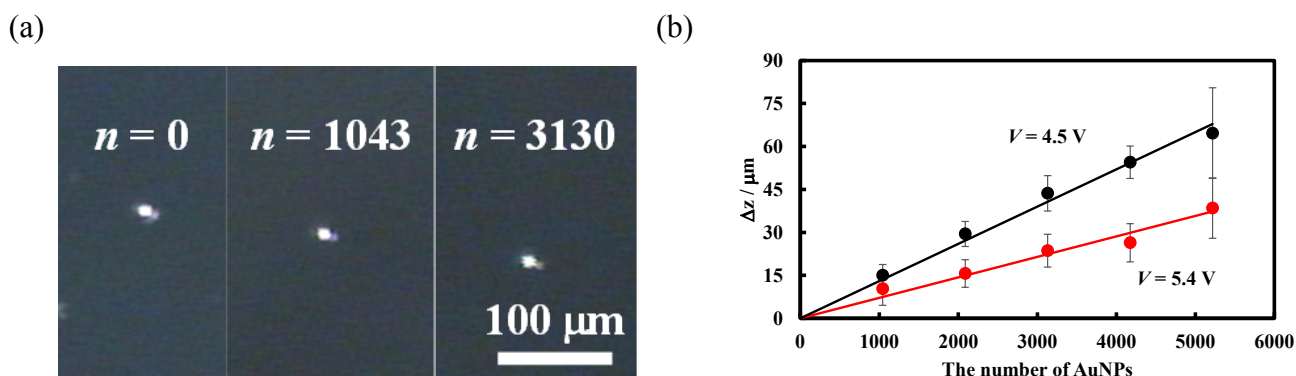


Figure 2: (a) Levitation of PS and AuPS at $V = 4.5$ V in an acoustic-gravitational field. (b) Relationship between Δz and n at different applied voltages. Measurements were repeated five times. The R^2 values for linear regression are 0.983 and 0.948 for $V = 4.5$ and 5.4 V, respectively.

Conclusion

We have demonstrated a novel principle for trace analysis using the acoustic-gravitational field. The LOD is about 1000 AuNPs per PS. This method is highly sensitive and enables zepto to yocto mole detection.

References

- [1] T. Masudo and T. Okada, *Anal. Chem.*, **73**, 3467-3471 (2001).
- [2] T. Masudo and T. Okada, *Anal. Sci.*, **20**, 753-755 (2004).
- [3] K. Yosioka and Y. Kawasima, *Acustica*, **5**, 167-173 (1955).
- [4] A. Miyagawa, Y. Inoue, M. Harada and T. Okada, *Anal. sci.*, in press (2017)



Travelling Surface Acoustic Waves for Particle Tweezing

Jia Wei Ng¹ and Citsabehsan Devendran,¹ Adrian Neild¹

¹ Laboratory for Microsystems, Department of Mechanical and Aerospace Engineering, Monash University, Clayton, Victoria 3800, Australia

E-mail: adrian.neild@monash.edu, URL: <http://www.labformicrosystems.com/>

Introduction

Particle manipulation can be achieved using bulk acoustic waves (BAW) or surface acoustic waves (SAW), both of which harness the acoustic radiation force generated by interaction of a suspended particle with an ultrasonic sound field. In the case of BAW the sound field is usually generated by exciting resonances in the fluid body, under such conditions waves reflected at the interfaces of the fluid constructively interfere creating a standing wave field the shape of which is related to the geometry of the fluid volume. In SAW systems reflections of fluid interfaces are usually weak as the fluid is typically enclosed in PDMS which has a similar acoustic impedance to water. Consequently, the standing waves required to trap particles in patterns, are produced using two separately generated counter propagating travelling waves.

Acoustic particle tweezing refers to the trapping of particles and then the subsequent movement of them by translation of the sound field. Whilst this is possible using BAW, it requires the careful suppression of reflected waves to obtain the required control over the pressure field [1]. However, SAW lends itself more naturally to this process due to the weak reflections present, displacement of the particles once trapped in a standing wave can be achieved by frequency or phase changes [2]. The result is movement of the pattern of particles created in the standing wave. A common factor in approaches to date is the use of a single excitation frequency at any moment of time. In this work, two different frequency travelling waves are excited, our analysis shows that under such conditions a standing wave is not produced, rather a single trapping location exists for the suspended particles, and this single trap's location can be altered very simply by adjusting the relative power of excitation of the two waves.

Working Principle

The acoustic radiation force exerted on a suspended particle can be found using [3]:

$$\mathbf{F}^{rad} = -\nabla U^{rad} \quad (1a)$$

$$U^{rad} = \frac{4\pi}{3} a^3 \left[f_1 \frac{1}{2} \kappa_0 \langle p_{in}^2 \rangle - f_3 \frac{3}{4} \rho_0 \langle v_{in}^2 \rangle \right] \quad (1b)$$

$$f_1(\tilde{\kappa}) = 1 - \tilde{\kappa}, \text{ with } \tilde{\kappa} = \frac{\kappa_p}{\kappa_0}; f_2(\tilde{\rho}) = \frac{2(\tilde{\rho} - 1)}{2\tilde{\rho} + 1}, \text{ with } \tilde{\rho} = \frac{\rho_p}{\rho_0} \quad (1c)$$

where U^{rad} is the acoustic potential, $\langle p_{in}^2 \rangle$ and $\langle v_{in}^2 \rangle$ are the temporal average second ordered fluid pressure and velocity at the particle's location, κ and ρ are the compressibility and density of the particle or the fluid with the subscript p or 0.

The difference in the shape of the force field generated by two counter-propagating waves is considered for two cases, that of two identical frequencies and that of two different frequencies. The pressure generated by the two counter propagating waves can be expressed as:

$$p = \rho \phi_A i \omega_a e^{i(\omega_a t - k_a x)} + \rho \phi_B i \omega_b e^{i(\omega_b t + k_b x)} \quad (2)$$

where ϕ_A and ϕ_B are the amplitudes, k_a and k_b are the wavenumbers and ω_a and ω_b are the angular frequencies. The decay of each wave is neglected in this equation. The total pressure is simply a linear summation of the pressures generated by each of the two waves. However, the forces generated are a non-linear effect, so no such superposition can be used. Once the real terms are taken, expanded out and squared, the following unwieldy expression is obtained:

$$\begin{aligned} & [\Re(p)]^2 \\ &= \rho^2 \phi_A^2 \omega_a^2 [\sin^2 \omega_a t \cos^2 k_a x + \cos^2 \omega_a t \sin^2 k_a x - 2 \sin \omega_a t \cos k_a x \cos \omega_a t \sin k_a x] \\ & \quad + \rho^2 \phi_B^2 \omega_b^2 [\sin^2 \omega_b t \cos^2 k_b x + \cos^2 \omega_b t \sin^2 k_b x - 2 \sin \omega_b t \cos k_b x \cos \omega_b t \sin k_b x] \end{aligned} \quad (3)$$

$$+2\rho^2\phi_A\phi_B\omega_a\omega_b[\sin\omega_a t \cos k_a x \sin\omega_b t \cos k_b x + \sin\omega_a t \cos k_a x \cos\omega_b t \sin k_b x - \cos\omega_a t \sin k_a x \sin\omega_b t \cos k_b x - \cos\omega_a t \sin k_a x \cos\omega_b t \sin k_b x]$$

The first square bracket expression is related to only terms related to wave a, the second to wave b, and the third to a mixture of a and b terms. When the time average is taken, it is the $\sin^2 \omega t$ and $\cos^2 \omega t$ which are non-zero and so contribute to the acoustic force. These are the first two terms in the first two of the square brackets. However, in the third square bracket, containing the mixed subscript a and b terms, the time average depends on whether $\omega_a = \omega_b$. If this is the case, then the first and final terms in the third square bracket contributes to the acoustic radiation force, and the expression can be reduced to $\langle p^2 \rangle = 2\rho^2\phi^2\omega^2 \cos^2 kx$, which predicts a periodicity in the particle patterning which aligns with the periodicity of the standing wave which is produced. However, if the frequencies are not equal, then none of the terms in the third square brackets are non-zero. This means that despite the non-linearity of the acoustic radiation force, the total value of $\langle p^2 \rangle$ is simple the summation of the $\langle p^2 \rangle$ of each individual wave. As the same can be shown for $\langle v^2 \rangle$ the total force is simply the summation of the force generated by the two individual travelling waves. In the case of equation 3, in which no decay is included in the strength of the travelling wave, the total force will be zero as an equal and opposite force is generated from each of the counter-propagating waves, if, however, decay is included a single collection location is achieved at the location at which the forces generated from each of the two waves equate. Under such a scenario, the location of this single trap location can be moved by adjusting the relative amplitude of the two waves.

Experimental Results

An experimental demonstration of the use of two different frequency travelling waves, each decaying due to attenuation of the surface wave as energy is coupled into the fluid, is shown in figure 1. With a comparison of the standing surface acoustic waves (SSAW) and decaying opposing travelling surface acoustic waves (DOTSAW), as well as the trajectory control via altering the relative amplitude of the two waves.

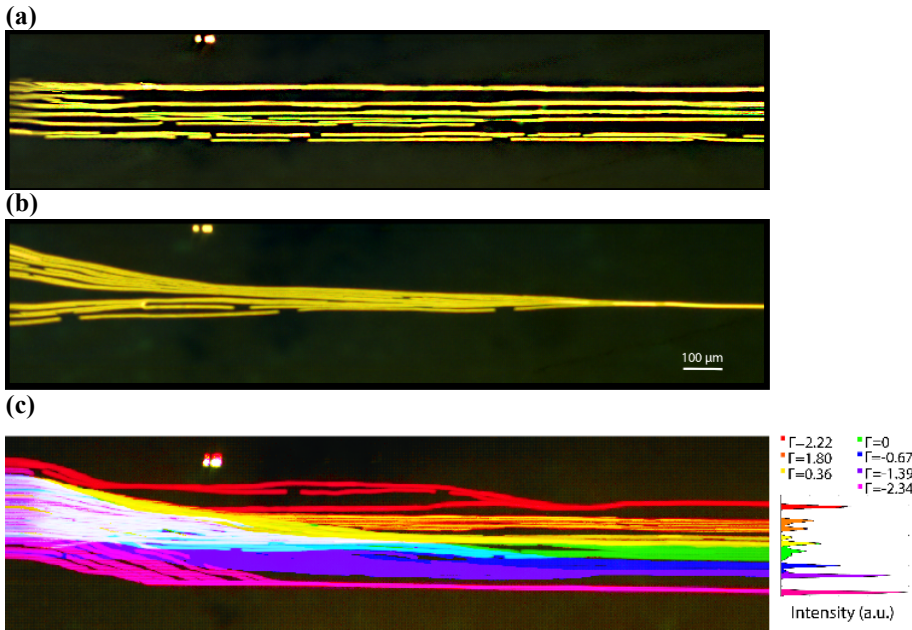


Figure 1: Stacked images of particle trajectories from experiments. (a) SSAW field; where multiple equidistant particle trapping location can be seen in a field generated by two counter-propagating waves of equal frequency. (b) DOTSAW field; where particles are focused to the channel center, in a file generated by decaying, opposing travelling waves of two different frequencies. (c) The trajectories of particles within DOTSAW fields with different relative wave amplitudes, each colour coming from a different experiment.

Conclusion

The use of two different frequency counter-propagating travelling waves has been shown to produce a force field distinctly different to that generated in a standing wave excited when identical frequencies are used. As a result of the properties of this type of excitation, the DOTSAW system can trap particles in a single location, and that location can be displaced via alteration of the relative amplitudes of the two waves.

References

- [1] C. R. P. Courtney, C. E. M. Demore, H. Wu, A. Grinenko, P. D. Wilcox, S. Cochran and B. W. Drinkwater, *Applied Physics Letters*, **104**, 154103 (2014).
- [2] F. Guo, Z. Mao, Y. Chen, Z. Xie, J. P. Lata, P. Li, L. Ren, J. Liu, J. Yang, M. Dao, S. Suresh and T. J. Huang, *Proceedings of the National Academy of Sciences*, **113**, 1522-1527 (2016).
- [3] H. Bruus, *Lab on a Chip*, **12**, 1014-1021 (2012).



***In situ* temperature monitoring during acoustophoresis using integrated thin film Pt temperature sensors**

Mathias Ohlin¹, Martin Andersson¹, Lena Klintberg¹, Klas Hjort¹, Maria Tenje^{1,2}

¹ Department of Engineering Sciences, Uppsala University, Sweden

² Science for Life Laboratory, Uppsala University, Sweden

E-mail: mathias.ohlin@angstrom.uu.se, URL: <http://www.teknik.uu.se/microsystems-technology/>

Introduction

In this paper we present an acoustophoretic system with internal temperature sensing that enables *in situ* and local temperature monitoring during operation.

The main source of heat in any acoustophoretic systems is the ultrasound generating transducer. Here the heat is generated due to electromechanical losses in the piezoelectrical material and heat losses in the glue layers connecting the transducer to the system. Acoustic absorption by which mechanical energy is converted into heat is rather low in acoustophoretic systems due to the often low-loss materials used such as silicon and glass [1,2] and the 1–10 MHz typically used for acoustophoresis [3]. Nevertheless, temperature elevation in acoustophoretic systems is a problem as the generated heat may be conducted to the fluid and in turn to the cells causing a thermal bio-effect [3]. To measure the temperature of the system the most common solution is to have an external temperature probe [4]. However, the temperature inside the system may differ from the externally measured one with uncounted biological side effects.

We have previously demonstrated fabrication of thin film metal sensors in glass chips [5]. In this paper, we integrate these thin metal film sensors for internal temperature sensing of the fluid in an acoustophoretic glass chip while demonstrating continuous acoustophoresis of *E. coli* bacteria.

Experimental

The experimental setup, Fig. 1, consists of the microfluidic glass chip with internal temperature sensing, a 2.5 MHz PZT transducer glued to the top glass surface using cyanoacrylate adhesive, and an external K-type thermocouple mounted on the glass top surface using thermal conducting paste, Fig. 1(a). The transducer was driven in frequency modulation saw tooth mode at 10 V_{pp} with center frequency 2.5 MHz and a span of 200 kHz with a rate of 1 kHz generating bulk acoustic waves. The channel has a semi-circular cross-section with a depth of 160 μm and a width of 360 μm, the channel is open to the sides of the chip allowing for fluid connection via glued glass capillaries. Due to the semi-circular design, an effect of the isotropic wet-etch fabrication process, the actuation frequency (2.5 MHz) was set to match a half-standing-wave for a channel width of 300 μm placing the pressure nodal-line approx. in the middle of the channel, both vertically and horizontally. The microfluidic chip was manufactured by structuring two borosilicate glass wafers, having metal electrodes on one side and etched channels on the other [5,6]. The Pt electrodes, Fig. 1(a):4, were deposited by a lift-off process on one of the wafers. Both the trenches for the electrodes and the microfluidic channels were fabricated using UV-lithography and isotropic wet-etching with HF. Glass bonding of the two wafers was done by heat treatment at 625 °C for 6 h.

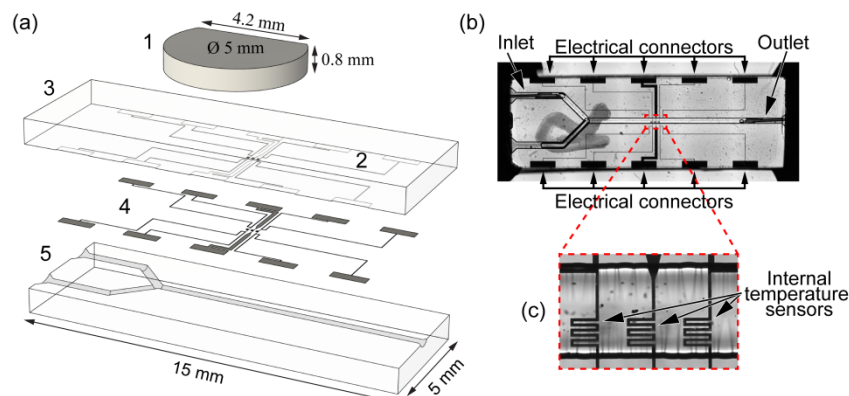


Figure 1: (a) Exploded view of the system: (1) transducer, (2) location of the external thermocouple, (3) structured glass wafer for the internal thin film metal sensors, (4) internal thin film metal Pt sensor elements, and (5) structured glass wafer containing the microfluidic channels. (b) Photo of the glass chip. (c) Inset showing the internal thin film metal Pt sensors exposed to the fluid within the channel.

The leftmost internal temperature sensors element was connected in a 4-point configuration in order to give a localized measurement of the resistance, Fig. 1(c), measured using a data acquisition control unit (cDAQ-9178 and NI-9219, National Instruments) and LabView. Acoustophoresis of *E. coli* bacteria was performed in six consecutive repetitions. During all repetitions both the internal temperature of the fluid filled channel measured by the Pt sensor and the external temperature of the chip glass surface measured by the thermocouple were logged using LabView. Bright field microscopy was applied with a 20x/0.45 objective and each experiment started with injection of *E. coli* bacteria suspended in growth LB-media, by manually compressing the syringe creating a slowly decreasing flow in the channel, passing by the internal temperature sensor, directed towards the outlet. Next, when a steady state temperature of the system was reached, the ultrasonic transducer was activated focusing the bacteria by the acoustic radiation force towards the pressure nodal-line in the center of the channel. Once the temperatures of both the internal Pt sensor and that of the external thermocouple had reached steady state the ultrasonic transducer was deactivated and the experiment was repeated.

Results

Figure 2(a) shows acoustophoresis of *E. coli* bacteria in the microfluidic channel in close vicinity to the Pt temperature sensor. Here, only the leftmost Pt temperature sensor element is active. With a transducer frequency of 2.5 MHz driven in frequency modulation mode the bacteria are focused in the center of the channel.

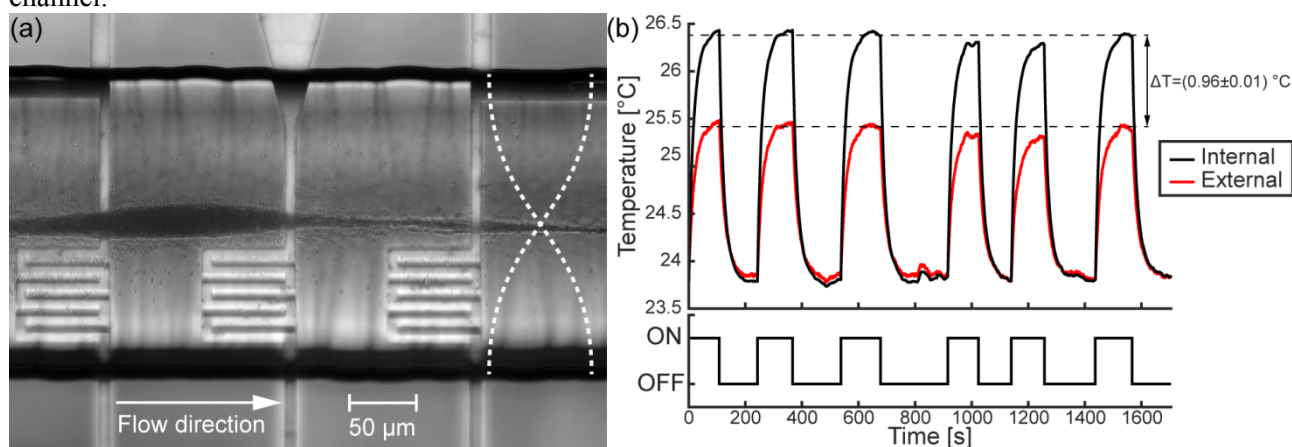


Figure 2: (a) Acoustophoresis of *E. coli* during temperature measurements. Here, the white dashed standing half-wave symbolizes the acoustophoretic effect resulting in a single pressure nodal-line in the center of the channel. (b) Internal and external temperature measurements during acoustophoresis of *E. coli*, six repetitions.

The internal temperature of the fluid filled channel measured by the Pt sensor and the external glass surface temperature measured by the thermocouple are plotted in Fig. 2(b). The temperature difference between the internal and external sensors was in the order of one degree Celsius for this system. It depends on both the material properties of the chip, here glass, as well as on the location of the two sensors relative to the heat generating transducer. There was a slight misalignment of the Pt temperature sensor relative to the channel centerline, approx. 100 μm . However, as with acoustophoresis and the fluid flow, any temperature deviation within the channel based on the misalignment is assumed to be negligible.

Conclusion

We have shown internal temperature sensing in an acoustophoretic glass system by using an integrated resistive Pt sensor element exposed to the fluid within. The performance of the internal temperature sensor was evaluated and found comparable to a normal K-type thermocouple. The 1 $^{\circ}\text{C}$ higher temperature that was measured in the channel can be of significant importance in biological assays, in which precise temperature control is often needed. Furthermore, the Pt sensor increases repeatability since the temperature of the external thermocouple depends on its placement relative the transducer and microfluidic channel.

Acknowledgements

Financial support is provided by Uppsala University, The Swedish Research Council and The Crafoord Foundation. The Knut and Alice Wallenberg foundation is acknowledged for funding the laboratory. The authors would like to thank Mats Walldén for the help and supply of the bacteria.

References

- [1] Evander, M., et al., *Anal. Chem.*, 2008. **80**(13): p. 5178.
- [2] Petersson, F., et al., *Anal. Chem.*, 2007. **79**(14): p. 5117.
- [3] Wiklund, M., *LOC*, 2012. **12**(11): p. 2018.
- [4] Augustsson, P., et al., *LOC*, 2011. **11**(24): p. 4152.
- [5] Andersson, M., et al., *JMM*, 2017. **27**(1): p. 015018.
- [6] Andersson, M., et al., *JMM*, 2016. **26**(9): p. 095009.



Analysis of ultrasound induced multi-cellular tumor spheroids by high throughput imaging

K. Olofsson¹, V. Carannate², K. Kushiro³, M. Takai³, A. Lundquist⁴, B. Önfelt^{1,2} and M. Wiklund¹

E-mail: karl.olofsson@biox.kth.se, URL: <https://www.aphys.kth.se/groups/biox>

¹Department of Applied Physics, KTH Royal Institute of Technology, Stockholm, SWEDEN

²Department of Microbiology, Tumor and Cellbiology, Karolinska Institutet, Stockholm, SWEDEN

³Department of Bioengineering, The University of Tokyo, Tokyo, JAPAN

⁴Department of Oncology-Pathology, Karolinska Institutet, Stockholm, SWEDEN

Summary

We have previously presented an ultrasonic standing wave (USW) 3D culture platform enabling parallel production, staining and processing of 100 uniformly sized multi-cellular tumor spheroids (MCTS) [1]. Here, we use the system for analysis of HepG2 and A498 renal carcinoma MCTS by on-chip automatic image analysis methods based on bright field and 3D confocal microscopy images.

Introduction

Tissue micro-engineering is important for modelling 3D biological structures to bridge the gap between *in vivo* and *in vitro* in cellular and pharmaceutical research. Regular 2D *in vitro* cell cultures do not reproduce the complex 3D micro-environment of cells, extra cellular matrix and soluble factors which governs cell behaviour and tissue function [2]. Recently, many MCTS culture methods has been developed based on either anchored-dependent (e.g. scaffolds) or anchored-independent (e.g. hanging drop, low-attachment surfaces) strategies [3] but many of them does not address the challenges of detailed imaging and overcoming MCTS light scattering in a high throughput manner [4].

In a previous study we presented an USW 3D culture platform where immunotherapy of adherent HepG2 MCTS were studied [1]. We further developed this platform with a protein repellent polymer coating (described in [5]) to produce un-anchored HepG2 MCTS [6] (Fig. 1). In this paper, we demonstrate culture and analysis of a more relevant A498 renal carcinoma MCTS by a novel on-chip automatic cell count estimation script. We also show a MCTS characterisation script based on bright field images of HepG2 MCTS formed in the multi-well microplate.

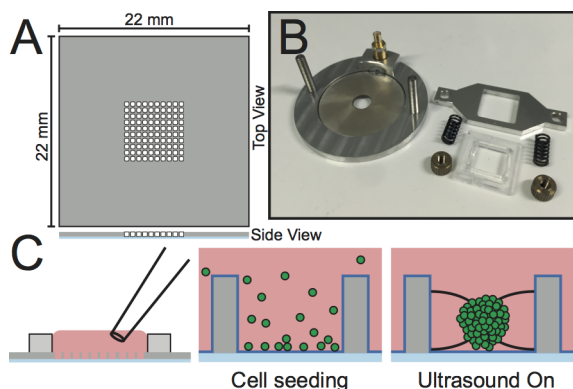


Figure 1: The silicon multi-well microplate is etched with 100 micro-wells ($350\ \mu\text{m} \times 350\ \mu\text{m}$, $300\ \mu\text{m}$ deep), bonded to a glass plate (A) and mounted onto the transducers (B) by clamping it with a frame. To produce spheroids, a single cell suspension is seeded into the multi-well microplate reservoir with a standard pipette and the cells sediment into the micro-wells (C). A protein repellent polymer coating (blue line) prevents cell adhesion to the micro-well. When the piezo ceramic disk is actuated with frequency modulation ($2,47\ \text{MHz} \pm 50\ \text{kHz}$ at $1\ \text{kHz}$ sweep rate) the ultrasonic radiation forces, originating from USW, focus the seeded cells into all 100 micro-well centers. Spheroids are then formed when incubated during continuous ultrasonic force focusing for 24 h.

MCTS characterization and analysis

The in-house developed MCTS characterization script based on bright field transmission microscopy images is able to find and label all micro-wells before binary segmentation and analysis of MCTS residing in the bottom of each micro-well. This allows for characterisation of living MCTS with high temporal resolution where e.g. growth and defragmentation can be assessed without staining. The script was tested on HepG2 MCTS where we compared spheroid formation with and without protein repellent coating and found a more compact and consistent MCTS formation in coated microplates compared to un-coated microplates (Fig. 2).

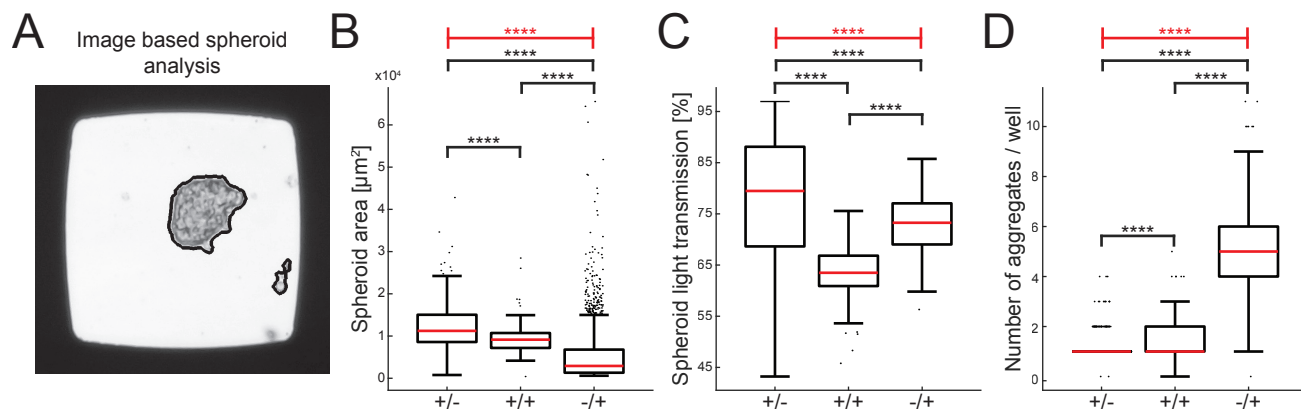


Figure 2: Bright field images of HepG2 spheroids where captured and analysed with an in-house developed MATLAB script (A) where the black line shows the found spheroid. Data of spheroid area (B), light transmission through the spheroids (C) and number of aggregates per well (D) is shown in the boxplots for spheroids produced under three different conditions; 24h active + 24h passive culture in an uncoated microplate (+/-), 24h active culture + 24h passive culture in a coated microplate (+/+) and 48h of passive culture in a coated microplate (-/+). In the plots, the boxes indicates the 25th and 75th percentiles with a red line marking the median. The whiskers shows the furthest observation that is less than 1.5 times the interquartile range away from the box edge and outliers are marked with a black dot. The horizontal red lines and stars indicates the overall significance of the three sets of data in each plot determined by the Kruskal-Wallis test (****; $p > 0.0001$). The horizontal black lines and stars indicates the pairwise significance between sets of data determined by the Mann-Whitney U test.

Single cell analysis

To overcome the MCTS light scatter and allow for deep tissue imaging, a Histodenz based refractive index matching solution (RIMS) protocol was developed where all MCTS are treated simultaneously while being retained in the micro-wells. Detailed confocal z-stacks of whole MCTS were acquired on-chip and an automatic cell count estimation script was developed where the sectioning step along the z-axis can be varied. Tests against manual counting in seven A498 MCTS z-stacks demonstrates that an accurate estimation was possible up to 5 μm sectioning step, hence indicating 5 times faster z-stack acquisition can be achieved compared to the optimal sectioning step 1 μm (Fig. 3).

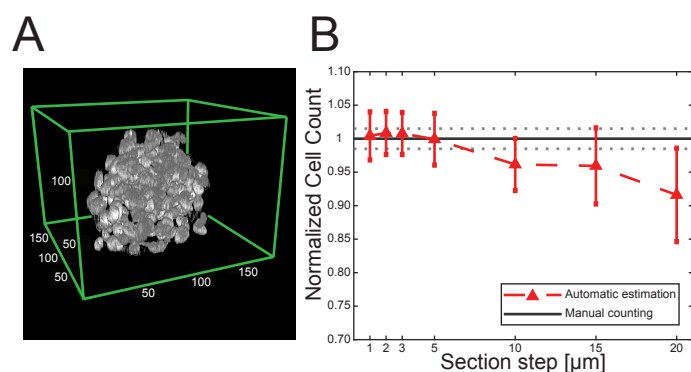


Figure 3: Spheroids of A498 renal carcinoma cells (24 h active + 24 h passive) were stained with Hoechst 33342, fixed in 4 % PFA, and treated with RIMS (3D rendering (A)). Z-stacks of seven A498 spheroids were used to test the spheroid cell number estimation script where the sectioning between the images can be varied. The number of cells in the spheroids were manually counted (147, 246, 183, 254, 216, 228 and 189 cells), normalised (solid black) and compared to the normalised automatic cell number estimation (red triangles, bar = standard deviation) with different sectioning step in the z-stack (B).

Conclusion

In summary, we have shown formation of A498 renal carcinoma MCTS through USW trapping and developed analysis methods to acquire data from a single cell level to a spheroid level which allows for high throughput analysis for e.g. drug development and immunotherapy research.

References

- [1] A. E. Christakou, M. Ohlin, B. Önfelt, M. Wiklund. *Lab Chip* **15**, 3222-3231 (2015).
- [2] C. J. Lovitt, T. B. Shelper, V. M. Avery. *Biology* **3**, 345-367 (2014).
- [3] C. R. Thoma, M. Zimmermann, I. Agarkova, J. Kelm, W. Krek, *Advanced Drug Delivery Reviews*, **69-70**, 29-41 (2014)
- [4] S. Nath, G. R. Navi, *Pharmacology & Therapeutics* **163**, 94-108 (2016)
- [5] K. Nagahashi, Y. Teramura, M. Takai. *Colloids Surf B Biointerfaces* **134**, 384-391 (2015).
- [6] K. Olofsson, V. Carannante, T. Frisk, K. Kushiro, M. Takai, B. Önfelt, M. Wiklund, *The 20th International Conference on Miniaturized Systems for Chemistry and Life Sciences*, Dublin, p. 409-410 (2016)



Refocusing focused surface acoustic waves.

Richard O'Rorke¹, David Collins¹ and Ye Ai¹.

¹ Singapore University of Technology and Design, 8 Somapah Road, Singapore, 487372.

E-mail: richard_ororke@sutd.edu.sg, URL: http://people.sutd.edu.sg/~ye_ai/

Introduction

In most acoustofluidic systems the acoustic field extends many wavelengths, meaning many particles are manipulated concurrently^{1,2}. Whilst useful in some applications, this has limited use in single cell manipulation. Instead, there is a growing interest in localising acoustic fields to a single acoustic trap^{3,4}. Focused surface acoustic waves show promise in this regard, as the acoustic beam can be constrained to several wavelengths, allowing single cell manipulation².

By analogy to optical lenses, focused IDTs are characterised by a focal length; however, in practice the focal length differs from the geometric focal length. Consequently, imaging of the SAW field is required to determine focal length and thus channel placement. Focus offset also complicates the design of focused standing waves, which may prove useful sources for single cell traps.

Here, we use finite element simulations of focused SAWs (COMSOL Multiphysics) – validated by experimental laser doppler vibrometry (data not shown) – to highlight the role of crystal anisotropy in focus offset. We then correct for this by tuning the pitch of the focused IDTs according to the acoustic velocity.

Numerical modelling

For a concentric ring IDT, the resonant frequency will change across the aperture according to the acoustic velocity in the direction normal to the IDT. When excited at a single frequency only a fraction of the IDT will resonate, which changes the effective focal length. In contrast, tuning the IDT pitch to the local acoustic velocity allows the entire IDT to resonate at a single frequency. The acoustic velocity for 128-YX lithium niobate was determined using an Eigenfrequency analysis and is plotted in Figure 1 (a); these values are consistent with literature values⁵. The IDT pitch was then tuned to have a common resonant frequency. Correcting for the anisotropic acoustic velocity in this way restores the focal length to the geometric focal length, as shown in Figure 1 (b-c).

With a predictable focal length, multiple sets of IDTs can be combined to generate highly focused standing wave fields. As an example, we show a 2D standing wave generated using two orthogonal pairs of tuned IDTs. The highly localised standing SAW field is shown in Figure 2.

Conclusion

A finite element model of a focused SAW has been presented, and is consistent with LDV scans of a comparable SAW device. We have shown that anisotropic acoustic velocity is the cause of focus offset in such devices, which can be avoided by tuning the local pitch of the IDT. This facilitates the incorporation of focused SAWs with microfluidic channels and waveguiding features for single cell manipulation, without the need for prior characterisation of the SAW field. As an example application, we show the formation of a highly localised standing SAW field, formed by the convergence of four focused SAWs on a common focal point.

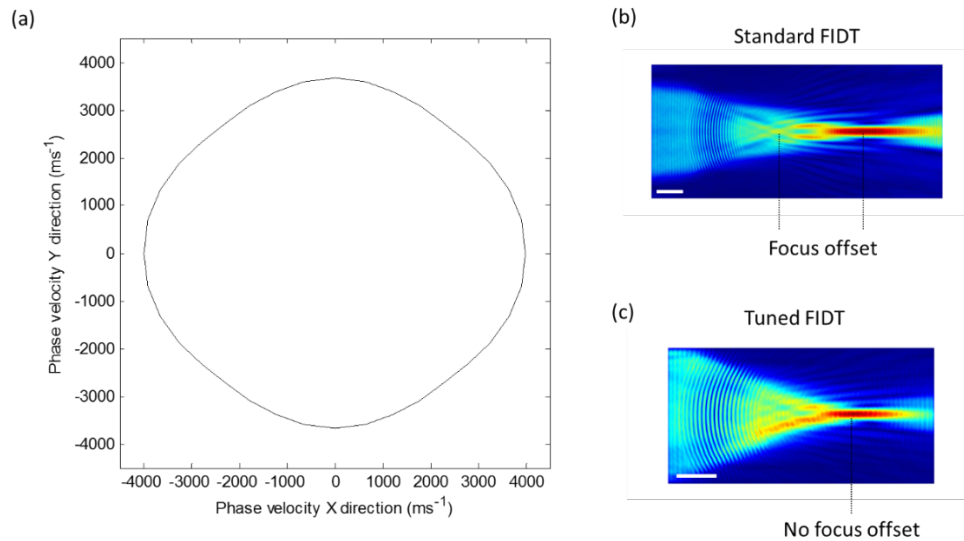


Figure 1. (a) Polar plot of phase velocity vs propagation direction from the crystallographic x axis for 128-YX lithium niobate, determined from FEM analysis. RMS time-averaged surface-normal displacement of a SAW emanating from a concentric ring (b) and tuned (c) FIDT on 128-YX lithium niobate. The scale bars in each image are 100 μm .

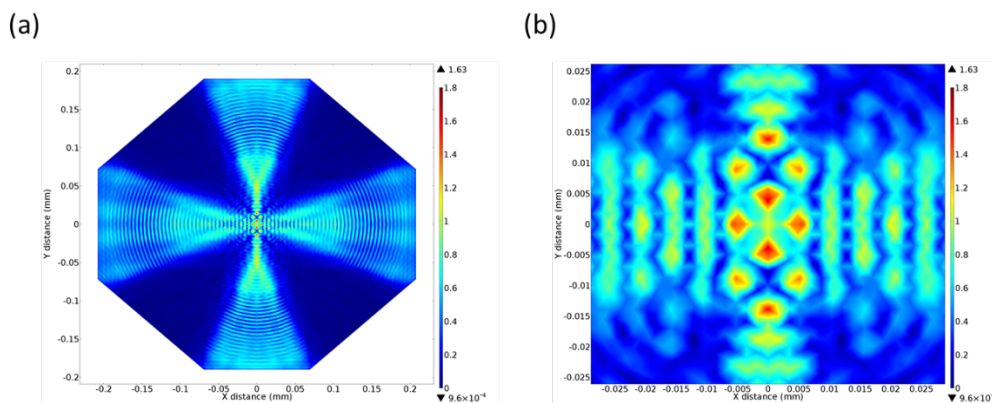


Figure 2. Surface plots of time-averaged (rms) surface normal displacement field for standing waves in the X and Y directions that are (a,b) in phase, and (c,d) $\pi/2$ out-of-phase. The incident waves converge upon the geometric focal point.

References

1. Wood, C. D. *et al.* Formation and manipulation of two-dimensional arrays of micron-scale particles in microfluidic systems by surface acoustic waves. *Appl. Phys. Lett.* **94**, (2009).
2. Collins, D. J., Ma, Z. & Ai, Y. Highly Localized Acoustic Streaming and Size-Selective Submicrometer Particle Concentration Using High Frequency Microscale Focused Acoustic Fields. *Anal. Chem.* **88**, 5513–5522 (2016).
3. Riaud, A., Baudoin, M., Matar, O. B., Becerra, L. & Thomas, J. Selective manipulation of microscopic particles with Precursor Swirling Rayleigh waves. **24007**, 2–6 (2016).
4. Hwang, J. Y. *et al.* Cell Deformation by Single-beam Acoustic Trapping : A Promising Tool for Measurements of Cell Mechanics. *Nat. Publ. Gr.* 1–8 (2016). doi:10.1038/srep27238
5. Holm, A., Stürzer, Q., Xu, Y. & Weigel, R. Investigation of surface acoustic waves on LiNbO₃, quartz, and LiTaO₃ by laser probing. *Microelectron. Eng.* **31**, 123–127 (1996).

Simulation-driven design of waveguides for single cell acoustic traps

Richard O’Rorke¹, David Collins¹ and Ye Ai¹.

¹ Singapore University of Technology and Design, 8 Somapah Road, Singapore, 487372.

E-mail: richard_ororke@sutd.edu.sg, URL: http://people.sutd.edu.sg/~ye_ai/

Introduction

There is growing interest in local confinement of acoustic fields for single cell manipulation^{1,2}. Acoustic waveguides have the potential to shape the acoustic field arising from surface acoustic wave (SAW) liquid interactions towards this end. The design of such waveguides can be accelerated by computational modelling, and fully coupled finite elements analysis is the typical approach for such studies^{3,4}. Such numerical modelling comes at a computational and financial expense, especially for geometry optimisation. We have developed an analytical model of the pressure in a liquid based on the propagation of spherical pressure waves, for which a range of waveguide geometry and SAW boundary conditions can be applied.

Analytical model

A fluid channel is discretised into pixel grids in the XY, XZ and YZ planes. The pressure at each pixel is given by the sum of spherical pressure waves propagating from each pixel on the fluid-substrate interface, as illustrated in Figure 1. Boundary conditions can be set for travelling and standing SAWs in one and two directions, according to Neild *et al*⁵. An acoustically-thin waveguide is considered by including only spherical waves emanating from pixels contained within the waveguide.

The pressure at point (x,y) on the evaluation plane at time t is equal to the pressure at point (x_i, y_i) at the interface at time $t - \frac{R}{v_l}$, where v_l is the acoustic velocity in the liquid and R is the distance between the two points. To account for the decreasing intensity of a spherical wave with R and normalise spherical wave amplitudes to unity at the interface the pressure is scaled by $(R + 1)^{-1}$. The total pressure, $P(x,y,t)$, is thus given by:

$$P(x, y, t) = \sum (R + 1)^{-1} P_s \left(x_i, y_i, t - \frac{R}{v_l} \right)$$

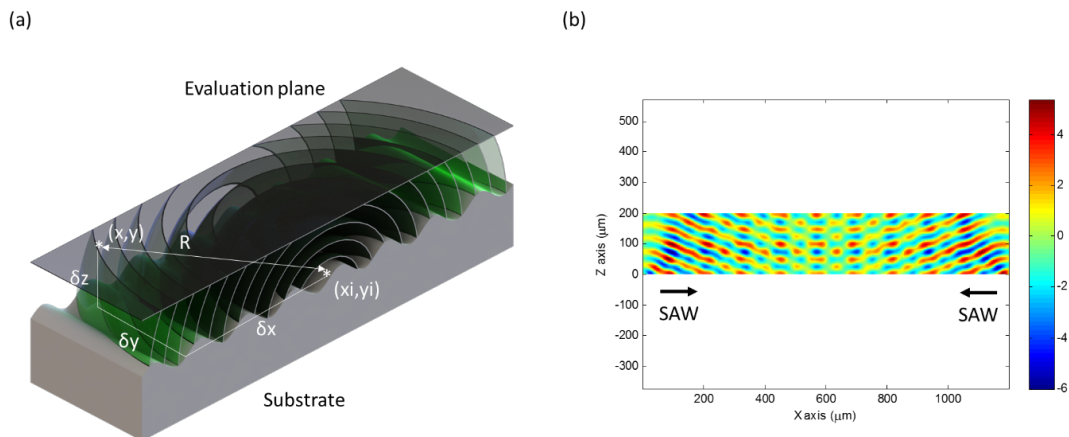


Figure 1. (a) Schematic of spherical waves (green) propagating a distance R from point (x_i, y_i) on the fluid-substrate interface to point (x, y) on the evaluation plane (grey). (b) Cross-section view of acoustic field in a liquid channel at a single time-point for two incident SAWs, using the boundary conditions given by Neild *et al*⁵.

Results

The acoustic field in a PDMS microchannel for two opposing SAWs (without a waveguide) is shown in Figure 1 (b), and is consistent with previous studies and our own fully coupled finite element models³. We then investigated waveguiding pillars with diameters in the sub-wavelength and wavelength size range. The time-averaged acoustic fields in a PDMS channel are shown in Figure 2 (a-d) for a 1D standing SAW, with a pressure node located at the centre of the waveguide. Whilst giving intricate 2D patterns, these structures did not lead to the anticipated single acoustic trap. Instead, a travelling SAW interacting with a pillar waveguide gave the single acoustic trap shown in Figure 2 (e).

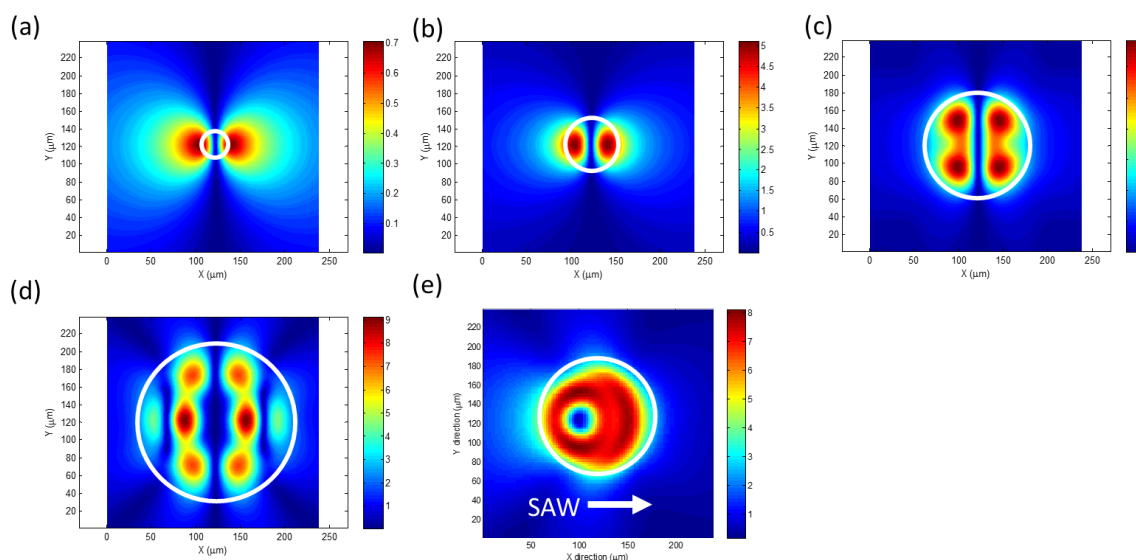


Figure 2. Time-averaged (rms) pressure fields $10\mu\text{m}$ above a waveguide in a $20\text{-}\mu\text{m}$ -deep PDMS microchannel. Pillar waveguides (highlighted in white) have diameters (a) $\lambda/4$, (b) $\lambda/2$, (c) λ , and (d) $3\lambda/4$ for a standing surface acoustic wave in X. A waveguide with diameter equal to λ is shown in (e) for a travelling SAW in the X direction.

Conclusion

We have developed a rapid analytical approach to deduce the acoustic field in a microchannel arising from SAW coupling, which enables the design of acoustic waveguides. Using this model, we have identified a waveguide and SAW field that allows a single acoustic trap, located directly above the waveguide that may be used for acoustic tweezing of single cells.

References

1. Riaud, A., Baudoin, M., Matar, O. B., Becerra, L. & Thomas, J. Selective manipulation of microscopic particles with Precursor Swirling Rayleigh waves. **24007**, 2–6 (2016).
2. Collins, D. J., Neild, A. & Ai, Y. Highly focused high-frequency travelling surface acoustic waves (SAW) for rapid single-particle sorting. *Lab Chip* **16**, 471–479 (2015).
3. Guo, J., Kang, Y. & Ai, Y. Radiation dominated acoustophoresis driven by surface acoustic waves. *J. Colloid Interface Sci.* **455**, 203–211 (2015).
4. Tan, M. K., Friend, J. R., Matar, O. K. & Yeo, L. Y. Capillary wave motion excited by high frequency surface acoustic waves. *Phys. Fluids* **22**, (2010).
5. Devendran, C., Albrecht, T., Brenker, J., Alan, T. & Neild, A. The importance of travelling wave components in standing surface acoustic wave (SSAW) systems. *Lab Chip* **16**, 3756–3766 (2016).



Investigation of Piezoelectric Actuator Performance for Acoustophoresis Applications

Mehmet Bülent Özer¹, Mehmet Akif Şahin¹, Begüm Beril İncecik¹, Barbaros Çetin², Z. Gökür Bükü³

¹Mechanical Engineering Department, TOBB University of Economics and Technology, Ankara, Turkey
E-mail: mozer@etu.edu.tr

²Microfluidics & Lab-on-a-chip Research Group, Mech. Eng. Dept., I.D. Bilkent University, Ankara, Turkey

³Material Science and Nanotechnology Department, TOBB University of Economics and Technology, Ankara, Turkey

Introduction

In recent years, acoustophoresis has been increasingly used for separation of cell populations. Demonstrated applicability of acoustophoresis on blood component separation and rare cell separation is promising for several applications in medicine such as plasmapheresis, thrombocytapheresis and separation of circulating tumor cells [1-3]. Such medical procedures require the separation method to be economic and high throughput with disposable components that are suitable for high volume manufacturability [4].

Requirement for high volume manufacturability and low cost push the material selection towards polymers for chip material even though they are known to have poor acoustic properties compared to commonly used materials in acoustophoresis such as silicon. Hence the overcome the adverse acoustic properties of polymers, piezoelectric actuator should be high performance. High throughput requirement promotes the applicability of acoustophoresis in larger channels (channel width in the order of millimeters) rather than micrometers. In order to setup a resonance condition at larger channel fundamental resonance frequency of the piezoelectric material should be low. Most studies in literature use resonance at 2-3 MHz which results in channel width of couple of hundred micrometer channels. Moreover, acoustic separation would be most efficient if the acoustic resonance conditions in the piezoelectric actuator, chip material and resonance inside the channel occurs at the same frequency. Due to uncertainties in the resonance frequencies of these components, this coincident resonance of all components is rather difficult to achieve. Therefore, it is desirable to be able to shift the resonance frequency of the piezoelectric material so that resonance frequency of the piezoelectric material can be tuned to chip and the channel resonance frequencies. In this study, vibration performance of different types and geometries of piezoelectric materials are tested and the effect of a series inductor to a piezoelectric element is investigated.

Materials and Experimental Set-up

A test setup is built for measuring the thickness mode vibrations of different piezoelectric materials. As shown in Fig.1, the piezoelectric material (4) is placed on the testing platform. Laser Doppler Vibrometer (LDV) (3) is attached to a linear translation platform. Vibration signal measured by the LDV and band limited white noise signal from the amplifier is sent to NI VirtualBench (6). Frequency response between the applied voltage and the vibration along the thickness mode of the piezoelectric material is calculated with a LABVIEW code. Tested piezoelectric materials are from Steminc Corp. USA two PZT 4 rectangular plates (20x15x1 mm and 20x15x3 mm) with resonances of 2 MHz and 700 kHz, from Eksen İleri Technologies, Turkey, PZT 4 with a disk shape (15 mm diameter and 1 mm thickness) with 2 MHz resonance, from Piezo Systems Inc., USA PZT-5A rectangular plate (25x10x1 mm) with 2 MHz resonance, from TRS Technologies Inc., USA PMN-PT rectangular plate(30x20x1 mm) with 2 MHz resonance and FerroPerm A/S, Denmark, PZ 26 rectangular plate (25x10x1 mm) with 2 MHz resonance. Also, an inductor 1 μ H inductor is connected in series to the 2 MHz PZT 4 piezoelectric plate from Steminc Corp. The frequency response with and without the inductor across the piezoelectric material is measured with the same set-up.

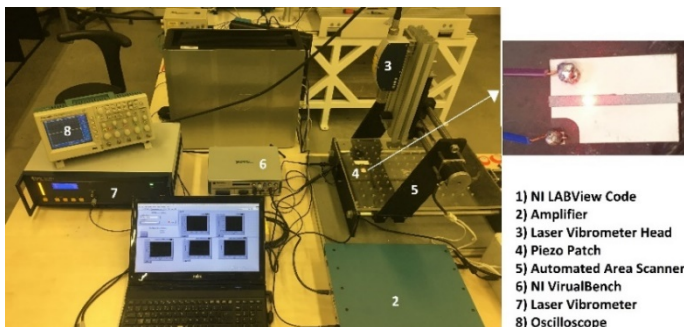


Figure 1: Test set-up for vibration testing of piezoelectric materials.

Results

The test results of the piezoelectric materials are shown in Fig. 2. For a unit voltage input, the highest amplitude of velocity is observed on the PZT-4 material with 700 kHz resonance frequency. The low resonance frequency material (700 kHz resonance) shows largest as well as the sharpest resonance peak. This result is rather promising for creating resonances in larger channels. Lowest amplitude oscillation is observed on PZT-5A material. PZT-5A is known to have better piezoelectric constants than PZT 4. However, since the material and dielectric losses are higher, it resulted in low amplitude vibrations. PZ 26 (which is similar to PZT 4) showed the highest vibration velocity in 2 MHz resonance actuators. Single crystalline piezoelectric material PMN-PT showed a rather wide resonance bandwidth which can be favorable for creating resonance at different frequencies. Also, the resonance frequency of 2 MHz actuators (5 different 2 MHz piezoelectric are tested) have more than 5% spread from the target value. This spread causes difficulty in matching the piezoelectric material resonance with the chip and channel resonance frequencies. An inductor of 1 μ H is connected to 2 MHz Steminc. Corp. PZT 4 in series and the amplifier is connected across the circuit. The frequency response plots before and after the connection of the inductor are shown in Figure 3. Approximately, 10% shift in the resonance frequency can be observed. Ability to shift the piezoelectric resonance using inductors in series can be advantageous for coinciding the resonance frequencies of the piezoelectric material, chip material and the channel.

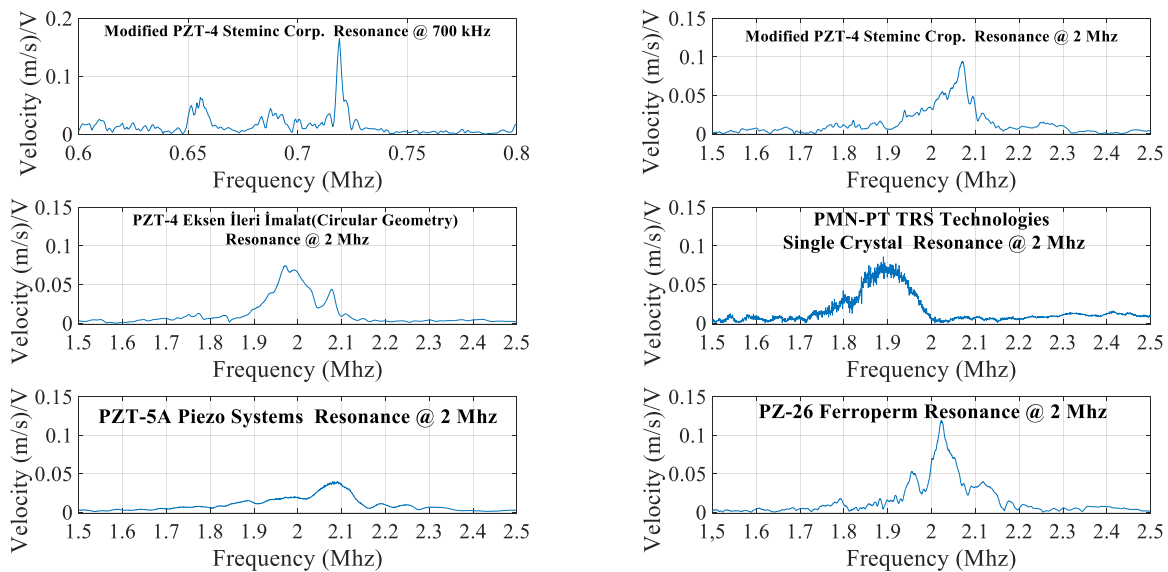


Figure 2. Thickness mode vibrations amplitudes per supplied voltage from the amplifiers for different piezoelectric material types and brands.

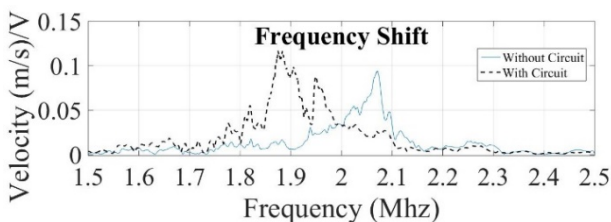


Figure 3. Shifted resonance frequency of Modified PZT 4 material from Steminc Corp. using an inductor of 1 μ H in series with the PZT.

Conclusion

We have tested different piezoelectric materials with target thickness resonance frequencies of 2 MHz (typically used frequency in acoustophoresis applications). It is observed that there is more than 5 % deviation in the actual resonance frequencies compared to target value. Also, a method to shift the resonance frequency of the piezoelectric material which can be helpful in matching resonance frequencies of the piezoelectric material, chip material and the channel resonance is demonstrated.

Acknowledgement:

Financial support from the Turkish Scientific and Technical Research Council, Grant No. 115M684, is greatly appreciated.

References

- [1] F. Petersson, L. Åberg, A.M. Swärd-Nilsson, and T. Laurell, *Analytical Chemistry*, 79(14), 5117-5123 (2007).
- [2] A. Lenshof, A. Ahmad-Tajudin, K. Järås, A.M. Swärd-Nilsson, L. Åberg, G. Marko-Varga, J. Malm, H. Lilja, and T. Laurell, *Analytical Chemistry*, 81(15), 6030-6037 (2009)
- [3] P. Li, Z. Mao, Z. Peng, L. Zhou, Y. Chen, P.H. Huang, C.I. Truica, J.J. Drabick, W.S. El-Deiry, M. Dao, S. Suresh, and T. J. Huanga, *PNAS*, 112(16), 4970-4975 (2015)
- [4] B. Çetin, M.B. Özer, and M.E. Solmaz, *Biochemical Engineering Journal*, 92, 63-82 (2014)



Acoustic droplet manipulation in a disposable microfluidic chip

Jinsoo Park, Jin Ho Jung, Kwangseok Park, Ghulam Destgeer, Husnain Ahmed, Raheel Ahmad, and Hyung Jin Sung

Mechanical Engineering, KAIST, Daejeon, Korea
 *E-mail: hjsung@kaist.ac.kr, URL: http://flow.kaist.ac.kr

Introduction

Acoustofluidic has made remarkable progress in the last decade especially for micro-object (particle, droplet, cell, etc.) manipulation (sorting, separation, focusing, merging, splitting, etc.) in a microfluidic chip [1,2]. Despite recent advances, most acoustofluidic devices reported to date have two common limitations: (1) a microfluidic chip is irreversibly bonded to a piezoelectric substrate; therefore, the microfluidic chip is irreplaceable, and the substrate and electrodes are non-reusable; (2) a heating problem occurs when dealing with PDMS microfluidic chips. Here, we propose a conceptual shift to address the abovementioned problems by investigating the PDMS thickness effect on acoustofluidic devices.

Our group recently developed acoustothermal heating and reported its application to droplet multichannel sorting in a disposable microfluidic chip [3]. As a follow-up study, we aim to experimentally investigate the effects of the PDMS membrane thickness on acousto-thermo-microfluidic phenomena. Based on our findings, we demonstrate an acoustic droplet volume control device for droplet tri-splitting and merging, which have not been reported in literature.

Effects of the PDMS membrane thickness

Acoustothermal heating has been regarded as an undesirable side effect of using PDMS microfluidic chips with acoustic waves. However, in our previous works, we demonstrated that acoustothermal heating can be utilized for microfluidic applications. In these devices, a thin PDMS membrane with its thickness of 200-300 μm (approximately 5λ) was used (1) to form a closed microfluidic chip and (2) to absorb acoustic energy and convert it into thermal energy (heat). Therefore, the microfluidic chip was disposable and thus easily replaceable, and the electrodes and the substrate can be reused. We further investigated the effects of the PDMS membrane thickness on acoustic and acoustothermal phenomena in the membrane.

PDMS membranes with varying thickness (t) were placed on an interdigital transducer (IDT) with electrode spacing ($\lambda/4$) that was deposited on a LiNbO_3 substrate (Fig. 1(a)). With AC signals applied, surface acoustic waves (SAWs) were produced, they were transformed into longitudinal waves (LWs) in the membrane. These LWs were attenuated in the membrane by viscoelastic damping, and thus acoustothermal heating occurred. The thickness was normalized with four times electrode spacing (t/λ), and the temperature measured by an IR camera was normalized with the room temperature (T_R) as $(T-T_R)/T_R$. As shown in Fig. 1(b), the normalized temperature increased until $t/\lambda \sim 2$ and reached a plateau when $t/\lambda > 2$. In other words, acoustic waves are incompletely attenuated in the membrane ($t < 2\lambda$) whereas they are completely attenuated with significant acoustothermal heating ($t > 2\lambda$), which are in agreement with our previous work [3].

Based on our findings, a closed microfluidic chip composed of microstructured PDMS stamp and a PDMS membrane can be placed and attached to the substrate by natural adhesion for acoustofluidic operations. The microfluidic chip in a disposable form can be easily replaced and thus, the substrate and IDTs can be reused. In addition, unlike most acoustofluidic devices [1,2], in which the acoustic field is excited in the direction perpendicular to the flow direction, the acoustic field can be applied in the direction parallel to the flow direction. These features enable disposable acoustofluidic device with significantly improved device functionality and flexibility.

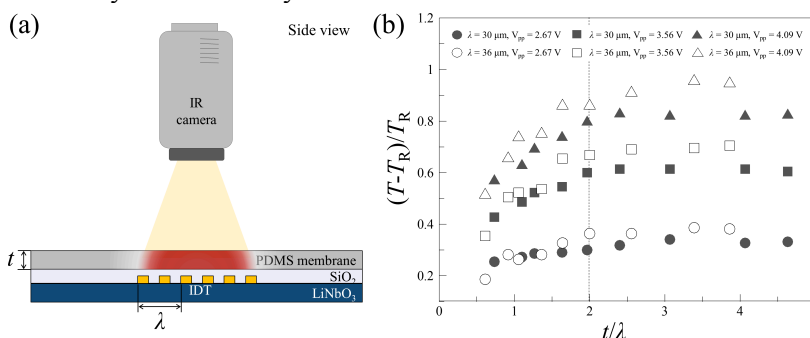


Figure 1: The effects of the PDMS membrane thickness: (a) Measurement of the temperature increase in the PDMS membrane using an IR camera. (b) The normalized temperature increase $(T-T_R)/T_R$ with respect to the normalized PDMS thickness t/λ .

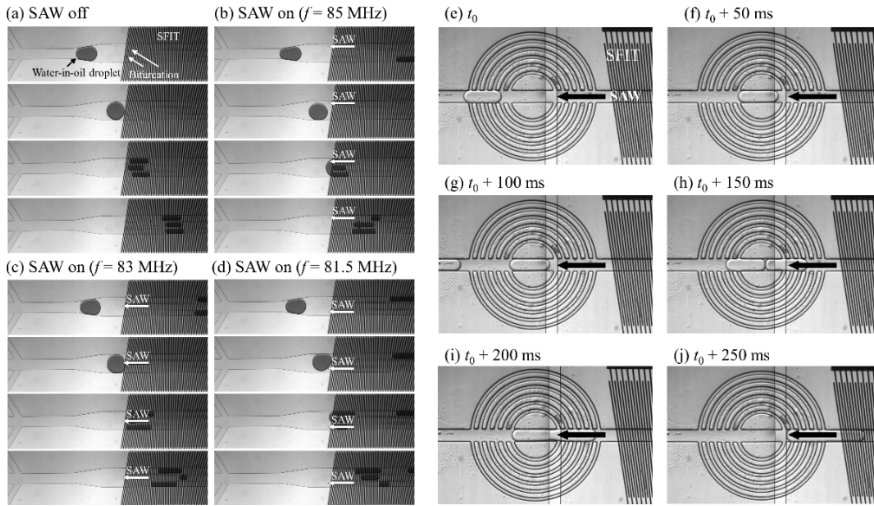


Figure 2: Acoustic droplet manipulation in a disposable microfluidic chip: (a-d) acoustic droplet tri-splitting. (e-j) acoustic droplet merging.

Acoustic droplet manipulation in a disposable microfluidic chip

In droplet microfluidics, droplet volume control is critical in various bio-physico-chemical applications. Such droplet volume control can be achieved by either splitting or merging droplets. A variety of methods have been proposed in the last decade: geometry-mediated, dielectric, thermocapillary, acoustic, magnetic, and optical methods [4]. However, most previous methods have limited functionality for on-demand droplet volume control. In respect of splitting, the external force is applied to the droplet in the direction perpendicular to the flow direction; thus, droplets cannot split into more than two daughter droplets. In addition, with respect to merging, most previous methods cannot perform droplet merging and mixing simultaneously. Furthermore, the previous methods all share a common limitation that they require irreversible bonding, leading to non-reusable device and non-disposable microfluidic chip.

We propose an acoustic device for on-demand droplet volume control using a slanted finger interdigital transducer (SFIT) with $\lambda/4 = 9\text{--}13\ \mu\text{m}$. As discussed in the previous sub-section, a disposable PDMS microfluidic chip with the membrane thickness of $20\ \mu\text{m}$ ($\sim 0.5\lambda$) was used. SAWs are selectively produced from the SFIT at a position where the corresponding electrode spacing matches with the applied frequency. Therefore, we can selectively impart an acoustic force to a certain part of a droplet. Compared to conventional droplet volume control devices, the proposed system significantly differs in two aspects.

First, an external force is exerted to the droplets in the inverse direction, instead of the perpendicular direction as in cross-type devices. This feature significantly improves functionality of droplet splitting. As in Figs. 2(a-d), a mother droplet can be split into three daughter droplets with a freely programmable droplet volume ratio. The presented results are the first demonstration of on-demand droplet tri-splitting. The number of daughter droplets can be further increased with ease by placing more bifurcations in the microchannel. Second, a closed microfluidic chip is used and it is bonded on the substrate by natural adhesion. Since no irreversible bonding is required, the substrate can be reused, and the microfluidic chip is disposable.

In addition to droplet splitting, droplet merging can be also performed in our system as in Figs. 2(e-j). The applied acoustic force holds a preceding droplet and thus merges it with a following droplet. In addition to droplet merging, the acoustic streaming flow induced by the acoustic waves can further accelerate inner vortex streaming and thus droplet mixing.

Conclusion

We have investigated the effects of the PDMS membrane in an acoustofluidic device and developed an acoustic device for on-demand droplet volume control (tri-splitting and merging) in a disposable microfluidic chip. We look forward to presenting these unprecedented results in more detail at *Acoustofluidics 2017*.

Acknowledgment

This work was supported by the Creative Research Initiatives (No. 2017-013369) program of the National Research Foundation of Korea (MSIP) and the KUSTAR-KAIST Institute, KAIST, Korea.

References

- [1] L.Y. Yeo and J.R. Friend, *Annual Review of Fluid Mechanics* **46**, 379-406 (2014).
- [2] G. Destgeer and H.J. Sung, *Lab on a Chip* **15**, 2722-2738 (2015).
- [3] J.Park, J.H. Jung, G. Destgeer, H. Ahmed, K. Park, and H.J. Sung, *Lab on a Chip* **17**, 1031-1040 (2017).
- [4] R. Seemann, M. Brinkmann, T. Pfohl, and S. Herminghaus, *Rep Prog Phys* **75**, 016601 (2012).

Acoustofluidic Whole Blood Hematocrit Assay

Klara Petersson¹, Ola Jakobsson¹, Pelle Ohlsson¹, Per Augustsson¹ and Thomas Laurell^{1,2}

¹Department of Biomedical Engineering, Lund University, Lund, Sweden

E-mail: Klara.petersson@bme.lth.se, URL: <http://www.bme.lth.se>

²Department of Biomedical Engineering, Dongguk University, Seoul, Republic of Korea

Introduction

We present a rapid acoustofluidic method for hematocrit determination. Hematocrit (HCT), the volume percentage of red blood cells, is routinely measured at the hospital, as abnormal values can indicate several disease states [1]. The gold standard for measuring HCT is a centrifugation based method where the height of packed blood cells is compared to the total blood sample height in a capillary after centrifugation. The acoustofluidic method to measure HCT, which can be performed in only 2 seconds, separates blood cells and plasma into discrete regions. Similar to the centrifugation based method, HCT can be calculated by comparing the two regions. This acoustic method, that is notably faster than the conventional centrifugation method and can be fully automated, is suitable for integration with further blood analysis operations [2,3].

Experimental

The setup consists of a microfluidic borosilicate chip with a straight channel, a syringe pump and two three-way valves for flow control, and a piezoceramic transducer glued to the chip that actuated the channel at $\frac{1}{2}$ wavelength resonance, see figure 1. Focusing of the red blood cells to the centerline pressure node was imaged by a grayscale CCD camera, see figure 1C. Light transmission along the centerline was blocked by the acoustically packed blood cells while the plasma on the sides was optically transparent. The acquired images were converted in Matlab to 1-bit binary images by grayscale thresholding, and the amount of dark pixels were compared to the total amount of pixels to give the acoustically packed cell area.

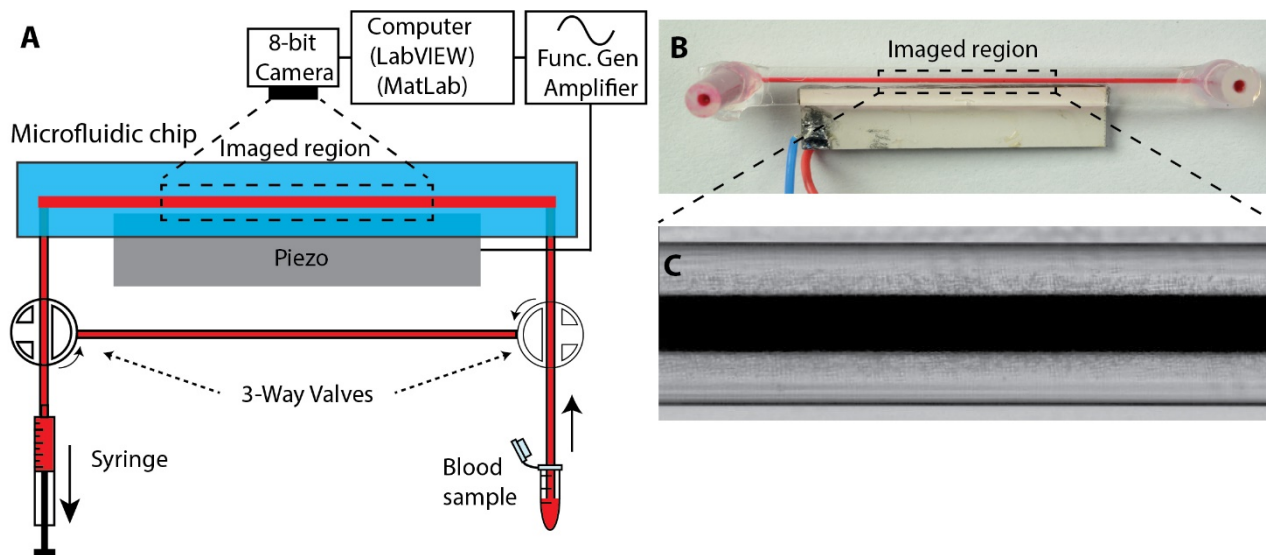


Figure 1: (A) Schematic illustration of the acoustofluidic setup. The channel in the microfluidic chip is filled with blood (syringe driven flow) and the flow is stopped by switching the three way valves. The piezo is actuated while a camera monitors part of the microfluidic chip. (B) Image of the microfluidic chip. (C) Acoustically focused whole blood in the channel.

A 200 μ l blood sample was used in each run. Blood samples with hematocrit ranging from 20% to 57%, used for a standard curve, was prepared by adding autologous plasma or blood cells to the blood sample. Blood samples used for proof of principle was undiluted whole blood.

Results and Discussion

The acoustically packed cell area was calculated for 17 samples (n=3) with HCT ranging from 20 to 57% after 2, 5 and 20 seconds of acoustic focusing. All samples were also measured by the reference centrifugation method, and the linear relationship between the HCT measured by the reference method and acoustically packed cell shows that they are proportional, though with a few percentage point (pp) offset, see figure 2.

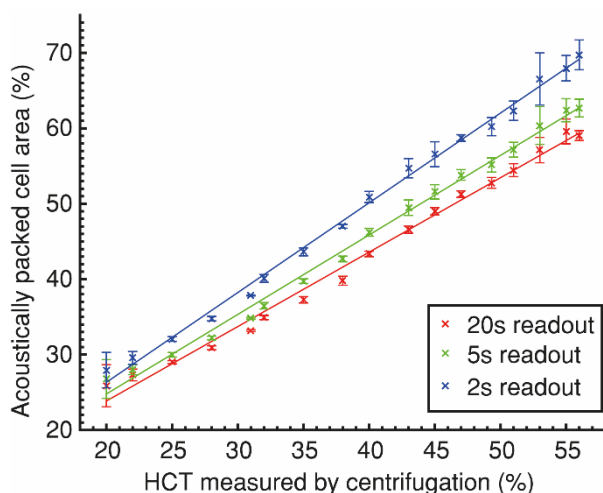


Figure 2: The linear relationship between Acoustically packed cell area and HCT measured by centrifugation is shown. The acoustically packed cell area measured after 2, 5 and 20 seconds of acoustic focusing for 17 samples with HCT ranging from 20-57% (n=3).

As a proof of principle, the acoustically packed cell area for 5 blood samples from healthy donors was measured and the acoustic HCT was estimated from the standard curve in figure 2 and compared with the HCT measured by centrifugation. For 20 seconds of focusing time, the acoustic method had a standard deviation (n=3) equal to or below 1 pp. Compared to HCT measured by centrifugation, the average error was 0.95 pp. For 5 and 2 seconds of acoustic focusing, the standard deviation was slightly higher, but still on or below 2.06 pp. and an average error of 1.16 pp and 1 pp.

Conclusion

The presented acoustofluidic method estimates a HCT value from 200 μ l of undiluted whole blood in only 2 seconds with an average error of only 1 pp. This could be integrated with sequential microfluidic in-line measurements for multiplex analysis.

References

- [1] Fernandez A. J. Spec Care Dent., **5**, 264-269 (1985)
- [2] Ohlsson, P. et al. Analytical Chemistry, **88**, 9403-9411 (2016)
- [3] Ahmad-Tajudin A. et al. Lab on a Chip, **13**, 1790-1796 (2013)



Particle capture and detection using acoustophoresis and antibody binding

Filip Plazonic¹, Chloe Rose^{1,2}, Xunli Zhang¹, Andrew Walls², Martin McDonnell³, Dario Carugo¹, Martyn Hill¹, Peter Glynne-Jones¹

¹Engineering and the Environment/²Medicine, University of Southampton, Southampton, United Kingdom

³Dstl Porton Down, Salisbury, Wiltshire, United Kingdom

E-mail: fp3g10@soton.ac.uk

Particle detection: from air pathogens to basophils

Airborne pathogens represent a serious threat to human health as they can spread easily and quickly [1]. Anthrax (*Bacillus anthracis*) is an especially dangerous airborne bacteria that can stay dormant for as long as 70 years in its spore form [2]. Anthrax is highly lethal [3] with mortality rates as high as 90% (although recently, with more effective treatment, this has dropped to 45%) [1,4]. Current detection methods do not provide a fast enough response due to complications in analyzing air particles as well as not having real-time capabilities [1].

When performing an allergy blood test, rare white blood cells, basophils, have to be extracted from a heterogeneous blood sample. Once isolated, these cells can be exposed to various allergens to determine the severity of the person's allergic reactions. The isolation process is a long and expensive one and the cell purities obtained can be disappointing [5].

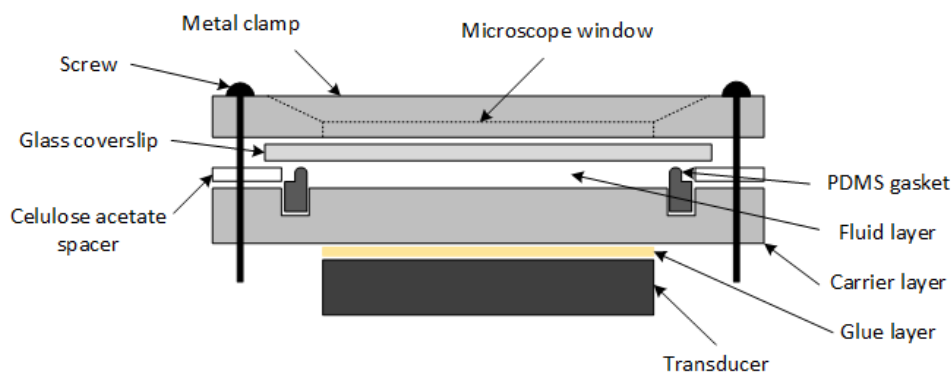
In both of these situations there is a need to concentrate and isolate a certain type of target cell in a sample and have it ready for further inspection. An ultrasonic standing wave (USW) field has the ability to move objects due to radiation forces that can push all particles towards a surface, for instance [6]. That surface can be coated with specific antibodies that will only capture the specific pathogens. This is the basic principle of operation for a device developed to speed up the two processes.

Device description

The device consists of a PZT transducer glued onto a 1 mm thick stainless steel carrier layer. The fluid channel is 130 μm thick and is separated from the 170 μm glass coverslip reflector layer by a PDMS gasket and a cellulose acetate spacer. The device is fairly robust and can tolerate variation in the carrier layer thickness of up to 0.1 mm, resulting in only a small decrease in radiation force (3%).

The device has two transducers. The first one, over the first half of the channel (in the lengthwise direction) is tuned to set up a half-wave (HW) field, while the second one is tuned to set up a thin-reflector (TR) mode [6]. As the cells flow within the US field, they are first concentrated in the mid-plane of the channel and then pushed towards the reflector layer on which an antibody (AB) coating has been applied to capture them. Figure 1 shows the device schematic.

In the case of airborne spore monitoring, the device would act on particles suspended in water following aerosol capture. The waterborne spores are then run through the device which renders itself suitable for continuous real-time use [7], if integrated with an appropriate detection method. When separating basophils, whole blood flows directly into the device.



a)

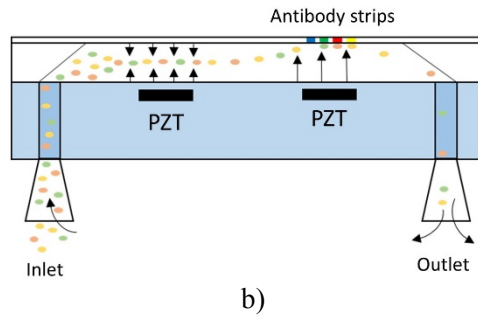


Figure 1: Schematic cross-sections of the device from the: a) front, b) side.

Experimental results

The initial device tests were done with 1 μm diameter fluorescent beads, for the ease of tracking the behavior. From the data it was established that up to 95% of pathogens are captured when using both transducers at a flow rate of 30 ml/hr.

To capture the BG spores (substitute for anthrax spores) an array of antibody spots was printed onto the reflector layer (one row of specific AB and one row as a control, which shouldn't capture the spores). A spore solution with a concentration of 10^4 spores/ml was flowed into the device. Figure 2 shows how the specialized AB successfully captured the spores. In the future it is expected that the spore concentration in the sample can go even lower while still retaining a successful capture rate.

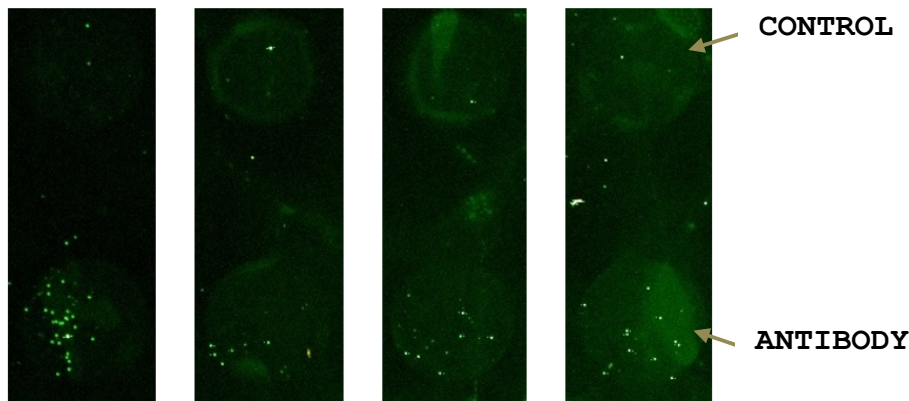


Figure 2: Examples of antibodies capturing spores with the aid of the TR mode USW field. The lower spots are coated with the specialized antibody that binds to BG spores, while the upper spots do not have antibodies

As basophils are larger than spores ($\sim 15 \mu\text{m}$ instead of $\sim 1 \mu\text{m}$) only the TR mode was used, since the radiation force increases with the volume of the object. Both purified basophils and whole blood were flowed at separate occasions with the reflector layer completely functionalized with specific antibodies that targeted basophils. Visual inspection showed basophils being captured, and a flow cytometric analysis (FACS) revealed that between 85 to 90% of basophils were captured on the antibodies.

Conclusion

We present an acoustofluidic device that uses ultrasonic radiation force in conjunction with specific antibodies to capture blood cells and spores. It has proven itself successful in detecting BG spores in a water solution (10^4 spores/ml), as well as capturing basophils from whole and purified blood. The device operates at high efficiency (around 95% capture rate, at a flow rate of 30 ml/hr) which will allow us to improve on current limits of particle/cell detection and concentration.

References

- [1] Fronczek, C.F., Yoon, J., 2015, *J Lab Autom*, 20(4), pp. 390-410
- [2] Guillemin, J., *Anthrax: The investigation of a deadly outbreak*, University of California Press (Berkeley, 1999)
- [3] Spencer, R.C., 2003, *J Clin Pathol*, 56, pp. 182-187
- [4] Leffel, E.K., Bourdage, J.S., Williamson, E.D., Duchars, M., Fuerst, T.R., Fusco, P.C., 2012, *Clin Vaccine Immunol*, 19(8), pp. 1158-1164
- [5] De Weck, A.L., Sanz M.L., Gamboa, P.M., Aberer, W., Bienvenu, J., Blanca, M., Demoly, P., Ebo, D.G., Mayorga, L., Monneret, G., Sainte Laudy, J., 2008, *J Invest Allergol Clin Immunol*, 18(3), pp. 143-155
- [6] Glynne-Jones, P., Boltryk, R.J., Hill, M., Harris, N.R., Baclet, P., 2009, *JASA*, 126(3), pp. 75-79
- [7] Carugo, D., Octon, D., Messaoudi, W., Fisher, A.L., Carboni, M., Harris, N.R., Hill, M., Glynne-Jones, P., 2014, *Lab Chip*, 14, pp. 3830-3842



Acoustic streaming in inhomogeneous fluids – an experimental study

Wei Qiu¹, Jonas T. Karlsen¹, Henrik Bruus¹ and Per Augustsson²

¹Department of Physics, Technical University of Denmark, Kongens Lyngby, Denmark

²Department of Biomedical Engineering, Lund University, Lund, Sweden

E-mail: weiqiu@fysik.dtu.dk, URL: www.fysik.dtu.dk/microfluidics

Introduction

Acoustic streaming is the time-averaged flow induced by an acoustic wave propagating through a fluid. It is caused by partial absorption of traveling waves (Eckart streaming [1]) or by viscous stresses in the acoustic boundary layer near rigid surfaces (Rayleigh streaming [2]). For microscale acoustofluidics, acoustic streaming is well characterized both theoretically and experimentally in fluids of homogeneous density and compressibility [3,4]. Recently, however, acoustofluidic properties of inhomogeneous systems have been studied in the literature: iso-acoustic focusing of cells in solute gradients was discovered and characterized experimentally [5], and a theory for the acoustic body force responsible for the stabilization of these gradients was developed [6]. Here, we extend this work to experimental studies of acoustic streaming in inhomogeneous systems, the main result being the remarkable suppression of streaming flow in the bulk of such systems. In a parallel study, we find the same behavior in a numeric simulation of the system.

Materials and experimental methods

In a standard 130- μm -high and 375- μm -wide long straight channel in a silicon-glass chip with a piezoelectric transducer bonded underneath, a laminated flow of water and a 20% iodixanol solution forms a density and compressibility gradient across the channel, as illustrated in Fig. 1. The motion of 1- μm -diameter polystyrene tracer beads is recorded using a general defocusing particle tracking (GDPT) method [7]. At time $t = 0$ s, the flow is stopped, and the GDPT measurements are conducted in a half-wavelength standing wave field with the PZT input voltage set to 3 $V_{\text{p-p}}$ and the frequency sweeping from 1.95 to 2.05 MHz. For each measurement set, the particle motions are recorded for 200 s to observe the evolution of acoustic streaming. The experiment is repeated several times to improve the statistics of the particle trajectories.

Results

Examples of the trajectories of the particles and the color plot of their velocity at 35 s and 160 s are shown in Fig. 2(a) and (b). We find that the streaming rolls are confined close to the channel wall at 35 s, which is not the case for homogeneous medium, see Fig. 2(c). Due to this confinement, and even though the particle size is well below the critical size where acoustic streaming normally dominates [3], the majority of the particles are focused in the vertical pressure nodal plane within the first 30 s after stopping the flow. As time evolves, the fluid is homogenized due to diffusion and mixing, and at 160 s the streaming pattern is similar to the homogeneous case. However, the ratio $v_y^{\text{top}} / v_y^{\text{mid}}$ between the velocity component in y direction near the top

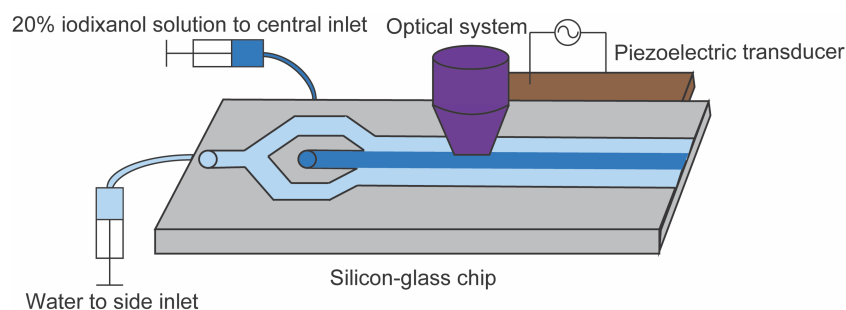


Figure 1. Schematic diagram of the measurement system consisting of a long straight channel with rectangular cross section of height 130 μm and width 375 μm etched in a silicon chip (gray) and closed with a glass lid. A 20% iodixanol solution (dark blue) flows in the center stream laminated by pure water (light blue). The motion of 1- μm -diameter polystyrene tracer beads are recorded through the optical system (purple). Acoustic waves are induced at MHz frequencies by a piezoelectric transducer (brown) attached under the silicon chip.

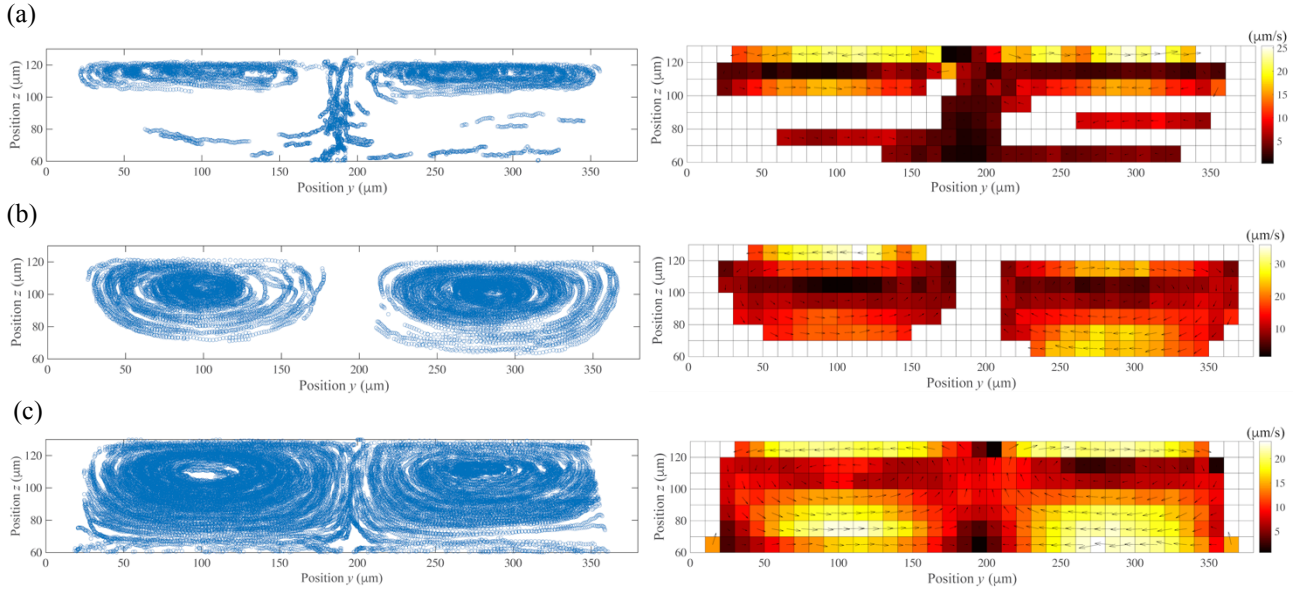


Figure 2. Particle trajectories (blue dots) and color plot of the particle velocities in the top half of the channel. (a) The inhomogeneous fluid at 35 s. (b) The inhomogeneous fluid at 160 s. (c) The steady pattern in the homogeneous fluid.

v_y^{top} and at the mid-height of the channel v_y^{mid} is different from what we find in homogeneous fluids, as illustrated in Fig. 3. Note that the part of the velocity, which is induced by the acoustic radiation force is not subtracted from the particle velocity presented here. The results provide preliminary support for the surprising predictions from our theoretical work that the iodixanol solution cannot be perfectly homogenized in this case owing to a balance between the diffusion and the advection caused by the standing wave field.

Conclusion

The results clearly show the suppression of acoustic streaming in the bulk of inhomogeneous fluids, and the time-evolution of the streaming rolls as the fluids become homogenized due to the diffusion.

The experimental results are in good agreement with theoretical predictions. More details and direct comparison between theoretical and experimental results will be discussed in the conference.

References

- [1] C. Eckart, Phys. Rev. **73**, 68-76 (1948).
- [2] L. Rayleigh, Philos. Trans. R. Soc. Lond. A **175**, 1-21 (1884).
- [3] P.B. Muller, R. Barnkob, M.J.H. Jensen, and H. Bruus, Lab Chip **12**, 4617-4627 (2012).
- [4] P.B. Muller, M. Rossi, A.G. Marin, R. Barnkob, P. Augustsson, T. Laurell, C.J. Kähler, and H. Bruus, Phys. Rev. E **88**, 023006 1-12 (2013).
- [5] P. Augustsson, J.T. Karlsen, H.-W. Su, H. Bruus, and J. Voldman, Nat. Commun. **7**, 11556 1-9 (2016).
- [6] J.T. Karlsen, P. Augustsson, and H. Bruus, Phys. Rev. Lett. **117**, 114504 1-6 (2016).
- [7] R. Barnkob, C.J. Kähler, and M. Rossi, Lab Chip **15**, 3556-3560 (2015).

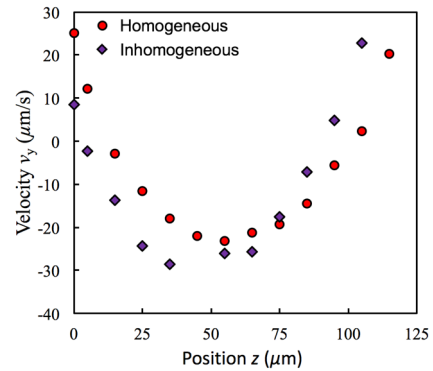


Figure 3. Particle velocities as a function of the vertical position z along the line $y = 275 \mu\text{m}$ in the inhomogeneous fluid at 160 s (purple) and the homogeneous fluid (red).



An ultrasonic resonator exploited in order to improve in-line Raman spectroscopy of crystallization processes

Stefan Radel^{1,2}, Samantha Derksen², Stefan Tauber¹, Hamid Rasoulimehrabani¹, Karin Wieland¹, Stephan Freitag¹, Bernhard Lendl¹, and Martin Gröschl²

¹Institute of Chemical Technologies and Analytics, Vienna University of Technology, Vienna, Austria
E-mail: stefan.radel@tuwien.ac.at, URL: <http://www.tuwien.ac.at>

²Institute of Applied Physics, Vienna University of Technology, Vienna, Austria

Introduction

We exploit the so-called radiation forces exerted on particles in an ultrasonic standing wave (USW) of approximately 2 MHz for purposes of in-line process analytical technology (PAT). More precisely the agglomerations of particles forming in the pressure nodal are used to increase the signal-to-noise ratio (SNR) of a Raman spectrum measured with an in-line probe.

Raman spectroscopy is a method holding great promise for in-line monitoring of crystallization processes due to its capabilities of discriminating between different polymorphs, i.e. crystal types, forming. Moreover the remaining solute concentration can be assessed as well. This would make Raman spectroscopy an ideal tool for the control of such processes. However, due to its quantum-mechanic nature, Raman spectroscopy has an inherently low sensitivity, only one of 10^8 photons is scattered in-elastically and therefore affected by the chemical composition of the analyte, thus delivering the desired information.

Therefore we set out to increase the sensitivity of a Raman spectroscopy in-line probe by the mentioned application of an USW to

- spatially increase the particle concentration in the nodal planes
- and create regions depopulated of particles between the planes to

be able to discriminate between signals coming from particles and such originating from the liquid. Exemplary we concentrate on a case of low particle concentration like at the onset of a crystallization process. Past work has shown, that the Raman signal of agglomerates brought about by the USW in a cuvette is comparable to the spectra of sediment [1]. The target of this research is the exploitation of this technique for the in-line, real-time Raman spectroscopy in a close-to-industrial environment.

Experimental work

In contrast to earlier work combining an USW and Raman spectroscopy, where the direction of sound propagation was coaxial to the observation direction [2], we have used a configuration like shown in Fig. 1 for the work presented here. The USW is build up between a transducer and a reflector building up a resonator perpendicular to the optical axis in front of an in-line Raman probe. This enables us to alter the spatial distribution of the collected particles in relation to the incoming excitation laser by simply changing the acoustic driving frequency.

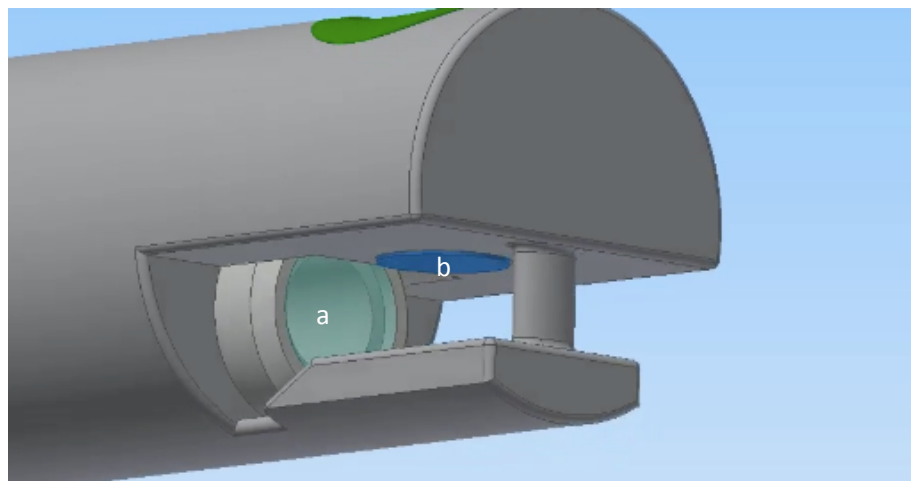


Figure 1: Prototype for measurements within a crystallization process holding an in-line Raman spectroscopy probe (a). The ultrasonic resonator comprises the transducer (b) and the reflector (not visible), the ultrasonic standing wave is orientated perpendicular to the axis of the in-line probe.

An angular spectrum approach (ASA), a fast and accurate method of calculating diffraction fields was used to numerically assess the resonator. The aim of this was to better understand the USW in the given resonator, as the space at the probe tip is narrow and therefore the need of optimization exists. Only the frequency and within certain limits the diameter of transducer and reflector can be chosen.

Fig. 2 shows the result of a calculation where both diameters were set to 8 mm and the resonator length was set to 21 half wavelengths. The interesting outcome is, that on the axis of the resonator, the acoustic pressure has a more complicated course than assumed. One would expect to be the USW strongest at the reflector and then decreasing monotonically towards the transducer.

The results in Fig. 2 show in contrary, that the field is not smallest at the transducer at $x=0$ but more to the center of the resonator around 2.5 mm and again at 5.3 mm. Moreover the local minima, i.e. the pressure nodes where the particles are collected, show rather high acoustic pressure values, where a pressure of almost zero is expected. Nevertheless, the maximum pressure is reached at the reflector.

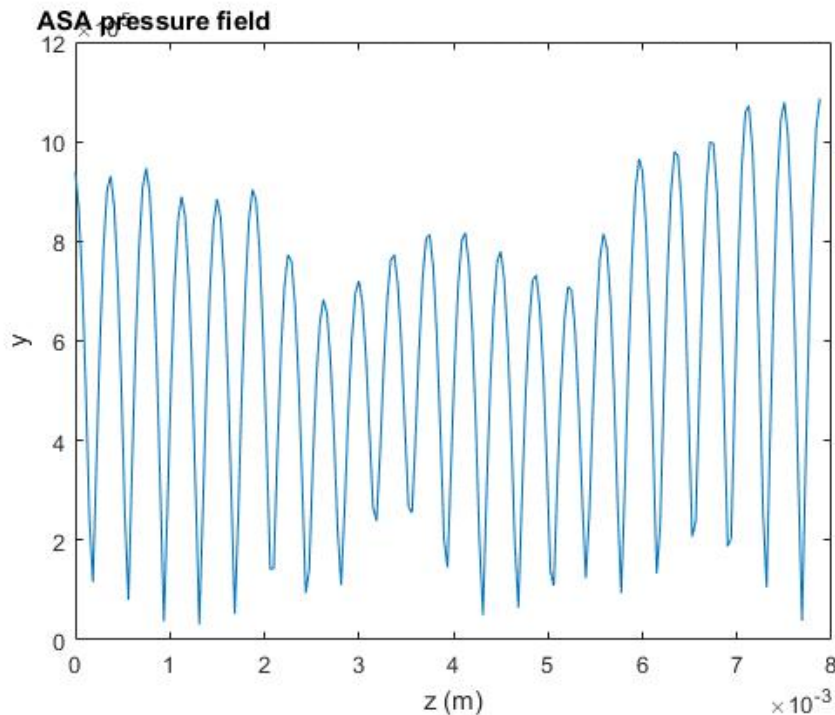


Figure 2: Acoustic pressure on the axis of a resonator calculated by an angular spectrum approach. Transducer and reflector were assumed to be circular and 8 mm in diameter, the distance between them was 7.875 mm representing 21 half wavelengths when driving the transducer a 2 MHz and the suspending liquid (water) has a speed of sound of 1.500 mm/s.

Measurements with model suspensions were used to test the setup (data not shown). It was well possible to discriminate between particles and carrier liquid. When the Raman excitation laser was aiming at an agglomerate brought about by the USW, signals were of comparable strength to that of sediment particles. When the driving frequency was shifting the pattern in a way that the laser was aiming between the pressure nodes, the Raman spectrum of the liquid could be measured undisturbed of signals stemming from particles.

Conclusion

A close-to-series prototype is presented capable of assessing the Raman spectrum of suspended crystals in-line. The setup was numerically assessed for optimization purposes, which delivered some unexpected learnings. By changing the excitation frequency it was possible to discriminate between the chemical composition of the solid fraction and the liquid. An increase of the signal strength (counts) by a factor of 100 when measuring the agglomerates brought about by the USW was observed.

Acknowledgement

Financial support from the EU project WaterSpy (this project has received funding from the European Union's Horizon 2020 research and innovation programme under the grant agreement no.: 731778) is gratefully acknowledged. Kaiser Optical Systems supports this research in a Center of Excellence action.

References

- [1] S. Radel, J. Schnöller, A. Dominguez, B. Lendl, M. Gröschl, and E. Benes. *Elektrotechnik & Informationstechnik* **125**, 82–85 (2008). DOI 10.1007/s00502-008-0515-2.
- [2] S. Radel. *Procs. Acoustofluidics 2016, c29*, Copenhagen, 22 - 23 September 2016.

Thin film PZT actuated BAW acoustophoresis

Peter Reichert¹, Dhananjay Deshmukh¹, Lukas Lebovitz¹, Jürg Dual¹

¹Department of Mechanical and Process Engineering, Institute for Mechanical Systems, Swiss Federal Institute of Technology Zurich, Zurich, Switzerland

E-mail: reichert@imes.mavt.ethz.ch, URL: www.zfm.ethz.ch/e/exp-dyn

Introduction

Similarly to the recent miniaturization towards implantable piezoelectric fluid pumps, thin film piezoelectric transducers can enable low voltage, miniaturized and precisely fabricated acoustofluidic chips [1]. Such transducers consist of a silicon membrane and a thin piezoelectric layer. The membrane is driven at resonance and is often called a Thin Film Bulk Acoustic Resonator (TFBAR) [2]. In this study, a special TFBAR was fabricated and tested for the acoustic particle manipulation by exciting a Silicon membrane by a thin lead zirconate titanate (PZT) film in a microfluidic Si/glass chip. Waves emitted by a vibrating membrane couple into a microfluidic channel and build up an acoustic field for the manipulation of micro-particles. As particles are manipulated by a coupled fluid-membrane resonance, variable boundary conditions away from the membrane, e.g. glue at the chip holder and fluid connectors or debris have little influence on the particle manipulation behaviour. High-quality piezoelectric layers can be produced using Solmates SMP-800 pulsed laser deposition (PLD) equipment. With this equipment stable processes have become available for large wafer sizes and at commercial throughput [3,4].

Particle manipulation principle and simulation

Designs of a TFBAR and a bulk acoustic wave (BAW) device were combined to form a TFBAR device as sketched in Fig. 1a. A membrane covers a microfluidic channel which is embedded in a silicon/glass chip. On this membrane a PZT layer (blue) was deposited between two electrodes. The top electrodes (green) are separated in the middle. The 2D FEM simulation with COMSOL in Fig. 1b shows the pressure field for a frequency of 2.87 MHz. To actuate the anti-symmetric membrane vibration, the PZT layer was actuated harmonically with a phase shift of half a period between the top electrodes. White arrows indicate acoustic forces calculated from the Gorkov potential for polystyrene spheres (PS). At this membrane vibration, particles (light blue) are forced to the channel middle as shown in Fig. 1a.

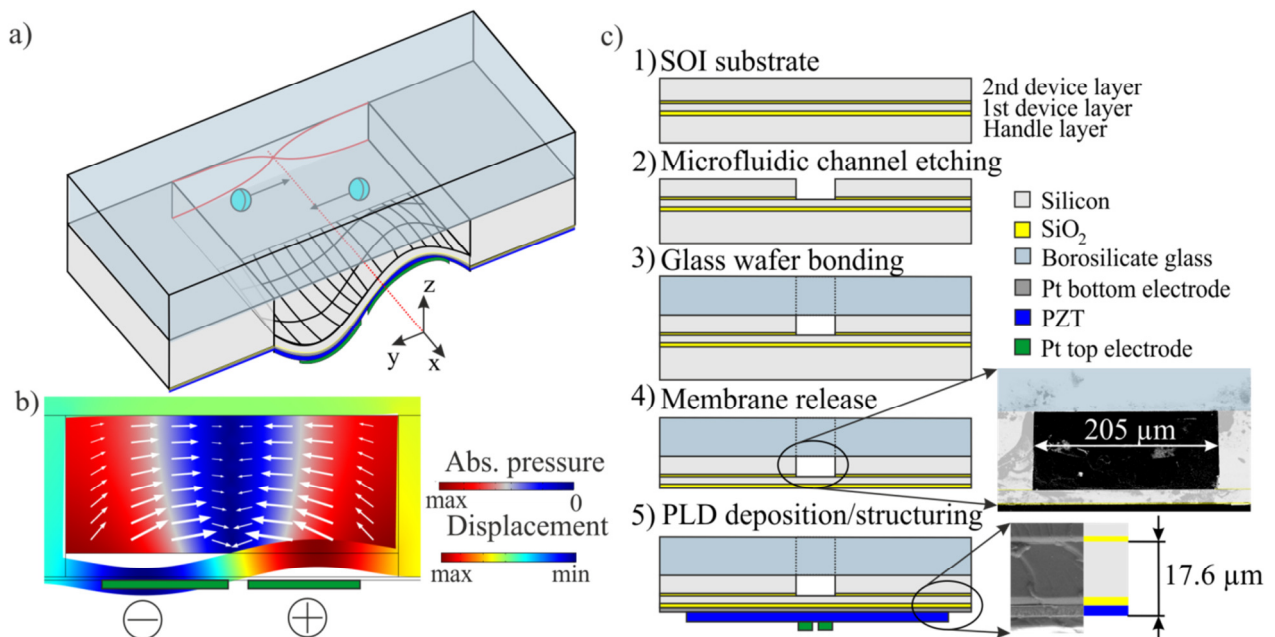


Figure 1: a) Sketch of a TFBAR device section with an antisymmetric silicon membrane vibration to manipulate particles inside a microfluidic channel. In b), the result of a 2D COMSOL simulation at 2.87 MHz is shown for a cross section of the TFBAR device. The fabrication process with the major steps is presented in c).

Device fabrication

An overview of the fabrication steps is presented in Fig. 1c. A Silicon On Insulator (SOI) wafer (1) with two SiO₂ “etch-stop” layers was used as a substrate. A microfluidic channel (205 μm x 86 μm x ~5 mm) was dry etched to the first stop layer in step (2). In step (3), a glass wafer with holes was anodically bonded to the SOI wafer. The glass wafer adds mechanical stability to the wafer stack. In the next step (4), the Si/SiO₂ membrane was released by etching the handle wafer. On top of this membrane, a piezoelectric stack of (Ti/Pt/LaNiO₃/PZT/Pt) was deposited. The Pt (111) bottom electrode was sputtered as an initial layer. A 2 μm textured PZT layer was deposited using Solmates SMP-800 PLD equipment. The PLD process showed to be suitable for the deposition of PZT on Si/glass substrates as rapid thermal annealing was not required and process temperatures did not exceed 600 °C. The membrane has a total thickness of 17.6 μm and a width of 205 μm as shown in the additional SEM pictures. The PZT layer was structured to get access to the bottom electrode. The Pt top electrode was structured using a lift-off process. The device was finished by adding holes to the glass wafer and wiring electrodes to a PCB chip.

Experiments

In the following experiments, the microfluidic channel was filled with a suspension of water and PS spheres with a diameter of 15.6 μm. The chip was positioned such that the z-direction is in direction of gravity to avoid a sedimentation of particles on the membrane surface. The displacement field in Fig. 2a was measured with a laser scanning vibrometer at a resonance frequency of 2.819 MHz. The transfer function for a single scan point on the membrane surface (black dot in Fig. 2a) is shown in Fig. 2b. The fluid filled channel and the particles initial position are shown in Fig. 2c. At resonance frequency, a voltage amplitude of 1 V_p and a maximum displacement of 5.4 nm, particles are moved along the trajectories in Fig. 2d. A pressure amplitude of 0.08 ± 0.01 MPa inside the cavity was estimated by fitting analytical and experimental trajectories. Analytical trajectories were calculated from a balance of the Stokes’ drag force (neglecting wall effects) and the 1D acoustic radiation force.

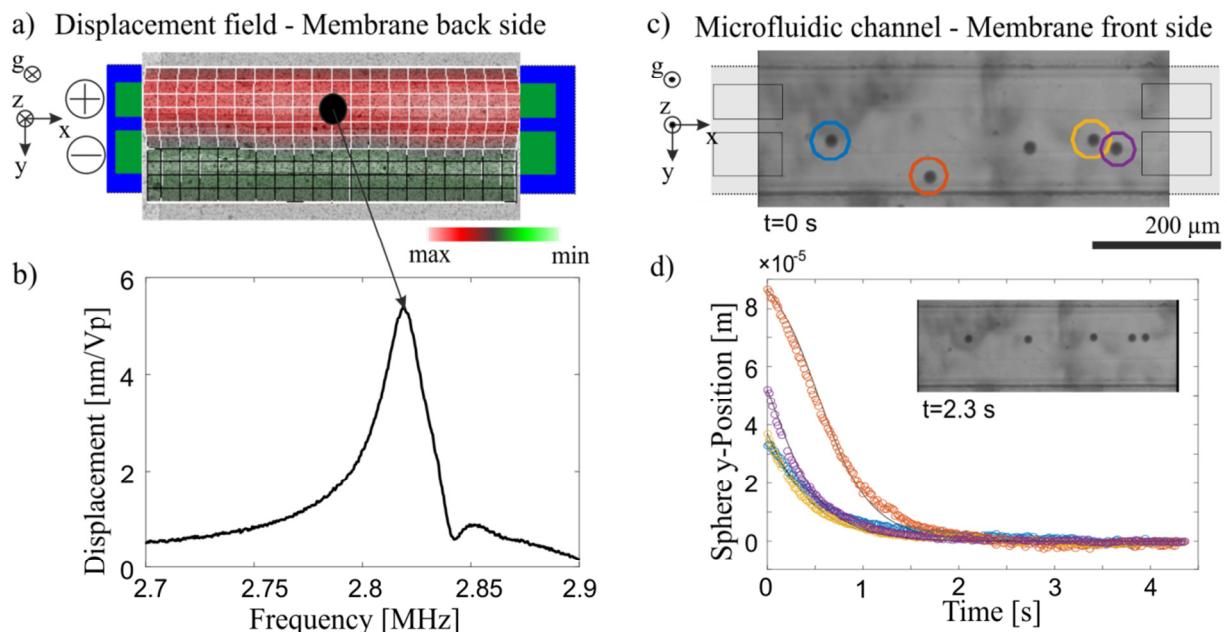


Figure 2: a) The displacement field of the membrane is shown for a frequency of 2.819 MHz. In b), the transfer function of the membrane is plotted for the indicated point in a). At the peak frequency of 2.819 MHz, PS spheres close to the glass surface are manipulated in c) and d). The experimental trajectories for four spheres and analytically fitted curves are shown in d).

Conclusion

With the presented fabrication process it becomes possible to embed a thin film PZT actuated membrane into an acoustofluidic device. The TFBAW chip is fully fabricated in a clean room environment with well controllable equipment. Overall, TFBAW devices have the potential to enable a predictable and stabilized acoustic particle manipulation at low power consumption.

References

- [1] P.-H. Cazorla, O. Fuchs, M. Cochet, S. Maubert, G. Le Rhun, Y. Fouillet and E. Defay, *Sensors and Actuators A: Physical*, **250**, 35-39 (2016).
- [2] S. Trolier-McKinstry and P. Muralt, *Journal of Electroceramics*, **12**, 7-17 (2004).
- [3] D. H. Blank, M. Dekkers and G. Rijnders, *Journal of physics D: applied physics*, **47**, 034006 (2013).
- [4] M. D. Nguyen, H. N. Vu, D. H. Blank and G. Rijnders, *Advances in Natural Sciences: Nanoscience and Nanotechnology*, **2**, 015005 (2011).



Cell Separation Using Dynamic Surface Acoustic Wave in Multiple Pressure Nodes

Chanryeol Rhyou¹, Byungjun Kang¹, Junyoung Lee¹, Seunghee Oh^{1,2}, and Hyungsuk Lee¹

¹School of Mechanical Engineering, Yonsei University, Seoul, Korea

²Samsung Electronics Co., Ltd, Suwon, Korea

E-mail: chan.rhyou@yonsei.ac.kr, URL: <http://leelab.yonsei.ac.kr>

Introduction

Manipulation of cells such as patterning, tweezing or sorting is essential tool for biology, chemistry and medical diagnostics, etc [1,2]. Recently, cell sorting techniques using surface acoustic waves (SAW) are emerging because of the label-free, non-contact, and energy-efficient features [3, 4]. Here, we develop a novel method, continuously phase modulated standing surface acoustic waves (CPM-SSAW), which is able to separate cells from a cell-bead mixture. The developed technique is manifested by demonstrating cell separation in a two-way microchannel as wide as multiple pressure nodes [5].

Theory

Balancing two major forces, the acoustic radiation force and the drag force in acoustofluidics, we obtain the optimal rate of phase shift at which the particles are displaced linearly with the moving pressure waves. The optimal rate of phase shift depends on the particle size and the applied frequency of SAW. The relationship is

$$\phi_{\text{opt}} = \frac{2kF_0}{b},$$

where $F_0 = \frac{\pi p_0^2 V_c \beta_w}{2\lambda} \phi$, $b = 6\pi a \eta$ and k , p_0 , λ , V_c , ρ_c , ρ_w , β_c , β_w , ϕ , a , and η are the wavenumber, acoustic pressure, wavelength, particle volume, particle density, fluid density, particle compressibility, fluid compressibility, contrast factor, particle radius, and fluid viscosity respectively. The rate of phase shift (ϕ) is constant and it is equal to the frequency shift Δf with relationship $\phi = 2\pi\Delta f$. When the optimal rate for cells with a target dimension is applied, target cells exhibit a linear displacement while particles smaller than the target size show an oscillatory motion. The difference in displacement between two objects for the same period of time causes target cells to be separated from the mixture. In order to apply the developed technique to cell separation in a closed microchannel, we design a Y shaped two-way channel consisting of 2 inlets and 2 outlets [Fig. 1]. When the CPM-SSAW is applied, cells in the mixture can be displaced by the moving pressure nodes and collected at the outlet located at one side of the channel. The separation efficiency is assessed by calculating the number ratio of cell to bead at both inlet and outlet. Our technique using phase-modulated surface acoustic wave can be applied to multiple pressure nodes and therefore advantageous in developing a high-throughput separation method.

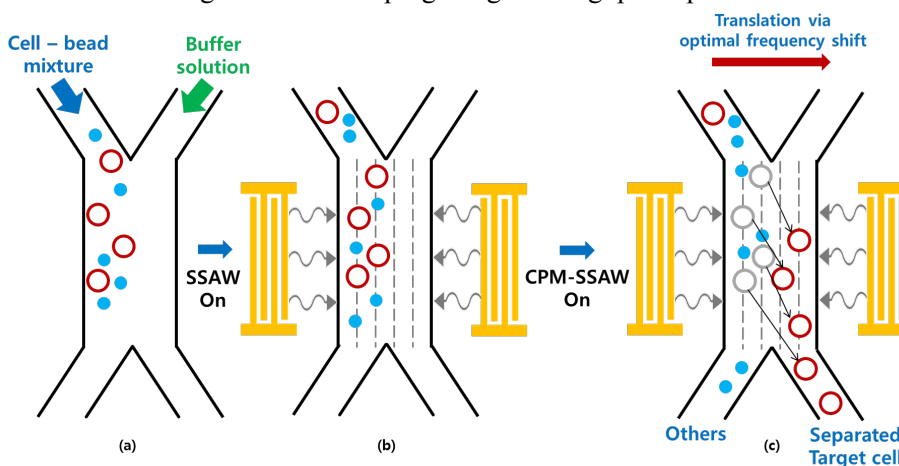


Figure 1. Schematic of the cell separation method using CPM-SSAW in multiple pressure nodes.

- (a) Cell-bead mixture is infused from the left inlet.
- (b) When SSAW is applied, all particles are aligned.
- (c) When CPM-SSAW is on, it enables to move the target cells to the right and eventually to be collected at the outlet for target cells.

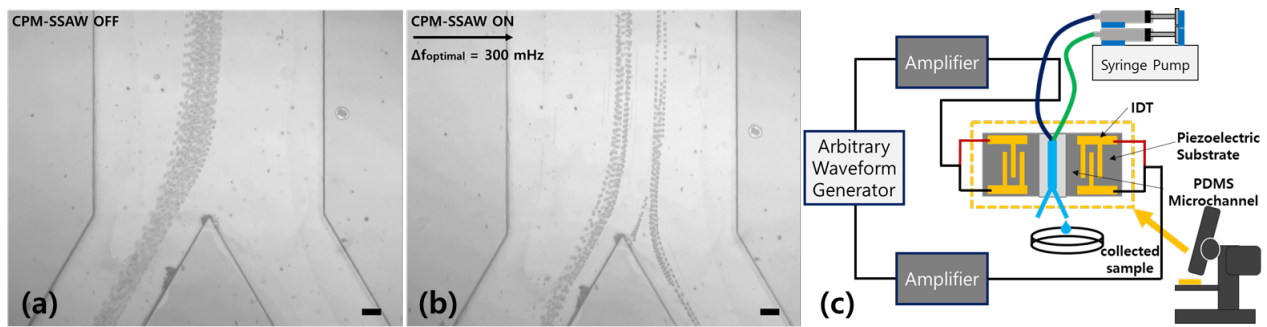


Figure 2. (a) and (b) Brightfield images of cell-bead separation before and after CPM-SSAW. (Data source from ref. [5]) Due to the CPM-SSAW, cells are moved to the right, transferred to the buffer solution and carried by the buffer solution to the right outlet. (c) Schematic of experimental set-up (Scale bar: 100 μm)

Experiment

First, an optimal rate of phase shift was obtained by observing cell displacement as a function of frequency shift. As we reduced Δf from 1000 mHz to 100 mHz by 100 mHz, we found that the optimal rate of frequency shift for fibroblasts was around 300 mHz in 14MHz, which was similar to the calculated value using the average size (21 μm) of cells and its contrast factor (0.26) [6].

After finding the optimal rate of cells, cell separation from cell-bead mixture was tested. In Fig. 2(a), a mixture of beads and cells were infused into one left inlet and a buffer solution, PBS, was infused into the other right inlet. Because the flow inside the channel was laminar, two infused fluids flowed along the channel without mixing in CPM-SSAW off. In contrast, in CPM-SSAW on, only cells were translated into the buffer solution and collected at the right outlet [Fig. 2(b)]. We analyzed that the number ratio of cell to bead was changed approximately from 1:1 before separation to 5:1 after separation, which meant that cells were translated by CPM-SSAW and eventually separated from the cell-bead mixture. The schematic of experimental setup is shown in Fig. 2(c).

Materials and methods

PDMS micro-channel (23mm length) was prepared with using SU8 mold provided by the manufacturer via conventional soft lithography. PDMS mixture of prepolymer (Sylgrad® 184) and curing agent at a ratio of 10:1 by volume were mixed over the SU8 mold inside the petri dish ($\Phi = 150 \text{ mm}$) and cured at 60 $^{\circ}\text{C}$ in the drying oven overnight. The width and height of the main channel are 1200 μm and 80 μm respectively. The piezoelectric substrate is a 128 $^{\circ}$ rotated Y-cut X-propagating Lithium Niobate (LiNbO_3). A sinusoidal RF input was generated by an arbitrary waveform generator (Keysight, HP33522). The RF input signal was amplified by the power amplifier (Mini-Circuits, LZY-22+). Beads were 6 μm (Polysciences BioMag®, Bright Blue) and NIH-3T3 mouse fibroblasts were used. The particle mixture was infused by using the syringe pump (Fusion 200T) and observed via both brightfield microscopy (Nikon Eclipse Ni-U). The flow velocity of each solution is 3 $\mu\text{L}/\text{min}$.

NIH-3T3 mouse fibroblasts were cultured in Dulbecco's Modified Eagle's medium (DMEM; LM 001-05, Welgene) supplemented with 10% fetal bovine serum (FBS; 16000-044, Invitrogen Corp.), and 1% penicillin/streptomycin (Pen/Strep; 15140-122, Invitrogen Corp.). All cells were subcultured every other day in 75 cm^2 flasks and incubated for 24 h at 37 $^{\circ}\text{C}$, 5% CO_2 in culture media. For cells sorting, cells were fixed in 4% paraformaldehyde (PFA; 15710, Electron Microscopy Science) for 30 mins.

Conclusion

Using CPM-SSAW with the optimal rate of frequency shift, we demonstrate cell separation from the cell-bead mixture. Our technique can be developed into a high-throughput separation method when the channel design is further optimized in terms of length, width or flow velocity. As the phase modulation is also determined by the contrast factor as well as size of particle, the method using CPM-SSAW can be applied to separate particle with the same size but different material properties.

References

- [1] J. Shi, D. Ahmed, X. Mao, ... and T. J. Huang. *Lab on a Chip* **9**, 2890-2895 (2009).
- [2] X. Ding, S. C. S. Lin, B. Kiraly, ... and T. J. Huang. *Proceedings of the National Academy of Sciences* **109**, 11105-11109. (2012).
- [3] J. Shi, H. Huang, Z. Stratton, ... and T. J. Huang. *Lab on a Chip* **9**, 3354-3359 (2009).
- [4] G. Destgeer, K. H. Lee, J. H. Jung, ... and H. J. Sung, *Lab on a Chip* **13**, 4210-4216 (2013).
- [5] J. Lee, C. Rhyou, B. Kang, and H. Lee. *Journal of Physics D: Applied Physics* **50**, 165401 (2017).
- [6] D. Hartono, Y. Liu, P. L. Tan, ... and K. Lim. *Lab on a Chip* **11**, 4072-4080 (2011).

3D numerical modeling of acoustic streaming in sessile droplets from first principles.

Antoine Riaud^{*1,2}, Michael Baudoin¹, Olivier Bou Matar¹, Jean-Louis Thomas², and Philippe Brunet³

¹*Institut d'Electronique, de Microélectronique et Nanotechnologie (IEMN), LIA LICS, Université Lille 1 and EC Lille, UMR CNRS 8520, 59652 Villeneuve d'Ascq, France*

Email: michael.baudoin@univ-lille1.fr, URL: http://films-lab.univ-lille1.fr

²*CNRS UMR 7588, UPMC Université Paris 06, Institut des NanoSciences de Paris (INSP), F-75005, Paris, France*

³*CNRS UMR 7588, UPMC Université Paris 06, Institut des NanoSciences de Paris (INSP), F-75005, Paris, France*

³*Laboratoire Matière et Systèmes Complexes, UMR CNRS 7057, Université Paris Diderot, 10 rue Alice Domon et Léonie Duquet, 75205 Paris CEDEX 13, France*

1 Introduction

Acoustofluidics of sessile droplets offers a large span of functions from mixing and droplet fusion to locomotion and spray atomization[1]. The large discrepancies of time scales (between acoustics and hydrodynamics) and space scales (between the wavelength and the droplet size) creates a major memory burden that has stalled the development of 3D numerical models in recent years. In this article, we develop two memory-efficient numerical recipes to expedite 3D calculations of acoustic streaming in sessile droplets from first principles[2].

2 A glimpse of the numerical models

Acoustic streaming simulations are processed in two steps under a steady-flow assumption. First, in order to minimize the memory requirements, the acoustic field \tilde{p} is computed exactly in cylindrical coordinates (r, θ) . Even though the acoustic wave is a plane surface acoustic wave ($\tilde{v}_z|_{z=0}$), it can be decomposed into a sum of cylindrical harmonics $\tilde{v}_{l,z}|_{z=0}$ by circular Fourier transform (CFT). The acoustic field is then reconstructed by the inverse transform (ICFT):

$$\begin{array}{ccc}
 \text{Cartesian (3D)} & & \text{Cylindrical (r,z)} \\
 \text{Boundaries} & \tilde{v}_z|_{z=0} & \xrightarrow{\text{CFT}} \sum_{l=-\infty}^{+\infty} e^{il\theta} \tilde{v}_{l,z}|_{z=0} \\
 & & \downarrow \text{Solves in cylindrical coordinates} \\
 \text{Bulk} & \partial_i \tilde{p} + k^2 \tilde{p} = 0 & \xleftarrow{\text{ICFT}} \left(k^2 - \frac{l^2}{r^2}\right) \tilde{p}_l = -\partial_{rr} \tilde{p}_l - \partial_{zz} \tilde{p}_l - \frac{1}{r} \partial_r \tilde{p}_l
 \end{array} \tag{1}$$

with $k^2 = \frac{\omega^2}{c^2(1+i/Re_{ac})}$ and $Re_{ac} = \frac{c^2}{\omega\nu b}$. In fluids of non-vanishing dynamic viscosity μ , the waves gradually attenuate. This release of momentum generates the acoustic streaming of velocity $\bar{\mathbf{v}}$. Assuming an incompressible creeping flow in the droplet, the hydrodynamic equations read:

$$0 = \mu \partial_{jj}^2 \bar{v}_i + \mathcal{F}_i - \partial_i \bar{p} \quad \mathcal{F}_i = -\partial_i \langle \mathcal{L} \rangle + \frac{\omega^2 \nu b}{c^4} \langle \Pi_i \rangle, \tag{2}$$

with \mathcal{L} and $\Pi_i = \tilde{p} \tilde{v}_i$ the Langrangian and the power flux of the wave respectively. Both of these terms are known explicitly from the acoustic field computed previously. The streaming force is composed of a large gradient and small solenoidal term. Under the hypothesis of creeping flow, the gradient term is exactly compensated by a hydrostatic pressure build-up, whereas the solenoidal term $\frac{\omega^2 \nu b}{c^4} \langle \Pi_i \rangle$ generates vorticity and thus acoustic streaming. Due to its quadratic nature, the forcing term exhibits rapid variations that can only be captured by a highly resolved grid. These fluctuations have little effect on the general flow pattern because they are quickly damped by the fluid viscosity. Similarly, the forcing term of our numerical model is smoothed over space before processing the 3D hydrodynamic equations.

^{*}Current affiliation: Université Paris Sorbonne Cité, INSERM UMR-S1147, CNRS SNC 5014, France. Équipe labellisée ligue contre le cancer

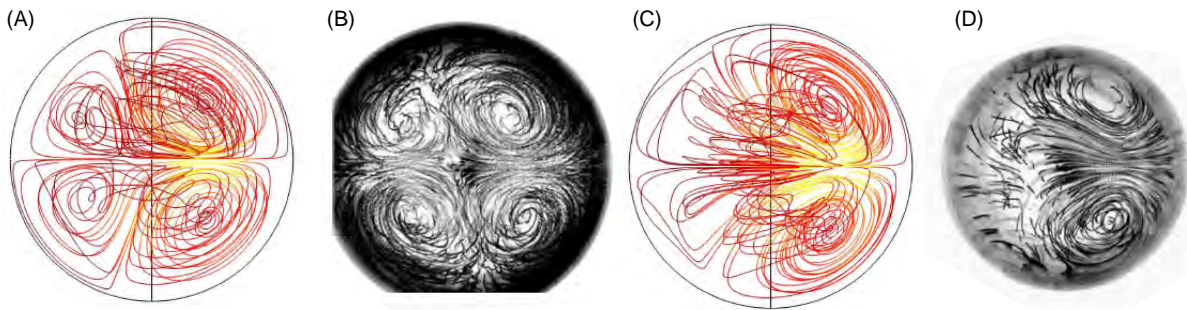


Figure 1: (A,B) Top view of acoustic streaming in 30 wt% and (C,D) 80 wt% glycerol droplets. (A,C) are streamlines from numerical results and (B,D) from experimental observations.

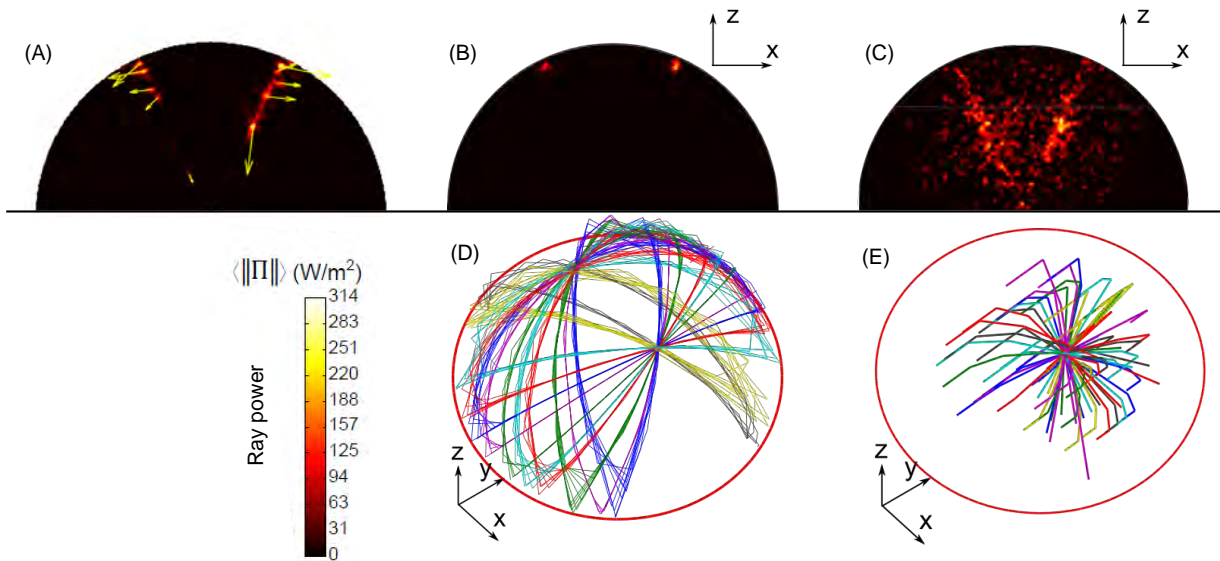


Figure 2: (A) Total acoustic field in water droplets, composed of (B,D) surface caustics and (C,E) volume caustics.

3 Key results and conclusion

These numerical studies agree quantitatively with experimental observations as shown in figure 1. This good agreement suggests that the forcing term and thus the acoustic field (shown in figure 2) are all correctly captured by the model.

According to the simulations, the acoustic field in aqueous droplets exhibits two types of focus points: surface caustics due to whispering gallery modes and volume caustics. In the case of hemispherical droplets, we observe that these whispering modes travel along the droplet surface in periodic orbits, a resonant phenomenon that enhances the acoustic streaming. We verified experimentally and numerically a variation in the flow pattern directly related to the change of the caustic structure.

Our study unveils for the first time the caustics that generate the flow in sessile droplets. Whispering gallery modes, non-Euclidian manifolds and caustics are all fundamental topics of wave physics. Their importance is here illustrated in the enhancement of acoustic streaming in sessile droplets.

References

[1] J. Friend and L. Yeo. *Rev. Mod. Phys.*, 83:647–704, 2011.

[2] A. Riaud, M. Baudoin, O. Bou Matar, J.-L. Thomas, and P. Brunet. *accepted for publication in J. Fluid. Mech.*, XX:xxxx, 2017.



Separation of submicron particles in Fabry-Perot acoustofluidic resonators

Prateek Sehgal¹ and Brian J. Kirby^{1,2}

¹Sibley School of Mechanical and Aerospace Engineering, Cornell University, Ithaca, New York 14853, US
E-mail: ps824@cornell.edu, URL: <http://blogs.cornell.edu/kirbyresearch/prateek-sehgal/>

²Department of Medicine, Division of Hematology & Medical Oncology, Weill–Cornell Medicine, New York, New York 10021, US

Introduction

Separation of submicron particles, particularly on the order of 100 nm, by acoustophoresis has been challenging to date because the acoustic radiation force (ARF) on the particles is weak and particle motion is often dominated by acoustic streaming. Some recent attempts have been made for size-based separation of submicron particles using surface acoustic waves (SAW) [1,2]; however, the size of the particles manipulated by ARF in these studies is limited to 500 nm, although numerous biological studies require manipulation of smaller particles. In this work, we present a SAW-based acoustophoretic device that integrates Fabry-Perot acoustic resonators in a microfluidic geometry to manipulate particles smaller than 500 nm. The Fabry-Perot type modality enhances the overall ARF on the particles and the SAW-based excitation suppresses the effects of Rayleigh acoustic streaming on the particles. To theoretically demonstrate the separation modality of our system, we present an analytical stochastic model that predicts size-dependent migration trajectories of the particles in acoustic potential landscape. Finally, we experimentally demonstrate the controlled acoustophoretic manipulation of 300-nm polystyrene particles and the separation of 300-nm and 100-nm particles with a separation efficiency of 86%. We also report good agreement between our analytical predictions and experimental observations.

Theory

Our device consists of one interdigitated transducer (IDT) that is bounded by Bragg reflectors on both sides, creating the Fabry-Perot acoustic resonator (FPAR). The PDMS microfluidic channel is bonded directly over the FPAR at an orientation angle ($\theta_f = 80^\circ$), as shown in Fig. 1. The transducer generates the standing SAW (SSAW) field by each finger-pair of the IDT and emanates the travelling SAW (TSAW) field from both sides of the IDT. The Bragg-reflectors reflect the TSAW and create a Fabry-Perot standing wave cavity. This cavity further enhances the overall SSAW field over the IDT, which is important to increase the ARF on submicron particles. The SSAW field couples to the fluid and generates standing acoustic field in the channel. The migration of particles in this acoustic potential landscape results in their size-dependent trajectories and sorting.

We obtain the migration trajectories of a Brownian particle, which is advected by the external flow field, with a vector chromatography-based model [3]. The migration angle (θ) of the particle is obtained as –

$$\tan \theta = \tan \theta_f \frac{Pe}{1 - e^{-Pe}} \int_0^1 \left[e^{Pe y - V_a(y)} \int_y^{y+1} \frac{dy'}{e^{Pe y' - V_a(y')}} \right] dy \quad (1)$$

where Pe is the particle Peclet number and $V_a(y)$ is the acoustic potential obtained from FEM simulations.

Analytical results: Transport of particles in the Fabry-Perot acoustofluidic device

Fig. 2a shows the size-dependent particle trajectories in our device at given pressure amplitude and flow velocity. The trajectories of the larger particles are dominated by acoustic potential and, therefore, align parallel to the IDT (i.e. $\theta = 90^\circ$). However, the trajectories of the smaller particles are dominated by advection strength (Pe) and, therefore, follow the flow field (i.e. $\theta = \theta_f = 80^\circ$). These size-dependent

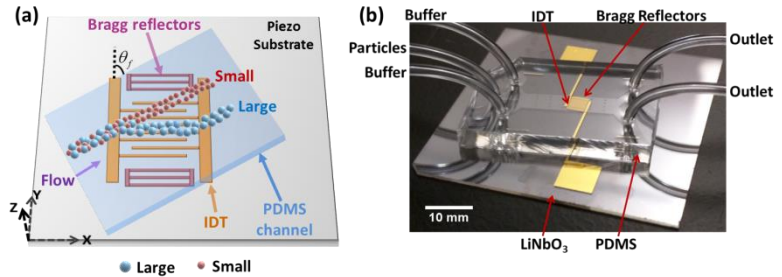


Figure 1: The Fabry-Perot acoustofluidic device. (a) Shows the schematic of the device. (b) Shows the device fabricated with standard lithography techniques.

differential trajectories result in size-based spatial separation of the particles. Fig. 2b demonstrates the size-dependent separation modality of our system.

From Fig. 2a, we also identify a size above which all particles migrate parallel to the IDT (i.e. $\theta = 90^\circ$) as threshold diameter. To separate bimodal populations, as in our study, with maximum spatial resolution, the threshold diameter should be located between the two populations and, importantly, close to the larger size population. Therefore, the threshold diameter should be appropriately tuned with the externally controllable system parameters, such as pressure amplitude (power) and flow velocity (flow rate), as shown in Fig. 2c. A smaller threshold, suitable for submicron particles, can be achieved at higher pressure amplitude and lower flow velocity. This also informs the use of the Fabry-Perot cavity, which enhances the pressure field in the system and enables higher throughput of separation.

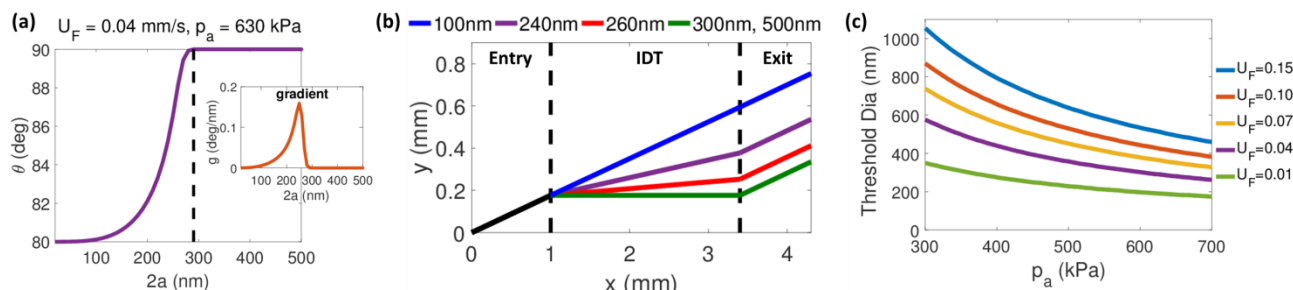


Figure 2: Analytical model for transport of particles in our device. (a) Shows the size-dependent migration trajectories of the particles, where ‘a’ is the particle radius. The inset shows the gradient (g) of the theta–size curve, which is used to tune the threshold diameter to obtain maximum separation resolution. (b) Shows the trajectory of the particles before (Entry), over (IDT), and after (Exit) the IDT region at same conditions as that of (a). (c) Shows the variation of the threshold diameter with externally controllable parameters – pressure amplitude (p_a) and flow velocity (U_F in mm/s).

Experimental results: Separation of 300-nm and 100-nm particles

Fig. 3a shows the controlled acoustophoretic manipulation of 300-nm polystyrene particles and the separation of 300-nm particles from 100-nm particles. The power density and the flow rate are tuned such that the threshold diameter is located between 300 nm and 100 nm. Consequently, the trajectory of the 300-nm population is dominated by the acoustic potential, whereas the trajectory of the 100-nm population is dominated by the flow field. The bands formation by 300-nm particles indicates that their transport is not dominated by acoustic streaming. Fig. 3b shows the quantification of fluorescent signal of each population and Fig. 3c shows that 86% of 300-nm particles are separated from the mixture. We obtained this separation at 3-fold lower power density and 6.7-fold higher total flow rate than previously reported parameters for the separation of 500-nm particles in one-port SAW device [1]. We attribute this enhanced acoustic effect and the capability of our device to manipulate 300-nm particles primarily to the Fabry-Perot modality.

From our analytical model, we also estimate the representative pressure amplitude in the fluid to be 3.07 MPa. At this pressure amplitude and average flow velocity (1.2 mm/s), we compare the analytical predictions with the experimental observations and obtain a good agreement, as shown by Fig. 3b.

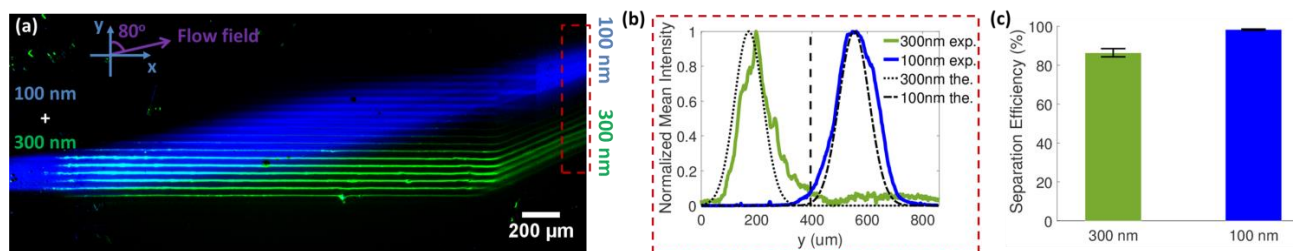


Figure 3: Separation of submicron particles. (a) Shows the mean fluorescent composite image of 100-nm (blue) and 300-nm (green) particles. The power density is 0.12 W/mm^2 and the total flow rate is 12.2 ul/min . The red dashed window after the exit of the IDT is analyzed for quantification. (b) Shows the experimental mean intensity distribution along y-direction for each population and analytical predictions for particle locations. (c) Shows the separation efficiency, which is calculated by assuming a splitter at $y=395 \text{ um}$ (vertical dashed line) in (b).

Conclusion

We have demonstrated, for the first time, the acoustophoretic separation of 300-nm and 100-nm particles in a Fabry-Perot acoustofluidic system. We have also presented an analytical model to predict the particle transport in our device, which matches closely with our experimental observations. We expect that our experimental platform can address biological challenges, such as separation of lipid vesicles, and our analytical model can be extended to precisely predict the transport of particles in numerous other systems.

References

- [1] D. J. Collins, T. Alan, and A. Neild, *Lab Chip* **14**, 1595 (2014).
- [2] M. Wu, Z. Mao, K. Chen *et al*, *Adv. Funct. Mater.* 1606039 (2017).
- [3] J. A. Bernate and G. Drazer, *J. Colloid Interface Sci.* **356**, 341 (2011).

Manipulation of sub-micro and nanoparticles using standing surface acoustic waves (SSAW) in a microchannel with air-jet impingement cooling system

Changdeok Seo¹, Sehyun Shin^{1†}

¹School of Mechanical Engineering, Korea University, Seoul, Korea

E-mail: s601010@korea.ac.kr

Introduction

Nanoparticle separation has been highly required in various biomedical applications for precision medicine. For instance, exosomes, which are cell-derived vesicles and observed in blood and urine, size range between 30 and 130 nm. The separation technique of cancer-cell-derived exosomes would be a critical clue to diagnose and treat cancer at earlier stages [1, 2]. In previous studies, we have found that surface acoustic waves (SAWs) are very effective at successfully separating fine particles and blood cells from one another in size [3, 4]. It should be noted that the acoustic force acting on the particles is proportional to the cube of the particle diameter (d^3), frequency (f) and square of the input voltage (V^2). In order to separate nanoparticles, the particle size becomes smaller, so input voltage and frequency must be increased significantly. Since the acoustical force is proportional to the square of the input voltage, it would be more efficient to increase the voltage. However, if the input voltage is increased, non-uniform temperature distribution related to heat generation will cause thermal cracking in the piezoelectric substrate, which can cause uneven heating of the substrate due to excessive thermal expansion near the heat source within 1 minute. Thus, in this article, we described a novel application of standing surface acoustic waves (SSAW) techniques with high input voltages for the separation of nanoparticles with air-jet impingement (AJI) cooling system which has large cooling capacity and without mechanical contact with piezoelectric substrate.

Air-jet Impingement (AJI) cooling system

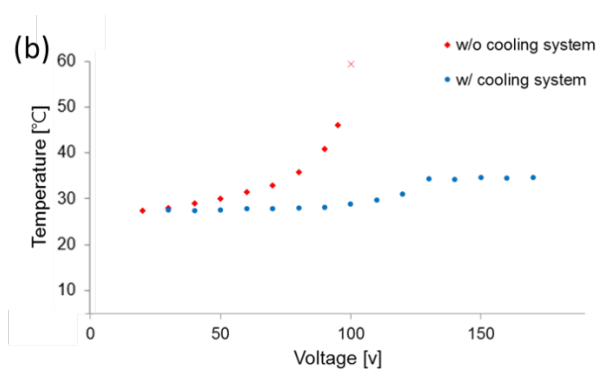
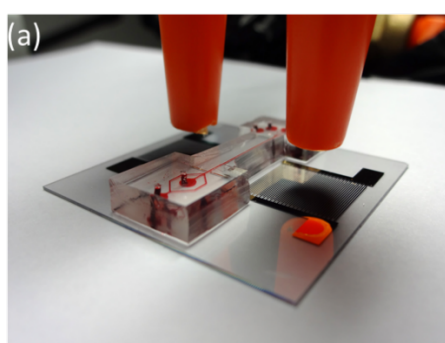


Fig. 1 (a) An optical image of SSAW-based microfluidic device with AJI cooling system. (b) Measured temperature at 1 min after applying various input voltages

The AJI cooling system using nitrogen gas was applied to the interdigitated transducer (IDT) center where heat concentration is the largest as shown in Figure 1 (a). Figure 1(b) shows measured temperature on the substrate near IDTs at 1 min after applying various input voltage. As the input voltage increases, the substrate temperature increases exponentially without the cooling system. When a maximum temperature is beyond 55°C at a room temperature (27°C), thermal crack was observed on substrate. With AJI cooling system, however, the substrate temperature near the IDT was maintained below 30°C at 1 min even for applying 150 V of the input voltage.

Manipulation of nano-particles

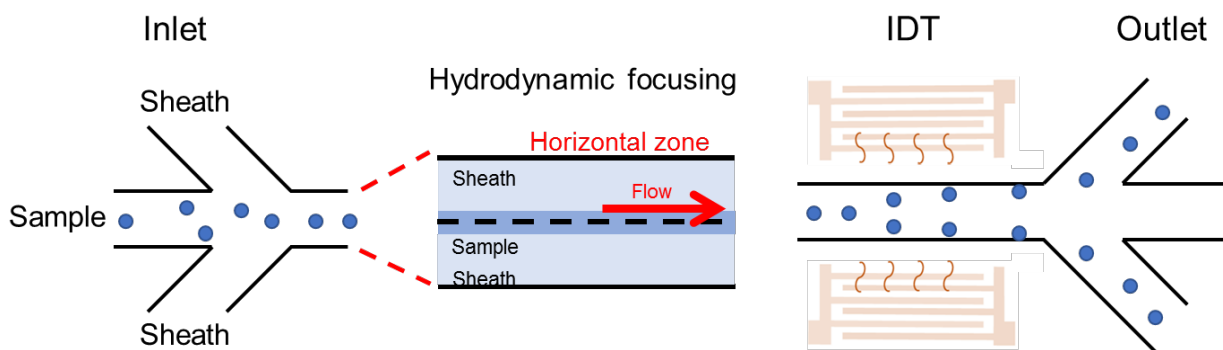


Fig. 2 Schematic image of manipulation of nano-particles. Sample nano-particles were focused to center of microfluidic channel by both sheaths hydrodynamically then pushed with acoustic force to the channel side walls. Acoustic power is applied by the voltages injected into both IDTs.

Nanoparticles were successfully pushed with acoustic force with 50 ~ 80 V of input voltage. For 500 nm sized particles, diffusion was not apparently observed at the exit and thus most of particles were collected in the mid-outlet without turning on SSAW. With SSAW-on, particles were easily pushed toward side walls and collected at the side-outlets. For 200 nm sized particles, even though diffusion was relatively large, most of particles were collected in the mid-outlet with controlling flow rate when SSAW is not activated. With activating the SSAW, 200 nm-particles were not effectively pushed with 62 V of input voltage. With increasing input voltage to 80 V, particles were pushed toward side walls and collected in the two side-outlets. For the 100 nm particles, it was observed that when the relatively high voltage (80 and 100 V) was applied, the particles concentrated in the center moved to side-outlets, but it was confirmed that many particles remained in the center channel. These results confirmed that nanometer-sized particles could be push with acoustic force with increasing input voltage.

Conclusion

We have demonstrated SSAW-based microfluidic technology to separate nano-sized particles. An essential feature of this technology is the application of a high voltage to the SSAW for one hour or more without heat cracking the substrate. Because this technology introduces a simple and easy air jet impingement cooling system, it is easy to apply this technology for SSAW's own experimental setup for high voltage applications. We demonstrate separation of nano-sized (100, 200 and 500 nm) engineering particles, but this technique can be extended to separate biological cells such as exosome, bacteria, and extra nano-sized cells. Therefore, due to the potential nature of current SSAW-based separation technology, it is possible to develop a wide variety of microsatellite analysis systems for deep tissue biopsy through integration with all detection systems in the near future.

References

- [1] C. Théry, M. Ostrowski, and E. Segura. *Nature Reviews Immunology* 9.8, 581-593 (2009).
- [2] R. Simpson, J. Lim, R. Moritz, and S. Mathivanan. *Expert review of proteomics* 6.3, 267-283 (2009).
- [3] J. Nam, H. Lim, D. Kim, and S. Shin. *Lab on a chip* 11, 3361–3364 (2011).
- [4] G. Destgeer, K. Lee, J. Jung, A. Alazzam, and H. Sung. *Lab on a chip* 13, 4210–4216 (2013).

Numerical modelling of acoustic radiation forces and streaming in microscale acoustofluidic devices with fluid-solid interactions

Nils Refstrup Skov and Henrik Bruus

Department of Physics, Technical University of Denmark, Kongens Lyngby, Denmark
 E-mail: nilsre@fysik.dtu.dk , URL: <http://www.fysik.dtu.dk/microfluidics>

Introduction

Microscale acoustofluidic devices are often complex systems, which cannot be modeled in their entirety due to a lack of computational resources. In setting up a numerical simulation of such devices, one must strike a balance between including the key physical phenomena and trimming away redundant elements that only add to computational cost. The former can for instance be fluid-solid interactions in soft and thin-walled devices [1], while the latter can be symmetries and regions with motion pointed entirely away from the regions of interest. In the following, we present improvements to our previous 2D model [1] and apply it simplifying modeling of a complex system.

Our prior model consists of a fluid domain and a solid domain, see Fig. 1(a). The fluid domain, governed by the Navier–Stokes equation, is encased to the sides and top by a solid domain, governed by the Navier–Cauchy equations, and on the bottom by a piezoelectric material along which a given surface acoustic wave is propagating. The fluid and solid domains are coupled through continuity in velocity and stress across the fluid-solid interface.

Improvements to the model

Perfectly matched layers (PML). The commonly used rubber PDMS has an acoustic damping length in the mm-range for frequencies around 5 - 10 MHz. PDMS-based acoustofluidic devices often have wall

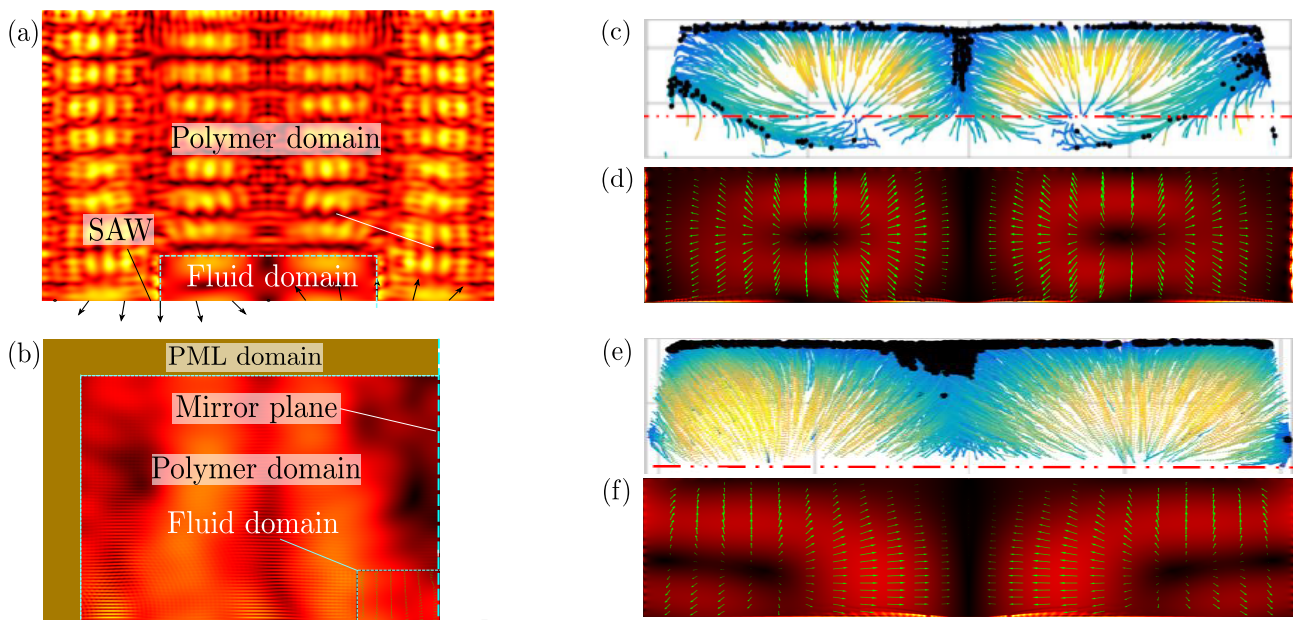


Figure 1: Sketch of the numeric model and comparisons between experimental and numeric results. (a) Velocity fields found in a polymer device using the numeric model before improvements. Due to computational restrictions, the device is shortened in both directions. (b) Velocity fields of the left half of the chip from (a), after implementing a PML domain and symmetry boundary conditions. (c) Experimental particle tracing results of 1 μm particles in a 600 μm -wide channel actuated at 6.404 MHz, from Ref. [2]. Black dots indicate final particle positions. (d) Numeric prediction of the acoustic radiation force of the device from (d), from zero (black) to high (red). (e) Experimental particle tracing results of 1 μm particles in a 300 μm -wide channel actuated at 6.404 MHz, from Ref. [2]. Black dots indicate final particle positions. (f) Numeric prediction of the acoustic radiation force of the device from (e), from zero (black) to high (red).

thicknesses in the cm-range, which thus absorbs all outgoing acoustic waves. Such perfect absorption can be modeled by implementing PML in the outer regions of the PDMS layer, see Fig. 1(b), which reduces the computational domain to sub-mm size, while maintaining a good representation of the acoustic fields in the physically relevant region near the channel, where the correct solid-fluid boundary conditions are maintained. *Symmetry and antisymmetry conditions.* Symmetrically actuated systems show a symmetric response, and similarly for antisymmetric systems. We utilize this in our model system, which is antisymmetrically actuated in the vertical direction and symmetrically in the horizontal direction: along the mirror-symmetry plane $y = 0$ in our model, the dotted line in Fig. 1(b), we implement the appropriate symmetry boundary conditions, effectively cutting the computational domain in half.

These two improvements of our numeric models open up for modeling of larger-scale acoustofluidic devices, and even allow for more realistic three-dimensional simulations. Using these improvements we have seen improved agreement between our simulation results and the experimental results in [2], as illustrated in Fig. 1(c)-(f)

Unit cell model of a multi-well system used in biophysical particle sorting

As a second example, we study the complex multi-well system of the Wiklund group at KTH, where an array of 10×10 wells is etched into a silicon substrate placed on thin glass place with a piezoelectric transducer attached below [3]. This system is too extensive in size and complexity to model in its entirety. We therefore proceed using the assumption that each of the 100 wells identical. For a single well, we therefore assume periodic boundary conditions in both lateral directions, which corresponds to an infinite array of identical wells with a homogeneous actuation from the bottom. The numeric model provides insight into how the acoustic fields vary with changes in the fluid reservoir height, the well geometry, and the crystalline direction of the anisotropic well material silicon, while ignoring inhomogeneous coupling effects between wells and the surrounding structures. Preliminary analysis of the pressure field in 3D is shown in Fig. 2(b), while a 2D snippet of the model with the acoustic streaming rolls within the well is shown in Fig. 2(c). Such patterns are also observed experimentally.

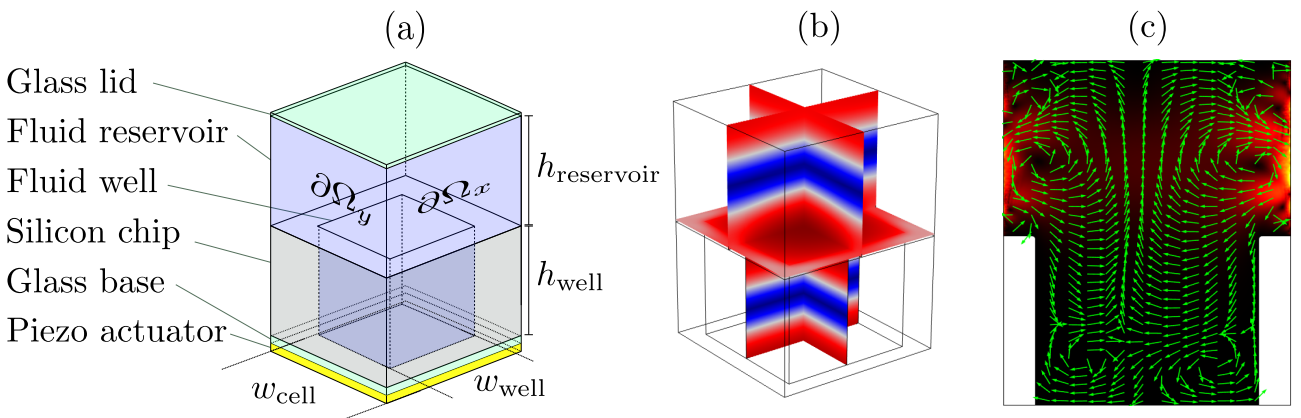


Figure 2: The unit cell of the multi-well system from the Wiklund group at KTH [3]. (a) Sketch of the layered glass-silicon-fluid-glass rectangular box with side length w_{cell} defining the computational 3D domain of the model. (b) Multi-slice plot of the first order pressure field in the fluid domain of the 3D model, from 0 Pa (blue) to 2 kPa (red). (c) Acoustic streaming patterns calculated in a 2D snippet of the model. Streaming rolls are seen within the well as well as in the reservoir above, corresponding to experimental observations.

Conclusion

Using the improved system shown in Fig. 1(b), our numeric model systems more closely represents experimental systems. We obtain a fair agreement between the experimental particle tracing results Fig. 1(c) and (e) and our numerically obtained acoustic radiation fields Fig. 1(d) and (f). The model still requires some fine-tuning by adjustments to the shear damping and velocity, which to date have not been measured reliably for PDMS.

The numeric unit-cell model in Fig. 2(a) show promise as a design tool for improving the full experimental multi-well system, based on the acoustic fields found in a single well. We are currently running simulations to study possible design improvements for the multi-well system defined in an off-stoichiometric thiolene polymer.

References

- [1] N. R. Skov and H. Bruus *Micromachines* **7**, 182 1-14 (2016).
- [2] N. Nama, R. Barnkob *et al.* *Lab Chip* **15**, 2700-2709 (2015).
- [3] B. Vanherberghen, O. Manneberg *et al.*, *Lab Chip* **10**, 2727-2732 (2010).



Detaching cells from cultivation flask using acoustic radiation pressure induced by Langevin transducer

Hanako Tauchi¹, Genichiro Fujii², Chikahiro Imashiro², and Kenjiro Takemura³

¹Futaba High School, Tokyo, Japan

²School of Open and Environmental System, Keio University, Yokohama, Japan

³Dept. of Mechanical Engineering, Keio University, Yokohama, Japan

E-mail: takemura@mech.keio.ac.jp, URL: <http://www.takemura.mech.keio.ac.jp>

Introduction

Cell culturing techniques are necessary for regenerative medicine and drug development applications. A cell culture process is, in general, manually conducted by a technician; cell seeding, culturing, detaching, collecting, and reseeded. Among these processes, the cell detaching process is highly affected by individual procedure and is exposed to serious risk of contaminations [1]. Automation of cell culture process has been developed [2], however, this messy detaching process still remains an open research problem. Here, we show a cell detaching method using acoustic radiation pressure from a standard, clinically ubiquitous cultivation flask. Notably, this approach provides stable cell detaching without possible contaminations.

Methods

Acoustic radiation pressure induced by a Langevin transducer is applied to a cell cultivation flask from the bottom (Fig. 1). A flask holder keeps the flask above the Langevin transducer with an appropriate gap. Water is introduced into the gap between flask and transducer to transmit the acoustic radiation pressure to the cells adhered to the flask surface. Note that cells are cultured in advance in the flask. With the acoustic radiation pressure exposure together with trypsinization, cells would be detached from the flask surface.

Mouse myoblast cells (C2C12) are used in cell detaching experiment. 1.0×10^6 cells are seeded in the 25-mL flask with 3-mL culture medium and are cultured for 24 hr in an incubator; shortly in the detaching experiment there are 2.0×10^6 cells on the flask. Then, cells are washed with 1 mL PBS twice followed by the introduction of 3-mL 0.005% trypsin-EDTA solution, which is a concentration of one tenth of trypsin-EDTA used in general trypsinization with pipetting for C2C12. Note that trypsin may damage cell membrane and decrease cell proliferation [3]. Acoustic radiation pressure induced by a 156.8-kHz ultrasonic vibration with the amplitude of $0.94 \mu\text{m}$ is applied to the cells for 30 sec after 2.5 min trypsinization without pipetting. For comparison, a control sample, which is not exposed to the acoustic pressure and detached with traditional pipetting method, is prepared. In this control method, cells are detached with 3 min trypsinization and 5 times thorough pipetting.

The number of cells collected with each method is estimated with a hemocytometer to evaluate the cell detachment capability of the proposed method. Additionally to demonstrate non-invasiveness of the proposed method, the proliferation rate of the collected cells with the both method are estimated. For the estimation of proliferation, 0.5×10^5 cells detached with each method are cultured for 24 hr, and the number of cultured cells are evaluated.

Results

The number of cells detached by the proposed method, N_p , is compared with that by the control method, N_c , in Fig. 2. As shown, N_p is statistically superior to N_c (ANOVA, $n = 4$, **: $p < 0.01$). As mentioned above, the number of cells adhered on the flask before the experiment is 2.0×10^6 . Thus the proposed method can successfully detach almost all cells from the flask with tenfold diluted 0.005% trypsin, meaning that the cell proliferation is possibly maintained high.

The number of cells after the 24-hr culture following the detachment by the proposed method, N_p^c , is compared with that by the control method, N_c^c , in Fig. 3. As shown, there is no significant difference in the proliferation of those methods. However, the standard deviation of N_p^c is much smaller than N_c^c . This result indicates that the proposed method gives no negative effect on cell proliferation and that the proposed method is more stable than the traditional pipetting method requiring a matured procedure.

Conclusion

This demonstration of cell detachment method using acoustic radiation pressure shows that cells adhered on a standard, clinically ubiquitous cultivation flask surface are detached without any manual procedures even with tenfold diluted trypsin. This novel technique potentially addresses one of the biggest challenges for the automation of cell culture process.

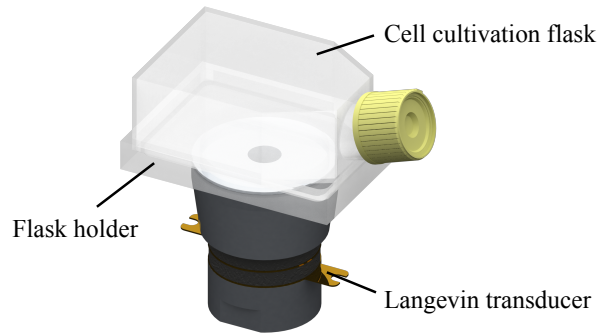


Figure 1: Schematic image of cell detaching device using Langevin transducer

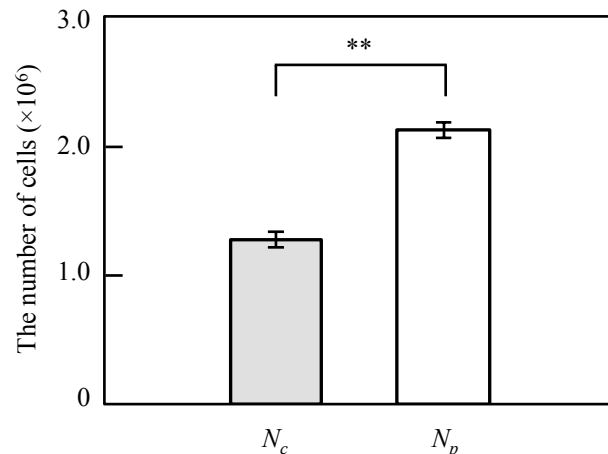


Figure 2: The number of cells detached with the control method, N_c , and the proposed method, N_p . Cells were seeded onto the flask, cultured for 24 hr and then detached with each method. The number of initially seeded cells was 1.0×10^6 (mean \pm SD, $n = 4$, **: $p < 0.01$).

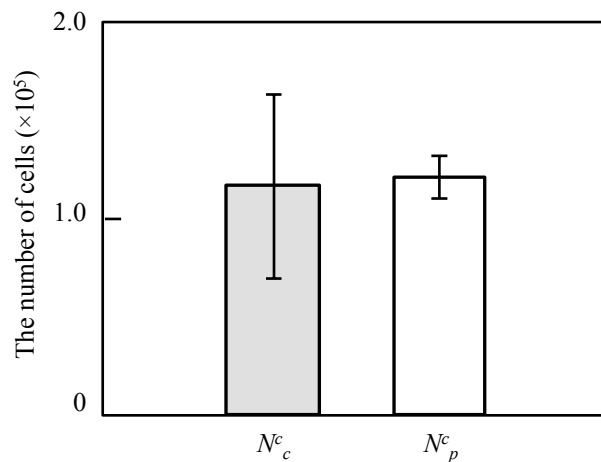


Figure 3: The number of proliferated cells detached with the control method, N_c^c , and the proposed method, N_p^c . Cells were seeded onto the flask following the detachment experiment, and were cultured for 24 hr. The number of initially seeded cells was 0.5×10^5 (mean \pm SD, $n = 4$).

Acknowledgement

This work was supported by Keio University Global Science Campus program supported by Japan Science and Technology Agency, and JSPS KAKENHI under Grant JP16H04259.

References

- [1] Maria E. Kempner and Robin A. Felder. SLAS TECHNOLOGY: Translating Life Sciences Innovation, **7**, 2 (2002)
- [2] Robert James Thomas, Amit Chandra, Yang Liu, Paul C. Hourd, Paul P. Conway, David, J. Williams, Cytotechnology, **55**, 1, 31–39 (2007)
- [3] Hirai H., Umegaki R., Kino-Oka M., Taya M., J Biosci Bioeng, **94**, 4, 351-356 (2002)



Acoustically driven elastic membrane-based microfluidic mixer

Abel L. Thangawng¹, James F. Tressler², and David C. Calvo¹

¹Acoustics Division (Code 7165), US Naval Research Laboratory, Washington DC, USA

²Acoustics Division (Code 7130), US Naval Research Laboratory, Washington DC, USA

E-mail: abel.thangawng@nrl.navy.mil

Introduction

Efficient mixing in a microfluidic system is a critical function necessary for the stand-alone lab-on-a-chip microdevices. Thus, both passive and active mixing in microfluidic channel have been studied by many different groups [1-4]. Using the resonant oscillation of trapped air bubbles, Ahmed, et al [3, 4] demonstrated the possibility of the fast mixing and simplicity of components integration for an acoustically induced mixing in a microdevice. In this work, we demonstrated a very robust, simple, and efficient microfluidic mixing using a suspended polydimethylsiloxane (PDMS) membrane inside microfluidic channels.

Device Fabrication and Experimental Setup

Unlike trapped air bubbles in a microfluidic channel as a source of acoustic cavitation, the suspended PDMS membrane is a permanent structure and is extremely robust. A 10 μm thick PDMS membrane was bonded onto a thin sheet of PDMS that has array of cylindrical cavities with a predetermined diameter to form suspended membranes. Soft lithography and plasma activated PDMS bonding process were used to make all the PDMS devices. See Figure 1 for a schematic of the experimental setup and the cross section view of the device. The PZT piezo element used to transduce acoustic signal was embedded in an acrylic base using epoxy. While the free PZT piezo element has a resonant frequency around 30 kHz, the acrylic plate-PZT base used in this work exhibits multiple peak frequencies, including 17.7 kHz and 24.0 kHz, as determined by the spiked responses in impedance spectral analysis.

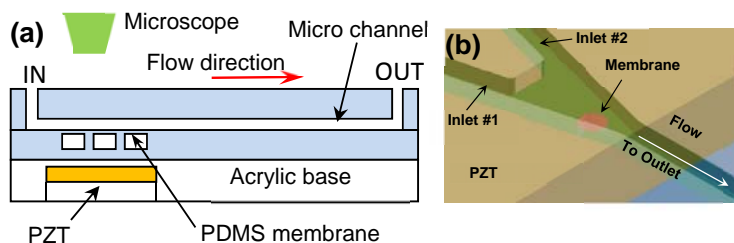


Figure 1: (a) Side view of experimental setup. The PZT transducer (embedded in acrylic base) is placed directly under the suspended PDMS membranes. The PZT driving frequency is tuned and is turned ON and OFF to observe the membranes' response. (b) The isometric perspective view of experimental device for clarity.

Results and Discussion

Two sets of experiments were carried out. First, for open chamber tests, a few microliters of polystyrene particle suspension was deposited on an array of suspended PDMS membranes. As the driving frequency of the piezo element is changed incrementally, acoustic streaming was observed (movement of particle suspension) directly on top of the membranes (Figure 2) when the membranes frequency closely matches to that of the acrylic-PZT base. Polystyrene particles were displaced all around each membrane, eventually forming the grid pattern as shown in the inset of Figure 2(b).

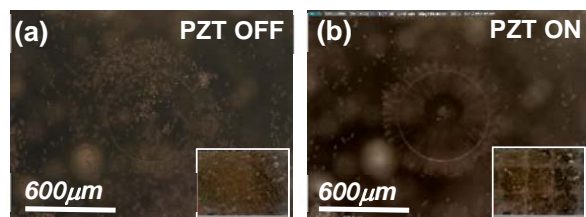


Figure 2: Open chamber test of acoustically induced elastic PDMS membrane (600 μm diameter) vibration at 22 kHz. Particles suspensions were displaced away from the active membrane regions (b). Images in insets show before (a) and after (b) the PZT were turned on to activate the array of membranes.

For the second set of experiments, mixing in microfluidic channels was demonstrated. Two different configurations of PDMS devices were used. In the first configuration, four 250 μm diameter PDMS membranes in series were imbedded in a microchannel with a cross section of 375 μm (width) x 125 μm (height). Two streams of fluids, dye and clear water, were pumped at 10 $\mu\text{l}/\text{min}$ each. The membranes were then driven at one of the resonant frequencies of the PZT base, 23.8 kHz, which is the closest to one of the

resonant frequencies of the membrane, 28.6 kHz. Though not driven at optimal setting, a complete mixing of the two fluid streams (dye and water) was achieved approximately within 135 milliseconds, which is estimated using the fluids volumetric flow rates and taking the mixing distance as the length spanned by the first two membranes (Figure 3) as the fluids appeared completely mixed by the time they passed the second membrane. This result is comparable to the best of micromixers as summarized by Lee, et al [1]. The darker region in Figure 3 is due to the imbedded PZT under the PDMS device.

The second microfluidic channel configuration tested has a single 600 μm diameter membrane strategically positioned at the merging region of a Y-channel. The estimated natural frequency of the membrane, closest to the acrylic-PZT base's natural frequency, is 19.7 kHz for a 10.0 μm thick PDMS membrane. In this configuration, the mixing was observed to be instantaneous at 17 kHz as a completely mixed stream can be seen at a few hundred microns upstream before the two separate streams reach the membrane (Figure 4). The unmixed fluids are presented only in the two separate input channels. This instantaneous mixing is attributed to the more vigorous mixing due to the membrane natural frequency that matches closely with the acrylic-PZT base which creates much stronger acoustic streaming, the slower average linear velocity due to the shape and dimension of the channel in the mixing region, and most importantly, the acoustic streaming that radiates in all radial direction (as evident from Figure 2b) from the PDMS membrane. Some of the discrepancies in the experimental and analytical frequency estimates are likely due to the variation or accuracy in the geometry, particularly the thickness, of the membrane.

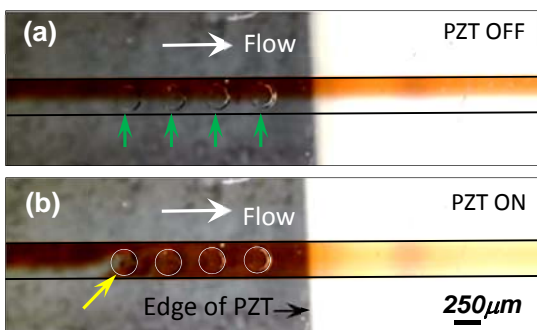


Figure 3: Mixing inside a microfluidic device. Before (a) and after (b) activation of 4-250 μm diameter PDMS membranes with PZT at 23.8 kHz. Flow rates for fluids: 10 $\mu\text{l}/\text{min}$ for dye and water. Green arrows in (a) indicate the membrane location and Yellow arrow in (b) indicates the first point of acoustic streaming due to membrane's vibration. The membranes are also identified with White circles in (b). The edges of the channel are highlighted for better visibility. Estimate mixing time is 135ms.

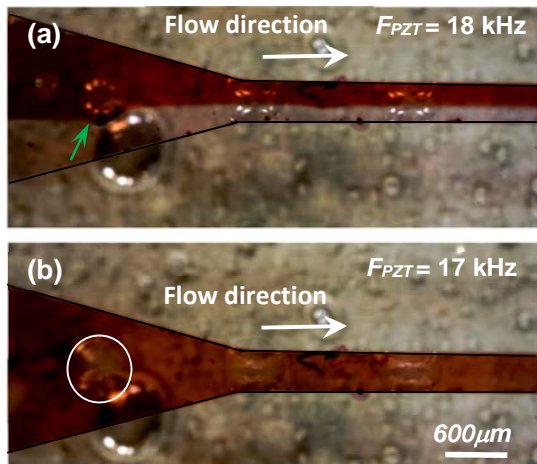


Figure 4: Improving mixing time by strategic placement of membrane element. A 600 μm diameter PDMS membrane located at the merging area of the Y-channel was actuated at (a) 18 kHz – no mixing and (b) 17 kHz – complete mixing. The mixing occurs *instantaneously* at 17 kHz. The complete mixing of the dye and clear fluid was observed a few hundred micrometers before the fluids reach the membrane. The unmixed fluids are only inside the input channels. Flow rates for fluids: 25 $\mu\text{l}/\text{min}$ for dye and water. Green arrows in (a) indicate the membrane location and the membrane is identified with a White circle in (b).

Conclusion

We have demonstrated a simple yet very effective elastomeric membrane-based microfluidic mixer that can be easily integrated into stand-a-lone microdevices. The membrane natural frequency can be easily tailored by changing the diameter and or the thickness, and by strategically placing the membrane within the device, instantaneous mixing can be achieved as demonstrated.

References

1. Lee C-Y, et al., "Microfluidic Mixing: A Review, Int. J. Mol. Sci. 2011, 12, 3263-3287
2. Garstecki, P, et al "Mixing with bubbles: a practical technology for use with portable microfluidic devices," Lab Chip, 2006, 6, 207–212.
3. Ahmed, D, et al., "A millisecond micromixer via single-bubble-based acoustic streaming," Lab Chip, 2009, 9, 2738–2741.
4. Ahmed, D, et al., "A fast microfluidic mixer based on acoustically driven sidewall-trapped microbubbles," Microfluid Nanofluid (2009) 7:727–731.



Acoustic streaming and instability of oscillatory boundary layers in an acoustofluidic channel.

Charles Thompson, Kavitha Chandra, and V. Mehta

University of Massachusetts Lowell, Lowell MA, United States
E-mail: charles_thompson@uml.edu

The fluid dynamic mechanisms that govern the stability of time-periodic boundary layer flows have been studied by numerous investigators starting with Li [1] over the past 60 years. The motivation for these studies stems from applications in mass transport and acoustic receptivity in mean-flow wall boundary layers [2].

For spatially varying two-dimensional channel flows the stability of the wall boundary layer to three-dimensional vortical disturbances is governed by the magnitude of three non-dimensional parameters. These are the wall slope ε , the Strouhal number S which equals to the ratio channel height to the particle displacement and finally the oscillatory Reynolds number R which is equal to the square of the ratio of the channel height to the Stokes layer thickness. The stability of the boundary layer is a function of the magnitude the streaming Reynolds number $R_s = R/S^2 = U^2/(\omega\nu)$, where U is the particle velocity amplitude, ω is the frequency of oscillation, and ν is the kinematic viscosity of the fluid. In physical terms, the streaming Reynolds number is the ratio of the inertial and viscous forces. Bifurcation from linear stability occurs for $R_s > R_c$ where R_c is the critical streaming Reynolds number.

Merkli and Thomann [3] were the first to identify the critical role that boundary geometry can play in boundary layer destabilization. In their experiments, conducted using a standing wave tube, they demonstrated that geometry perturbations that result from the introduction of a hot-wire anemometer placed in the wall of the tube can trigger instability at four times lower amplitude, $R_c/4$. For the spatially varying two-dimensional channel, when the wall boundary curvature is introduced, it has been shown that the critical streaming Reynolds number will depend on the boundary geometry as well as the amplitude of the basic oscillatory flow [4,5].

In this work, we will examine the mechanisms governing the generation of unstable vortical disturbances and their spatiotemporal characteristics. Time-harmonic boundary and pressure gradient generated flows are of particular interest. In the inner region near the solid-fluid interface, the vorticity stretching due to fluid compressibility is not considered. A curvilinear coordinate based pseudo-spectral method is developed to accommodate temporal variations in the channel's geometry. The method allows for the direct numerical solution of the three-dimensional time-dependent Navier-Stokes equation for high streaming Reynolds conditions and the comparison with theoretical nonlinear stability results. An examination of the conditions for centrifugal destabilization and transition is undertaken, and the interconnection between acoustic streaming and acoustically induced instability established.

References

- [1] H. Li, Stability of oscillatory laminar flow along a wall, US Army Beach Erosion Board Tech Memo. 47 (1954).
- [2] C. Thompson and M. Manley, Linear Stability of stagnation flow, *Physics of Fluids*, **1**, 1350 (1990).
- [3] P. Merkli and H. Thomann, Transition to turbulence in oscillating pipe flow, *J. Fluid Mech.*, **68**, 567 (1975).
- [4] C. Thompson, A. Mulpur, V. Mehta and K. Chandra, Transition to chaos in acoustically driven flows, *J. Acous. Soc. Am.*, **90**, 2097 (1991).
- [5] V. Mehta, C. Thompson, A. Mulpur and K. Chandra, Chaotic motion in a oscillatory boundary layer, *Chaos*, **6**, 601, (1996).



Acoustophoretic manipulation of sub-micron particles using density gradients

David Van Assche, Per Augustsson

Department of Biomedical Engineering, Lund University, Lund, Sweden
 E-mail: davassch@gmail.com, per.augustsson@bme.lth.se

Direct and precise manipulation of sub-micron particles such as bacteria, platelets, organelles, microvesicles, exosomes or virus particles is challenging. Here we show experimental evidence of separation of two particles that are both below the critical size as determined by the classical theory for Rayleigh streaming and acoustic radiation on spheres. We do this by introducing a gradient in acoustic impedance across the width of a standard bulk acoustic wave half wavelength flow through resonator. Stabilizing forces acting directly on the interface region between the two fluids efficiently reduce the acoustic streaming in the bulk.

Acoustophoresis is a gentle and robust method that has been demonstrated for concentrating, trapping, washing and sorting cells [1]. Due to acoustic streaming acoustophoresis was limited to objects larger than $\sim 2 \mu\text{m}$ but was recently extended to sub-micron particles by redirecting, but not stopping, the acoustic streaming by 2D-acoustic-wave action [2]. The method enabled concentration of bacteria in a rotating acoustic streaming field but is not applicable to separate sub-micron objects or to translate sub-micron particles across molecular gradients. Sub-micron particle separation was recently demonstrated using surface acoustic waves [3].

Acoustic force density acting on inhomogeneous fluids, i.e. fluids with an acoustic impedance gradient, relocates fluids into a stable configuration and that this configuration is different from the typically layered configuration caused by gravity [4]. It was observed that acoustic streaming is suppressed in the bulk of the inhomogeneous fluid. The suppression of acoustic streaming would allow separation of sub-micron particles and enable transfer of particles across molecular gradients. **Fig. 1.**

Our results show that it is possible to separate $0.5\text{-}\mu\text{m}$ -diameter and $1\text{-}\mu\text{m}$ -diameter particles in a standard acoustophoresis channel. A typical silicon-glass microchannel, with two inlets and two outlets, was used for the experiments. To create an inhomogeneous medium two fluids with different acoustic impedance were introduced using Ficoll PM70 as density modifier. A water solution with $0.5 \mu\text{m}$ and $1 \mu\text{m}$ polystyrene particles in suspension was introduced at the sides, while a Ficoll solution (5%) without beads was introduced in the center. The sample throughput was $10 \mu\text{L}/\text{min}$.

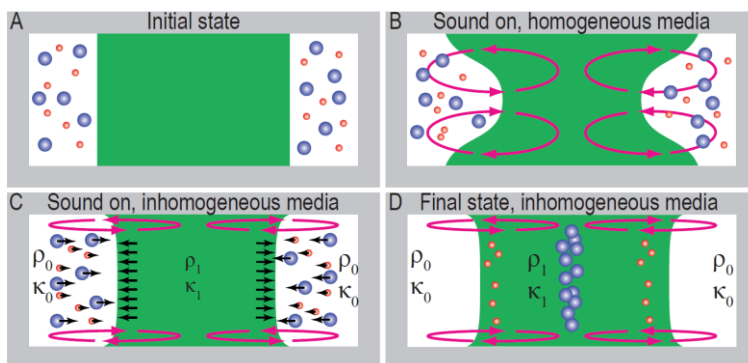


Figure 1: Separation principle. (A) Particles ($1 \mu\text{m}$ blue and $0.5 \mu\text{m}$ red) are injected at both sides of a central particle-free medium. (B) For homogeneous medium streaming dominates the motion of all particles. (C) For inhomogeneous medium stabilizing forces confine streaming rolls to the floor and ceiling enabling (D) particles to separate based on differences in radiation velocity.

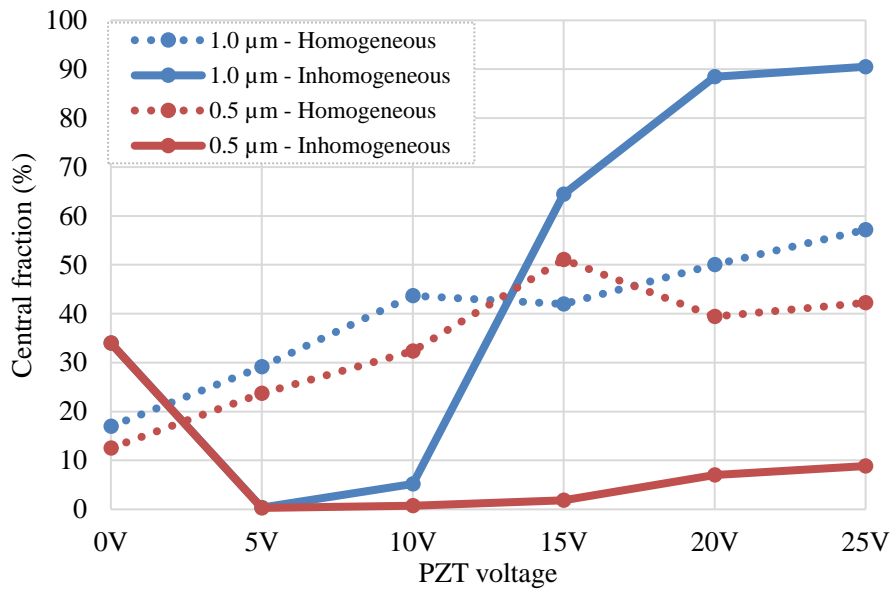


Figure 2: This figure shows the fraction of particles collected in the center outlet. Using a homogeneous medium (dotted lines) the central fraction of both 1.0 μm (blue) and 0.5 μm (red) increase in a similar way due to the mixing effect of acoustic streaming. For the inhomogeneous medium (solid lines), an increase in the collected fraction of 1.0 μm can be observed, compared to the 0.5 μm particles, because of the difference in radiation velocity.

The results show that for a homogeneous medium the central fraction of both particles increases to 50% with applied piezo voltage which is indicative of mixing due to acoustic streaming. Using an inhomogeneous medium the acoustic streaming is suppressed and this allow the 1 μm particles to migrate to the central outlet while the 0.5 μm particles remain at the sides. The purity of both particles increased from initially 50% to 90% in the central respectively the side outlet with a recovery of >50% where 80% is the theoretical max for the flow system and sample volume used.

We conclude that our results correspond well to the experimental and numerical work on particle trajectories in inhomogeneous acoustic media that will be presented in parallel with this work. We believe that the development points towards new acoustic separation and assay strategies for sub-micron biological particles such as bacteria, virus and exosomes.

References

- [1] Bruus, H., et al., Lab on a Chip, 2011. 11(21): p. 3579-80.
- [2] Antfolk, M., et al., Lab on a Chip, 2014. 14(15): p. 2791-2799.
- [3] Wu, M., et al., Advanced Functional Materials, 2017. 27(14). DOI: 10.1002/adfm.201606039
- [4] Karlsen T. J., et al., Physical Review Letters, 2016. 117(11): 114504.



Reproducible bubble-driven acoustic streaming for flow and particle manipulation in a microchannel

Andreas Volk and Christian J. Kähler

Institute of fluid mechanics and aerodynamics, Bundeswehr University Munich, Neubiberg, Germany
 E-mail: andreas.volk@unibw.de

Introduction

Miniaturized acoustofluidic devices receive growing interest in biological and medical applications. In this context, ultrasound-driven bubbles can be used to create a second order streaming field which allows to manipulate flows and particles on microscales. As the size of the bubble, which has a strong influence on the streaming field, is typically unstable, an automatized bubble size control system is presented in this work that allows performing reliable and reproducible experiments. The three dimensional structure of the bubble-induced streaming field is analyzed with particle tracking velocimetry (PTV) and the capability of the system to sort particles based on their physical properties is shown.

Reproducible bubble induced streaming

Acoustically-driven bubbles induce a secondary acoustic streaming field in the surrounding liquid that can be used to manipulate particles, cells and microorganisms in microchannels [1,2]. By adding a lateral side pit to a microfluidic channel, the bubble can be placed at a well-defined location. As the channel is filled with water, air is trapped in the side pit and a bubble of cylindrical shape is formed as shown in Fig. 1. This method is very flexible as the strength and shape of the streaming field can easily be changed by varying the actuation frequency and voltage. Despite these advantages a common but often unspoken problem when using acoustically actuated microbubbles is the reproducibility of the experiments. Bubbles in silicone microchannels, that are commonly used in the community, show a typical growth that alters the strength and shape of the streaming fields as shown in Fig. 2 (a), leading to non-reproducible results. A key goal for reliable investigations with bubble induced streaming is therefore their control and size stabilization. We present an automatized pressure control system, shown Fig. 1, that is capable to stabilize the protrusion depth d of a $80\ \mu\text{m}$ -wide microbubble with a precision of $\sim 0.5\ \mu\text{m}$. We explain how humidity, temperature, and pressure influence the growth of the bubble and how the control setup compensates these effects to achieve a constant bubble size [3].

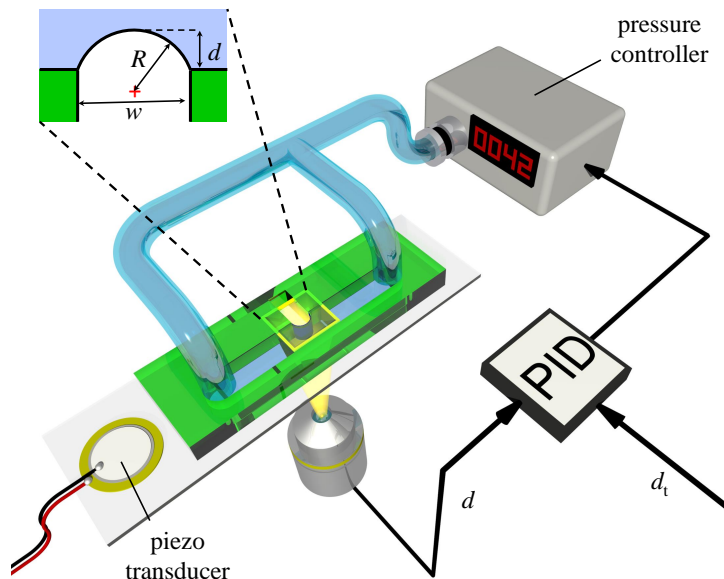


Figure 1: (a) System for automatized bubble control. A PDMS-microchannel is filled with liquid (PDMS in green, liquid in blue). Air gets trapped inside a lateral side pit of width w and a cylindrical bubble with Radius R is formed. The bubble interface is observed with a microscope and its protrusion depth d is detected. A PID-algorithm compares d with the target protrusion depth d_t and adapts the bubble by adjusting the pressure in the channel with a pressure controller.

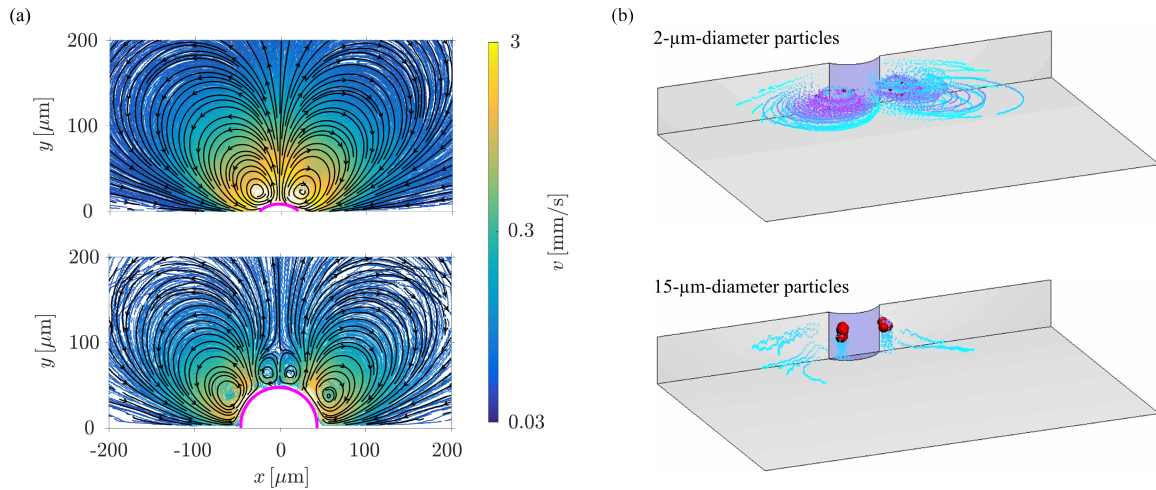


Figure 2: Bubble-driven acoustic streaming. (a) PTV-measurements of flow fields. Bubbles are actuated at a frequency $f = 21.8$ kHz and a peak to peak voltage $U = 40 V_{pp}$. Bubbles with small protrusion depth d show a typical flow field of two counter-rotating vortices. For larger bubbles additional vortices appear in the center of the bubble with inverse direction of rotation. (b) Trajectories of finite-sized particles. Large particles are focused at two distinct 3D-locations symmetric to the bubble center within a short time scale of ~ 1 s. Smaller particles also focus in the vertical direction forming ring structures within a time scale of ~ 10 s. Time-line illustrated by colors (cyan to magenta).

Topology of bubble-driven streaming flow

The topology and strength of bubble-driven streaming fields are investigated as a function of the bubble height by using a three-dimensional particle tracking technique [4]. The bubble is actuated with a piezo transducer as shown in Fig. 1 at a frequency $f = 21.8$ kHz and a peak to peak voltage $U = 40 V_{pp}$. The flow field near a small bubble ($h = 0.11 w$) consists of two counter-rotating vortices, whereas additional vortical structures are observed for larger bubbles ($h = 0.68 w$) as shown in Fig 2 (a). Besides the qualitative difference of the flow field, the mean streaming velocity is changing from $272 \mu\text{m/s}$ for small to $173 \mu\text{m/s}$ for large bubbles. It can be seen that the protrusion depth d of the bubble has a strong influence on the streaming field. In applications, the bubble size should therefore be adjusted to the specific purpose of a microfluidic device.

Size-sensitive particle migration in bubble driven streaming

One application example of bubble-driven streaming is the sorting of particles. In this experiment, differently sized polystyrene-particles ($2 \mu\text{m}$ diameter and $15 \mu\text{m}$ diameter) are introduced into the liquid and their trajectories are determined with PTV. In general, particles migrate across the streamlines and get focused towards the center of the vortical structures as shown in Fig 2 (b). For increasing particle diameter, a faster and more pronounced focusing can be observed such that the largest particles are focused at a distinct location whereas smaller particles end up in a ring structure. Whereas the focusing time for large particles is in the order of ~ 1 s, it is much larger for small particles ~ 10 s. As the behavior of particles in the streaming flow depends on their size, this system can be used in applications to sort, focus and enrich particles of a specific type. As this method can be also applied to cells and microorganisms it is an interesting tool for biomedical applications.

Conclusion

In this work we show how a bubble-driven acoustic streaming flow is influenced by the bubbles protrusion depth. We present a system that allows to control the bubble in order to achieve a reproducible streaming flow which is then quantified with PTV-measurements. By introducing finite sized particles, we show the capability of this system to sort and focus particles based on their physical properties.

References

- [1] P. Marmottant and S. Hilgenfeldt. Proc. Natl. Acad. Sci. USA **101**, 9523 (2004).
- [3] D. Ahmed, A. Ozcelik, N. Bojanala, N. Nama, A. Upadhyay, Y. Chen, W. Hanna-Rose, and T. J. Huang, Nat. commun. **7**, 11085 (2016).
- [3] A. Volk, M. Rossi, C. J. Kähler, S. Hilgenfeldt, and A. Marin. Lab Chip **15**, 4607 (2015).
- [4] R. Barnkob, C. J. Kähler, and M. Rossi, Lab Chip **15**, 3556 (2015).



Drastic sensing enhancement using acoustic bubble-induced agitation

Jie Xu¹, Andrea De Vellis¹, and Dmitry Gritsenko²

¹Department of Mechanical and Industrial Engineering, University of Illinois at Chicago, Chicago, USA
 E-mail: jieuxu@uic.edu, URL: <http://xu.uic.edu>

Introduction

There is a high demand for ultrasensitive and cost effective sensors in many pressing situations, varying from biodefense, disease detection to environmental monitoring. Since the sensor signal-to-noise ratio increases with decreasing sensor size, many researchers are expending considerable effort to fabricate smaller devices. However, being small has its own problem: mass transport become less effective. Therefore, most micro/nanoscale affinity-based sensors are limited by diffusion. For example, it will take more than a day for the first molecule (in case of a 20-based ssDNA) to find a 10 nm sized sensor at 1 fM concentration via diffusion only [1]. In the past, convection has often been used to help with analyte delivery to sensors' surface. Unfortunately, increasing the flow rate will only drastically increase the pressure in the channel up to the device breakage point. Therefore, an effective mixing method that can be easily integrated to a sensing device is highly desirable. Microfluidic-based mixing devices can generally be classified as passive and active mixers, both of which have attracted considerable attention in the microfluidic community. Passive micromixers usually rely on specific geometry designs to cause secondary flows inside a laminar pressure-driven flow. Passive mixers (such as herringbone grooves [2]) often require long channel length and rely upon high flow rates, and thus high pressure drops. Active micromixers, in contrast, employ external energy to introduce a local turmoil in a liquid to enhance mixing, thus providing better and more controllable mixing without global increase in pressure. As a unique active actuation scheme, microscale oscillating bubbles in an acoustic field can be used to create microstreaming flow and is perfectly suitable for sensing enhancement due to the remote actuation and easy system integration [3]. In this presentation, we demonstrate that significant sensing enhancement for graphene based nanosensors can be achieved using acoustic bubbleblers. The reduction of sensor response time exhibited resonant behavior with a resonant peak when plotted with respect to frequency. The working frequency range is therefore determined from this peak for sensor operation.

Results and Discussion

Our results shown in Figure 1 and Table 1 demonstrated that significant sensing time reduction (up to 95.5%) for graphene-based nanosensors could be achieved once the diffusion limits were overcome with the help of surrounding microbubbles. These microbubbles were passively trapped in microcavities fabricated on four side walls and were actuated by a piezoelectric actuator.

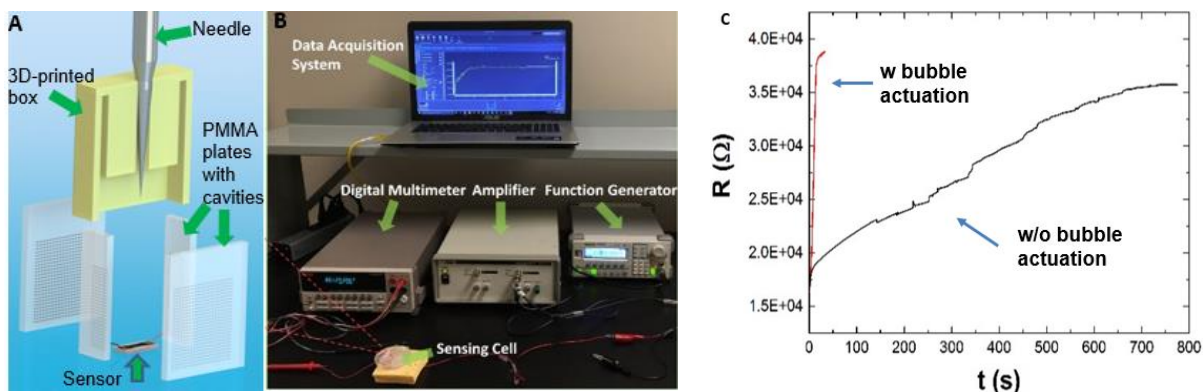


Figure 1. A) PMMA plates with microcavities were fixed vertically inside a 3D-printed box and placed above a graphene nanosensor. PH buffers were injected into the box from the top and microbubbles were trapped passively inside the cavities. B) Experimental setup. A piezoelectric actuator glued at the bottom of the sensing cell was used for acoustic actuation. C) Example sensing curves for pH=4.

The results in Table 1 show that without bubble actuation, sensing times are longer in acid, and with bubble actuation, sensing times are longer in alkali, which indicates that diffusion limit were indeed overcome by bubble actuation. The following explanation can be adopted. The sensing mechanism changes when moving from acids to alkali. Two different types of ions are primarily adsorbed on the sensor surface, namely hydroxonium/ H_3O^+ (in acids) and hydroxyl/ OH^- (in alkalis). The sensing time has two contributions: from mass transfer step and adsorption step, or $T = T_{\text{mass transfer}} + T_{\text{adsorption}}$. Without actuation, the sensing process is limited by mass transfer ($T_{\text{mass transfer}} \gg T_{\text{adsorption}}$); since hydroxonium ions are larger compared to hydroxyl ions and have lower mobility the sensing time is higher for hydroxonium ions, i.e., in acid buffer. When the bubbles are actuated, adsorption becomes the limiting step ($T_{\text{mass transfer}} \ll T_{\text{adsorption}}$). It is likely that hydroxonium ions have higher adsorption rate compared to hydroxyl ions due to the ease of ion rearrangement on graphene, and therefore the sensing time is shorter in acid.

Table 1. Sensing time reduction with and without bubble actuation for pH 4~10.

pH	T w/o bubbles (s)	T w/ bubbles (s)	Sensing time reduction (%)
4	780	35	95.5
5	760	45	94.1
6	740	35	95.3
7	475	35	92.6
8	490	50	89.8
9	270	70	70.2
10	460	55	88.0

Additionally, we also studied the changes in sensing time as the piezo was detuned from the working frequency (23.5 kHz) and with varying voltages. The buffer with pH=4 was used for these tests. It was shown that sensing time reduction improves with increasing driving voltage (up to 4 times) (Figure 2A) and sensing time reduction η exhibited resonant behavior (Figure 2B) with a resonant peak. Thus, the operating frequency range for this sensing cell was determined ($\Delta f = 10$ kHz).

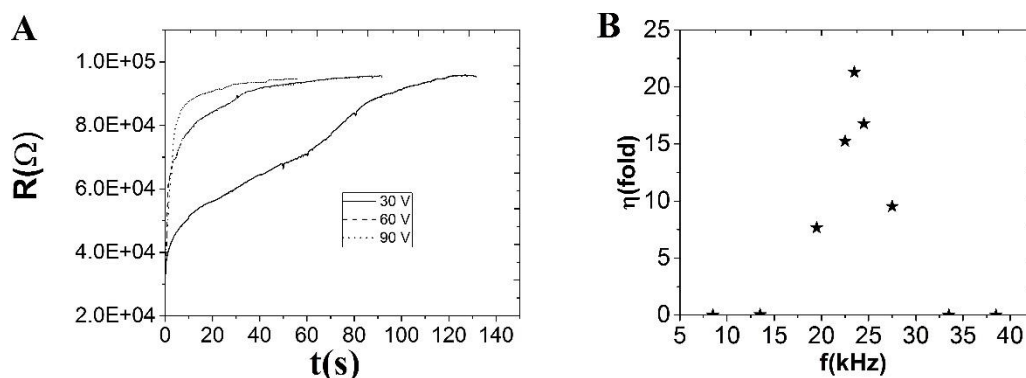


Figure 2. Operation optimization. A) Sensing time reduction for various driving voltages; B) Working frequency range for pH=4.

Conclusion

We have demonstrated the possibility to overcome the diffusion limits and reduce the sensor response time with actuated air-liquid bubbles trapped on prefabricated cavities. We suppose that the reduction in the sensor response time was caused by the enhanced mass transport near the sensor due to the microstreaming phenomenon. Finally, sensing enhancement was demonstrated for wide pH range (4–10). The best performance of the sensor was achieved for pH = 4 (95.5% time reduction). The proposed prototype can be useful for biochemical applications such as detection of large target molecules including glucose, DNA, cancer markers and proteins.

References

- [1] P.E. Sheehan, L.J. Whitman, Detection limits for nanoscale biosensors, *Nano Lett.* **5** (4) (2005) 803–807.
- [2] A.D. Stroock, S.K. Dertinger, A. Ajdari, I. Mezic, H.A. Stone, G.M. Whitesides, Chaotic mixer for microchannels, *Science* **295** (5555) (2002) 647–651
- [3] A. Hashmi, G. Yu, M. Reilly-Collette, G. Heiman, J. Xu, Oscillating bubbles: a versatile tool for lab on a chip applications, *Lab Chip* **12** (21) (2012) 4216–4227.



Acoustofluidic Platform for Organizing an Array of Single Cells

Benjamin B. Yellen^{1,2,3}, Korine A. Ohiri^{1,2}, Sean T. Kelly¹, Kevin H. Lin⁴, and Kris C. Wood⁴

¹Department of Mechanical Engineering and Materials Science, Duke University, Durham, NC 27708, USA
E-mail: yellen@duke.edu, URL: <https://sites.duke.edu/yellen/>

²NSF Research Triangle Materials Research Science and Engineering Center, Duke University, Durham, NC 27708, USA

³Department of Biomedical Engineering, Duke University, Durham, NC 27708, USA

⁴Department of Pharmacology and Cancer Biology, Duke University, Durham, NC 27708, USA

Introduction

Large-scale single cell analysis can be used to identify rare, but important, cellular events associated with poor clinical outcomes, with promising applications in drug discovery and development for oncology and infectious disease. For example, the fraction of cancer cells having intrinsic resistance to a therapy is often exceedingly low (i.e., occurring at frequencies of 1 in 10,000 or less); however over the course of treatment these drug-resistant cells become enriched leading to incurable tumors. This has motivated the development of integrated microfluidic platforms with the required scale and throughput needed to identify these rare events. A number of passive and active cell organization approaches have been devised, such as those based on harnessing differential fluidic resistance in microchannels¹⁻⁴, using stochastic deposition of cells into microwells⁵, and various trapping techniques based on electric⁶, magnetic⁷, optical⁸, or acoustic⁹ force fields. While each system has unique promising features, their individual limitations make it difficult to organize and maintain small communities of cells long enough to identify the rare phenotypes of interest.

We believe that combining the advantageous features of these different approaches into a hybrid microfluidic system offers the most flexibility in organizing more complex patterns of cells and reagents, which are increasingly necessary for advanced multi-dimensional phenotypic analysis and genomic profiling. Towards this end, we have developed a “trap and transfer” approach, which combines passive microfluidic trapping and active acoustic forces to transfer cells from a high-shear microfluidic trapping region into low-shear, spacious chambers that allow the outgrowth of each clone to be individually tracked over time. Figure 1 provides a general overview of the approach. Cells are first captured in microfluidic constrictions (Fig. 1a). Next, they are transferred to the opposite corner of the flow channel by reversing the flow rate and activating a piezoelectric transducer mounted underneath the chip (Fig. 1b). The corner position is in a flow stream that allows cells to be moved into the larger partition (Fig. 1c-d) under slow laminar flow. The density of the array elements shown in Fig. 1 allows up to 3,840 single cells (approximately 4/mm²) to be arranged in devices size of a typical glass slide. We have also designed higher density chips having more than 10,000 apartments on a glass slide.

We tested the acoustic transfer step on both polystyrene beads and a human lung cancer cell line of PC9 cells, which is a good model system for EGFR-inhibition based drug resistance mechanisms. An acoustic sweep shows that the transfer efficiency is optimal around 1.40MHz, but varies slightly for each array element. Thus, an acoustic sweep from 1.35 -1.42 MHz was found to work best with excitation voltage of 40V for the beads and 140V for the cells. As shown in Fig. 2, a single cell array with an efficiency of ~70% is achieved in a typical experiment. Cell organization efficiency can be improved by functionalizing the surface of the chip with a non-fouling brush and by limiting the number of pre-existing cell clumps.

One of the key advantages of the “trap and transfer” approach is that the microfluidic trap is reset after each step, which allows the process to be repeated to organize multi-component cellular patterns, including pairs of cells, as well as small communities of cells. Since this technique does not require cell labeling, is independent of cell type, and can be conducted directly in cell culture media, it can be used to organize a wide range of cell types as well as unique biological reagents, such as biosensing beads. Our current work is focusing on maintaining the cells inside the microfluidic chips for sufficient time, such that rare events of interest can be identified and more deeply probed and profiled with next generation genomic methods.

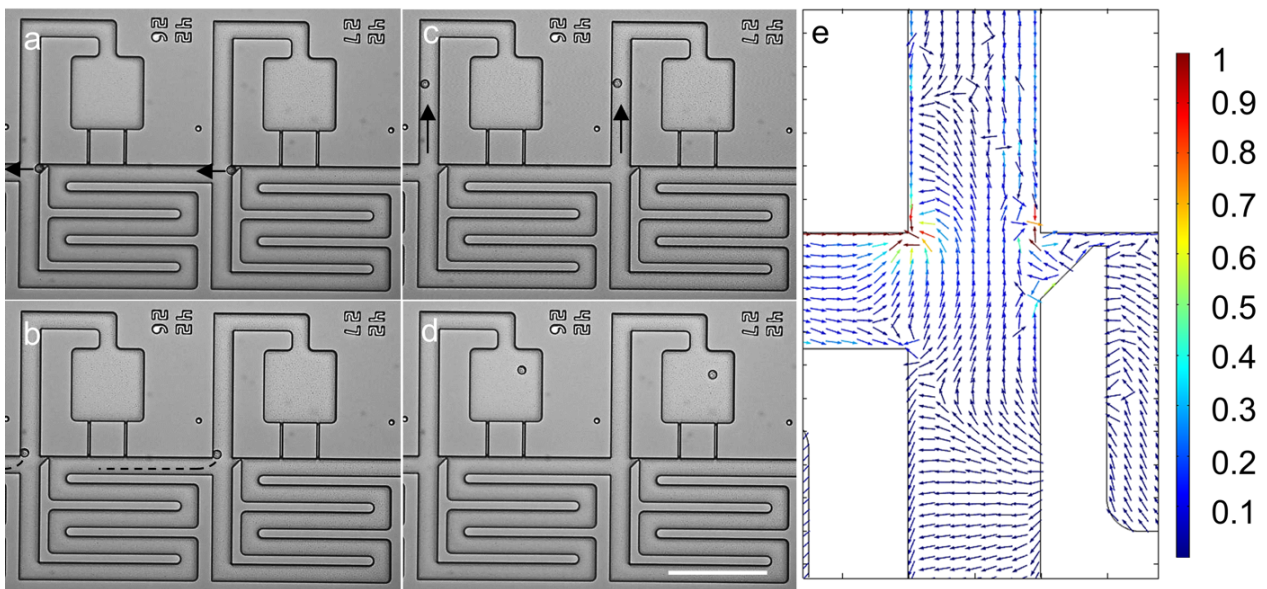


Figure 1: Optimization of acoustic switching mechanism. Cells are loaded into microfluidic traps (black arrows), shown in (a), next fluid flow is reversed and acoustic forces are used to attract cells to corner adjacent to the entryway into the partition and switched into flow fields entering the compartment region, shown in (b). Forward flow then pushes cells into the partitions as shown in (c) and (d). COMSOL calculations show that time-averaged acoustic force field when driven at 1.35 MHz. Scale bar represents 200 μm .

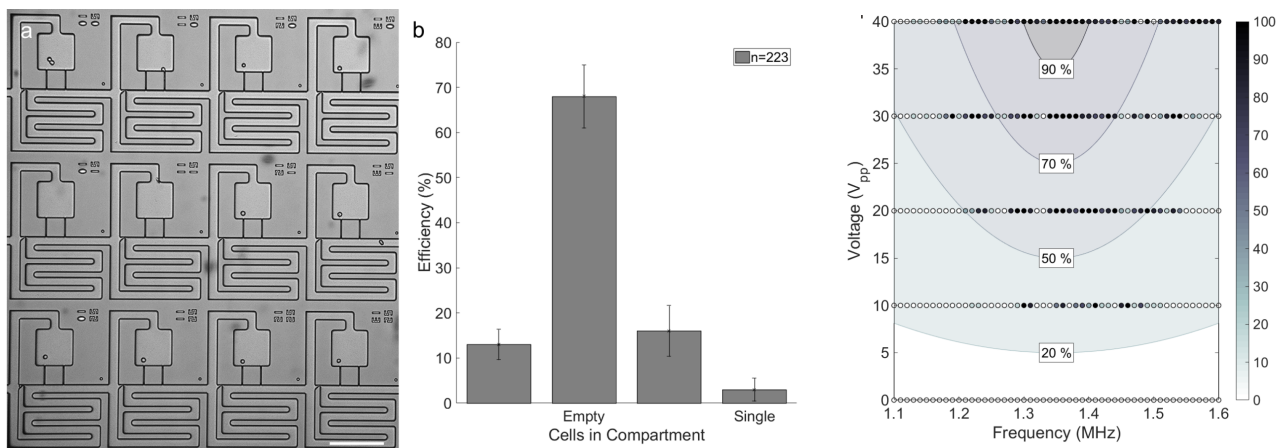


Figure 2: Generation of a single cell array. (a) Image of single cell array. Scale bar, 200 μm . (b) Distribution of cells in $n=223$ compartments in the acoustofluidic chip. (c) Acoustic transfer efficiency as a function of frequency and voltage.

References

- [1] A. R. Wheeler, et al. Microfluidic device for single-cell analysis, *Anal. Chem.*, 2003, 75, 3581–3586.
- [2] D. Di Carlo, L. Y. Wu and L. P. Lee, Dynamic single cell culture array, *Lab Chip*, 2006, 6, 1445–1449.
- [3] W. H. Tan and S. Takeuchi, A trap-and-release integrated microfluidic system for dynamic microarray applications, *PNAS* 2007, 104, 1146–1151.
- [4] Y. C. Chen, Z. Zhang, S. Fouladdel, Y. Deol, P. N. Ingram, S. P. McDermott, E. Azizi, M. S. Wicha, and E. Yoon, Single cell dual adherent-suspension co-culture micro-environment for studying tumor–stromal interactions with functionally selected cancer stem-like cells, *Lab Chip*, 2016, 16, 2935-2945
- [5] J. C. Love, J. L. Ronan, G. M. Grotenbreg, A. G. van der Veen, and H. L. Ploegh, A microengraving method for rapid selection of single cells producing antigen-specific antibodies, *Nat. Biotechnol.*, 2006, 24, 703–707.
- [6] B. M. Taff and J. Voldman, A scalable addressable positive dielectrophoretic cell-sorting array, *Anal. Chem.*, 2005, 77, 7976–7983.
- [7] B. Lim, V. Reddy, X. Hu, K. Kim, M. Jadhav, R. Abedini-Nassab, Y. W. Noh, Y. T. Lim, B. B. Yellen, C. G. Kim (2014) Magnetophoretic circuits for digital control of single particles and cells. *Nat Commun.* 5:3846.
- [8] Y. Chiou, A. T. Ohta and M. C. Wu, Massively parallel manipulation of single cells and microparticles using optical images, *Nature*, 2005, 436, 370–372.
- [9] F. Guo, Z. Mao, Y. Chen, Z. Xie, J. P. Lata, P. Li, L. Ren, J. Liu, Ji. Yang, M. Dao, S. Suresh, T. J. Huang, Three-dimensional manipulation of single cells using surface acoustic waves *PNAS* 2016 113 (6) 1522-1527.



Acoustofluidic system with integrated microvalves

Sinan Yigit¹, Han Wang², and Arum Han¹

¹Department of Electrical and Computer Engineering, Texas A&M University, College Station, TX
 E-mail: syigit@tamu.edu, URL: <http://biomems.tamu.edu/>

²Department of Biomedical Engineering, School of Medicine, Tsinghua University, Beijing, 100084, China

Introduction

Bulk acoustic wave-based (BAW) transversal resonator is one of the most commonly used configurations in acoustofluidics. In these systems, acoustic standing wave is generated between the two sidewalls of the microfluidic channel by exciting a piezoelectric transducer (PZT) attached to the bottom of the microchip [1]. However, this configuration has limited material choice in fabricating the microdevices since high characteristic acoustic impedance is needed for generating acoustic resonance field. Recently researchers have reported that some soft polymers such as (PDMS) can also be utilized in these systems. Leibacher et al. presented that stacking a PDMS layer to the sidewall in BAW-based acoustofluidic system can provide separated fluidic boundary and acoustic boundary [2]. This is because PDMS has similar characteristic acoustic impedance to water, and thus the acoustic wave transmits continuously across PDMS-water boundary [3]. However this modification to BAW-based devices using PDMS blocks in the lateral direction is of no help to provide active fluidic control such as switching different solutions on-chip, and also is unable to perform cell culture due to low gas permeability. In this research, we constructed a silicon/glass acoustofluidic microsystem that integrates a PDMS membrane to enable cell culture, with pneumatically actuated PDMS microvalves to provide the capability of fluidic control. This can be a milestone that may lead to a complete acoustofluidic lab-on-a-chip system more capable of performing biological and biomedical experiments using bulk acoustic wave.

Experiments

In this work we designed a prototype acoustofluidic device with integrated PDMS microvalves that has a long straight channel and a circular trapping chamber for characterization. Acoustic particle alignment and particle trapping were demonstrated with this design. The experiments were conducted by flowing 10 μm diameter polystyrene (PS) beads (Life technologies CA, USA) through the channel using a syringe pump (Fusion 400, Chemyx, Stafford, TX). Fabrication steps for the acoustofluidic device with integrated microvalves are summarized in Fig.1 and can be explained as follows: The top glass layer was fabricated using standard wet etching of borofloat glass (Silicon Quest International, CA) and the bottom layer was fabricated using wet etching (KOH) of silicon. The bottom silicon layer had a channel width of 375 μm , and the circular trapping chamber had a diameter of 2000 μm . Fluidic and pneumatic access holes were drilled in the top glass layer using a benchtop drill press (DP101, Ryobi Ltd, SC). The PDMS (Sylgard® 184, Dow Corning Corp., MI) membrane (thickness: $\sim 30 \mu\text{m}$) was fabricated by spin-coating liquid-phase PDMS at 3800 rpm for 40 sec on a transparency film (CG7060, Apollo) taped to a PMMA substrate, and pre-cured at 80°C for 30 min. Then the transparency film was separated from the PMMA substrate and the thin PDMS membrane was bonded to the top glass layer using oxygen plasma (Expanded plasma cleaner, Harrick Plasma, NY). Fluidic inlet/outlet holes were punched in the PDMS layer with a tweezer. This partial assembly was then post-baked for another 6 hr at 80°C, and connected to Tygon® tubing (Saint-Gobain Performance Plastics, OH) via flat-bottom ferrules (P-200N, Upchurch Scientific, WA). Then the partial assembly was bonded to the bottom silicon layer using oxygen plasma. Since the valves are normally closed, vacuum was applied to the top pneumatic valve layer by a syringe to prevent the PDMS layer from bonding to the silicon substrate at the microvalve region during the bonding process. Curing of the complete structure was done at 80°C for another 30 min. A piece of PZT (PZ26, Ferroperm Piezoceramics A/S, Denmark) was bonded to the bottom of the device by applying a thin layer of cyanoacrylate glue (Loctite Super glue, Henkel, Rocky Hill, CT).

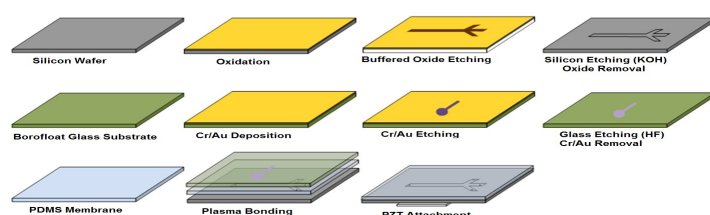


Figure 1: Summary of the fabrication steps

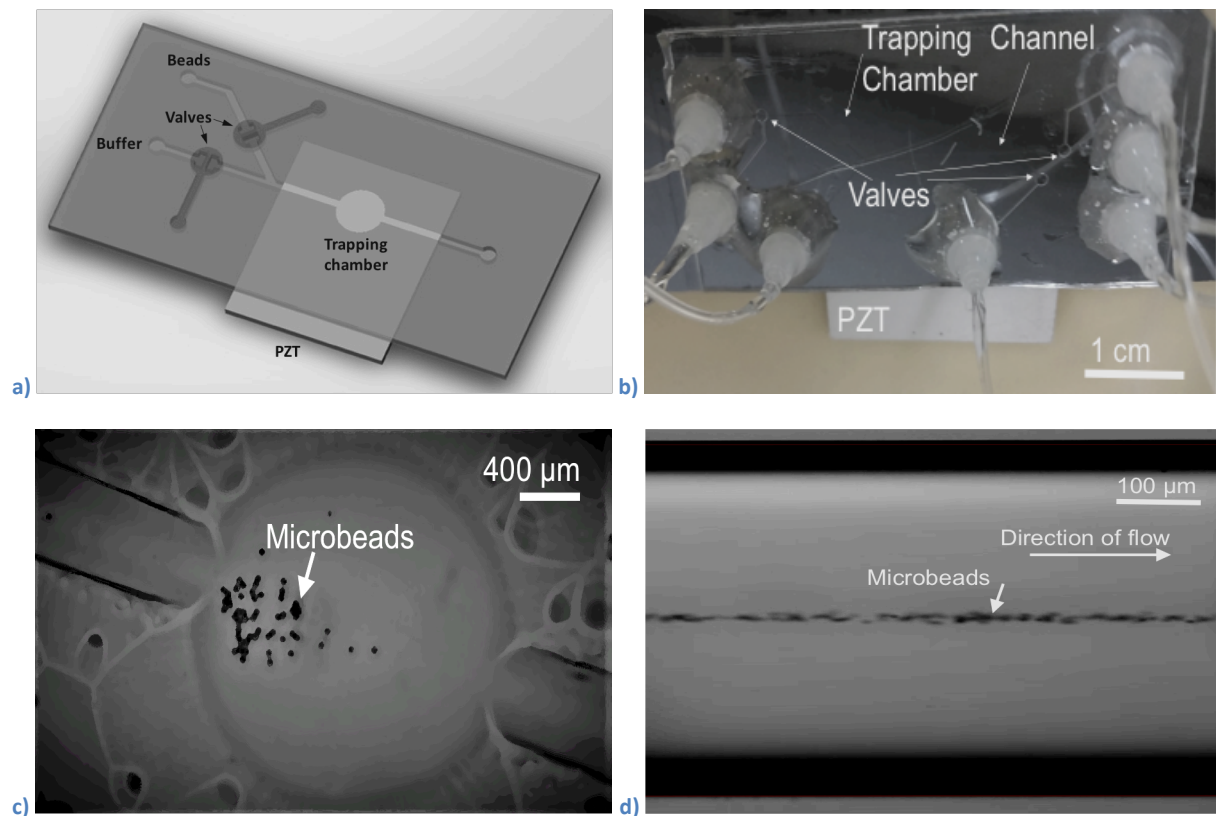


Figure 2: a) Illustration of an example acoustofluidic microsystem with integrated PDMS pneumatic valves. b) Fabricated device image. c) The microscopic image of the trapped polystyrene beads inside the trapping chamber when first harmonic frequency (0.75 MHz) is applied. d) The microscopic image of the focused polystyrene beads inside the straight channel when the channel width is 375 μm and first harmonic frequency (1.96 MHz) is applied.

Results

The device was characterized for its particle trapping efficiency compared to that of a typical silicon/glass device to understand the impact of the PDMS membrane. When trapping 10 μm diameter polystyrene (PS) beads (see Fig. 2.c) that flowed at a rate of 50 $\mu\text{l/hr}$ at the 2000 μm diameter circular trapping chamber, the applied voltage through a 50 dB power amplifier (2100L, Electronics & Innovation, Ltd., NY) had to be 80 mV as the minimum required voltage. On the other hand, acoustic alignment of PS beads to the acoustic pressure node in the microchannel was evaluated using 10 μm PS beads flown at a rate of 500 $\mu\text{l/hr}$. As can be seen in Fig. 2.d, PS beads were aligned in the middle at an applied voltage of 100mV through the 50 dB power amplifier. Using these results and previous works it is possible to say that although higher power is required when using PDMS/glass as the top cover of a microchannel compared to an anodic bonded glass cover, acoustofluidic manipulation and trapping of particles can still be achieved at a reasonable applied voltage level.

Conclusion

Here we proposed a novel method by adding PDMS membrane and microvalves to an acoustofluidics system for providing fluidic control capability. This shows the possibility that acoustic microsystems can benefit from proper integration with PDMS as structural material. Using the PDMS membrane will provide gas permeability which is essential for long-term cell culture. Further work will outline the effect of PDMS membrane to the cell viability.

Acknowledgment: Sinan Yigit is supported by the Ministry of National Education of the Republic of Turkey.

References

- [1] A. Lenshof, M. Evander, T. Laurell and J. Nilsson, *Lab on a Chip*, **12**, 684-695 (2012).
- [2] Leibacher, I., Schatzer, S. and Dual, J., *Lab on a Chip*, **14(3)**, pp.463-470 (2014).
- [3] Gedge, M. and Hill, M., *Lab on a Chip*, **12(17)**, pp.2998-3007 (2012).
- [4] Rune Barnkob, *Procs. pp. 19-20, Acoustofluidics 2016*, Kongens Lyngby, Denmark, 22 - 23 September 2016.



Acoustofluidic particle manipulation inside a droplet using Lamb wave resonators

Hongxiang Zhang, Zifan Tang, Zhan Wang, Shuting Pan, Chongling Sun, Xuexin Duan, and Wei Pang

State key Laboratory of Precision Measuring Technology and Instruments, Tianjin University, Tianjin, China
E-mail: weipang@tju.edu.cn

Introduction

Electromechanical transducers, such as bulk acoustic wave resonator (BAW) and surface acoustic wave resonator (SAW), have been employed in stimulating acoustic streaming, trapping particles even molecules at special position in microfluidic platform [1-4], due to their small size, convenient driving, low consumption, excellent biocompatibility, and easy integration. In this work, we studied the acoustic streaming effects of multiple Lamb wave resonators (LWRs) in liquid. A novel device array which consists of 4 LWRs was designed and fabricated on a $1.5 \times 1.5 \text{ mm}^2$ silicon die. A 3D finite element model was built to simulate the distributions of multiple micro-vortexes induced by the LWR array. Experimentally, we demonstrated the LWR array can efficiently drive multiple cylindrical vortexes in a $1 \mu\text{L}$ drop above the device and further trapped the bioparticles at the center of the vortex, which shows a great potential for biomolecular manipulations and biosensing applications.

The structure of the Lamb wave resonators

The structure of the LWR in this system is schematic drawn in Fig. 1(a). The piezoelectric film formed by $1.5 \mu\text{m}$ aluminum nitride (AlN) is sandwiched by bottom and top electrodes, and each of the electrode layer is $0.2 \mu\text{m}$ molybdenum. When the LWR working in liquid at its resonant frequency, the S_0 mode of Lamb wave can be excited in the resonator and then propagate to liquid from each side of boundaries. The attenuation of the acoustic wave in fluid induces a constant force, which motivate a directional flow, i.e. acoustic streaming. On the basis of the above analysis, we design and fabricate an LWR array to trigger microvortices and concentrate the particles in liquid. Four 384 MHz LWRs are designed on the same silicon die as shown in Fig. 1(b). Fig. 1(c) shows the scanning electron micrograph (SEM) image of the device consisting of four LWRs and metal connecting wires. The die size of the LWR array device is $1.5 \times 1.5 \text{ mm}^2$ in square.

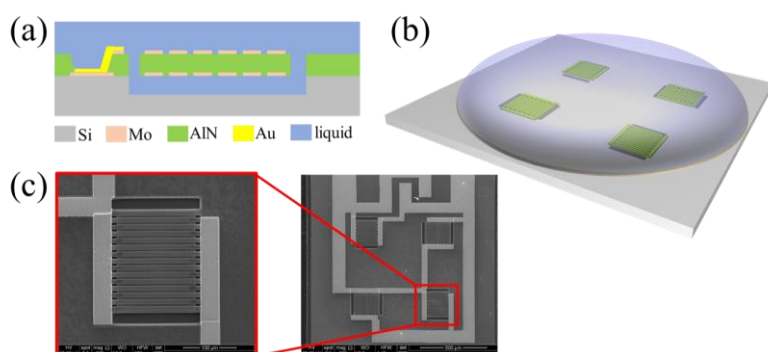


Figure 1: (a) Schematic illustration of the structure of an LWR in liquid. (b) Schematic illustration of the LWR array on the silicon chip with a drop of liquid. (c) The SEM images of the single LWR and the LWR array on the silicon chip.

Numerical simulation method

A commercial finite element analysis software COMSOL, is used to simulate the vibration of the LWR and the acoustic streaming in liquid. This model involves in four modules coupling, including solid mechanics, electrostatics, acoustic pressure, and laminar flow. The first three modules can be synchronously solved in frequency domain to calculate the vibration in piezoelectric film and liquid. As is shown in Fig. 2(a), the simulation result of acoustic wave in liquid is cylindrical with a spindle-shaped pressure distribution p :

$$p(\mathbf{r}, t) \sim A \frac{e^{-(ik+\beta)\rho}}{\sqrt{\rho}} \sin \frac{\pi}{L} y e^{i\omega t}$$

Next, the laminar flow module is coupled by adding the body force \mathbf{f} , obtaining by the vibration of the acoustic wave \mathbf{v}_1 . \mathbf{f} is set as a domain condition to compute the flow field under the vibration of device:

$$\mathbf{f} = -\left[(\mathbf{v}_1 \cdot \nabla \bar{\mathbf{v}}_1 + \bar{\mathbf{v}}_1 \cdot \nabla \mathbf{v}_1) + c.c. \right]$$

The simulation result of the acoustic streaming generated by the LWR array device is demonstrated in Fig. 2(b). The liquid is pushed away from both sides of each LWR by the driving force, in the same direction with the wave propagation. The negative pressure of the fluid above each LWR leads to the convergence of two flows along the electrodes. An anticlockwise horizontal cylindrical vortex (main vortex) dominates the flow in the center of the field, accompanied by eight secondary vortices in the surrounding.

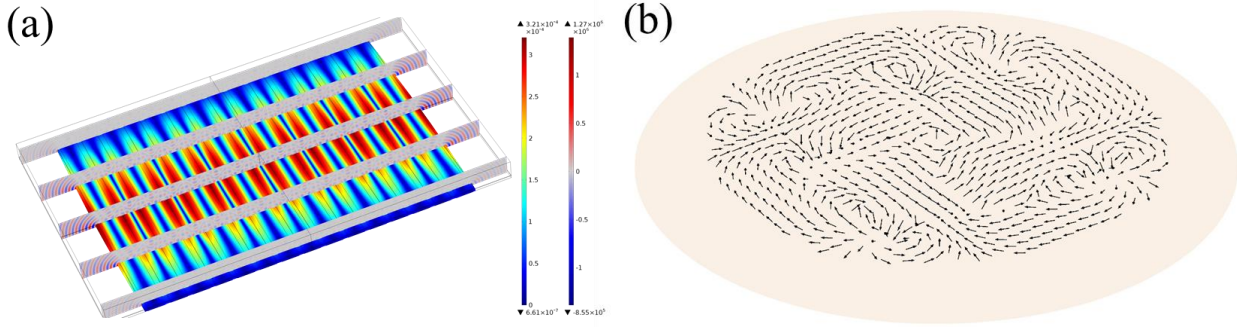


Figure 2: (a) Simulation results of the displacement distribution of the Lamb wave in solid and the pressure distribution of the cylindrical acoustic wave in liquid. (b) Simulation result of the 3D acoustic streaming induced by the LWR array.

Experimental results

A 40 mW, 384 MHz alternating current signal was applied to the device, and 1 μL solution of 5 μm polystyrene particles was dropped on the device and covered the whole area of the LWR array. The image of the particle trajectories at the initial moment, when signal source was turned on, is shown in Fig. 3(a), and the main vortex with eight secondary vortices can be seen. In 2 minutes, most of the particles were trapped into the main vortex and the cluster reached to the maximum radius of 200 μm (Fig. 3(b)).

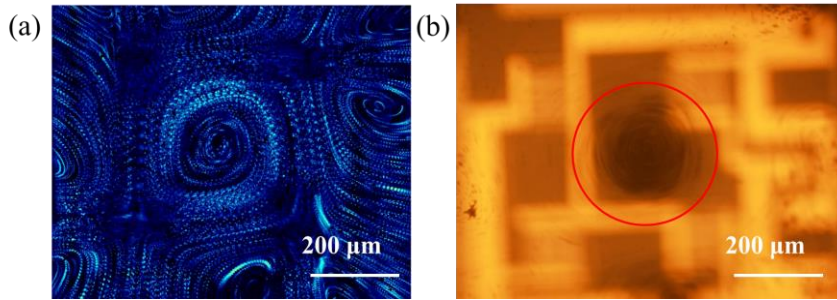


Figure 3: (a) The image of the particle trajectories at the initial moment. (b) Microscope images of the distributions of the polystyrene particles 2 min after the power of the driving signal turning on.

Conclusion

We have investigated the behavior of the Lamb wave resonator in fluid by theoretical analysis and numerical simulation. An AlN MEMS device consisting of 4 LWRs which structured on a $1.5 \times 1.5 \text{ mm}^2$ silicon die, has been designed, simulated, fabricated, and applied to stimulate nine vortices in a 1 μL drop. The experiment results that 5 μm polystyrene particles can be trapped in the center of the main vortex, shows the potential of the LWR based microfluidic platform for biosensing applications.

References

- [1] Guo, F; Mao, ZM; Chen, YC; Xie, ZW; Lata, JP; Li, P; Ren, LQ; Liu, JY; Yang, J; Dao, M; Suresh, S; and Huang, TJ, Proc. Natl. Acad. Sci., **113**(6), 1522-1527, (2016).
- [2] Friend, J.; and Yeo, L.Y., Reviews of Modern Physics, **83**(2), 647-704, April-June 2011
- [3] Hahn, P.; Leibacher, I.; Baasch, T.; and Dual, J., Lab on a Chip, **15**(22), 4302-4313, 21 Nov. 2015.
- [4] Junjun Lei; Hill, M.; and Glynne-Jones, P, Lab on a Chip, **14**(3), 532-541, 7 Feb. 2014